Galaxy Evolution from the SDSS and EDisCS Surveys

Dissertation der Fakultät für Physik
der
Ludwig-Maximilians-Universität München

vorgelegt von

Anja von der Linden

aus Stuttgart

München, den 2. November 2007

Meinen Eltern gewidmet.

Contents

Contents

Contents

Zusammenfassung

Die Galaxienpopulation in Galaxienhaufen unterscheidet sich systematisch von jener im Feld, und es ist eines der Ziele der modernen Astrophysik, die Prozesse zu identifizieren, durch welche dies zustandekommt. In dieser Arbeit charakterisiere ich verschiedene Aspekte der Galaxienpopulationen in Galaxienhaufen:

Im ersten Teil der Arbeit untersuche ich *Hellste Haufengalaxien* (auf englisch *Brightest Cluster Galaxies*, BCGs). In den Zentren der meisten Galaxienhaufen befindet sich eine hellste, dominante Galaxie, zumeist eine elliptische Galaxie. Es ist bereits bekannt, dass diese Galaxien sich von anderen unterscheiden: Zum Beispiel enthalten sie oft einen radio-lauten Aktiven Galaktischen Nukleus (AGN), und folgen nicht den gleichen Skalierungsrelationen elliptischer Galaxien. Allerdings gehören BCGs zu den massereichsten Galaxien im Universum und es war bisher nicht klar, ob diese Unterschiede auf ihre höhere Masse, oder auf ihre Lage im Haufenzentrum zurückzuführen sind. Um diese beiden Faktoren zu unterscheiden, habe ich ein Sample von mehr als 600 BCGs aus Daten des *Sloan Digital Sky Survey* (SDSS) erstellt und diese verglichen mit einem Sample nicht-BCGs, welche die gleichen stellaren Massen, Rotverschiebungen, und Farben haben. Trotz dieser Abgleichung unterscheiden sich BCGs systematisch von nicht-BCGs. In der Tat enthalten sie öfters einen radio-lauten AGN. Zudem haben sie größere Durchmesser und höhere Geschwindigkeitsdispersionen, welches impliziert, dass sie einen höheren Anteil Dunkler Materie enthalten. Durch dieses unterschiedliche Masse-zu-Leuchtkraft-Verhältnis liegen elliptische BCGs auf einer anderen Fundamentalebene (einer Beziehung zwischen Geschwindigkeitsdispersion, Durchmesser und Flächenhelligkeit) als normale elliptischer Galaxien. Auch folgen sie einer anderen Faber-Jackson-Beziehung (einer Beziehung zwischen Helligkeit und Geschwindigkeitsdispersion), eine Bestätigung der Vorhersagen von Simulationen, in denen BCGs durch Verschmelzung von Gas-armen Galaxien auf radialen Orbits entstehen. Diese Resultate zeigen, dass die Entstehung von BCGs eng an die Entstehung von Galaxienhaufen geknüpft ist.

Während BCGs sicherlich ein spektakuläres Beispiel dafür sind, wie sich Haufengalaxien von Feldgalaxien unterscheiden, besteht eine Beziehung zwischen der Umgebung und den Galaxieneigenschaften auch für die anderen Haufengalaxien, zumindest im statistischen Sinn: In Galaxienhaufen gibt es mehr Galaxien ohne aktive Sternentstehung, sowie mehr elliptische Galaxien. In einem hierarchischen Universum, in dem Strukturbildung auf kleinen Skalen anfängt, und später größere erfasst, wachsen Galaxienhaufen durch Akkretion anderer Strukturen, also auch Galaxien. Diese hinzukommende Galaxienpopulation kann vorhandene Beziehungen zwischen Umgebungsdichte und Galaxienpopulation verändern, oder diese Galaxien werden tatächlich zu Haufengalaxien transformiert. In diesem Szenario muss sowohl die Sternentstehung unterbunden werden, wie auch die Galaxienmorphologie geändert werden.

Inzwischen gibt es vermehrte Hinweise, dass es primär die Sternentstehungsrate ist, die mit der Umgebung korreliert, und dass Morphologie nur eine sekundäre Korrelation darstellt.

Deshalb habe ich mich in den weiteren Teilen der Arbeit auf Sternentstehungsindikatoren konzentriert. Im zweiten und dritten Teil der Arbeit untersuche ich die Galaxienpopulationen als Funktion des Abstands zum Haufenzentrum, indem ich über ein Sample von 500 Galaxienhaufen im lokalen Universum mittle, wiederum mit Daten des SDSS. Diese *Radialprofile* eines *zusammengesetzten Galaxienhaufens* haben die weitere Interpretation, dass der Abstand zum Haufenzentrum nicht nur mit der lokalen Dichte, sondern auch mit der Zeit, die seit dem Einfall in den Haufen vergangen ist, anti-korreliert.

Im zweiten Teil der Arbeit benutze ich die photometrischen Kataloge des SDSS, um das durchschnittliche Anzahldichteprofil dieser Haufen zu erstellen. Dieses hat eine ähnliche Form wie jenes von Halos Dunkler Materie. In Bezug auf rote Galaxien (also solche mit wenig aktiver Sternentstehung) finde ich, dass die Anzahl leuchtschwacher zu leuchtstarker Galaxien zum Haufenzentrum hin zunimmt. Ebenso nimmt ihre typische Masse ab. Wenn allerdings auch die blauen Galaxien berücksichtigt werden, so bleibt die charakteristische Masse konstant. Dies weist darauf hin, dass die Sternentstehung in Galaxien, die in den Haufen fallen, in einem Zeitraum unterbunden wird, der von ähnlicher Größenordnung ist wie die Zeit, die Galaxien brauchen, um einen Haufen zu durchqueren, als ein paar Giga-Jahre. Dadurch schwindet die Leuchtkraft der Galaxien, und ihre Farbe ändert sich von blau zu rot.

Die Untersuchung der Sternentstehung in Haufengalaxien wird fortgesetzt im dritten Teil der Arbeit, in dem ich die kürzliche Sternentstehungsgeschichte jener Galaxien untersuche, welche auch spektroskopisch beobachtet wurden. Ich finde eine starke Beziehung zwischen Entfernung vom Haufenzentrum und Sternentstehungsaktivität: Im Haufenzentrum haben fast alle Galaxien aufgehört, Sterne zu bilden. Diese Beziehung ist am stärksten ausgeprägt für Galaxien mit geringer stellarer Masse - im Feld trifft dies nur für wenige Galaxien zu. Auch dieses Resultat ist konsistent mit einem Szenario, in dem die Sternentstehung auf einer Zeitskala von ein paar Gigajahren unterdrückt wird. Diese Interpretation wird zudem dadurch gestützt, dass in jenen Galaxien, die (noch) Sterne bilden, die typische Sternentstehungsrate zum Haufenzentrum abnimmt.

Im vierten und letzten Teil der Arbeit erweitere ich die Untersuchung auf Galaxien des ESO Distant Cluster Surveys (EDisCS). Die Galaxiengruppen und -haufen des EDisCS Samples befinden sich bei Rotverschiebungen $0.4 - 0.8$, und werden deshalb zu früheren Zeiten beobachtet als die Haufen des SDSS Samples. Ihre Massen legen allerdings nahe, dass sie ein repräsentatives Sample der Vorgängersystem der lokalen Haufen sind, so dass Vergleiche der zwei Samples es erlauben, auf die Evolution der durchschnittlichen Eigenschaften zurückzuschließen. Auch in den EDisCS Haufen ist die Beziehung zwischen Entfernung zum Haufenzentrum und Sternentstehungsaktivität bereits ausgeprägt. Die Mehrheit der Haufengalaxien hat aufgehört, Sterne zu bilden, obwohl diese Anzahl in den lokalen Haufen weiter ansteigt. Diese Ähnlichkeit suggeriert, dass es die gleichen Prozesse sind, die auf einfallende Galaxien wirken, zumindest über die Zeitspanne, die hier untersucht wird. Insbesondere finde ich keine Hinweise, dass Prozesse, die auf wesentlich kürzeren Zeitskalen wirken, bei höheren Rotverschiebungen eine größere Rolle spielen. Der höhere Anteil Galaxien mit aktiver Sternentstehung kann alleine auf die höhere Sternentstehungsdichte im Feld und die höheren Einfallsraten zurückgeführt werden.

Summary

The galaxy population in clusters of galaxies is known to differ systematically from the field population, and it is one of the goals of modern astrophysics to understand by which processes the differences in the galaxy populations arise. In this thesis, I characterize the cluster galaxy populations in several ways:

In the first part of the thesis, I investigate *Brightest Cluster Galaxies* (BCGs). Many clusters have a central, dominant galaxy, usually an elliptical. It has been noted before that these galaxies differ from other galaxies, e.g. they are found to often harbor a radio-loud Active Galactic Nucleus (AGN), and they do not follow some of the scaling relations which typically describe elliptical galaxies. But they are also among the most massive galaxies in the universe, and up to now, it was not clear whether they are different because of their large mass or because of their location at the cluster center. To distinguish mass effects from environmental effects, I have compiled a sample of more than 600 BCGs from the *Sloan Digital Sky Survey* (SDSS), and compare these BCGs to a sample of non-BCGs, matched in stellar mass, redshift, and color. I find that BCGs are indeed special, and differ systematically from other galaxies. At fixed stellar masses, they are indeed more likely to host a radio-loud AGN, which is likely due to the large gas reservoir the cluster provides as fuel for the AGN. They have larger radii and higher velocity dispersions, which implies that BCGs have a larger dark matter fraction. Because of the different mass-to-light ratio, elliptical BCGs do not lie on the same Fundamental Plane (a relation of velocity dispersion, radius, and surface brightness) as other elliptical galaxies. They also lie on a steeper Faber-Jackson relation (a relation between luminosity and velocity dispersion), as has been suggested by models in which BCGs assemble via dissipationless mergers along preferentially radial orbits. These results demonstrate that the assembly of BCGs is intricately linked to the assembly of clusters themselves.

While BCGs are a striking example of how the galaxy population in clusters differs from the field, a systematic relation between the environment and galaxy properties applies at least statistically also to other galaxies: clusters are found to harbor more galaxies in which star formation has ceased, as well as more elliptical galaxies, than the field. This relation can arise in two ways: the differences may reflect different conditions at the time of formation, or galaxies may be transformed upon entering the cluster environment. In a hierarchical universe, where structure formation takes place 'bottom-up', both are thought to play a role. Galaxies in dense environments formed earlier than their low-density counterparts, and thus to possibly different conditions. But the hierarchical scenario also predicts that galaxy clusters grow by accreting mass and galaxies. The infalling galaxy populations could alter the density gradients imprinted at earlier times, or the galaxies are indeed transformed to resemble cluster galaxies. For this scenario, the processes acting on the infalling galaxies need to halt star formation and affect the galaxy morphology.

Summary

There is increasing evidence that it is mainly star formation which correlates with environment, and morphology is only a secondary correlation. For this thesis, I have focused on star formation indicators to investigate galaxy populations. In the second and third part of the thesis, I investigate the galaxy population as function of distance from the cluster center, averaging over a sample of 500 clusters in the local universe, again using data provided by the SDSS. These *radial profiles* of a *composite cluster* have the intriguing interpretation that distance from the cluster center anti-correlates not only with local density, but also with the time since infall into the cluster environment.

In the second part of the thesis, I use the photometric SDSS catalogs to reconstruct the average number density profile of these clusters, which is found to be of similar shape as the density profiles of dark matter halos. Considering the population of red galaxies (i.e. galaxies with little on-going star formation), I find that the ratio of faint-to-luminous galaxies increases towards the cluster center, along with a decrease in the average stellar masses of red galaxies. However, if also blue galaxies are taken into account, the average galaxy mass remains constant. These findings argue for a scenario where infalling galaxies cease forming stars on a time scale similar to a cluster crossing time, i.e. a few Gigayears, and subsequently fade and redden.

The investigation of the star formation activity of cluster galaxies is further refined in the third part of the thesis, where I study the recent star formation history of the subset of galaxies with available spectroscopic SDSS data. I find a strong star formation – radius relation, with almost all galaxies in the cluster core having ceased star formation. The dependence of the galaxy mix on clustercentric distance is most pronounced for galaxies with small stellar masses - in the field, only few low-mass galaxies are quiescent. Also these results are consistent with a scenario where star formation is quenched predominantly on a time scale of a few Gigayear. This scenario is further supported by the decrease of the typical star formation rate of those galaxies which are (still) forming stars.

In the fourth and last part of the thesis I extend the study of galaxy populations to clusters in the *ESO Distant Cluster Survey* (EDisCS). The groups and clusters in the EDisCS sample are at redshifts $0.4 - 0.8$, and are thus seen at much earlier cosmic times than the SDSS cluster sample The distribution of cluster masses suggests that they are a representative sample of progenitor systems to the latter, allowing to study the evolution of the ensemble cluster properties over almost half of cosmic time. I find that the star formation – radius relation is already well in place in the EDisCS clusters. The majority of galaxies are quiescent, although this fraction further increases in the local clusters. These results suggest that the processes acting on infalling galaxies are similar over the redshift range studied. In particular, I do not find evidence that processes affecting star formation on significantly shorter timescales than a Gigayear play an increased role at higher redshifts. The increased number of non-quiescent galaxies in high redshift clusters can be accounted for by the increased star formation rate in field galaxies and the increased infall rate at higher redshifts.

1

Context and Framework

This introductory chapter places the thesis within the context of the study of galaxies and clusters. After a general motivation for the study of galaxy evolution in galaxy clusters, I give a brief historical introduction, and continue with two observational concepts that are crucial to the study of galaxies, and of their interaction with cluster: galaxy bimodality and the morphology–density relation. Interpretations of the latter need to be placed within the context of structure formation in the universe, and thus I briefly review the basic concepts of the current cosmological paradigm in Sect. 1.4. This allows to consider the formation and evolution of galaxies within the concept of hierarchical structure formation. I summarize previous results and current perceptions of the redshift dependence of cluster galaxy populations and end with a statement about the aims and content of this thesis.

1.1 Galaxy clusters as sites of galaxy evolution

Galaxy clusters offer a compelling environment to study the properties of galaxies. Cluster centers are characterized by a high density of galaxies and intracluster gas, as well as high relative galaxy velocities. This is a substantially different environment than the field, and indeed, cluster galaxies differ at least statistically from field galaxies. The identification of the processes which link galaxy properties to the host cluster are a matter of on-going research. Observations of galaxy clusters are a convenient tool to studying the possible environmental processes acting on galaxies: the number densities of galaxies in clusters are higher than in the field, so that many galaxies can be observed in a single image. Observing galaxies in the cluster center to the cluster outskirts probes a range of environment, which aids in determining which processes influence galaxy properties, and their relative strengths.

Furthermore, one class of galaxies, the cD galaxies, are found only in cluster cores. cD galaxies are a special case of the Brightest Cluster Galaxies, which typically reside at the cluster center. Their formation, and evolution, must therefore be intricately linked with the host cluster.

In terms of mass, galaxies are the smallest cluster constituent; they are the "frosting on the cake". This thesis focuses mainly on studying how the cluster environment influences the cluster galaxies. However, the cluster galaxies and their evolution are also important for other cluster components, in particular the intracluster medium: The star formation in galaxies produces the heavy elements which enrich the hot gas, thereby affecting its radiative cooling properties. Also dissipative processes, such as heating by a central Active Galactic Nucleus, are a connection between the galaxies and the intracluster gas.

1.2 The study of galaxies and galaxy clusters - historical beginnings

For eons, mankind perceived the night sky to consist of the about five thousands stars visible to the unaided eye, the Moon, six "wandering stars" (planets), a diffuse band across the sky - the *Milky Way* - and a few diffuse, faint *nebulae*. This view changed profoundly when Galileo turned a telescope to the sky. Among other discoveries, he realized that the diffuse light seen as the Milky Way stems from a myriad of stars. This led the philosopher Immanuel Kant to speculate that the Milky Way is a rotating disk of stars, and that other such "island universes" should exist.

Better telescopes, and more observers, led to the discovery of many more nebulae. A first catalog of about a hundred such nebulae was compiled by Messier towards the end of the 18th century, and was later followed by Herschel's list of about two thousand nebulae. In the middle of the 19th century, Lord Rosse noted distinct spiral shapes in some nebulae. He believed that these nebulae were systems of stars similar to the Milky Way itself. Other astronomers maintained that the nebulae were gas clouds within the Milky Way. The question of the nature of the *spiral nebulae* was of considerable importance, as it set the scale of the universe: did the Milky Way fill the entire universe, or was it one of many systems, as proposed by Kant? This controversy culminated in *The Great Debate* between Shapley and Curtis on April 26, 1920. But it was not until Hubble's observations of Cepheid variable stars in the Andromeda nebula a few years later that the existence of other galaxies was placed on firm observational grounds: the relation between the pulsation period and intrinsic luminosities of Cepheids allows distance measurements and proved the Cepheids in the Andromeda nebula to be at much greater distances than any objects in the Milky Way. It was thus established that there are other "Milky Ways", or *galaxies*, from the Greek expression for "milky circle", beyond our own.

While the concept of galaxies has been established only recently, the concept of *galaxy clusters* has been developed along with it. Already Messier noted an accumulation of "nebulae" within the Virgo constellation and also Herschel noted a "remarkable collection of many hundreds of nebulae" in the constellation of Coma Berenices. Today we know that the Virgo cluster is the closest galaxy cluster, whereas the Coma cluster the closest truly massive cluster of galaxies. Due to their proximity, both of these have played important roles in the study of galaxy clusters.

At the beginning of the 20th century, spectroscopy was first applied in astronomical observations. In 1912 Slipher noted that the spectral lines of some *spiral nebulae* were shifted, predominantly towards redder wavelengths. This *redshift* (or blueshift in some cases) was widely interpreted via the Doppler shift to be due to galaxy velocities relative to the Milky Way.

Figure 1.1: The galaxy cluster RXJ1347-1145. (Giant) elliptical galaxies are visible, as well as blue late–type galaxies. The features aligned tangentially to the cluster center are strongly–lensed arcs.

Hubble found that the redshift increases with galaxy distance, determined from Cepheids. This was first observational evidence for an expanding universe. But the velocity measurements also proved particularly interesting for galaxy clusters: Zwicky (1933) applied the virial theorem to the velocity measurements of galaxies in the Coma cluster and showed that the velocity dispersion is considerably larger than expected from the cumulative stellar mass of the cluster galaxies. He speculated that clusters must contain a component of *dark matter* which keeps them gravitationally bound. Although this concept was unpopular at Zwicky's time, dark matter has become an important aspect of today's standard cosmological paradigm. Various observations indicate that $\sim 85\%$ of the mass in galaxy clusters is in the form of dark matter.

The studies by Hubble and Zwicky profited vastly from the systematic surveys for nebulae that had become possible with photographic plates at the end of the 19th century. Galaxy clusters, however, were discovered largely serendipitously from these surveys. This situation changed with the work of Abell (1958), who compiled the first homogeneously selected sample of about 1600 galaxy clusters [1]. Abell categorized the clusters by *richness*, a proxy for the cluster mass, and by distance. The radius within which he counted cluster members was defined as a function of distance, approximating a set physical radius for each cluster. For a long time, the Abell cluster sample has been used as the standard cluster sample.

With the advent of X-ray astronomy, it was discovered that galaxy clusters are bright X-ray sources (Meekins et al. 1971). The source of the X-ray emission is mostly the intracluster medium (ICM), diffuse hot gas, which accumulates in the potential well of the clusters. The ICM is the second largest mass component after the Dark Matter, accounting for 10-15% of the total cluster mass. Owing to the lack of fore-/background contamination, and the rigorous scaling of X-ray luminosity with gas density, X-ray observations have become an important tool to identify and to study clusters.

Galaxy clusters as a whole have become powerful cosmological probes, and a review of the more recent, exciting developments in cluster physics is beyond the scope of this thesis (a comprehensive review is found in Biviano 2000). Rather, this introductory chapter concentrates on the relation of clusters and galaxies, as this is the central topic of this thesis.

1.3 The morphology–density relation and the bimodality of galaxies

Already Lord Rosse had noticed spiral structures in some nebulae, while other nebulae appear as homogeneous, elliptical clouds. With the use of photographic plates, it became clear that galaxies come in various flavors. This led Edwin Hubble to develop a classification scheme based on the morphological appearance of galaxies (Fig. 1.2). The two main morphological types are elliptical galaxies and spiral galaxies. At the time, it was thought that elliptical galaxies develop into spiral galaxies, hence the former were coined early-type, the latter late-type galaxies. The intermediate type, lenticular or S0 galaxies (galaxies with a disk, but no spiral arms) are considered early-type, as well.

Shapley first noted in 1926 that galaxies in the Coma cluster are predominantly early-types, but thought that this was simply a resolution issue. It was Hubble (1936) who first corre-

---

[1] Abell's milestone paper was "a portion of a thesis submitted in partial fulfillment of the requirements for the Ph.D. degree"
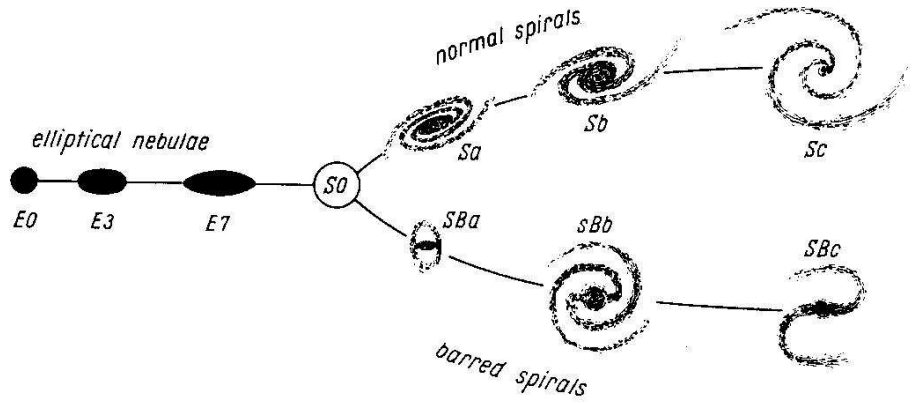
Figure 1.2: The Hubble "tuning fork" of galaxy morphologies. Elliptical galaxies (on the left) are shown as a sequence of different axis ratios; whereas spiral galaxies are divided into those with and without strong bars, and further subdivided by the opening angle of the spiral arms.

lated the occurrence of morphological type with the cluster density - the *morphology–density relation*. He found that elliptical galaxies were the most frequent galaxies in clusters, whereas the field is dominated by late-type spirals. An extreme example of morphological segregation was found by Morgan & Lesh (1965) - they identified a class of elliptical galaxies, the "super-giant" cD galaxies, which are found only in the centers of clusters. Oemler (1974) found that the degree of morphological separation depends on the overall cluster properties, but Dressler (1980) showed that the morphology-density relation is driven mainly by the local density of galaxies. Dressler's paper strikingly demonstrates and quantifies the occurrence of elliptical, S0s, and spiral galaxies as a function of projected galaxy density.

As galaxies separate into two distinct morphological types, also other properties show clear bimodal distributions. In particular, galaxies show a bimodal distribution of their average color. Since most of the galaxy light comes from stars, this indicates that the average stellar populations must be different. Hot, blue stars have rather short lifetimes; thus, blue galaxies must be forming stars (or have formed stars very recently). As stellar populations age, the more massive (and bluer) stars die, and the average color becomes redder. Red galaxy colors therefore indicate old stellar populations, with no appreciable level of current or recent star formation. The distinction between blue and red galaxies corresponds to a distinction between star-forming galaxies and quiescent galaxies.

The morphological and the color bimodality are not entirely independent: early-type galaxies are generally redder than late-type galaxies (Fig. 1.3). Galaxies thus come mainly in two flavors: disk galaxies with young stellar populations, and spheroidal galaxies with old stellar populations. Kauffmann et al. (2003b) show that the bimodality is a function of the stellar mass of the galaxy with a transition occurring at $3 \times 10^{10} M_\odot$. Lower mass galaxies are typically actively forming stars in a disk, higher mass galaxies are mostly quiescent ellipticals. However, the correlation between morphology and star formation rate is not absolute, i.e. there are disk galaxies with little star formation and red colors (Fig. 1.4), and elliptical galaxies with blue colors (Fig. 1.5).

Still, the morphology–density relation translates also to a color–density relation (Balogh et al.
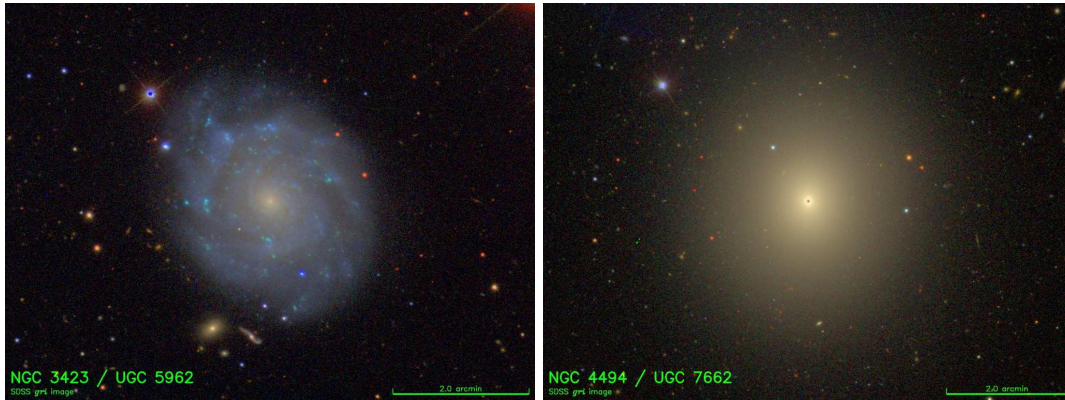
Figure 1.3: Left: a typical spiral galaxy with an overall blue color due to active star formation. Right: a typical elliptical galaxy, with an overall redder color than spiral galaxies and little ongoing star formation. From `http://cosmo.nyu.edu/hogg/rc3/`
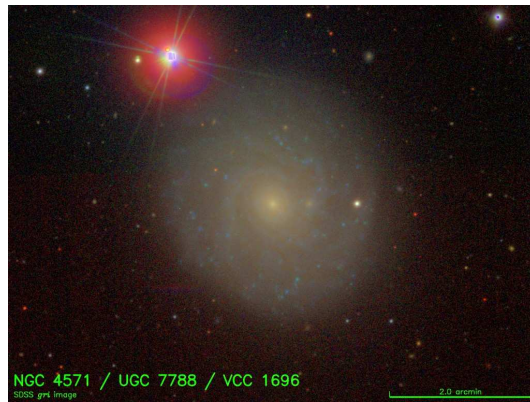
Figure 1.4: A galaxy with a clear disk and spiral structure, but an overall red color more typical of elliptical galaxies. From `http://cosmo.nyu.edu/hogg/rc3/`

Figure 1.5: Two neighboring dwarf elliptical galaxies in the Virgo cluster. The one on the right has a red color typical of (giant) elliptical galaxies. The one the left, however, is unusually blue. Spectral analysis reveals strong Balmer absorption lines in the latter, i.e. it likely experienced a burst of star formation in the recent past (see Sect. 4.2.1). From Gavazzi et al. (2001).

2004b), and a star formation – density relation (Gómez et al. 2003). Galaxies at the centers of clusters are predominantly early-type galaxies without ongoing star formation. Further towards the outskirts of the clusters, the density drops, and more disk galaxies with on-going star formation are found. The correlations with density therefore is also seen as correlations with clustercentric radius (Whitmore et al. 1993; Balogh et al. 2000; Ellingson et al. 2001).

Recent works find that it is in fact star formation which correlates most strongly with environment, and that morphology is only a secondary correlation. The evidence has been found both in terms of local density (Kauffmann et al. 2004; Blanton et al. 2005a), as also from studies of clusters (Christlein & Zabludoff 2005; Quintero et al. 2006). To understand how such a correlation may come about, the assembly of clusters and galaxies needs to be placed into context of how structure forms in the universe.

1.4 Structure formation

On small scales, the universe is highly heterogeneous, as the existence of galaxy clusters, galaxies, stars, planets, and MPA shows. But on scales much larger than galaxy clusters, the universe can be assumed to be homogeneous and isotropic. World models therefore work within the framework of a homogeneous and isotropic universe, upon which inhomogeneities are imposed.

1.4.1 The world we live in

The current cosmological paradigm is that the universe began in a hot *Big Bang* about 13.4 Gyr ago, and has been expanding ever since. Matter as it is known to the standard model of particle physics (summarized as *baryonic matter* by astronomers, as almost all the mass is in baryons, i.e. protons and neutrons) contributes only little ($\sim 4\%$) to the overall energy density of the universe. The *dark matter* proposed by Zwicky accounts for 22%. Dark matter is assumed to be a yet undiscovered particle which interacts gravitationally, and possibly via weak interaction. Among the possible candidates are the neutralino, the lightest stable particle within the theory of supersymmetry, or the axion, a particle postulated within quantum chromodynamics. The bulk of the universe however is in the form of *dark energy*, which exerts negative pressure and thus counteracts gravity. The nature of dark energy remains speculation (even more than the nature of dark matter).

Various independent observations support this scenario. The dynamics of an expanding (or contracting) universe can be described with three cosmological parameters, and for a long time, the aim of observational cosmology was to determine these three parameters:

- The *Hubble constant* H_0. A homogeneous and isotropic universe can expand or contract, but apart from this overall scaling, the relative distances will not change. The distance between two points can then be thought of as composed of two terms, the *proper distance*, which always remains the same in a universe without structures and proper motions, and a term which accounts for the overall expansion (or contraction) of the universe. The latter is called the *scale factor* $a(t)$. The rate of change of $a(t)$ is often expressed as the Hubble parameter, $H(t) = \dot{a}/a$, and H_0 is the value of the Hubble parameter today, $H_0 = H(t_0)$.

One of the main goals of the Hubble Space Telescope was the determination of the Hubble constant. In the local universe, the recession velocity of a galaxy as given by its redshift z is proportional to its distance, related via the Hubble constant:

$$v_{\text{rec}} = c\,z = H_0 D \ , \tag{1.1}$$

as Hubble had first noticed (Sect 1.2). The Hubble Key Project measured the brightness and variability of Cepheids in other galaxies to determine their distance via the Cepheid Period-Luminosity-Relationship. The result was $H_0 = 72 \pm 8$ km s^{-1}/Mpc (Freedman et al. 2001).

- The matter density of the universe $\rho_{\text{m}}(t_0)$, defined in terms of the critical density ρ_{cr}:

$$\Omega_{\text{m}} = \frac{\rho_{\text{m}}(t_0)}{\rho_{\text{cr}}} \qquad ; \qquad \rho_{\text{cr}} := \frac{3H_0^2}{8\pi G} \ . \tag{1.2}$$

The critical density marks the border case between a universe dense enough to recollapse, and a universe expanding forever (in the absence of dark energy). Both dark matter and baryonic matter contribute to Ω_{m}.

Galaxy clusters have been used as a cosmological tool particularly in the determination of Ω_{m}. Their number density, and particularly its evolution with redshift, is strongly dependent on Ω_{m}. Furthermore, since the matter content in galaxy clusters is thought to be representative of that of the universe, it can be used to measure the ratio of baryonic mass to the total mass, Ω_b/Ω_m. Ω_b is the energy density of baryonic matter, defined analogous to Ω_m (Eq. 1.2), and can be constrained from the abundances of light elements. In clusters, most of the baryonic mass is in the form of hot gas, the *intracluster medium* (ICM), which can be detected via its X-ray radiation. The total cluster mass may be determined from the profile of the X-ray radiation or from gravitational lensing. Both number counts of clusters and their gas mass fraction indicate that $\Omega_{\text{m}} \approx 0.3$ (e.g. Allen et al. 2007).

- The cosmological constant Λ (the simplest form of dark energy), also expressed in terms of ρ_{cr}:

$$\Omega_{\Lambda} := \frac{\rho_{\Lambda}}{\rho_{\text{cr}}} := \frac{\Lambda}{8\pi G}\frac{1}{\rho_{\text{cr}}} = \frac{\Lambda}{3H_0^2} \tag{1.3}$$

The main evidence for dark energy, i.e. $\Omega_{\Lambda} > 0$ comes from measurements of type Ia supernovae (Riess et al. 1998). These can be regarded as standard candles, i.e. sources of known luminosity and are excellent cosmological probes due to their brightness. Assuming $\Omega_{\text{m}} = 0.3$, supernovae measurements indicate $\Omega_{\Lambda} \approx 0.7$.

Today the most important cosmological probe is the Cosmic Microwave Background (CMB), relic radiation from the time of reionization, when neutral hydrogen formed from protons and electrons. The temperature fluctuations in the CMB trace the density fluctuations in the universe at that time (about 300,000 years after the Big Bang), and thus the precursors to the structures we observe today. In particular, observations of the CMB can constrain the sum of Ω_{m} and Ω_{Λ}, which reflects the geometry of the universe, very precisely. Along with the priors from the Hubble Key Project and the Supernovae measurements, data from the Wilkinson Microwave Anisotropy Probe (WMAP) is consistent with $\Omega_{\text{m}} + \Omega_{\Lambda} = 1$, i.e. the universe has a flat geometry (Spergel et al. 2007).
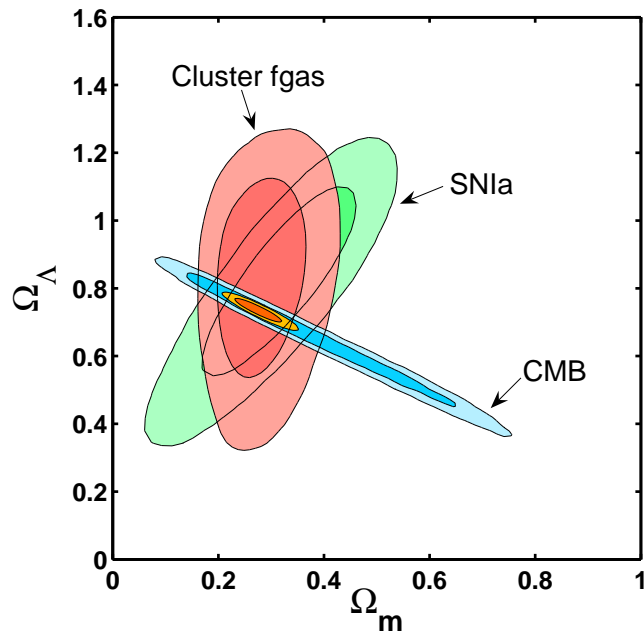
Figure 1.6: An illustration of the constraints on the cosmological parameters derived from various methods. The red contours show the constraints derived from the cluster gas mass fraction; the green contours those from supernovae; and the blue those from the CMB. The joint constraints are shown in orange. From Allen et al. (2007).

It is remarkable how well different and independent methods agree on a set of parameters of approximately $\Omega_{\rm m} = 0.3$, $\Omega_\Lambda = 0.7$ and $H_0 = 100\,h\,{\rm km/s/Mpc}$, where $h = 0.7$. Throughout this thesis, I assume this *concordance cosmology*.

1.4.2 Linear growth of structure

Of course, the study of galaxy clusters (or of anything) is only possible in an inhomogeneous universe. The framework of a homogeneous and isotropic universe serves as the description of the universe on average, and on large scales. On small scales, gravity causes the growth of inhomogeneities: If a part of the universe is at some point slightly denser than the average, the self-gravity of that part will brake the normal Hubble expansion stronger than the average. It will thus expand slower, so the deviation from the average density of the surrounding universe increases and the process continues. Underdense regions, on the other hand, expand faster since they experience a smaller braking force from gravity. This is how structures can form in the universe.

The density contrast at a position $\mathbf{r}$ at time t is:

$$\delta(\mathbf{r}, \mathbf{t}) = \frac{\rho(\mathbf{r}, \mathbf{t}) - \bar{\rho}(\mathbf{t})}{\bar{\rho}(\mathbf{t})} \, , \tag{1.4}$$

with $\bar{\rho}(t)$ the average density at that time. The growth of structure can be described by following the development of the density contrast with time.

Structure growth commenced with density fluctuations with $\delta \ll 1$, which are readily described by perturbations of a homogeneous density field. In the regime of weak gravitational fields and on scales smaller than the horizon, matter can be treated as a fluid with density $\rho(\mathbf{r}, \mathbf{t})$ and a velocity field $\mathbf{v}(\mathbf{r}, \mathbf{t})$, and thus be described by the set of Continuity, Euler, and Poisson equations. The homogeneous Hubble expansion presents a trivial solution to this set of equations. For $\delta \ll 1$, the density fluctuations can be treated as perturbations to the Hubble expansion. Within the linear regime, the shape of density fluctuations in comoving space does not change, only their amplitude does so with time.

1.4.3 Non-linear structure growth

The description of structures by linear perturbation theory breaks down latest when $\delta \approx 1$ (galaxy clusters are well in the non-linear regime with $\delta \sim 100$). As overdensities grow, they also expand slower than the average Hubble expansion. If the overdensity is large enough, it will actually cease expanding at a time t_{turn} and recollapse. For the particular case of a spherically symmetric, homogeneous overdensity in an Einstein–de Sitter universe ($\Omega_m = 1, \Omega_\Lambda = 0$), the density contrast at this time of turn-around is

$$\delta_{\mathrm{turn}} = \frac{9\pi^2}{16} \approx 5.56 \; . \tag{1.5}$$

If the overdensity were indeed homogeneous and spherically symmetric, it would collapse to a point at a time $t_{\mathrm{coll}} = 2t_{\mathrm{turn}}$. But even slight inhomogeneities will lead to deviations from purely radial orbits; the particles scatter and virialize. The collapsed, virialized system has a radius of $R_{\mathrm{vir}} = R_{\mathrm{turn}}/2$. Its density has therefore grown by a factor of 8 from the turn–around time, whereas the average density has decreased by a factor of $(2^{2/3})^3 = 4$. In total, the density contrast of the virialized structure is $18\pi^2 \approx 178$. Galaxy clusters are considered virialized within a volume for which the density is 200 times the critical density.

1.4.4 Hierarchical Structure Formation

Early on, density fluctuations were small enough to be well described by linear theory. In this regime, the amplitudes of the density peaks grow at the same rate. When the density contrast becomes of the order unity, also their shape may change, as they start to affect ("pull in") the surrounding space. If the density contrast is high enough, the peaks decouple from the Hubble flow, collapse, and form the seeds of the structures we see today. At smaller scales, the initial density fluctuations typically have higher amplitudes; thus, smaller structures (proto-galaxies and galaxies) are expected to form first, and to larger merge to form larger structures (clusters and superclusters). This is called the *bottom-up* scenario.

However, today's galaxy clusters also correspond to density fluctuations in the early universe, albeit with larger scales (and generally lower amplitudes) than those from which galaxies form. These underlying large-scale fluctuations boost the density contrast, and cause the smaller-scale fluctuations in the same area to reach the critical density earlier (Fig. 1.7). Hence, galaxies in dense regions are expected to have formed slightly earlier than galaxies low-density regions.
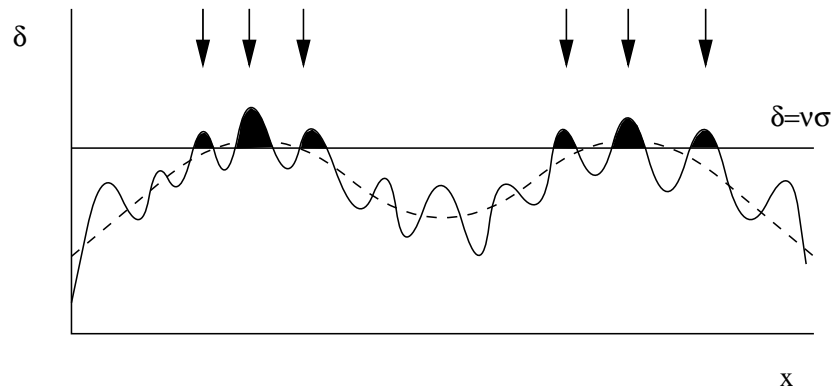
Figure 1.7: A simple model for *biased* structure formation. Density fluctuations are assumed to collapse when they reach a threshold density, indicated by the horizontal line. An underlying peak of a large-scale fluctuation (which would correspond to a cluster today) causes small-scale fluctuations to collapse earlier than small-scale fluctuations located in the trough of large-scale fluctuations.

1.4.5 Clusters as nodes of the cosmic web

Zwicky believed that clusters fill the universe "just like bubbles fill a volume of suds". Today, the large-scale structure of the universe is indeed often compared to the structure of suds, but the bubbles are not the clusters, but voids - regions devoid of matter. This is a natural consequence of structure formation in an expanding universe: empty regions expand faster, and thus the voids grow with time.

Within the suds analogy, galaxies are found predominantly where bubbles join. "Sheets" or "pancakes" of galaxies have been found, as analogy to the two-dimenioal surface separating two bubbles. Even more prominent are galaxies along filaments (the line between three bubbles), and finally, galaxy clusters as the points where (at least) four bubbles join.

However, the suds analogy is not complete, as it lacks the time evolution of the cosmic large-scale structure. As the density grows large enough, not only the amplitude of the density perturbation grows, but they also affect the surrounding space. Since galaxy clusters originate at the intersections of filaments, they grow predominantly by accreting matter along these filaments. Likewise, filaments accrete matter from sheets of galaxies. Although this growth scenario is dictated by the dark matter, it has important implications for the galaxies in clusters: apart from a population of galaxies which were formed within the overdensity from which the cluster originates, clusters constantly accrete galaxies. These galaxies are likely to have passed through intermediate density environments such as filaments and galaxy groups before infall into the cluster.

The galaxies in clusters thus likely have varied histories: those which have always been part of the cluster overdensity, and those which were born in lower density environments, and accreted later on. This is an important aspect of the galaxy populations in clusters.

1.5 Galaxy formation and formation

The formation of structure on large scales is governed only by gravity, and is therefore (relatively) straightforward to describe. For galaxies however, the properties of the baryonic

components are essential, and the dark matter halo is "simply" the environment into which they are embedded. Many more physical processes therefore have to be considered to follow the formation and evolution of galaxies. A term sometimes used in conjunction with galaxy evolution is *gastrophysics*, and indeed, any model of galaxy formation needs to describe how primordial gas is turned into the building blocks of galaxies, i.e. stars, dust, metal-rich gas, as well as the dynamical distributions of the components (disks and/or spheroids), and finally, the different kinds of galaxies.

In this section, I give an overview of the physical processes which govern star formation in galaxies, and discuss how they relate to the galaxy bimodality and the environmental dependence of galaxy properties.

1.5.1 The basic recipe

The reservoir of baryons available to form galaxies is mostly distributed in the form of diffuse gas, and thus needs to be condensed.

Gas cooling: In dark matter halos of a minimum mass, the gravitational pull overcomes the thermal gas pressure, so that gas can infall into the gravitational well of the halos. The loss of gravitational energy leads to heating of the gas (along with shock heating, this is the origin of the hot intracluster gas). For star formation, the gas needs to cool and condense, which is possible via radiative cooling in the dense core. Cooling and condensing the hot halo gas is the essential prerequisite for star formation to occur.

Stellar feedback: To some extent, star formation is a self-regulatory process. Each star formation episode is accompanied by stellar winds and supernova explosions, which may expel surrounding gas from the site of star formation, thus removing the necessary fuel (e.g. Larson 1974; Bertone et al. 2007). In dwarf galaxies, the energy injected into the gas may be enough to drive the gas from the (shallow) potential well, thus quenching star formation after a single eposide (e.g. Ferrara & Tolstoy 2000). The potential well of more massive galaxies is too deep to permanently remove the gas from the galaxy, but winds play a role in (temporarily) quenching star formation, particularly in star bursts (Heckman et al. 1990).

1.5.2 Disk galaxies

With this in mind, it seems fairly straightforward to explain the formation of disk galaxies. As hot gas cools, it sinks towards the center of the dark matter halo. However, even a small net angular momentum will cause the gas to settle into a disk. When the mass density in the disk becomes large enough, it can start forming stars (Schmidt 1959; Kennicutt 1998). Although the basic scenario is set, the details of disk galaxy formation, the interplay with the dark matter halo, and stellar feedback are still a challenge for galaxy simulations (e.g. D'Onghia & Burkert 2004).

1.5.3 Elliptical galaxies

The formation of elliptical galaxies, on the other hand, is a more puzzling question. Their stellar populations are found to be quite old, with formation redshifts $z_f > 2$. In the 'monolithic collapse' scenario, elliptical galaxies form from a single gas cloud, forming all their stars
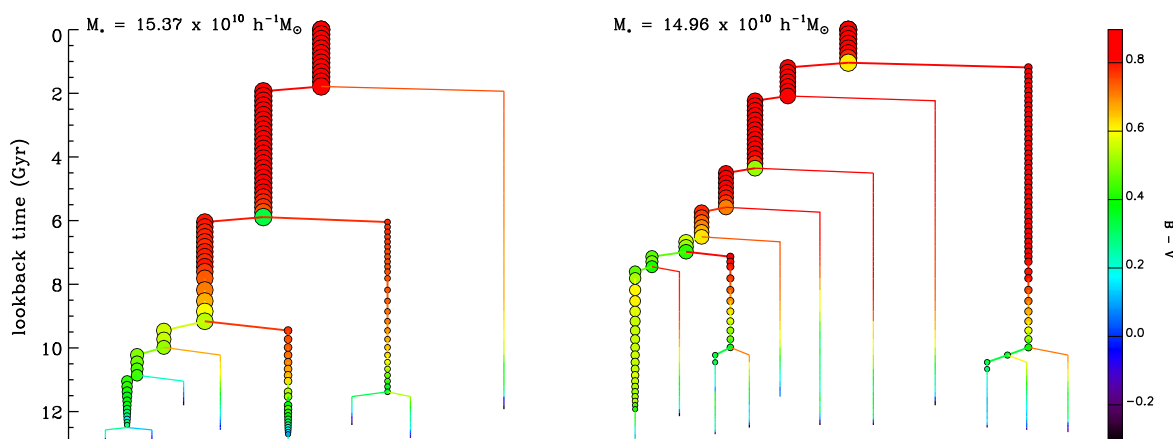
Figure 1.8: Two examples of merger trees of elliptical galaxies in the simulations of De Lucia et al. (2006). The final galaxy is shown at the top; at each previous time-step (shown below), its progenitor galaxies are shown. The sizes of the symbols indicate the stellar mass, whereas the color indicates the $B - V$ color of the integrated light of the stellar populations. As can be seen, most of the star formation (traced by the color) takes place early on, and the progenitor galaxies have used up most of the gas by the time they merge. The residual gas may cause a brief episode of star formation, but not enough to noticeably alter the characteristics of the integrated stellar population.

in a single star-forming episode early on. This scenario easily explains the ages of the stellar populations in ellipticals. But it also predicts that the most massive ellipticals should have formed first, since the most massive ellipticals are also the oldest. This scenario is therefore difficult to reconcile with the hierarchical structure formation scenario postulated by the standard cosmological paradigm (Sect. 1.4.4). Even if elliptical galaxies assembled anti-hierarchically (the most massive first), this would require a population of massive, passively evolving elliptical galaxies at higher redshifts, which is at odds with the observed number counts of such objects (e.g. Kitzbichler & White 2006).

Thus, the role of galaxy mergers in building up elliptical galaxies is vital to explain their evolution within the standard cosmological model.

Major mergers: Numerical simulations suggest that major mergers of disk galaxies can indeed form elliptical galaxies, i.e. the stellar remnant forms a spheroid (Toomre 1977; Burkert & Naab 2004). However, spiral galaxies are also rich in cold gas, and mergers and collisions will trigger star formation in the gas clouds. The remnants of major mergers of spiral galaxies should therefore have considerable amounts of young stars, which is at odds with the old ages found for the stellar populations of ellipticals.

Dry mergers: Thus, mergers of gas-poor galaxies (i.e. *dissipationless* or *dry* mergers) are likely to play an important role in the assembly of ellipticals. Indeed, there are observations of on-going mergers of red (and thus presumbaly gas-poor) galaxies in galaxy clusters (e.g. van Dokkum et al. 1999; Tran et al. 2005). De Lucia et al. (2006) find that they can reproduce the number density and colors of today's elliptical galaxies by combining a suite of semi-analytic models to describe galaxy formation and evolution with the currently largest N-body dark matter simulation, the Millenium Run Springel et al. (2005). They find that the stars that make up elliptical galaxies today

formed early ($z_f \sim 5$), but merged only quite late into larger systems (Fig. 1.8). The progenitor galaxies have used up most of their cold gas by the time they merge, so that the actual merging event causes only brief, weak episodes of star formation (so–called "frosting"). The more massive the galaxy today, the more progenitor systems it has.

AGN feedback: Some galaxies harbor *Active Galactic Nuclei* (AGN). The growth of the central black hole and the galaxy are thought to be tightly connected (Heckman et al. 2004). In particular, AGN feedback has been proposed to solve the *overcooling* problem: In massive halos, cooling from the hot gas phase is highly efficient, which would predict that the most massive galaxies (which reside in the most massive halos) are actively forming stars. Instead, the most massive galaxies are red, quiescent elliptical galaxies. Furthermore, the mass function of massive galaxies does not follow the mass function of dark matter halos, but cuts off exponentially, implying that some mechanism must keep galaxies in these massive halos from further forming stars. A likely process is (radio-) AGN activity (Croton et al. 2006; Best et al. 2006).

1.5.4 Brightest Cluster Galaxies

A particularly interesting class of galaxies are Brightest Cluster Galaxies (BCGs). The central galaxies are often found to be the most luminous and most massive cluster galaxies, i.e. the BCGs. Some BCGs are cD galaxies, giant elliptical galaxies with an extended envelope. In fact, the cluster center is the only environment in which cD galaxies are found. The formation of BCGs must therefore be tightly linked to clusters.

Cannibalism: Dynamical friction will cause the more massive cluster galaxies to sink towards the cluster center. Before the importance of hierarchical structure formation was realized, it was argued that BCGs could form from clusters in situ when these galaxies merge (Ostriker & Tremaine 1975; White 1976).

It has later been argued that the cluster tidal forces would strip a significant amount of galaxies sinking to the center, thereby extending the dynamical timescale to the point that cannibalism in static clusters cannot account for the masses of cD galaxies (Merritt 1985).

Another proposed mechanism to form BCGs in situ are *cooling flows*, the extreme extrapolation of gas cooling to the center of clusters. However, the star formation rates from cooling flows have been found too low to form galaxies as massive as BCGs (Crawford et al. 1999).

De Lucia & Blaizot (2007) have investigated the formation of BCGs in the context of the Millenium Run simulation (Springel et al. 2005), which follows the hierarchical assembly of dark matter. They find that the BCGs build up from a multitude of galaxies which form at early times (Fig. 1.9). Similar as for elliptical galaxies, the progenitor galaxies form at early times, and have used up most of their gas by the time they merge. This scenario is supported observationally in that most BCGs are indeed elliptical galaxies with old stellar populations, and observations of on-going dry mergers of BCGs with satellite galaxies (Rines et al. 2007).

1.5.5 "Nature vs. Nurture"

Brightest Cluster Galaxies, in particular cD galaxies, are an extreme example that the galaxy population depends on the environment. The search for the origin of the observed relation
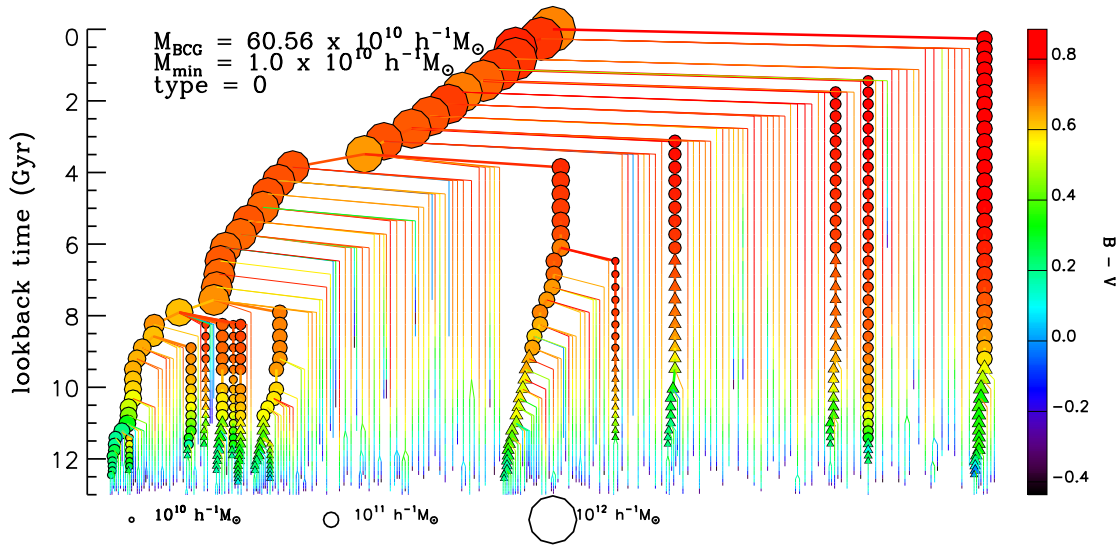
Figure 1.9: The merger tree of a Brightest Cluster Galaxy, from the modeling of De Lucia & Blaizot (2007). The final BCG is shown at the top; at each previous time-step (shown below), its progenitor galaxies are shown. The size of the symbols indicate their stellar mass, whereas their color indicates the $B - V$ color of the integrated light of their stellar populations. Galaxies that are in the same halo as the most massive progenitor are shown as circles; those outside as triangles.

between star formation / morphology and density has often been phrased as a "nature vs. nurture" debate. In the *nature scenario*, the properties of a galaxy are determined by the conditions at its birth. In the *nurture scenario*, all galaxies form the same, but their later properties are driven by the environment, and changes in the environment.

Combined with hierarchical structure formation, a simple "nature" scenario actually predicts a correlation of star formation rate with density: A large fraction of today's cluster galaxies have always been in a dense environment. If galaxy assembly follows the assembly of dark matter, then they have formed earlier than the average galaxy population (Sect. 1.4.4). They have likely used up more fuel for star formation than younger galaxies, and thus have lower star formation rates. On the other hand, in hierarchical structure formation, clusters *must* be accreting galaxies - do these merely alter the population mix, or are they transformed to a cluster galaxy population upon entry?

Likely, both "nature" and "nurture" play a role in determining galaxy properties. It is then the goal of galaxy astrophysics to identify the relative importance of the two, as well as to identify the physical processes which affect and alter galaxy properties. To a large part, this thesis focuses on the star formation properties of galaxies rather than their morphology, and hence attention is given primarily to processes which affect the star formation rate, rather than change galaxy morphology.

1.5.6 Environmental processes

Several mechanisms can play a role in affecting the star formation rate in galaxies in the cluster environment, i.e. contribute to the "nurture" scenario:

Galaxy mergers: The likelihood for galaxies to merge depends on the local density of galaxies, and on their relative velocities. The favored environment for mergers are therefore galaxy groups. In massive clusters, high relative velocities (as indicated by the cluster velocity dispersion) are unlikely to occur frequently. In the bottom-up scenario, galaxy groups can form an important intermediate step between galaxies and clusters, both in the sense that clusters may start out as groups, and that galaxies may be accreted first onto groups, which are subsequently accreted onto clusters.

On short timescales, mergers (or, more generally, strong galaxy-galaxy interactions) trigger enhanced star formation or even starbursts through compression of gas. However, mergers between equally massive disk galaxies are also thought to be a primary channel to form elliptical galaxies (or galaxy bulges). Simulations predict that after $\lesssim 1\text{Gyr}$, the morphologies of merger remnants of disk galaxies resemble normal elliptical galaxies (Mihos 1995). For a similar timescale, the galaxy spectrum may display (post-)starburst features.

Harassment: Encounters between galaxies which do not lead to merging can still affect galaxy properties via tidal forces. This mechanism is referred to as *harassment*, and has been used primarily to explain the transformation of spiral galaxies to (dwarf) spheroidals in the cluster environment. The harassment rate is predicted to be largely independent of local density (Moore et al. 1998). Numerical simulations suggest that this process can transform spiral galaxies to (dwarf) spheroidals in a timescale of a few Gyr (Moore et al. 1998). Furthermore, it acts to concentrate a considerable fraction of the cold gas at the galaxy center, where it undergoes a short period of increased star formation, thus depleting the fuel for star formation.

Tidal forces: Apart from galaxy-galaxy encounters, galaxies are also subjected to the tidal field of the cluster. Tidal forces may strip some of the galaxy mass to the point of destroying the galaxy (Merritt 1983). The stellar debris of these events is thought to be the origin of the diffuse intracluster light observed in rich cluster of galaxies (Willman et al. 2004; Zibetti et al. 2005), and/or could account for the envelopes of cD galaxies. Furthermore, the tidal forces may enduce gas compression and thus trigger star formation (Byrd & Valtonen 1990). Tidal heating could transform disk galaxies into S0s, but not into ellipticals (Gnedin 2003). The tidal forces are strongest in the cluster core, but a galaxy on an elliptical orbit may encounter several passages close to the core, each time briefly encountering tidal forces. Any such triggering of star formation will therefore be bursty in nature, whereas the morphological transformation accumulates over several orbits, i.e. several Gyr.

Strangulation: The prerequisite for any star formation to occur is the existence of a supply of cold gas. In the field, spiral galaxies have a halo of hot gas, from which gas cools, settles into a disk, and provides the fuel for on-going star formation. As a galaxy enters the cluster environment, interaction with the hot intracluster medium will strip this gas halo from the galaxy and star formation will then cease after the cold gas in the disk has been used up (Larson et al. 1980). The gaseous envelope is stripped within a few Gyr, even in the cluster outskirts (Bekki et al. 2002).

Strangulation is thought to be one of the most important processes to quench star formation in clusters on long timescales. Even simple models where galaxies infalling

into the cluster are subject to strangulation are able to qualitatively reproduce the star formation – radius relation (Balogh et al. 2000).

Gas stripping: If the density of the ICM is high enough, then *ram-pressure stripping* can sweep the cold disk out of the galaxy, thus truncating star formation very rapidly (Gunn & Gott 1972). Support for this scenario comes from observations of the HI gas disks of spiral galaxies. While the neutral gas disks of field spiral galaxies typically extend far beyond the stellar disks, the neutral gas disks of spiral galaxies in the center of the Virgo cluster are significantly smaller (Cayatte et al. 1990). Moreover, these disks are observed to be notably disturbed, often with gas tails pointing away from the cluster center (Chung et al. 2007). This suggests that ram-pressure stripping, even at intermediate densities is effective in disturbing the outer (non-star-forming) cold disks. To also affect the inner disks and truncate star formation likely requires higher densities, which are met only at the centers of rich clusters.

Ram-pressure stripping is the prime candidate for *truncating* star formation, i.e. shutting it off on a very short timescale ($\sim 10^7$ yr, Abadi et al. 1999).

Several observational indications can identify which of these processes are at work in clusters. E.g. if mergers frequently trigger a starburst, after which star formation is shut off, then this leaves a spectral signature which can be observed for ~ 0.5Gyr. The role of mergers can thus be constrained by the rate of post-starburst galaxies in the cluster outskirts (where the relative velocities are low enough for merging to be effective) compared to the field value. The spectral signature of star formation truncation is similar to a post-starburst spectrum. The most likely mechanism for truncation is ram-pressure stripping, thus, if ram-pressure stripping is a dominant mechanism, then galaxies in the cluster center should display these spectral signatures frequently.

For infalling galaxies, the time it takes them to traverse the cluster from the outskirts to the center is of the order of Gyr, and thus comparable to the timescales of harassment and strangulation. Thus, if the typical star formation rate changes on lengthscales comparable to the cluster radius, then these two process likely play an important role.

1.6 Redshift Evolution: the Butcher–Oemler effect

In massive local clusters, galaxies with appreciable levels of star formation, and thus blue colors, are rare. At intermediate redshifts, $z \sim 0.2 - 0.5$, (some) clusters show an increased fraction of blue cluster galaxies, as first noted by Butcher & Oemler (1984). This seems to be mostly due to a higher occurrence of spiral galaxies, and a decrease in the number of S0 (Dressler et al. 1997). The fraction of elliptical galaxies, on the other hand, remains almost constant.

It seems that if a plausible physical process can be found to turn the spirals in $z \sim 0.5$ clusters into S0s in local clusters, a large part of the Butcher-Oemler effect can be explained. Ram-pressure stripping would be a suitable process, since the removal of cold gas from the disk would leave a disk without star formation. But ram-pressure stripping can be effective only in the very centers of rich galaxy clusters, where the gas density is highest. However, S0s are found also in poor clusters, in the cluster outskirts, and in the field, and hence, ram-pressure stripping cannot be the sole mechanism to transform spirals into S0s.

Several studies have found that the increase in the fraction of blue galaxies is caused by, or at least accompanied by, a deficit of faint red galaxies with increasing redshift (De Lucia et al. 2004b, 2007; Tanaka et al. 2005; Stott et al. 2007; Gilbank et al. 2007). This has the intriguing interpretation of witnessing the build-up of the red sequence with cosmic time. These results have, however, been challenged by Andreon (2007).

The Butcher-Oemler effect is also seen in spectroscopic indices: the fraction of galaxies with on-going or recent star formation is higher in intermediate redshift clusters than in low redshift clusters (Couch & Sharples 1987; Tran et al. 2003). In particular, clusters at intermediate redshifts host a population of galaxies with strong Balmer absorption lines, which are indicative of a recent star-burst, or at least recent truncation of star formation activity; hence these galaxies are commonly referred to as *post-starburst* galaxies (other names include "E+A" or "k+a" galaxies). Notably, the overall fraction of post-starburst varies widely in the literature, from about 1% (Balogh et al. 1999), to up to 30% (Dressler et al. 1999). It is not entirely clear how this compares to the fraction in the intermediate redshift field. In the local universe, post-starburst galaxies are found in environments of all densities (Zabludoff et al. 1996; Hogg et al. 2006).

The high occurrence of (post-)starburst galaxies in their sample led Dressler et al. (1999) to infer that infall into the cluster triggers star formation. However, at higher redshifts, the rate of galaxy infall is higher than in the local universe, where it is slowed due to the acceleration of the universe. Moreover, the star formation rates of (spiral) galaxies are higher at earlier epochs. Hence, other studies find that this increase in the infall of blue galaxies suffices to account for the population of blue galaxies in intermediate redshift clusters (Ellingson et al. 2001).

Not only its interpretation, but also the reality (or at least the strength) of the Butcher-Oemler effect has been questioned. The major issues here are sample selection / bias effects. The fraction of blue galaxies is traditionally defined for galaxies in a luminosity-limited sample, selected in the V-band. De Propris et al. (2003) find that for galaxies selected in the K-band, the Butcher-Oemler effect is much weaker. Selection in the near-infrared K-band is close to a selection in stellar mass, whereas selection in a blue optical band is partial to low-mass galaxies with high mass-to-light ratios. This suggests that the Butcher-Oemler effect could at least partially be due to a population of luminous (possibly star-bursting) dwarf galaxies, which fade from the selection limit in local clusters.

Furthermore, the fraction of blue galaxies varies widely, even in clusters of similar redshifts (Smail et al. 1998). There is no evidence for a dependence on X-ray luminosity (Wake et al. 2005). Also the dependence on redshift (apart from an increase between the local clusters and clusters beyond $z \gtrsim 0.2$) has been questioned (Fairley et al. 2002).

1.7 Recent developments: the role of surveys and semi-analytic models

The recent years have seen an astounding development of our understanding of galaxy properties and evolution. The properties of galaxies in the local universe have been well determined by large-scale observational surveys, such as the Sloan Digital Sky Survey (SDSS). But also

the number of known high-redshift clusters has increased, allowing better statistics on the average properties and their scatter. An important aid in interpreting these observations has been the coupling of semi-analytic models of galaxy evolution to high-resolution simulations of dark matter structure formation.

1.7.1 Local galaxy surveys: SDSS and 2dFGRS

The Sloan Digital Sky Survey (Stoughton et al. 2002; York et al. 2000) is a survey of about a quarter of the extragalactic sky, obtaining photometry in five bands ($ugriz$) of more than 200 million objects and spectra of more than a million objects. Its original main purpose was to map the three-dimensional structure of a large part of the local universe, as well as detect quasars at high redshift. But the quality and homogeneity of the SDSS data has allowed to not only map the positions of distances of galaxies, but also to investigate their physical properties. For instance, the SDSS data has allowed to measure the overall luminosity distribution of local galaxies with unprecedented accuracy (Blanton et al. 2001, 2003a), thus providing the necessary baseline to measure evolutionary or environmental trends. Baldry et al. (2004) have quantified the galaxy bimodality in terms of the color-magnitude diagram. In a series of papers, Kauffmann et al. (2003a), Brinchmann et al. (2004) and Tremonti et al. (2004) used spectral modeling of galaxy spectra to recover the underlying physical properties, such as stellar mass, star formation rate, and mean stellar age. With this data, Kauffmann et al. (2003b) quantified the galaxy bimodality in terms of these physical properties.

Within the SDSS, also environmental influences can be studied. One measure is local galaxy density. Kauffmann et al. (2004) investigated the stellar masses, star formation rates, and galaxy structure as function of local density, quantified as the number of galaxies within a fixed physical surrounding volume. They find that the physical property which depends most strongly on environment is star formation, suggesting that the star formation – density relation is the underlying physical cause for the observed morphology – density relation. They argue that the timescales for quenching star formation must be long, $\gtrsim$ 1Gyr, and that the underlying process is unlikely to significantly alter galaxy structure, i.e. that strangulation is the most viable mechanism. Blanton et al. (2005a) confirm the primary correlation of star formation with environment based on galaxy colors. Hogg et al. (2004) show that while the ratio of blue to red galaxies varies with environment, there is only negligible change in the mean color-magnitude relation of red galaxies.

Another way to study environmental influences is the compilation of cluster catalogs. Several cluster samples have been derived from SDSS data. The C4 cluster sample by Miller et al. (2005) uses the spectroscopic SDSS data to reconstruct the galaxy density field and identifies clusters as its peaks. The group catalogs by Yang et al. (2007) and Berlind et al. (2006) are also based on the spectroscopic data. Use of the spectroscopic catalogs limits the redshift range of the resulting cluster sample, and most of these samples reach a high completeness only to $z \lesssim 0.2$. By using cluster selection algorithm based on the photometric data, the redshift range can be extended (Goto et al. 2002; Koester et al. 2007). The results from investigation of galaxy properties in these cluster samples are somewhat less clear than from the local density estimates. While most studies agree that ram-pressure stripping is unlikely to play a major role, the relevance of galaxy-galaxy interactions vs. strangulation is disputed. Quintero et al. (2006) investigate the correlations of galaxy properties as function of cluster-centric distance and confirm the conclusions of Kauffmann et al. (2004) and Blanton et al. (2005a) that star formation is more directly connected with environment than morphology,

which argues in favor of strangulation. Also van den Bosch et al. (2007) conclude that strangulation is the dominant mechanism, based on a systematic comparison of central and satellite galaxies. On the other hand, based on the velocity distributions of different galaxy types, Goto (2005b) conclude that galaxy-galaxy interactions must play a major role. Also Balogh et al. (2004a) have argued in favor of galaxy-galaxy interactions, as they do not find a systematic decline of the star formation rate with density in galaxies which are forming stars (which would be expected from the strangulation scenario).

In a series of papers, Popesso et al. (2004) have chosen a different method of identifying galaxy clusters in SDSS paper: they have used the ROSAT All Sky Survey to identify clusters based on their X-ray emission. Much of their work has focused on quantifying various scaling relations between optical and/or X-ray properties. They further find that the luminosity function in clusters differs markedly from the field, with an excess population of dwarf galaxies (Popesso et al. 2005b, 2006). In Popesso et al. (2007b), they find that the star formation rate per galaxy (or per unit stellar mass) does not depend systematically on the overall cluster properties such as cluster mass, velocity dispersion, X-ray temperature, or richness. Contrary to the other studies, they conclude that ram-pressure stripping plays a large role in quenching star formation.

Although SDSS has taken much of the glory, many of these issues have also been studied with data from the 2dF Galaxy Redshift Survey (2dFGRS; Colless et al. 2001, 2003). The 2dFGRS area is smaller than that of the SDSS, but the spectroscopic limit is fainter. From a study of 17 (previously known) clusters, Lewis et al. (2002) find that the suppression of star formation can be traced to distances about three times the virial radius, and that the observed trends can be adequately modeled using only strangulation. With a larger set of clusters, De Propris et al. (2004) investigated the fraction of blue galaxies. Like Balogh et al. (2004a, whose study included both SDSS and 2dFGRS clusters), they find that, if only star forming galaxies are selected, the distribution of star formation rates is independent of environment, and thus also argue in favor of galaxy-galaxy interactions.

1.7.2 High-redshift cluster surveys

There is now also an increasing amount of data on galaxy clusters at higher redshifts beyond the sample of Butcher & Oemler (1984). Many of the cluster samples are based on X-ray surveys (Gioia et al. 1990; Ebeling et al. 1998, 2001; Böhringer et al. 2000, 2001). The MORPHS cluster sample, on which the study of Dressler et al. (1999) was based, is a sample of 10 X-ray detected cluster with varying X-ray luminosities, richnesses, and masses, which were subsequently observed with HST (to classify galaxy morphologies). Galaxies targeted for spectroscopy were selected particularly to study the star-forming cluster galaxies. The CNOC1 sample of Yee et al. (1996), which is the basis for the studies of Balogh et al. (1999) and Ellingson et al. (2001), was also selected from an X-ray cluster sample. The target selection was based simply on magnitude and position.

Also the ACS Intermediate Redshift Cluster Survey (Mei et al. 2006) is largely based on X-ray detected clusters, with subsequent HST imaging and spectroscopy. These are some of the highest-redshift clusters ($z \sim 1$) with spectroscopic and morphological optical observations. From this sample, Postman et al. (2005) confirm the evolutionary trend found by Dressler et al. (1997), that the morphology-density relation changes with redshift, due to a decrease in the fraction of S0 galaxies, while the fraction of elliptical galaxies remains con-

stant. Holden et al. (2007) find that the evolution must be driven primarily by galaxies less massive than $10^{10.6} M_\odot$, whereas for more massive galaxies, the morphology-density relation does not evolve.

However, selecting clusters based on their X-ray luminosities is likely to bias the high-redshift cluster samples towards the most massive and most virialized systems at that time. There are few such clusters in the local universe (due to the smaller volume probed), and so these clusters are likely not representative progenitors of local clusters. Hence, an increased effort has been made to select high-redshift clusters based on galaxy overdensities. One of the first such surveys conducted on a large scale was the Las Campanas Distant Cluster Survey (LCDCS, Gonzalez et al. 2001), which identified cluster candidates as peaks in the diffuse optical background light distribution. The ESO Distant Cluster Survey (EDisCS), which will be further discussed in the course of this thesis, is the follow-up survey of the most promising LCDCS cluster candidates. One of the first results from EDisCS was the observation of a deficit of faint red galaxies in high redshift clusters De Lucia et al. (2004b, 2007). Poggianti et al. (2006) studied the on-going star formation in EDisCS and SDSS galaxies and argued that the quiescent population is made up of two separate populations: "primordial" galaxies which ceased star formation long ago ($z \gtrsim 2.5$) and galaxies whose star formation has been quenched upon entering the cluster environment, presumably on a long timescale ($\sim$3 Gyr).

A powerful technique to identify galaxy clusters makes use of the star formation – radius relation and identifies galaxy clusters by searching for overdensities of galaxies with similar, red colors (e.g. the Red Sequence Cluster Survey, RCS, Gladders & Yee 2000). Several clusters have been identified and confirmed by RCS and its successor, RCS2, and follow-up observations are being taken. Preliminary analyses find similar trends as in X-ray selected samples, but possibly slight dependences on cluster richness (Yee et al. 2005; Gilbank et al. 2007).

1.7.3 Semi-analytic modeling

The increase in observational data has been matched by developments in the theoretical modeling of galaxy evolution. With increased computing power, structure formation in a Cold Dark Matter universe has been well modeled (Springel et al. 2005). To include the physical processes into these simulations in a self-consistent fashion is still difficult and time-consuming, and cannot be undertaken for representative fractions of the universe. However, apart from gravity, dark matter and baryons are largely decoupled. Theoretical galaxy evolution has therefore resorted to "painting" galaxies into dark matter halos, thus following the structure formation governed by the dark matter. In these models, galaxy evolution is described by a few analytic expressions, representing the current knowledge of the dependences of e.g. the gas cooling rate. The idea was put forward by White & Rees (1978), and has been extended by several groups (e.g. White & Frenk 1991; Lacey & Silk 1991; Kauffmann et al. 1993, 1999; Somerville & Primack 1999). Recent refinements have been the incorporation of chemical enrichment (De Lucia et al. 2004a; Nagashima et al. 2005) and AGN feedback (Croton et al. 2006; Bower et al. 2006).

These "semi-analytic models" have been very valuable in interpreting observations. One of the early successes was in fact to reproduce the Butcher-Oemler effect, but only in low-density cosmologies (Kauffmann 1995). Recently, Croton et al. (2006) and Bower et al. (2006) were

able to explain the different functional forms of the halo mass function and the galaxy luminosity function by including both supernova feedback and AGN heating. Current challenges for semi-analytic models include the simultaneous reconstruction of the luminosity function and correlation function (Wang et al. 2007), and the details of AGN feedback.

1.8 Aims and structure of this thesis

My thesis aims at characterizing the properties of galaxies in clusters at low and high redshifts, as a method of identifying the physical processes which act on galaxies in clusters. Special attention is given to the Brightest Cluster Galaxies in the local cluster sample. The other cluster galaxies are characterized mainly by their stellar mass and their star formation history, rather than their morphology. This allows inferences to the physical processes which affect star formation in cluster galaxies.

A major technical focus of this thesis has been the compilation of a reliable sample of galaxy groups and clusters at low redshifts ($z \lesssim 0.1$), to be used as a local comparison sample for cluster surveys at higher redshift, in particular for the ESO Distant Cluster Survey (EDisCS). The cluster sample must provide the local equivalent to the high quality deep observations being gathered for high-redshift cluster samples, while at the same time encompassing many more systems in order to reduce statistical uncertainties.

Such datasets have recently become possible with the increasing number of large sky survey projects. Arguably the one that is best suited for the construction of a local cluster sample with the desired properties is the Sloan Digital Sky Survey (SDSS). Various cluster catalogs have been compiled for the SDSS, and it was not the purpose of this thesis to provide yet another one. Rather, I have used an existing cluster sample, the C4 catalog, and have modified it to match the specifications.

An important improvement to the original C4 catalog has been the identification of the Brightest Cluster Galaxies (BCGs). As described in Sect. 2.1, BCGs are a particularly intriguing class of galaxies. In Chapter 2, I ask "How special are Brightest Cluster Galaxies?" and investigate the systematic differences between BCGs and sample of non-BCGs of equal mass, redshift, and color. Between these matched samples, the difference lies in the location: the BCGs lie at the centers of galaxy clusters, the comparison galaxies not. This allows to single out systematic differences in galaxy properties due to the location, as well as the associated assembly history. Such a systematic comparison has only become with the sample of BCGs which I have compiled in this work.

There are two complementary methods to identify the physical processes which act on galaxies upon infall into the cluster: one is the fossil record in cluster galaxies, the other direct comparison of cluster samples at different cosmic epochs. In Chapters 3 and 4, I investigate the fossil record, i.e. the galaxy populations in the local SDSS clusters. Chapter 3 aims to characterize the galaxy distribution within the clusters, i.e. the number density profile, and how the distribution depends upon galaxy color and luminosity. In Chapter 4 I make use of the Principal Component Analysis developed by Wild et al. (2007) to characterize the recent star formation history of galaxies in clusters and the field. Several studies have investigated the star formation rate in clusters, but this work sets itself apart by the large sample size, the

use of spectroscopic indicators for recent and current star formation and AGN activity, and characterizing the cluster galaxy population as function of galaxy stellar mass rather than luminosity.

Finally, in Chapter 5, I compare the population mix in the high-redshift EDisCS clusters to the low-redshift clusters. The EDisCS clusters have been selected optically rather than with X-rays, and are thus not biased towards more massive, relaxed systems as X-ray selected high-redshift cluster samples are. The distribution of cluster velocity dispersions suggests that the EDisCS clusters can indeed be regarded as progenitor systems of the SDSS cluster sample, making a direct comparison of the samples feasible. This comparison is performed via the same spectroscopic analysis used in Chapter 4. The compatibility in selection, mass range, and spectroscopic coverage make this a robust study of evolutionary trends of the galaxy populations in clusters.

2

How special are Brightest Cluster Galaxies?

In this chapter, I use the Sloan Digital Sky Survey to construct a sample of 625 brightest group and cluster galaxies (BCGs) together with control samples of non–BCGs matched in stellar mass, redshift, and color. I investigate how the systematic properties of BCGs depend on stellar mass and on their privileged location near the cluster center. The groups and clusters that I study are drawn from the C4 catalogue of Miller et al., but I have developed improved algorithms for identifying the BCG and for measuring the cluster velocity dispersion. Since the SDSS photometric pipeline tends to underestimate the luminosities of large galaxies in dense environments, I have developed a correction for this effect which can be readily applied to the published catalog data. I find that BCGs are larger and have higher velocity dispersions than non-BCGs of the same stellar mass, which implies that BCGs contain a larger fraction of dark matter. In contrast to non–BCGs, the dynamical mass-to-light ratio of BCGs does not vary as a function of galaxy luminosity. Hence BCGs lie on a different fundamental plane than ordinary elliptical galaxies. BCGs also follow a steeper Faber–Jackson relation than non-BCGs, as suggested by models in which BCGs assemble via dissipationless mergers along preferentially radial orbits. I find tentative evidence that this steepening is stronger in more massive clusters. BCGs have similar mean stellar ages and metallicities to non-BCGs of the same mass, but they have somewhat higher α/Fe ratios, indicating that star formation may have occurred over a shorter timescale in the BCGs. Finally, I find that BCGs are more likely to host radio–loud active galactic nuclei than other galaxies of the same mass, but are less likely to host an optical AGN. The differences I find are more pronounced for the less massive BCGs, i.e. they are stronger at the galaxy group level.

2.1 Introduction

The central galaxies in galaxy clusters seem to be special - in many cases, the differences are visually obvious, because central cluster galaxies often have extended envelopes (i.e. they are cD galaxies) and they are usually the brightest (and most massive) galaxies in their clusters. The term *brightest cluster galaxy* (BCG) has thus become synonymous with the term *central galaxy.*

At first glance, it might seem evident that the location of the BCG at the bottom of the potential well of a cluster must be the cause for any property which distinguishes it from other (cluster) galaxies. However, BCGs are also the dominant population at the massive end of the galaxy luminosity function, and thus, their properties are influenced both by their large masses and by the cluster environment. It is very difficult to disentangle these two influences, because it is difficult to find equally massive non-BCGs for comparison. Since most BCGs are early-type galaxies, their properties are often compared with the known scaling relations for elliptical galaxies. It has been claimed that BCGs lie on the same Fundamental Plane as other ellipticals (Oegerle & Hoessel 1991), but that they lie off its projections (e.g. the Faber–Jackson and Kormendy relations) in that they have lower velocity dispersions and larger radii than predicted by these relations (Thuan & Romanishin 1981; Hoessel et al. 1987; Schombert 1987; Oegerle & Hoessel 1991). More recently, it has been claimed that the slopes of the Faber–Jackson and Kormendy relations change as a function of galaxy luminosity for all elliptical galaxies (Lauer et al. 2006; Desroches et al. 2007). On the other hand, Brough et al. (2005) find that the surface brightness profiles (and thus the radii) of BCGs depend on the host cluster properties.

The formation mechanism of BCGs is also a subject of much debate. Early on, it was suggested that BCGs form when galaxies sink to the bottom of the potential well of a cluster and merge (termed *galactic cannibalism*; Ostriker & Tremaine 1975; White 1976). However, Merritt (1985) argued that tidal stripping would reduce the masses of cluster galaxies to the point where dynamical friction is too slow for this to be a viable mechanism. These analyses assumed that clusters are *static entities.* A further mechanism to form BCGs *in situ* in the cluster is star formation in cluster *cooling flows.* At the centers of clusters, gas reaches high enough density to cool and condense into the cluster core (Silk 1976; Fabian 1994). But while the mass deposition rates inferred from the X-ray luminosities of cooling flow clusters are of the order of several hundreds to $> 1000 M_\odot \mathrm{yr}^{-1}$ (e.g. Allen et al. 1996), observed star formation rates are at most $\sim 100 M_\odot \mathrm{yr}^{-1}$ (Crawford et al. 1999). Recent X-ray studies have furthermore demonstrated that the cluster gas does not cool below ~ 2 keV (e.g. Peterson & Fabian 2006). Moreover, this scenario predicts that the stellar populations of BCGs should be young and blue, which is clearly inconsistent with observations.

These scenarios were proposed before hierarchical structure formation was fully established as the standard cosmological paradigm, and for simplicity they neglected many of the processes that take place when clusters assemble through mergers. Dubinski (1998) used N-body simulations to show that a dominant galaxy forms naturally by merging of massive galaxies when a cluster collapses along filaments. Recently, De Lucia & Blaizot (2007) investigated the formation of BCGs in the context of the Millenium Run simulation (Springel et al. 2005). In their model, the stars that make up BCGs today are formed in a number of galaxies at high redshifts, which subsequently merge to form larger systems (see Fig. 1.9). The final BCGs assemble rather late: by a redshift of $z \sim 0.5$, on average about half of the final stellar mass

lies in the largest progenitor galaxy. Since many of these mergers take place very late when most galaxies have converted the bulk of their gas into stars, the merging events are very nearly dissipationless and are not associated with significant star formation. This scenario is supported by observations that demonstrate that BCGs exhibit little scatter in luminosity over a wide range of redshifts (Sandage 1972; Schneider et al. 1983; Postman & Lauer 1995; Aragon-Salamanca et al. 1998), and that their color evolution is consistent with a passively evolving stellar population that formed at high redshifts ($z_{\mathrm{form}} \sim 2-5$).

Boylan-Kolchin et al. (2006) used two–component N–body simulations of galaxy mergers to show that the remnants of dissipationless mergers remain in the fundamental plane. They showed, however, that the locations of the remnants *within* the fundamental plane, and thus on projected relations such as the Faber–Jackson and size–luminosity relations, depend on the orbits of the merging galaxies. During cluster assembly, infall occurs primarily along filaments, suggesting that mergers onto the BCG may take place preferentially on radial orbits. Boylan-Kolchin et al. (2006) show that BCGs would then be predicted to lie on steeper Faber–Jackson and size–luminosity relations than field galaxies.

Although BCGs are probably not formed in cooling flows, they are believed to play an important role in regulating the rate at which gas cools at the centers of groups and clusters. The central cluster galaxies often harbor radio–loud active galactic nuclei (AGN), which may provide the necessary heating to counteract radiative cooling. Burns (1990) find that 10 out of 14 cD galaxies in cooling flow clusters are radio–loud, compared to 3 out of 13 in clusters without cooling cores. However, Best et al. (2005b) show that radio–loudness also depends strongly on other galaxy parameters such as stellar mass.

2.2 The Sloan Digital Sky Survey

The Sloan Digital Sky Survey (Stoughton et al. 2002; York et al. 2000) is a survey of about a quarter of the extragalactic sky, obtaining photometry in five bands ($ugriz$) of more than 200 million objects and spectra of up to a million objects. The observations are carried out in drift-scan mode on a dedicated 2.5m telescope at Apache Point Observatory, with a large-array CCD camera that allows near-simultaneous photometry. The imaging data is reduced by an automatic pipeline, PHOTO (Lupton et al. 2001), and various classes of objects are then classified for subsequent spectroscopy; those galaxies with $14.5 < m_r < 17.7$ and $\mu < 24.5$ mag arcsec^{-2} comprise the 'main galaxy sample' (Strauss et al. 2002). The spectra are obtained using a fiber-fed spectrograph on the same telescope. On each spectroscopic plate, which has a circular field of view of radius $1°49$, 592 object fibers can be placed. Due to the finite fiber size, any two fibers on the same plate need to be spaced at least $55''$ apart. The fiber allocation is performed by a tiling algorithm, which maximizes the number of objects that can be observed (Blanton et al. 2003b). In the case of a "fiber collision" (i.e. two objects that are closer than $55''$), no preference of objects is given within the usual constraints.

Our analysis is based on the fourth data release (DR4) of SDSS, whose main galaxy sample provides spectra for more than 500 000 galaxies.

2.2.1 Spectral analysis

A multitude of physical properties have been derived for galaxies in the spectroscopic database via stellar population synthesis fitting and are publicly available[1]. The stellar continuum of each galaxy is modelled as a sum of template spectra generated from population synthesis models (Tremonti et al. 2004; Kauffmann et al. 2003a). These fits also lead to measures of the stellar mass–to–light ratio, star formation histories, and mean stellar ages (Kauffmann et al. 2003a, b). After subtracting the stellar continuum, emission line fluxes can be accurately measured, allowing studies of the star formation rates (Brinchmann et al. 2004) and AGN activity (Heckman et al. 2004; Kauffmann et al. 2003c).

2.2.2 Photometry and Stellar Masses

It has recently been noted that the SDSS photometry systematically underestimates the luminosities of nearby BCGs (Bernardi et al. 2006; Lauer et al. 2006). The problem arises because the level of sky background is overestimated both for large objects and in crowded fields. This is not only a problem for BCGs, but for all large galaxies, and the problem is worse in dense cluster environments. Since any estimate of the stellar mass of a galaxy is derived from its luminosity, it is crucial for our analysis to avoid biases in the luminosity measurement.

Apart from the `local sky` background measurement, which is estimated and applied for each galaxy, PHOTO provides a `global sky` measurement estimated over a whole field. In Appendix A, we argue that by adding up to 70% of the difference between `local` and `global sky` to the radial surface brightness profiles (as provided by PHOTO), more accurate photometry can be achieved. We test this procedure using aperture photometry of 35 BCGs from the survey of Postman & Lauer (1995) that are contained in the area of sky covered by the SDSS DR5. We also test our corrected magnitudes by comparing with the photometry provided by 2MASS (Skrutskie et al. 2006). Our correction method (described in detail in Appendix A) has been applied to the BCGs as well as to about 200,000 unique galaxies at $z \lesssim 0.1$, which form the basis of our comparison samples for the BCGs.

Since many BCGs are observed to have surface brightness profiles which do not follow a simple de Vaucouleurs profile (Gonzalez et al. 2005; Bernardi et al. 2006), we choose not to use a magnitude measurement that assumes a certain profile, or is sensitive to the profile shape (this includes Petrosian magnitudes, which include about 80% of the light from galaxies with de Vaucouleurs brightness profiles, but almost 100% of the light from galaxies with exponential light profiles). Instead, we measure isophotal magnitudes, defined as the light within the radius r_{iso23} where the 1D surface brightness profile reaches a surface brightness of $(23 + 10 \log(1 + z)) \, \mathrm{mag}/\square''$ in the r-band (the redshift term accounts for cosmological surface brightness dimming). This is a relatively bright isophote limit, chosen both to avoid residual uncertainties in the sky background subtraction (cf. Fig. A.1) as well as to exclude light from the cD envelope present in some BCGs (which is noticable typically at surface brightness levels one or two magnitudes fainter, cf. Gonzalez et al. 2005). We refer to these magnitudes as *iso23* magnitudes.

Other studies of BCGs have quantified their luminosities within metric apertures (e.g. Postman & Lauer 1995). These studies were focused on cD galaxies, whereas our study includes BCGs of a much broader range in mass and size. Hence metric apertures would

---

[1]http://www.mpa-garching.mpg.de/SDSS/

include very different fractions of light for BCGs at the extreme ends of the mass range, c.f. Fig. 2.3, and any result based on them would be very difficult to interpret. It can be argued that the *iso23* magnitudes are also dependent on the profile shape: For shallower brightness profiles, a larger fraction of the total light / mass is missed. But an estimate of the total light is unfortunately not feasible, due to residual uncertainties in the sky subtraction. We therefore adopt the *iso23* magnitudes as the least biased and least problematic luminosity measurements. However, we have verified that our (qualitative) results do not change if we use Petrosian magnitudes as an attempt to measure total magnitudes.

Stellar mass estimates for the BCGs and the comparison galaxies are derived from these luminosity measurements using the KCORRECT algorithm (Blanton & Roweis 2007), which is also used to determine the k-corrections for our galaxies. BCGs that were not observed spectroscopically (see Sect. 2.3.1) are assumed to have a redshift identical to the cluster redshift. Just as the luminosities should not be taken as an estimate of the total light, the quoted stellar masses are not an attempt to measure the total stellar mass. But since our analysis is based on comparing objects with similar masses and colors, this is not an issue.

2.2.3 Radio catalog

Best et al. (2005a) identified the radio–emitting galaxies within the main spectroscopic sample of the SDSS DR2, by cross–comparing these galaxies with a combination of the National Radio Astronomy Observatory (NRAO) Very Large Array (VLA) Sky Survey (NVSS; Condon et al. 1998) and the Faint Images of the Radio Sky at Twenty centimetres (FIRST) survey (Becker et al. 1995). They then used the optical properties of the galaxies to separate the radio–loud AGN from the radio–detected star–forming galaxies. This work has now been extended to include the DR3 and DR4 data (Best et al., in preparation), and these results were used to identify those galaxies that are radio-loud AGN.

2.3 Selection of clusters and brightest cluster galaxies

The basis of our cluster sample is the C4 cluster catalog (Miller et al. 2005). The C4 catalog is derived using the SDSS spectroscopic sample and is currently available for Data Release 3. It identifies clusters in a parameter space of position, redshift, and color. The algorithm assumes that at least a fraction of the cluster galaxies form a color–magnitude–relation. It identifies galaxies in clustered regions, with neighbors of similar colors, as "C4 galaxies" (see Miller et al. 2005, for a detailed discussion of this selection). From these C4 galaxies, it reconstructs the local density field, and identifies the C4 galaxies at the peaks of this density field as cluster centers (coined the *mean* galaxies).

The C4 catalog identifies 1106 clusters within $0.02 \leq z \leq 0.16$. In order to ensure that our clusters span a large angular extent compared to the minimum distance between fibers (55 arcsec), we limit our cluster sample to $z \leq 0.1$. At this redshift, the magnitude limit of the spectroscopic sample corresponds to $M_r \sim -20$, i.e. slightly fainter than an L^* galaxy. This cut results in a starting sample of 833 clusters.

2.3.1 Selection of the brightest cluster galaxy

Our aim is to find the galaxy closest to the deepest point of the potential well of the cluster. In many rich clusters, this choice is obvious, and the central galaxy can easily be recognized

as a cD elliptical galaxy by its extended envelope. Typically, this is also the Brightest Cluster Galaxy (BCG). However, in some clusters the central, dominant galaxy may not be the brightest galaxy. An example is the cluster C4_2003 [2] , shown in Fig. B.1. The obvious central galaxy is SDSS J215729.42-074744.5 at the center of the image, but it is 0.3 mag fainter than SDSS J215701.71-075022.5, about 6′west-south-west of the former. We identify the former as the BCG (but concede that the term is a misleading nomenclature in this case).

The C4 catalogue lists two galaxies for each cluster that could be considered the BCG: the *mean* galaxy (described above) and the brightest galaxy from the spectroscopic catalog within 500 h^{-1} kpc of the position of the mean galaxy, four times the velocity dispersion, and without strong Hα emission. However, due to the problem of fiber collisions, the true BCG is not included in the SDSS spectroscopic data for about 30% of the clusters and is thus missed by the C4 algorithm.

An earlier version of the C4 catalog tried to correct for this by selecting a brightest cluster galaxy based on the photometric catalog. This object was selected to lie within 1 h^{-1} Mpc of the cluster center, and have a color compatible with the color-magnitude relation of that cluster. Visual checks revealed, however, that this did not provide a reliable BCG: out of a subsamble of 128 clusters, 17 of the photometric BCGs identified by C4 were stars misclassified as galaxies, and 36 were spiral galaxies (some of these located at the edge of the cluster).

To identify the BCG for each cluster, we use the following procedure:

1. Based on the cluster redshift and velocity dispersion given by C4, we estimate the virial radius of the cluster:

$$R_{200} = 1.73 \frac{\sigma_{\rm v,cl}}{1000 \text{ km s}^{-1}} \frac{1}{\sqrt{\Omega_\Lambda + \Omega_0(1 + z_{\rm cl})^3}} h^{-1} \text{ Mpc} \qquad (2.1)$$

(see Finn et al. 2005). As C4 lists velocity dispersions within fixed physical radii (0.5, 1, 1.5, 2, 2.5 h^{-1} Mpc), we use the minimum non–zero value of these different values in this step.

2. Within the projection of the larger of R_{200} and 0.5 Mpc around the *mean* galaxy, we select the two brightest galaxies that meet the following criteria:

   – The concentration index $c = R_{90}/R_{50}$ is larger than 2.5 (where R_{90} is the radius containing 90% of the petrosian flux measured in the i-band amd R_{50} is the radius containing 50% of this flux), and `fracDeV_r`> 0.5 (this is a measure of the contribution of the de Vaucouleurs profile to the SDSS model r–magnitude). These cuts select galaxies likely to be early–types.

   – The color is compatible with that of the C4 *mean* galaxy to within $\Delta(u - g) \leq 0.6$ (unless one of the u magnitudes has a large error estimate), $\Delta(g-r) \leq 0.5$, $\Delta(r-i) \leq 0.4$, and $\Delta(r - i) \leq 0.4$ (these are the dimensions of the color criteria originally used in the C4 algorithm to identify clustering in color space).

   – The flag `TARGET_GALAXY` has been set and the flag `SATURATED` is not set (these criteria allow us to identify stars that have been misclassified as galaxies, but they also apply to some low-redshift, bright galaxies).

---

[2]A note on the cluster IDs: the IDs used in the DR3 version of C4 are not identical to those in the DR2 version. Since the DR3 catalog was released only within the SDSS collaboration, the DR2 IDs are the "official" IDs, so whenever possible, we identify clusters by their DR2 ID (e.g. C4_2003). For those clusters without a DR2 ID, we use the DR3 ID, and denote these as e.g. C4_DR3_2004.

– If the object has spectroscopic data, we require that the redshift is within $\Delta z < 0.01$ from the cluster redshift.

The brightest galaxy that meets these criteria is our initial BCG candidate. However, it is possible that these criteria select a foreground elliptical. Thus, if the second brightest galaxy is more than one magnitude fainter than the brightest, we also consider it as a BCG candidate.

3. We then loosen some of these critieria:

– we require only $c > 2.3$,

– there is no constraint on $\Delta(u - g)$,

– TARGET_GALAXY does not need to be set, and SATURATED can be set.

Galaxies which meet this second set of criteria and are brighter than (both) the candidate(s) selected in the previous step enter the list of candidates. Unfortunately, misclassified stars enter our candidate lists at this stage.

4. a) If this procedure returns only one candidate, which agrees with the spectroscopic BCG given by C4, then this is automatically considered the correct choice. This is the case for 242 clusters.

b) If this is not the case, then the BCG candidates (those given by C4 and those identified by our criteria) are inspected visually. For this purpose, we examine $2\!.\!5 \times 2\!.\!5$ color images of the BCG candidates (provided by the DR4 Catalog Archive Server [CAS][3]). These thumbnail images allow us to

– identify cD galaxies by their extended envelope

– identify stars misclassified as galaxies

– identify obvious foreground ellipticals

In the same step, a color image of the cluster (encompassing a field slightly larger than R_{200}) can be viewed, with the BCG candidates marked. An impression can thus be gained of how the positions of the candidates relate to the C4 cluster center(s) (as given by the *mean* galaxy and the geometric cluster center, based on the mean of the positions of the C4 cluster galaxies), visible galaxy overdensities and other structures in the field. If there is more than one galaxy left in the candidate list, this color image allows us to choose the (brightest) one at the center of the galaxy overdensity identified by C4. In case such an overdensity is not apparent, we choose the brightest elliptical galaxy in the vicinity of the *mean* galaxy.

For 472 clusters, the BCG can be identified fairly easily by means of these thumbnail images and the cluster image.

c) In case the previous step does not allow an unambiguous choice of the BCG, we enlarge the candidate list by adding galaxies within 2 Mpc that meet the criteria cited above. Along with this set of thumbnail images, we also inspect a color image where galaxies within $\Delta z < 0.01$ from the cluster redshift and 2 Mpc from the *mean* galaxy have been marked (see Fig. B.1). It is this image that allows us to visualize the clustering and to follow the galaxy distribution at the redshift in question. BCG candidates belonging

---

[3]http://cas.sdss.org/astro/en/

to neighboring clusters can be identified. Conversely, if the C4 cluster corresponds to a weak number density fluctuation within another cluster, the BCG of this larger cluster is chosen. We identify the BCG of 54 clusters in this step.

d) The remaining 65 clusters require further scrutiny. For some of these clusters, this is necessary because the galaxy we identify as the central, dominant galaxy is not contained in the list of candidates. In other cases, it is evident from the cluster images that the cluster is in fact part of a larger cluster. In this step, we use the `Finding Chart`, `Navigate`, and `Explore` tools of the CAS website interactively. We start by marking galaxies within 2 Mpc and $\Delta z < 0.01$ from the *mean* galaxy (as before), but then altering the radius, center, and redshift range to gain an impression of the clustering. We identify the center of the nearest galaxy overdensity and choose the most likely BCG within it. The color and brightness criteria that were previously used to determine the BCG candidate(s) are not applied in this step.

At this stage, a given galaxy may have been identified as the BCG for more than one cluster. We then keep only the cluster whose *mean* galaxy is closest to the BCG. This rejects 101 clusters as being substructures of other clusters.

2.3.2 Determination of the velocity dispersion and the virial radius

The C4 algorithm measured velocity dispersions within fixed radii (see Sect. 2.4.3 for a more detailed discussion of the C4 velocity dispersions). We prefer to measure the velocity dispersion $\sigma_{\mathrm{v,cl}}$ within the virial radius R_{200}, which can be related to the velocity dispersion and cluster redshift z_{cl} via Eq. (2.1). We thus developed an iterative algorithm to determine these three quantities:

1. From the catalog of galaxies described in Sect. 2.2.1, we select those that lie within $2R_{\mathrm{start}}$ from the BCG, where R_{start} is determined using Eq. (2.1) with $\sigma_{\mathrm{v,cl}}$ given by the average value of the cluster velocity dispersions measured by C4. We also require the galaxies to lie within $\Delta z < 0.025$ of the cluster redshift.

2. For our first estimate of z_{cl}, we take the redshift given by C4, $z_{\mathrm{cl}}^{\mathrm{C4}}$. For the first estimate of $\sigma_{\mathrm{v,cl}}$ (and R_{200}), we use the median absolute deviation of the starting sample of galaxies with respect to $z_{\mathrm{cl}}^{\mathrm{C4}}$. We also limit this first estimate to be less than 500 km/s, a step that is necessary to exclude surrounding large–scale structure.

3. For each galaxy, we calculate its velocity within the cluster rest-frame:

$$\frac{v_i}{c} = \frac{z_i - z_{\mathrm{cl}}}{1 + z_{\mathrm{cl}}} \tag{2.2}$$

4. From those galaxies within $\pm 3\sigma_{\mathrm{v,cl}}$ of z_{cl}, and within R_{200} from the BCG, we re-determine z_{cl}, $\sigma_{\mathrm{v,cl}}$ (and thus also R_{200}) using the biweight estimator from Beers et al. (1990).

5. Steps 3 and 4 are repeated until convergence is reached, i.e. subsequent iterations differ by less than 0.1% in z_{cl} and $\sigma_{\mathrm{v,cl}}$. Galaxies are allowed to re-enter the sample. The galaxies contained in the final sample are considered the cluster galaxies.

   It may happen that the iteration finds an oscillating solution, i.e. iteration $n+2$ yields the same solution (and the same galaxies) as iteration n. In this case, the algorithm modifies

the input $\sigma_{\mathrm{v,cl}}$ to a random value between the two solutions and continues. Also, the convergence criterium is relaxed by factor of two every 200 iterations. A maximum of 1000 iterations is allowed.

6. To estimate the error on the velocity dispersion, we draw $10\,000$ bootstrap realizations from the cluster galaxies and calculate the velocity dispersion of each. We adopt 68% confidence intervals as our estimate of the $\pm1\sigma$ error .

For 55 clusters, the algorithm does not converge or its sigma– and radius–clipping subsequently remove all (or all but one) of the galaxies from the starting sample. Since these systems cannot be considered bound, they are removed from the cluster list.

At this point, all the clusters are inspected visually. We check a color image of the cluster with the cluster galaxies marked, as well as the redshift histogram. We mark clusters with the following indications that either the choice of BCG or the definition of cluster membership may be improved:

- The redshift histogram does not justify the value of the velocity dispersion. For clusters in very rich environments, the velocity dispersion can be overestimated if galaxies of neighboring groups and filaments are included. Clusters with a velocity dispersion exceeding 1500 km/s are automatically flagged, but also those with two or more spikes in the redshift histogram. 59 clusters are marked in this step.

- Some of the cluster images show that the selected BCG is not at the center of the clustering. In others, there may be another bright elliptical present which could be the BCG, or the true BCG did not meet the criteria used to select BCG candidates (i.e. mostly late–type BCGs). 67 clusters are listed for re-investigation in this step.

- Clusters in which the BCG redshift (if in the spectroscopic database) differs from the cluster redshift by more than $\Delta z = 0.002$ are also flagged (15 clusters).

In this second round of visual checking, the choice of BCG or the sigma– and radius–clipping limits can be changed. The former is done if the previously selected BCG is clearly associated with a substructure of a larger cluster, but also if there is a possibly better BCG candidate that was previously missed. Note that many of these alternative BCGs are in fact foreground objects – whenever possible, we retrieve redshift information on these objects from CAS or the Nasa/IPAC Extragalactic Database, NED[4]. For 21 clusters, the "new" BCG has not previously been selected as the BCG of another cluster. For 35 "clusters", the BCG has been attributed to another cluster, and so these systems are considered infall regions of these other clusters and discarded from the list. The sigma– and radius–clipping limits are changed for 53 clusters to avoid galaxies in nearby structures being included as cluster members (the sigma–clipping is typically changed from 3σ to 2.5σ or 2.0σ – note that this affects only the choice of galaxies from which $\sigma_{\mathrm{v,cl}}$ and z_{Cl} are determined; cluster membership is still defined to be within $3\sigma_{\mathrm{v,cl}}$ and R_{200}). For 67 clusters, nothing is changed.

At this stage, we discard those systems that only contain 2 or 3 galaxies within $3\sigma_{\mathrm{v,cl}}$ and $1R_{200}$. This leaves 625 entries in our cluster sample. Fig. 2.1 shows a histogram of the number of spectroscopic members for our cluster sample. The original C4 catalog considered only clusters with at least 8 galaxies within $1h^{-1}\mathrm{Mpc}$ and $\Delta z = 0.02$. This is a much larger volume than we probe, and it is thus not surprising that we typically assign fewer galaxies to each cluster.
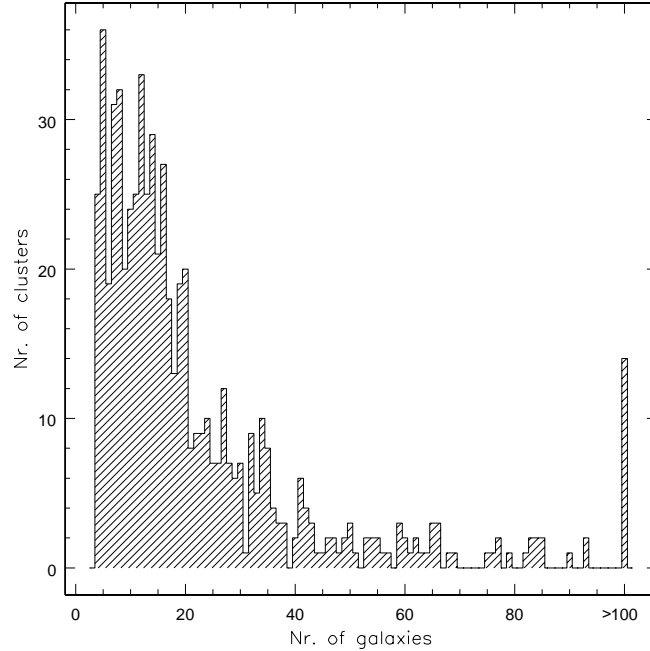
Figure 2.1: Histogram of the number of spectroscopic members within $\pm 3\sigma_{\mathrm{v,cl}}$ and $1R_{200}$ for our final cluster sample. Those clusters with ≥ 100 members are grouped into a single bin. The cluster with the most members is C4_DR3_3031 (Abell 2199) with 263 members.

Our final cluster sample spans a large range in velocity dispersion, from groups of $\lesssim 200$ km/s to clusters of over 1000 km/s (Fig. 2.2). The positions of our BCGs as well as the cluster properties determined by our algorithm are listed in Table 2.1. Those systems with velocity dispersions $\lesssim 300$ - 400 km/s are more likely to be galaxy groups than galaxy clusters. We use the terms 'cluster' and 'brightest cluster galaxy' loosely in this paper to refer to both clusters and groups.

Fig. 2.3 presents a gallery of BCGs, sorted according to the velocity dispersion of the parent cluster (every 18th BCG is shown). The appearance of the BCG is certainly a function of $\sigma_{\mathrm{v,cl}}$, but it is not a monotonic one. While the BCGs of groups are mostly fairly isolated, rather spherical elliptical galaxies, the BCGs of more massive systems are in general larger and more elongated, they often have a cD envelope and are surrounded by many satellite galaxies.

2.4 Comparison to C4

2.4.1 Selected BCGs

For 31 clusters in the final sample, the BCG we identified corresponds to both the C4 *mean* galaxy and the spectroscopic BCG identified by C4. 19 of these were classified automatically, as there was no other candidate in our list.

---

[4] http://nedwww.ipac.caltech.edu/

Table 2.1: Excerpt of our catalog of Brightest Cluster Galaxies for the C4 cluster catalog, along with the cluster properties derived by our algorithm. The complete catalog is available electronically. Note that columns (1) and (2) refer to the C4 cluster ID (see footnote in Section 2.3.1); column (7) gives the number of galaxies from which the cluster redshift and velocity dispersion were determined.

| ID_2	ID_3	α_{BCG} [°]	δ_{BCG} [°]	z_{cl}	σ_{v} [km/s]	N_{gal}
(1)	(2)	(3)	(4)	(5)	(6)	(7)
1000	1000	202.5430	-2.1050	0.087	648^{81}_{-90}	35
1001	1001	208.2767	5.1497	0.079	746^{57}_{-59}	82
1002	1002	159.7776	5.2098	0.069	800^{57}_{-56}	90
1003	1004	184.4214	3.6558	0.077	966^{58}_{-60}	127
1004	1005	149.7174	1.0592	0.081	458^{48}_{-52}	21
1005	1006	191.3037	1.8048	0.048	340^{53}_{-55}	24
1007	1009	177.4721	5.7008	0.075	404^{40}_{-43}	27
1009	1011	198.0566	-0.9745	0.085	631^{71}_{-75}	36
1010	1012	192.0112	-1.6528	0.088	420^{77}_{-80}	14
1011	1013	227.1073	-0.2663	0.091	748^{61}_{-66}	42
-	1014	220.1785	3.4654	0.027	459^{34}_{-35}	105
1013	1015	203.0701	1.2233	0.079	327^{59}_{-74}	10
1014	1016	175.2992	5.7348	0.098	660^{54}_{-56}	55
1015	1017	182.5701	5.3860	0.077	596^{53}_{-59}	41
1016	1018	154.9344	-0.6384	0.093	455^{137}_{-153}	17
1017	1019	227.8480	-0.0593	0.091	509^{59}_{-64}	36
1018	1020	214.3980	2.0532	0.054	605^{51}_{-53}	69
1019	1021	195.7262	3.3174	0.071	496^{56}_{-59}	24
-	1024	199.8197	-0.9954	0.083	579^{87}_{-91}	37
1023	1025	153.4095	-0.9254	0.045	790^{52}_{-57}	66
1341	1026	155.6325	2.3608	0.072	580^{71}_{-76}	26
-	1027	191.9269	-0.1373	0.088	1020^{87}_{-91}	55
1027	1028	199.1357	0.8702	0.080	364^{54}_{-60}	16
1030	1030	206.1357	2.9541	0.077	511^{66}_{-73}	29
-	1032	218.4964	3.7780	0.029	570^{58}_{-60}	76
1032	1033	211.4731	-1.2045	0.054	184^{47}_{-64}	4
-	1034	165.7398	7.6039	0.072	321^{41}_{-44}	20
1034	1036	192.3087	-1.6874	0.085	771^{63}_{-67}	64
1036	1038	151.8861	0.5942	0.097	550^{61}_{-65}	29
-	1039	186.8781	8.8246	0.090	846^{63}_{-66}	50
1037	1040	213.6360	1.7316	0.054	299^{37}_{-39}	16
1038	1041	179.3707	5.0891	0.076	678^{66}_{-69}	62
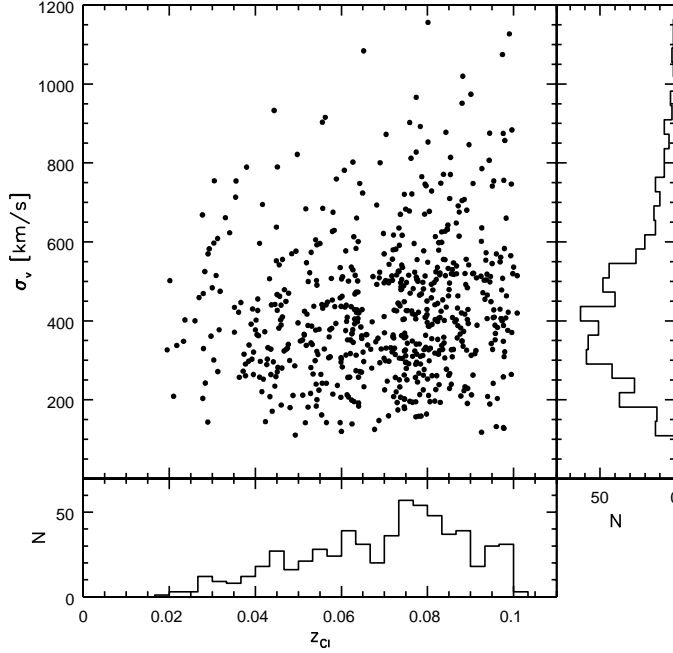
Figure 2.2: Distribution of the redshifts and velocity dispersions we measure for our final cluster sample. Error bars have been omitted for clarity. The marginal histograms show the distribution binned in redshift (lower panel) and in velocity dispersion (right panel).

In 343 clusters, our BCG is the same as the C4 spectroscopic BCG, but not the *mean* galaxy (183 automatically classified).

In 41 cases, the BCG is the same as the C4 *mean* galaxy, but not the C4 spectroscopic BCG. These are predominantly small systems, where the C4 spectroscopic BCG belongs to another system.

The BCGs of 210 clusters correspond neither to the *mean* galaxy, nor to the C4 spectroscopic BCG. Of these, 141 (i.e. 23% of the whole sample) are not in the spectroscopic catalog.

In Fig. 2.4, we compare the positions of our BCGs with those of the C4 *mean* galaxies. For the majority of the clusters, these two positions fall within 500 kpc of one another. 53 BCGs lie farther than 500 h^{-1} kpc from the *mean* galaxy [5] and of these, 21 lie farther away than 1 Mpc. At these distances, the original cluster center is well in the outskirts of the structures we identify.

An example is C4_DR3_1283 (see Fig. B.2), where the BCG and the original *mean* galaxy are separated by 2.8 Mpc, equivalent to $1.6R_{200}$ according to the velocity dispersion we measure. The *mean* galaxy is a $10^{10} M_\odot$, star–forming galaxy at $z = 0.099$, in a rich field that is likely to be an infall region of the cluster. The BCG we identified (a $4 \times 10^{11} M_\odot$ elongated elliptical with a cD envelope) is at the center of a cluster of 22 other galaxies. It is curious that this cluster was not picked up by the C4 algorithm. The comparatively high redshift of

---

[5]500 h^{-1} kpc is the radius within which the C4 algorithm identifies its spectroscopic BCG
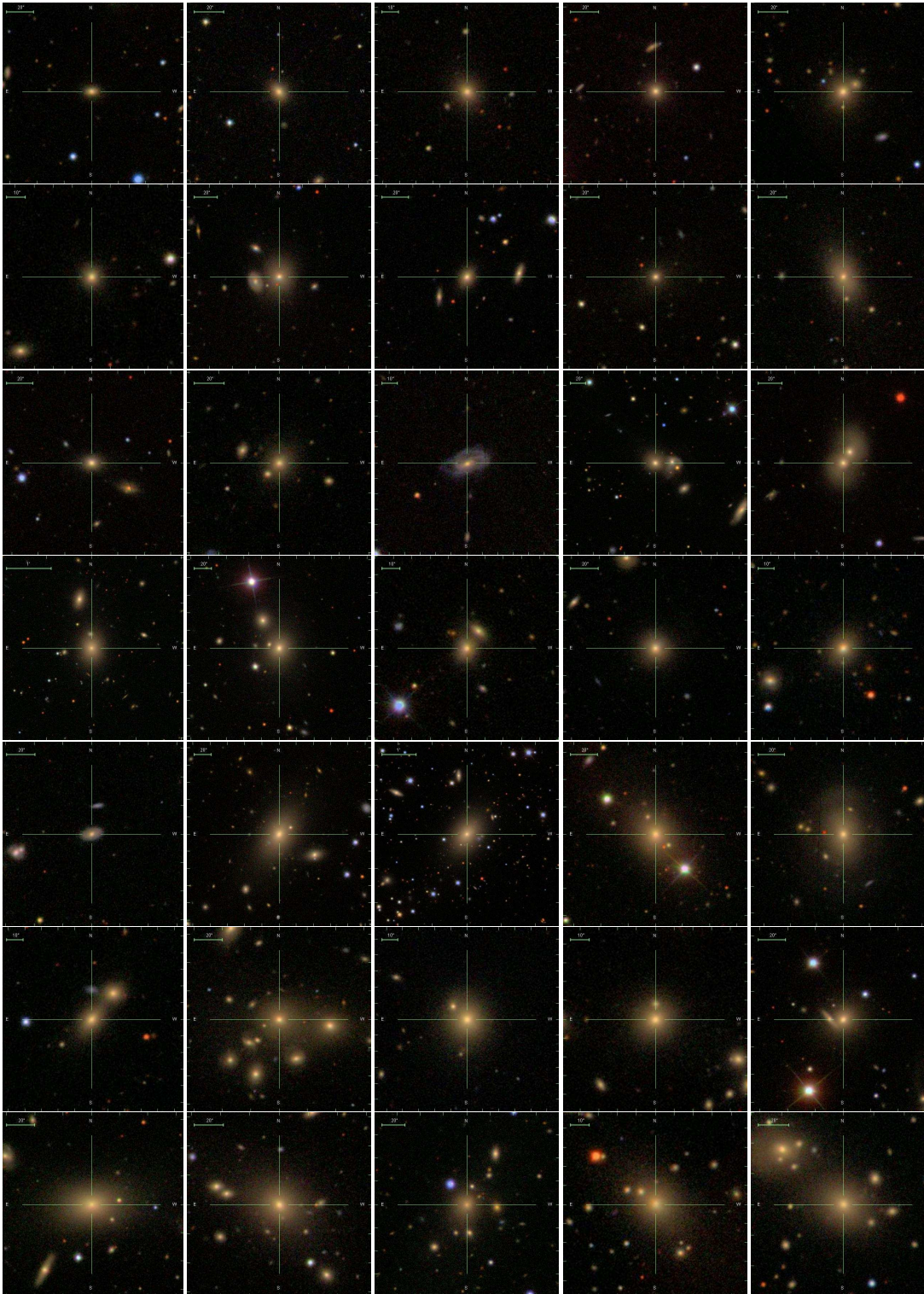
Figure 2.3: A gallery of BCGs. Each image is 200 kpc on the side. From left to right, top to bottom: C4_DR3_3351, C4_2042, C4_DR3_1343, C4_3275, C4_3087, C4_DR3_3201, C4_DR3_3106, C4_1224, C4_3206, C4_2065, C4_DR3_3272, C4_DR3_1366, C4_DR3_2140, C4_3059, C4_DR3_3386, C4_DR3_1355, C4_3068, C4_DR3_3034, C4_1025, C4_1226, C4_DR3_1360, C4_3055, C4_DR3_1356, C4_1024, C4_1076, C4_1191, C4_1073, C4_DR3_3105, C4_3009, C4_DR3_1275, C4_DR3_3027, C4_1058, C4_DR3_3084, C4_DR3_3349, C4_3002.
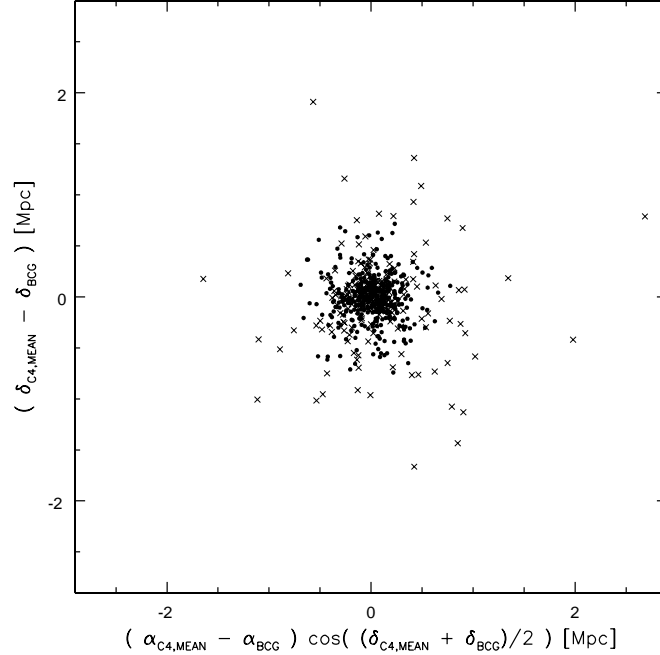
Figure 2.4: The differences in the positions of the C4 *mean* galaxy and our BCG, expressed in Mpc. Clusters in which the BCG is neither the *mean* galaxy nor the C4 spectroscopic BCG are shown as crosses, the other clusters are shown as filled circles.

the cluster ($z = 0.095$) may possibly play a role in this. The cases of the other clusters with large separations between the BCG we identify and the C4 *mean* galaxy are similar, though less striking.

2.4.2 Cluster redshift measurements

The original C4 algorithm measures the cluster redshift using the biweight estimator of Beers et al. (1990) applied to all spectroscopic members within an aperture of 1 h^{-1} Mpc from the luminosity-weighted geometrical center of the cluster and within $\Delta z = 0.02$ of the peak of the redshift histogram defined by these galaxies. While 1 h^{-1} Mpc is comparable to R_{200} for a cluster with a velocity dispersion of $\sim$ 600 km/s, the corresponding redshift interval from which we determine the redshift of such a cluster would be only $\Delta z = 0.006(1 + z_{Ccl})$.

In Fig. 2.5, we plot the relative differences between the two redshift measurements as a function of the velocity dispersion $\sigma_{v,cl}^{C4}$ measured by C4 within 1 h^{-1} Mpc. Our new redshift lies outside the $1\sigma_{v,cl}^{C4}$ redshift interval for only a few clusters , and only one lies outside the $3\sigma_{v,cl}^{C4}$ limit. The most notable outlier is C4_DR3_2163, with a velocity offset of about 2400 km/s. In our cluster sample, C4_DR3_2163 is a group of four galaxies at a redshift of $z_{cl} = 0.070$ and a velocity dispersion of 225_{-101}^{+73} km/s. Its redshift histogram shows another spike of galaxies at a redshift of 0.082 which can be associated with C4_2124(see Fig. B.3 and Fig. B.4). We thus conclude that the C4 algorithm considered these two structures as a single cluster, whereas our algorithm was able to separate them.
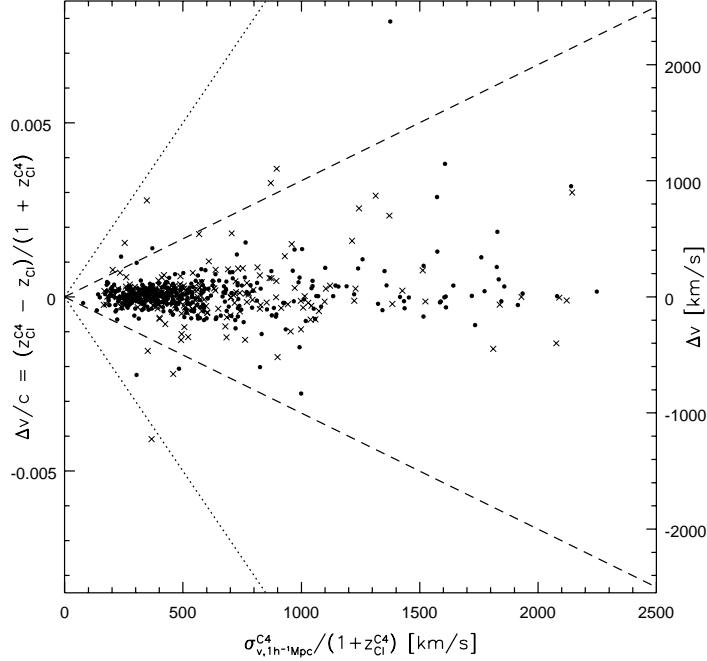
Figure 2.5: The differences between the C4 and our cluster redshift measurement (expressed as relative velocity) compared to the velocity dispersion $\sigma_{v,cl}^{C4}$ measured by C4 within $1\ h^{-1}$ Mpc (expressed in the cluster rest-frame). The dashed line indicates $\sigma_{v,cl}^{C4}$, and the dotted line $3\sigma_{v,cl}^{C4}$. As in Fig. 2.4, clusters in which the BCG is neither the *mean* galaxy nor the C4 spectroscopic BCG are shown as crosses, and as filled circles otherwise.

2.4.3 Velocity dispersion measurements

The C4 catalog provides five measures of a cluster's velocity dispersion, measured within 0.5, 1, 1.5, 2, and 2.5 h^{-1} Mpc from the positional centroid measured on the sky. A first estimate for the velocity dispersion is made using the biweight estimator for all galaxies within $\Delta z = 0.02$ of the estimated cluster redshift. The final velocity dispersion (expressed in the observer's frame) is recomputed from galaxies within the redshift interval equal to $\pm 4\sigma_{v,cl}^{C4}$.

Fig. 2.6 shows a comparison of our velocity dispersions to the C4 velocity dispersion within the radius that best corresponds to our estimate of the virial radius. At low velocity dispersions ($\sigma_{v,cl} \lesssim 600$km/s), the measurements agree well for many clusters. At higher velocity dispersions (as measured by C4) our algorithm obtains lower values for the majority of the clusters. As was previously shown for C4_DR3_2163, this is mainly caused by the fact that our iterative algorithm separates neighboring groups/clusters better than C4.

2.5 Radio–loud AGN activity of BCGs

It is known that BCGs often host radio–loud AGNs (e.g. Burns 1990). It has previously not been investigated whether this is simply a consequence of the strong dependence of radio–AGN activity on galaxy stellar mass ($f_{radio-loud} \propto M_*^{2.5}$ (Best et al. 2005b)), or whether this is a special property of BCGs. With our large sample of BCGs, it is possible to disentangle
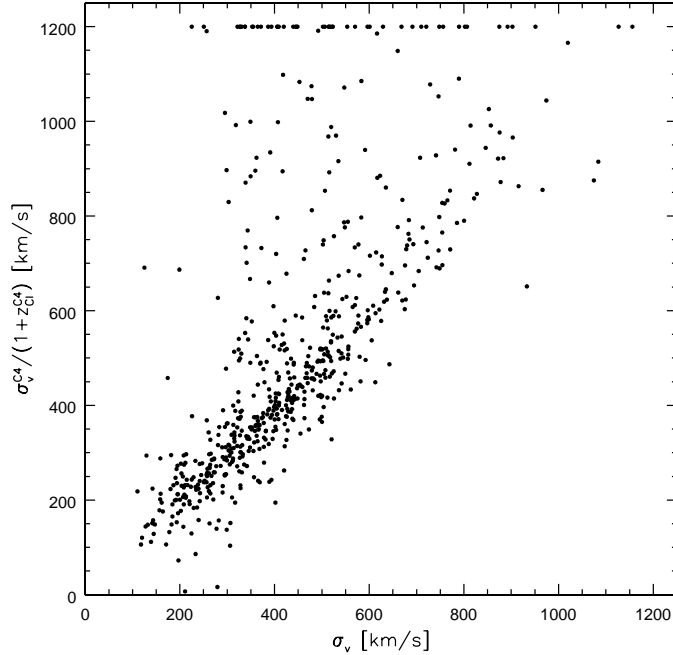
Figure 2.6: Comparison of the cluster velocity dispersions measured by C4 and by our algorithm. We adopt the C4 velocity dispersion measured within the radius that best corresponds to the virial radius measured from our algorithm. Those C4 values that are larger than 1200 km/s are plotted at this value.

the mass dependence and the influence of the cluster environment. Fig. 2.7 compares the fraction of galaxies that are radio–loud for the BCG sample with the results found for all SDSS galaxies that overlap the NVSS and FIRST surveys. BCGs of all luminosities / masses are more likely to be radio–loud than other galaxies of the same luminosity / stellar mass. This enhancement ranges from a factor of 10 at masses of $5 \times 10^{10} M_\odot$ to less than a factor of two above $4 \times 10^{11} M_\odot$. Best et al. (2005b) have argued that radio–AGN activity is fuelled from the hot gas envelopes of galaxies. In this scenario, groups and clusters provide an additional hot gas reservoir, which boosts the radio–AGN activity of the central galaxies. This result, and its implications for the cooling flow model, are investigated in more detail in the accompanying (Best et al. 2007).

In this work, we use the enhanced radio–AGN fraction of BCGs as a diagnostic for the *reliability* of the BCG selection, i.e. are our BCGs indeed better tracers of the bottom of the clusters' potential wells than the original C4 BCGs? In Fig. 2.8, we repeat the previous analysis for C4 BCGs. At the highest mass bins ($> 10^{11.1} M_\odot$), the C4 BCGs have a similar radio–loud fraction to our BCGs, but at lower masses, the radio–loud fraction is lower than in ours. We also investigate the radio–loud fraction in clusters where our method and the C4 algorithm select different BCGs (252 clusters). Here, the difference becomes even clearer: our BCGs have a much higher radio–loud fraction than those identified by C4.

In the right panel of Fig. 2.8 we repeat this analysis on the C4 *mean* galaxies. A similar trend as for the C4 BCGs is seen.

These results can easily be explained by the difference in selection algorithm: in a cluster
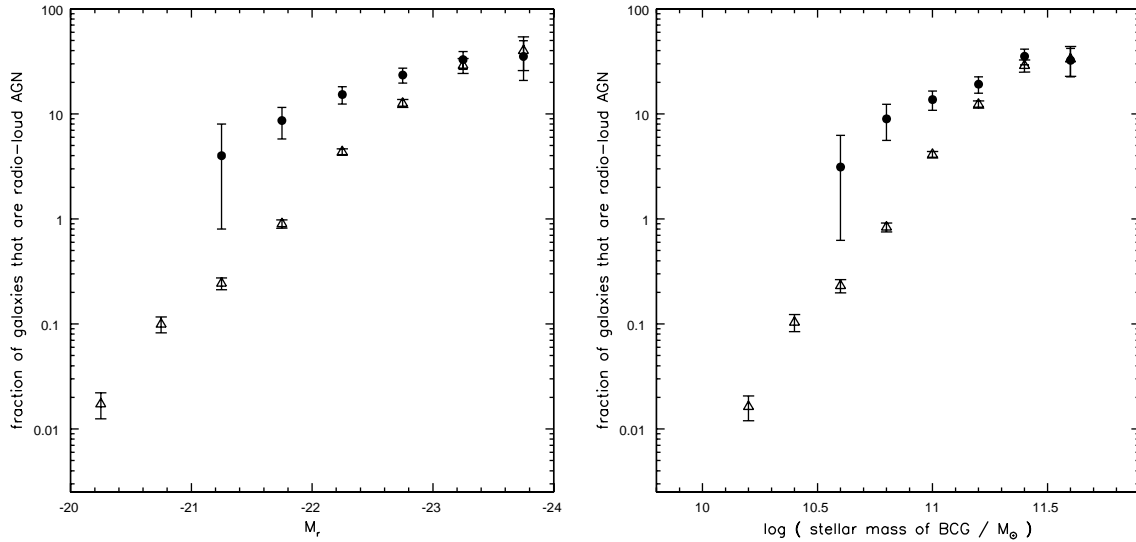
Figure 2.7: The fraction of galaxies that are radio loud AGN, as a function of luminosity (left) and stellar mass (right). Results are plotted for all galaxies at $z < 0.1$ (open triangles), and for the BCGs (solid circles). Galaxies are considered radio–loud if their 1.4 GHz radio luminosity is greater than 10^{23} W/Hz, and they are not classified as star-forming.

where the BCG is the most massive and brightest galaxy and has spectroscopic information available, C4 will correctly identify it, and hence the agreement is good in the high mass bins. However, if C4 misses the 'real' BCG, for example due to fiber collisions, it classifies a less massive galaxy (typically not at the bottom of the potential well) as a BCG. Since these galaxies are normal cluster galaxies, their radio–loud fraction is lower than that of BCGs of equal mass. Hence, the C4 algorithm results in an underestimate of the radio–loud fraction at low masses.

2.6 Optical properties of BCGs

Our large sample of BCGs and the extensive SDSS database allow us to compare the structural properties of BCGs with those of non-BCGs in order to distinguish the roles of mass and environment in governing their properties. In order to perform the comparison, we construct a comparison sample of "control" galaxies for each BCG by finding its three closest neighbors in a space spanned by (the logarithm) of galaxy stellar mass, redshift, and $g - r$ color. The "redshift axis" of this space is scaled by a factor of five, so that a difference of 0.1 in $\log M_\star$ corresponds to a redshift difference of 0.02 , and a difference of 0.1 in $g - r$. The matching is performed in order of decreasing BCG mass, and galaxies are not allowed to enter the comparison sample more than once.

By matching in redshift, redshift–dependent aperture effects are avoided. The matching in $g - r$ ensures similar stellar populations and mass–to–light ratios in the BCGs and their controls, i.e. effectively, early–type BCGs are matched to early–type galaxies. Without the $g - r$ matching, there are more late–type galaxies in the control sample than the BCG sample. But since our method of selecting BCGs is somewhat biased towards selecting early–type
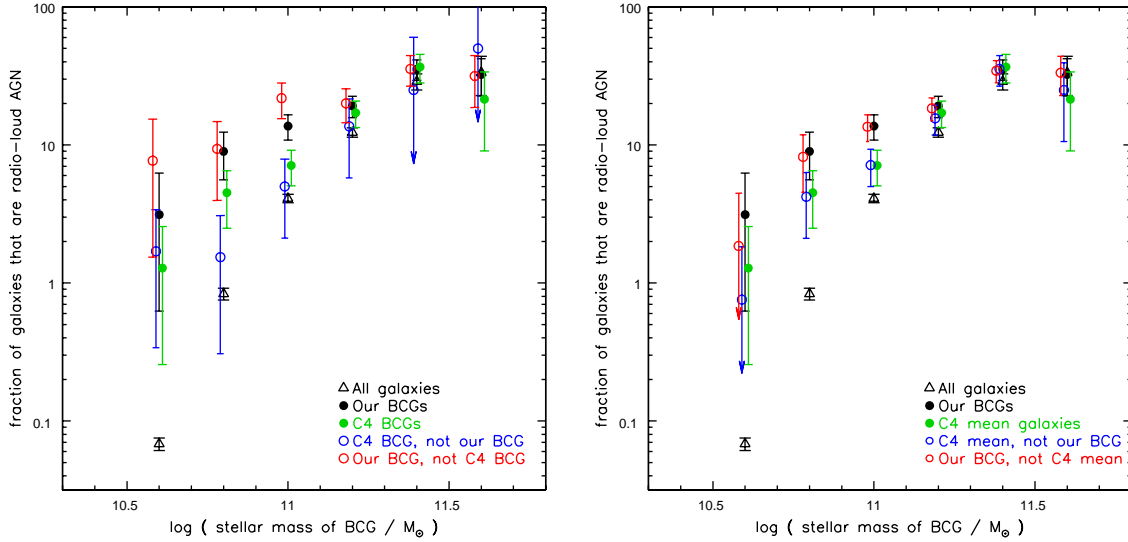
Figure 2.8: Left: The radio–loud fraction of BCGs identified by C4 (green, filled circles), compared to those identified by our method (black, filled circles). We also show the radio–loud fractions derived only from clusters where the two choices differ: C4 BCGs are shown as blue, open circles, our BCGs are shown as red, open circles. Arrows indicate that the result is an upper limit only. The points are slightly offset in mass for clarity. Right: The same for the C4 *mean* galaxies.

galaxies over late–types, we cannot unambiguously deduce that BCGs are more likely to be early–types.

The pool of galaxies from which the control sample is drawn consists of all galaxies in the DR4 spectroscopic catalog that have not been identified as a BCG in our sample. Yet, at the very massive end ($\log M_\star/M_\odot > 11.5$) there are not enough non–BCGs to provide three control galaxies per BCG. On the other hand, since we draw comparison galaxies from the full DR4 database, whereas the C4 catalog is based on DR3, the control sample is "contaminated" by BCGs that failed to enter our sample, particularly for the most massive galaxies. [6] Hence, for a large part of the analysis, we restrict the sample to BCGs with $\log M_\star/M_\odot <$ 11.3; this avoids the problem of finding three suitable non–BCGs for the comparison sample, and also purifies the comparison sample since at very high masses, a significant fraction of the comparison galaxies may themselves be BCGs. With these criteria, we construct two comparison samples, one for the full set of BCGs, and the other for the subset of BCGs with spectroscopic information.

In order to study scaling relations over a larger range in mass, we construct two more comparison samples (one drawn from all BCGs and one of them for BCGs with SDSS spectroscopy) with only one matched galaxy. Restricting to one comparison galaxy per BCG minimizes the problem of lack of comparison galaxies at the high mass end. For this matching, we restrict our analysis to only early–type BCGs and comparison galaxies by requiring

---

[6]We have also attempted to clean the matched sample by applying the algorithm described in Sect. 2.3.2 to these galaxies, and considering those which are the brightest in structures of more than four galaxies to be possible BCGs. About one third of the matched galaxies are such BCG candidates. Basing our analysis on the remaining BCGs and the respective matched galaxies does not qualitatively alter our results.

$M_g - M_r > 0.75$ and `fracDeV_r` > 0.8.

Our four comparison samples are summarized below:

CS3p: A comparison sample of three matching galaxies for BCGs with $\log M_\star/M_\odot < 11.3$. The galaxies are matched in mass, redshift, and $g - r$ color.

CS3s: Like CS3p, but for BCGs contained in the spectroscopic database.

CS1p: A comparison sample of one matching galaxy for each BCG (with no upper mass limit). The sample is matched in mass, redshift, and $g - r$ color, and restricted to only early-type BCGs and comparison galaxies ($M_g - M_r > 0.75$ and `fracDeV_r` > 0.8).

CS1s: Like CS1p, but for BCGs contained in the spectroscopic database.

The first two samples are used to compare the *distributions* of physical parameters for BCGs and non-BCGs. The latter two samples are used to analyze early-type galaxy scaling relations, and to probe them to the highest masses.

In Fig. 2.9 and Fig. 2.10 we present the distributions of a variety of photometric and spectroscopic parameters for the BCGs and the comparison samples CS3p and CS3s. For each parameter, we list the decimal logarithm of 1 minus the Kolmogorov-Smirnov confidence level at which the null hypothesis that the distributions are drawn from identical parent populations is rejected (i.e. a 99% probability that the distributions are different will have a value of -2) .

By construction, the BCGs and the comparison sample are identical in stellar mass, redshift, and color. Because both stellar mass and color are the same, the distributions of luminosity are also equivalent.

Note that our stellar masses are calculated using the `kcorrect` algorithm applied to isophotal magnitudes that have been corrected for sky-subtraction errors. These masses are not the same as the stellar masses estimated using the methods described in Kauffmann et al. (2003a), which we compare in Fig. 2.10, panel (c). For the latter, the mass-to-light ratio determined from the continuum spectrum is applied to the SDSS petrosian magnitude. Since these magnitudes underestimate the luminosity, the galaxy mass is underestimated as well. We also find that non-BCGs show stronger gradients between their fiber colors and their iso23 aperture colors (Fig. 2.9, cf. Sect. 2.6.3). Color gradients imply that the mass-to-light ratio varies across the galaxy and this is not accounted for when deriving stellar masses from the spectra.

2.6.1 Structural parameters

2.6.1.1 Radii and surface brightness

In agreement with previous studies, we find that BCGs are larger (Fig. 2.9, panels [f] and [g]) and have lower surface brightnesses than non–BCGs (Fig. 2.9, panels [h] and [i]). The difference is more prominent for the inner characteristic radius R_{50} (defined as the radius containing half the galaxy's light measured within the $r = 23\,\mathrm{mag}/\square''$ isophote) than for the outer isophotal radius R_{iso23}, within which we measure the luminosity of the galaxy. This is also evident in the distributions of the concentration parameter $c' = R_{\mathrm{iso23}}/R_{50}$: for a given R_{iso23}, a BCG has a larger R_{50} than a non-BCG. This indicates that the light profiles of BCGs are systematically different to those of non–BCGs. To first order, these differences
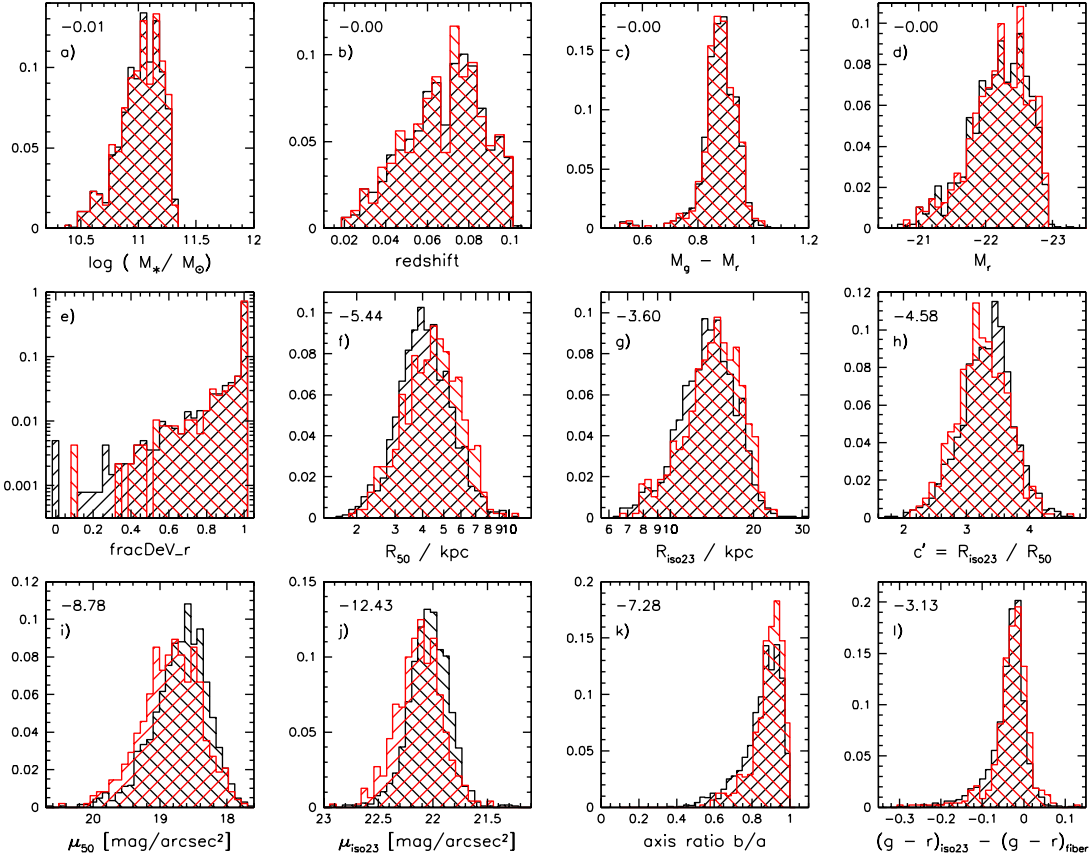
Figure 2.9: Distributions of a variety of photometric parameters for the sample of BCGs (red histograms) and the comparison sample, matched in stellar mass, redshift and $g-r$ (black histograms). The ordinate of each plot shows the fraction of galaxies in a particular bin. In the top left corner of each panel we list the logarithm of the Kolmogorov-Smirnov probability that the two distributions are drawn from an identical parent population. From left to right, top to bottom, the panels show: stellar mass; redshift; $M_g - M_r$; M_r; `fracDeV_r`; the inner characteristic radius R_{50}, defined as the radius enclosing half the light measured within the isophotal radius R_{iso23}; the $r = 23\,\mathrm{mag}/\square''$ isophote radius R_{iso23} (within which our magnitudes are defined); concentration parameter $c' = R_{iso23}/R_{50}$; average surface brightness μ_{50} within R_{50}; the average surface brightness μ_{iso23} within R_{iso23}; axis ratio (from the flux-weighted second moments measured by PHOTO); and the color gradient between the iso23 and the fiber apertures; .

Table 2.2: The 16%, 50%, and 84% percentiles (left, middle, right columns respectively) of the distributions presented in Fig. 2.9. The values for the matched sample are listed in the top rows (black), those for the BCGs in the bottom rows (red).

$\log(M_\star/M_\odot)$			z			$M_g - M_r$			M_r		
10.84	11.04	11.19	0.05	0.07	0.09	0.83	0.88	0.94	-22.62	-22.24	-21.76
10.84	11.04	11.20	0.05	0.07	0.09	0.84	0.88	0.94	-22.63	-22.24	-21.77
fracDeV_r			R_{50} / kpc			R_{iso23} / kpc			c'		
0.86	1.00	1.00	3.14	4.08	5.41	10.76	13.79	17.20	2.92	3.34	3.69
0.89	1.00	1.00	3.24	4.49	5.89	11.14	14.47	17.96	2.84	3.23	3.65
μ_{50}			μ_{iso23}			b/a			$\Delta(g - r)$		
18.31	18.65	19.09	21.86	22.04	22.21	0.76	0.88	0.95	-0.07	-0.03	-0.00
18.41	18.82	19.26	21.93	22.12	22.32	0.81	0.90	0.96	-0.06	-0.02	0.00

Table 2.3: The 16%, 50%, and 84% percentiles (left, middle, right columns respectively) of the distributions presented in Fig. 2.10. The values for the matched sample are listed in the top rows (black), those for the BCGs in the bottom rows (red).

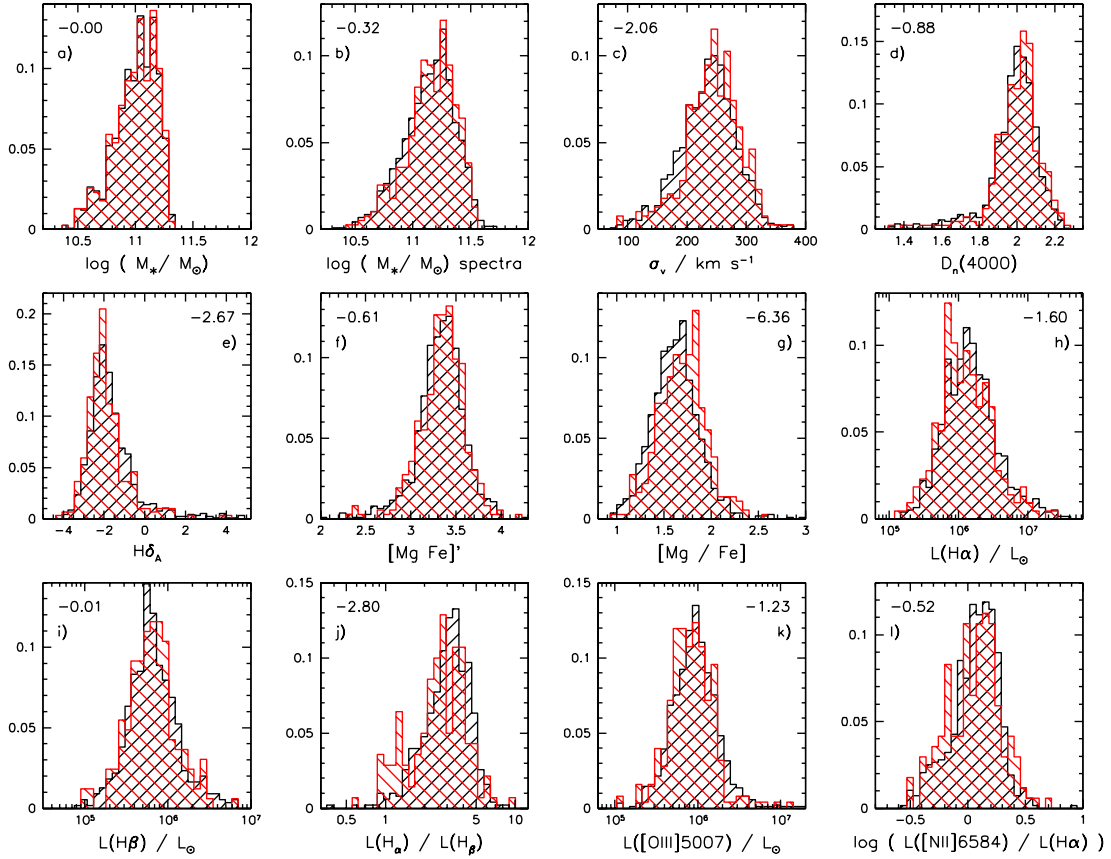| $\log(M_\star/M_\odot)$			$\log(M_\star/M_\odot)_{\mathrm{spectra}}$			σ / km s^{-1}			$D_n(4000)$		
10.82	11.03	11.18	10.91	11.17	11.36	187	239	279	1.89	2.00	2.09
10.82	11.03	11.19	10.92	11.17	11.37	203	246	288	1.91	2.02	2.10
Hδ_{A}			[Mg Fe]'			Mgb/$\langle$Fe$\rangle$			$\log(L_{\mathrm{H}\alpha}/L_\odot)$		
-2.57	-1.88	-0.80	3.11	3.35	3.56	1.38	1.62	1.85	5.81	6.14	6.53
-2.72	-2.07	-1.09	3.10	3.37	3.58	1.45	1.70	1.93	5.75	6.07	6.47
$\log(L_{\mathrm{H}\beta}/L_\odot)$			$L_{\mathrm{H}\alpha}/L_{\mathrm{H}\beta}$			$\log(L_{\mathrm{[OIII]}}/L_\odot)$			$L_{\mathrm{[NII]}}/L_{\mathrm{H}\alpha}$		
5.55	5.80	6.09	1.96	3.11	4.32	5.70	5.96	6.22	-0.13	0.09	0.25
5.53	5.81	6.07	1.34	2.67	3.94	5.69	5.92	6.17	-0.19	0.07	0.26

Figure 2.10: As Fig. 2.9, but for a comparison sample matched to the BCGs in the spectroscopic database; showing the distributions of various (mainly) spectroscopic parameters. The first panel demonstrates the match in stellar mass. The other panels show: stellar mass as extrapolated from the mass-to-light ratio derived from the continuum spectrum; velocity dispersion; strength of the 4000Å-break; Hδ_A index; the metallicity index [Mg Fe]'; the alpha-to-iron index Mgb/$\langle$Fe$\rangle$; Hα line luminosity; Hβ line luminosity; the Balmer decrement Hα/Hβ; the [OIII]5007 line luminosity; and the line ratio [NII]/Hα (a projection of the BPT diagram).
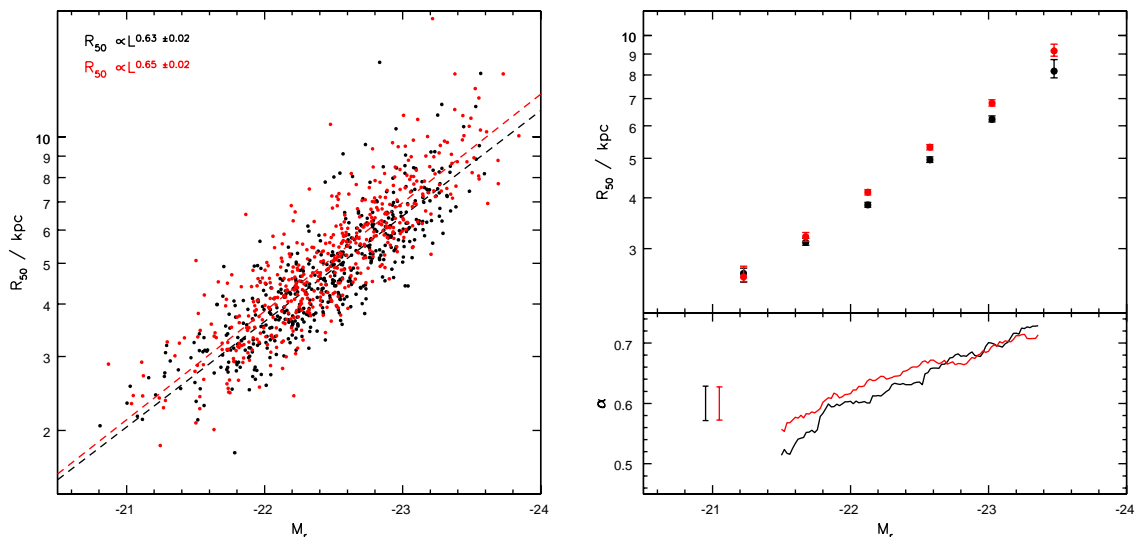
Figure 2.11: Left panel: the size-luminosity relation for the BCGs (red) and for the comparison sample CS1p (black) along with the best-fit linear relations (dashed lines). Top right panel: the median radii in bins of magnitude. The error bars represent the 68% confidence levels divided by the square root of the number of galaxies in the respective bin. Lower left panel: the variation of α, the exponent of the size-luminosity relation, as a function of magnitude M_r, determined from galaxies within $M_r \pm 1.0$.

can be explained by BCGs having shallower light profiles. Indeed, Gonzalez et al. (2005) and Bernardi et al. (2006) find comparatively large Sersic indices (and thus shallow profiles) when fitting BCG light profiles with Sersic profiles.

2.6.1.2 Size-luminosity relation

The sizes and luminosities of elliptical galaxies have been shown to obey the scaling $R_{50} \propto L^{\alpha}$, with $\alpha \simeq 0.6$ (e.g. Bernardi et al. 2003b). However, at the massive end, this relation steepens (Lauer et al. 2006). Bernardi et al. (2006) argue that BCGs have larger radii and that this steepening is caused by an increasing fraction of BCGs. Desroches et al. (2007) still find a steepening after removing the C4 BCGs from their sample of SDSS elliptical galaxies and argue that the steepening is not solely attributable to 'contamination' from a population of galaxies with intriniscally larger radii (BCGs).

The top right panel of Fig. 2.11 *demonstrates* that BCGs are larger than non-BCGs at all luminosities or stellar masses. Symmetric linear fits to the individual data points yield very similar exponents for the radius-luminosity relation for the BCG sample and the comparison sample:

$$
\begin{aligned}
R_{50,\text{BCGs}} &\propto L^{0.65 \pm 0.02} , \\
R_{50,\text{CS1s}} &\propto L^{0.63 \pm 0.02} .
\end{aligned}
$$

However, we also find that the relation displays curvature, i.e. it steepens with luminosity. This is shown in the lower right panel of Fig. 2.11. The range of exponents we find ($\alpha \sim$

$0.5 - 0.7$) is broadly consistent with that of Desroches et al. (2007). We note that α is only slightly larger for the BCGs than the non-BCGs, even at the highest luminosities. We do not find the significantly steeper relations claimed by Bernardi et al. (2006, $\alpha = 0.92$) and Lauer et al. (2006, $\alpha = 1.18$). Both of these samples include both BCGs and non-BCGs - the Bernardi et al. (2006) study uses the original C4 BCGs, which we have shown to be contaminated by non-BCGs, and the Lauer et al. (2006) study is based on galaxies with $M_V < -21$ and detectable core radii. Such contamination from non-BCGs is likely to be most important at lower luminosities, and will thus mimic a steeper slope. Even if we take this effect into account, our data do not support very large values of α; if we fit a relation to the BCGs at $M_r \sim -23.5$ and non–BCGs at $M_r \sim -23$, we find a value of α of only 0.93. We speculate that one possible source for the discrepancy could be the different definitions of R_{50} used in the different studies.

2.6.1.3 Ellipticity

We calculate the axial ratios of the galaxies in our sample (Fig. 2.9, panel [k]) from the flux-weighted second moments as measured by PHOTO, i.e.

$$b/a = \frac{1 - \sqrt{Q^2 + U^2}}{1 + \sqrt{Q^2 + U^2}} \tag{2.3}$$

where Q and U are the Stokes parameters listed in the PHOTO database. We choose this measurement since it is not based on fitting a particular model to the surface brightness profile of the galaxy and it is also not as sensitive to the sky subtraction as isophotal ellipticity measures. The majority of BCGs and non-BCGs are round, with axis ratios $b/a \gtrsim 0.8$. Both samples exhibit a tail to lower axial ratios, but this tail is more prominent for the non-BCGs. The median axial ratio is very similar for both samples (0.90 for the BCGs and 0.88 for the non-BCGs). This is qualtitatively consistent with the results of Ryden et al. (1993). It should be noted, however, that Porter et al. (1991) find that the ellipticity of BCGs increases as a function of the radius at which it is measured (see also Gonzalez et al. 2005).

2.6.2 Dynamical Structure

2.6.2.1 Velocity dispersion

As in previous studies of elliptical galaxies that used spectra taken within fixed-sized apertures (Jørgensen et al. 1995; Bernardi et al. 2003a), we correct the galaxy velocity dispersion to its expected value at one-eighth of the effective radius:

$$\sigma_{\mathrm{v}} = \sigma_{\mathrm{v,meas}} \left(\frac{r_{\mathrm{fiber}}}{r_{50}/8} \right)^{0.04} \tag{2.4}$$

where $\sigma_{\mathrm{v,meas}}$ is the measured velocity dispersion, r_{fiber} is the radius of the SDSS fiber ($1.5''$), and r_{50} is the inner characteristic radius, measured in arcseconds. Strictly speaking, since the iso23 magnitudes do not attempt to measure the total galaxy light, r_{50} is not exactly the same as the effective radius, but because the correction does not scale very steeply with radius, this difference is negligible. This correction also assumes a universal velocity dispersion profile. While this seems to be applicable to most elliptical galaxies (Jørgensen et al. 1995), it has not yet been demonstrated that it also applies to BCGs.
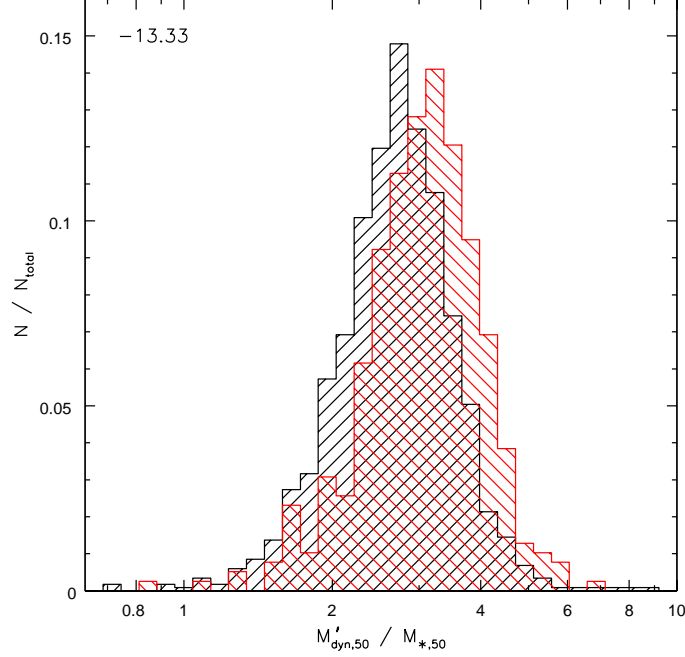
Figure 2.12: The ratio of dynamical mass to stellar mass (within R_{50}) for the BCGs (red) and the comparison sample CS3s (black). We have assumed that $c_2 = (1.65)^2$.

We find that BCGs have systematically larger velocity dispersions than non-BCGs ((Fig. 2.10, panel [c]; this also holds for the uncorrected velocity dispersions).

2.6.2.2 Dynamical mass

The larger radii and higher velocity dispersions of BCGs imply that they have larger dynamical-to-stellar mass ratios than non-BCGs. The dynamical mass within R_{50} can be derived via a projection of the scalar virial theorem onto observable quantities:

$$M_{\mathrm{dyn},50} = c_2 \frac{\sigma_{\mathrm{v}}^2 R_{50}}{G} \qquad (2.5)$$

where c_2 depends on the profiles of both the dark matter and the luminous matter components. If the former follows an NFW profile (Navarro et al. 1997), and the latter a Hernquist (1990) profile, then $c_2 = (1.65)^2$ (Padmanabhan et al. 2004). For calculating the dynamical mass, we assume that $c_2 = (1.65)^2$:

$$M'_{\mathrm{dyn},50} = M_{\mathrm{dyn},50} \frac{(1.65)^2}{c_2} = (1.65)^2 \frac{\sigma_{\mathrm{v}}^2 R_{50}}{G} \qquad (2.6)$$

We also assume that the stellar mass within R_{50} is 50% of the stellar mass within R_{iso23} (Padmanabhan et al. 2004). We find that the ratio of dynamical mass to stellar mass is indeed considerably larger for BCGs (Fig. 2.12). This difference is likely the consequence of the position of BCGs at or near the centers of galaxy clusters. As a result, there is a greater contribution from the dark matter halo to the dynamical mass of the BCG.
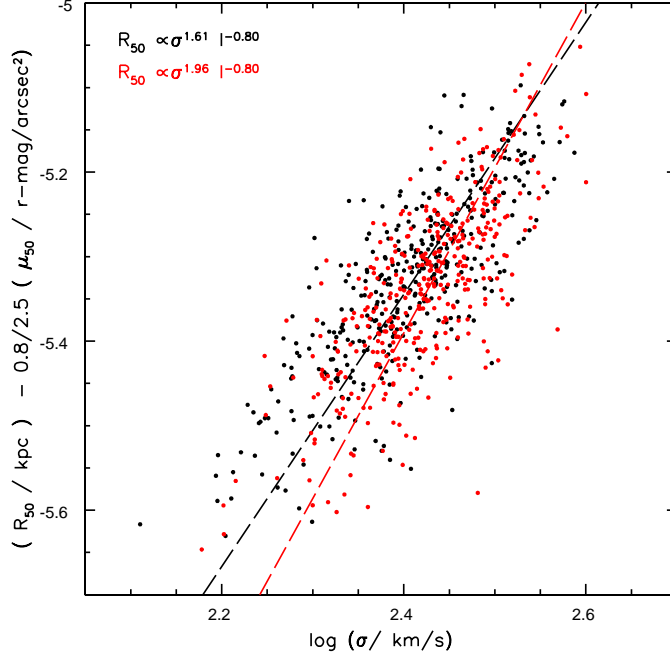
Figure 2.13: Projection along the fundamental plane BCGs (red) and the galaxies of CS1s (black). The dashed lines show the respective best fit for a, keeping $b = 0.8$.

2.6.2.3 The fundamental plane

Early-type galaxies seem to be well described by a two-parameter set of equations, as is evidenced by the Fundamental Plane: they lie on a plane in a coordinate system defined by the logarithmic values of velocity dispersion σ_v, effective radius, and average surface brightness within the effective radius (Djorgovski & Davis 1987). The plane is typically expressed as

$$R_e \; \propto \; \sigma_v^a \, I_e^{-b} \; . \tag{2.7}$$

While there is agreement that $b \simeq 0.8$, the parameter a is dependent on filter bands and may also be sensitive to a variety of selection effects and the precise definitions of σ_v, R_e and I_e. Typical values of $a \sim 1.2 - 1.6$ are quoted in the literature (see for example the compilation of observed FP coefficients in Bernardi et al. 2003c).

We assume that $b = 0.8$ and plot $\log(R_{50} I_{50}^{0.8})$ as a function of $\log \sigma_v$ in Fig. 2.13 for the early–type BCGs and the comparison sample CS1s. In this diagram, the BCGs and the comparison galaxies only diverge for galaxies with small radii and/or high surface brightness (i.e. these are not the cD galaxies). The difference is in the sense that the velocity dispersions of the BCGs are larger. A symmetric fit (`fitexy` from Press et al. 1992) yields

$$
\begin{aligned}
a_{\mathrm{BCGs}} &= 1.96 \pm 0.10 \;, \\
a_{\mathrm{CS1s}} &= 1.61 \pm 0.07 \;.
\end{aligned}
$$

For the comparison sample, the value of a lies close to the values that have been measured in the near-infrared (e.g. Pahre et al. 1998, $a = 1.53 \pm 0.08$), and also in the SDSS

(Bernardi et al. 2003c, $a = 1.49 \pm 0.05$). For the BCGs, a is significantly larger, indicating that BCGs do not lie on the same fundamental plane as "normal" ellipticals. It is interesting to note that it is predominantly the small, low velocity dispersion BCGs which deviate from the generic fundamental plane.

The fundamental plane relation is essentially an expression of the virial theorem. If we write

$$M_\star = c_1 L \quad \text{and} \quad L = 2\pi I_{50} R_{50}^2 \ , \tag{2.8}$$

Eq. (2.5) can be rewritten as

$$R_{50} = \frac{1}{2\pi G} \frac{c_2}{c_1} \frac{M_\star}{M_{\mathrm{dyn},50}} \sigma_{\mathrm{v}}^2 I_{50}^{-1} \ . \tag{2.9}$$

The deviation of the observed fundamental plane from the theoretical one ($a = 2$ and $b = 1$) is referred to as the 'tilt' of the fundamental plane. The tilt implies that $\frac{c_2}{c_1} \frac{M_\star}{M_{\mathrm{dyn},50}}$ varies for different elliptical galaxies. The proportionality constant c_1 is an expression of the stellar mass-to-light ratio and varies for different stellar populations. c_2 depends on the profile shapes of both the luminous and the dark matter components. If c_2 were constant, elliptical galaxies would be structurally homologous systems. There are contradictory results in the literature as to whether it is predominantly non–homology or variation in $L/M_{\mathrm{dyn},50}$ that is responsible for the tilt of the fundamental plane.

We are unable to distinguish non–homology from variation of $L/M_{\mathrm{dyn},50}$ with our data. When calculating dynamical mass, we assume $c_2 = (1.65)^2$ (Eq. [2.6]), but we caution that this approach necessarily neglects effects from non–homology.

In Fig. 2.14, we investigate how the pre-factor $\frac{c_2}{c_1} \frac{M_\star}{M_{\mathrm{dyn},50}} = \frac{L}{M_{\mathrm{dyn},50}/c_2}$ varies as a function of stellar mass for BCGs compared to non-BCGs. The results show that the variation is much smaller for the BCGs. This is an affirmation of our previous result that BCGs lie on a different fundamental plane than non-BCGs. It also demonstrates that this result does not come from a few outliers, but applies to the majority of galaxies with $M_\star < 10^{11.3} M_\odot$. Since $\frac{L}{M_{\mathrm{dyn},50}/c_2}$ varies so little, the BCG fundamental plane is closer to the expectations of the virial theorem ($a = 2$ and $b = 1$).

Again, it is for low mass galaxies that BCGs differ most from non–BCGs. The similarity between BCGs and non–BCGs at high stellar masses implies that the process(es) which cause this ratio to be approximately constant for BCGs also apply to massive non–BCGs. Possibilities include assembly history (e.g. the influence of the orbital elements during dissipationless mergers, Boylan-Kolchin et al. 2006), and the fact that both BCGs and massive galaxies in general are found in dense environments (Kauffmann et al. 2004).

2.6.2.4 Faber-Jackson relation

Several studies suggest that BCGs follow a different relation between luminosity and velocity dispersion than less massive elliptical galaxies (Oegerle & Hoessel 1991; Lauer et al. 2006; Bernardi et al. 2006). Parametrizing this relation as $L \propto \sigma^\beta$, the canonical value is $\beta = 4$, as can be seen from Eq. (2.8) and Eq. (2.9), assuming that $\frac{c_2}{c_1} \frac{M_\star}{M_{\mathrm{dyn},50}} \frac{1}{I_{50}}$ is constant. Most measurements reported in the literature are consistent with $\beta \simeq 4$ (e.g. Bernardi et al. 2003b). However, for samples of BCGs (Oegerle & Hoessel 1991) and very massive galaxies (Lauer et al. 2006), it is found that $\beta > 4$, i.e. σ increases less steeply with luminosity than predicted by the standard Faber-Jackson relation.
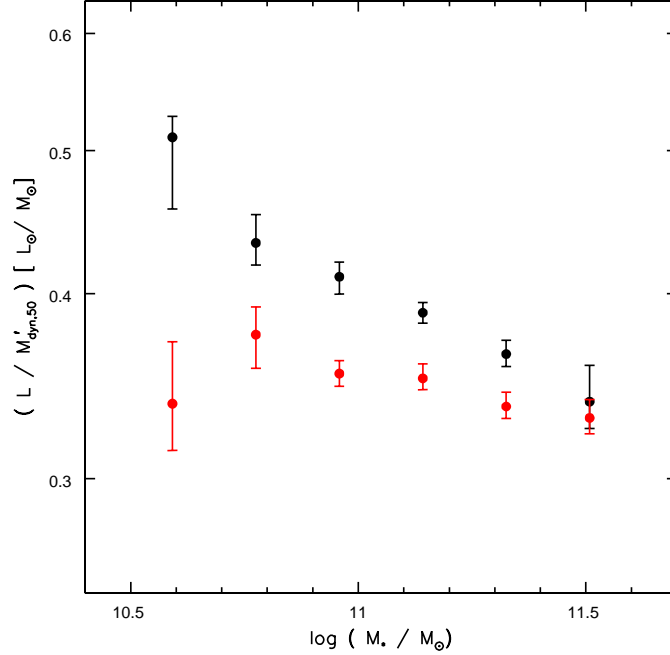
Figure 2.14: The median luminosity to dynamical mass ratio of BCGs (red) and the comparison sample CS1s (black) in bins of galaxy stellar mass. It is the variation of this ratio which determines the tilt of the fundamental plane.

In Fig. 2.15, we show the Faber-Jackson relation for the BCGs and CS1s. Symmetric linear fits to each sample yield:

$$L_{\mathrm{BCGs}} \propto \sigma^{5.32\pm0.37} ,$$
$$L_{\mathrm{CS1s}} \propto \sigma^{3.93\pm0.21} .$$

We find a slope that is compatible with the standard $L \propto \sigma^4$ relation for non-BCGs and we confirm that σ rises less steeply with luminosity for BCGs. [7]

In the bottom panel of Fig. 2.15, we investigate how β changes with luminosity. We find that for BCGs, β is approximately constant (within the typical error bars) and has a value ~ 5.5. For non–BCGs, β varies from values ~ 3 at the low-luminosity end to values ~ 4.5 at high luminosities (a similar range of β, albeit over a larger luminosity interval, as was found by Desroches et al. 2007).

Boylan-Kolchin et al. (2006) find that in simulations of dissipationless mergers, β increases with the eccentricity of the merger orbit. They also argue that BCGs are expected to form through anisotropic merging due to the filamentary structure surrounding galaxy clusters.

We test whether β depends on cluster mass by splitting the BCG sample according to cluster velocity dispersion, and fitting β separately for the two samples. We allow the sample

---

[7]We find a similar change in slope of the Faber–Jackson relation when using the K-band luminosities of those BCGs with 2MASS photometry and a set of comparison galaxies. This is contrary to recent claims by Batcheldor et al. (2007), who use a much smaller sample of BCGs for their analysis.
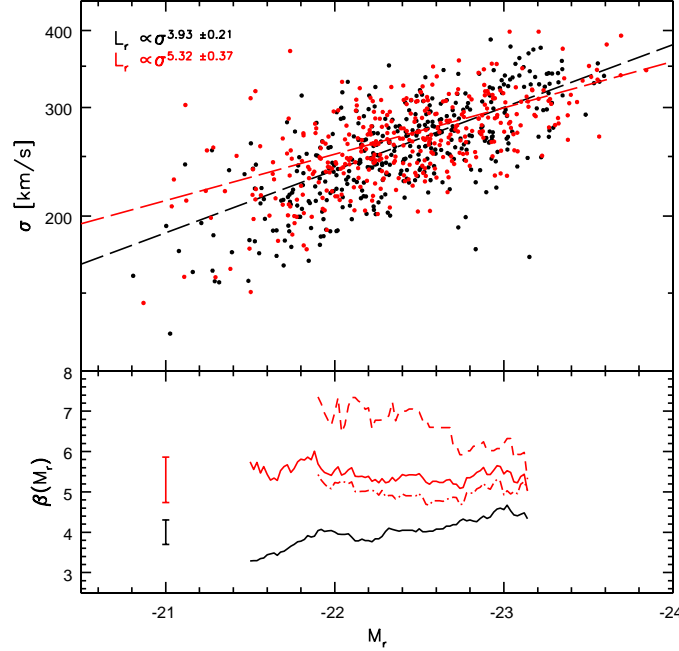
Figure 2.15: Top panel: the Faber-Jackson relation for BCGs (red) and for the comparison sample CS1s. The dashed lines show the best linear fits to the relations. Bottom panel: the variation of β with M_r, i.e. β determined from galaxies within $M_r \pm 1.0$ for BCGs meeting the early-type criteria (solid red line) and the corresponding CS1s sample (solid black line). The dashed line shows the subset of these BCGs located in clusters with $\sigma_{v,cl} > 400\,\mathrm{km/s}$, the dash-dotted line the subset of BCGs in clusters with $\sigma_{v,cl} < 500\,\mathrm{km/s}$. The typical error bars are displayed on the left.

to overlap in $\sigma_{v,cl}$ to gain higher statistical significance. We obtain the following results:

$$L_{\mathrm{BCGs}}\,(\,\sigma_{v,cl} < 500\,\mathrm{km/s}\,) \quad \propto \quad \sigma^{\,5.22\pm0.46}$$
$$L_{\mathrm{BCGs}}\,(\,\sigma_{v,cl} > 400\,\mathrm{km/s}\,) \quad \propto \quad \sigma^{\,5.91\pm0.69}$$

The two values of β are just consistent with each other within the errors, and thus we cannot draw strong conclusions. Our results indicate that β is larger for BCGs in more massive clusters. If the scenario put forward by Boylan-Kolchin et al. (2006) is correct, this might imply that the merger orbit eccentricity increases with cluster mass. Another explanation might be that the number of (dissipationless) mergers is larger for BCGs in more massive clusters.

2.6.3 Stellar Populations

The availability of measurements of spectral indices for galaxies in the spectroscopic SDSS catalog allows us to investigate the stellar populations in BCGs and non–BCGs. Both the distributions of the 4000Å-break (Fig. 2.10, panel (d), measured as $D_n(4000)$, Balogh et al. 1999) and the $H\delta_A$ index (Fig. 2.10, panel (e); Worthey & Ottaviani 1997) demonstrate that the stellar populations of the BCGs and the comparison galaxies are old, as is generally found for galaxies in this mass range (Kauffmann et al. 2003b). The metallicity, measured using
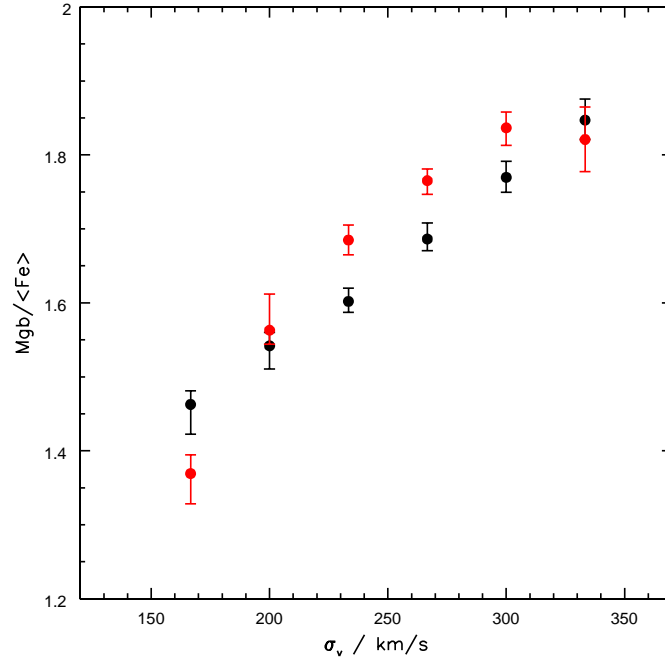
Figure 2.16: The median value of Mgb/⟨Fe⟩ as a function of velocity dispersion for the BCGs (red) and the comparison sample CS1s (black).

the index [MgFe]' (Fig. 2.10, panel (f); Thomas et al. 2003) is also typical for giant elliptical galaxies. There is a slight indication that the stellar populations of BCGs are slightly older (larger $D_n(4000)$, lower $H\delta_A$, and higher metallicity), but this is only significant for the $H\delta_A$ index.

It should be noted that these measurements apply only to the galaxy light contained within the fiber, i.e. the inner 3″, whereas the samples are matched in $g - r$ color within the 23 mag/□″ isophote. In panel (l) of Fig. 2.9 we find that the color gradient between the fiber aperture and the iso23 aperture is more prominent in the non–BCGs. This is a confirmation of previous results that color gradients in BCGs are weak or absent (Garilli et al. 1997), while non-BCG elliptical galaxies are generally redder in the center (La Barbera et al. 2005). The presence of color gradients is typically attributed to metallicity gradients (James et al. 2006), however, we do not find evidence for different metallicities in BCGs.

We use the index Mgb/⟨Fe⟩ as an indicator of the α/Fe ratio (Thomas et al. 2003) and we find that BCGs have a systematically higher Mgb/⟨Fe⟩ value than non-BCGs (Fig. 2.10, panel [g]). However, this index is known to correlate strongly with velocity dispersion, so this result is not independent of our previous result that BCGs have systematically larger velocity dispersions. In Fig. 2.16, we plot Mgb/⟨Fe⟩ as a function of velocity dispersion for the BCGs and the comparison sample CS1s. Except in the outermost bins, we do find systematically higher α/Fe ratios in the BCGs. Higher α/Fe ratios can be interpreted as an indication that star formation in the galaxy occurred over a shorter time-scale (Granato et al. 2004). The enhanced radio-AGN activity we find in BCGs (Sect. 2.5) may explain why star formation has been shut off on shorter timescales in the BCGs.

2.6.4 Emission line properties

We also investigate the strengths of the four emission lines Hα, Hβ, [O$\textsc{iii}$]λ5007, and [N$\textsc{ii}$]λ6584 that are commonly used to classify galaxies according to whether their emission line luminosity is driven by star formation or AGN activity (Baldwin et al. 1981). We limit our sample to galaxies with a signal-to-noise SNR > 3 in the respective line measurement(s). For the individual line measurements Hα / Hβ / [O$\textsc{iii}$] / [N$\textsc{ii}$] , this holds for 56% / 42% / 64% / 50% of the BCGs and 66% / 47% / 77% / 63% of the comparison sample (note that this applies to the CS3s sample). Requiring that SNR > 3 in all four bands simultaneously leaves only 30% of the BCGs and 40% of the comparison sample. These numbers already indicate that the emission lines in BCGs are in general weaker than in non-BCGs, a result which is further confirmed by the distributions of Hα and [O$\textsc{iii}$] line luminosities shown in Fig. 2.10, panels (h) and (k). We note that it is particularly the high–mass BCGs in which the emission line strength is suppressed compared to the comparison sample.

Fig. 2.17 shows the BPT diagram of BCGs and the comparison sample for those galaxies which satisfy SNR > 3 in all four bands, i.e. 119 (out of 391) BCGs and 472 (out of 1173) non-BCGs. Of these BCGs, 7 (i.e. 6% of the line–emitting sample / 2% of the complete sample) are classified as star-forming, 83 (70% / 21%) as AGN, and 29 (24% / 7%) as composite. Of the non-BCGs, 29 (6% / 2%) are star-forming, 364 (77% / 31%) AGN, and 79 (16% / 6%) composite. Our sample is too small to draw detailed conclusions from these numbers, except that for both samples, the emission line flux is dominated by AGN–like emission. Their low [O$\textsc{iii}$] luminosities place the BCGs somewhat lower in the BPT diagram than the non-BCGs, i.e. the BCGs are almost exclusively classified as LINERs, whereas a few galaxies in the comparison sample could be classified as low-luminosity Seyferts.

For case B recombination, the unattenuated value of the Balmer decrement is $\sim$ 3 (more specifically, it is Hα/Hβ = 2.86 in star-forming galaxies and Hα/Hβ = 3.1 in AGN, Osterbrock 1989). Remarkably, a considerable fraction of the BCGs in our sample have Balmer decrements below this value (Fig. 2.10, panel [j]). It has been noted by Kewley et al. (2006) that 33% of LINERs in the SDSS sample have Hα/Hβ < 2.86. A possible explanation is that the fits to the stellar continuum are not entirely reliable for the most massive galaxies, which tend to have very strong metallic absorption lines in their spectra.

2.6.5 Star formation in BCGs

The results of the previous section suggest that BCGs do not have increased amounts of star formation with respect to the comparison sample. This is somewhat surprising, as there are several BCGs known with signs of recent star formation (blue colors, Hα emission; see Crawford et al. 1999), and some cluster cores are known to have extended Hα emission structures (e.g. Crawford et al. 2005). The latter are found to occur exclusively in cooling core clusters (Crawford et al. 1999). However, since the SDSS fiber only probes the inner galaxy, it is insensitive to such surrounding filaments. As for nuclear line emission, Edwards et al. (2007) find that only BCGs at the centers of cooling core clusters are more likely to display emission lines than other massive (cluster) galaxies. They also confirm that in optically selected cluster samples (such as our sample), the BCGs are not more likely to display emission lines than massive comparison galaxies.

Some of the line emission could be attributed to cluster cooling flows instead of optical AGN activity (e.g. Voit & Donahue 1997). In addition, only half of the galaxies have detectable
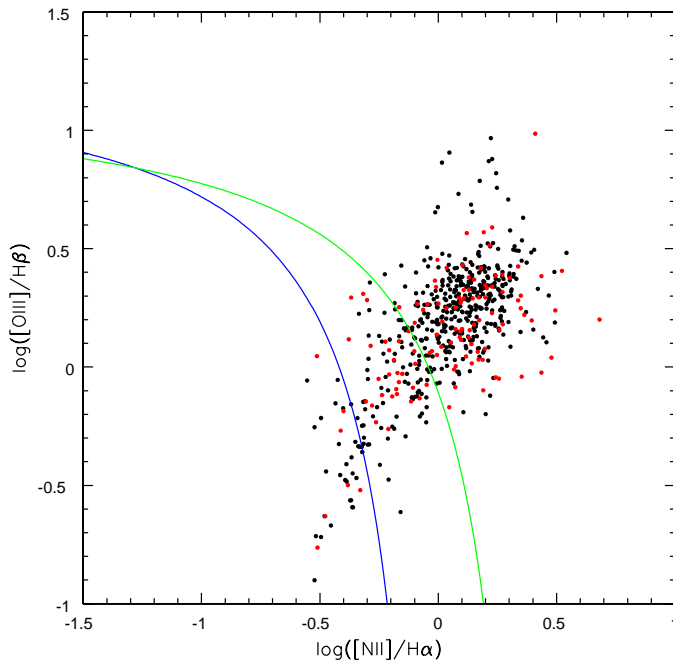
Figure 2.17: BCGs (red) and the comparison sample CS3s (black) placed into the BPT diagram. Galaxies to the left of the blue line are classified as purely star-forming (Kauffmann et al. 2003c), galaxies to the right of the green line as purely AGN (Kewley et al. 2001), and galaxies inbetween the lines as composite. Only galaxies with SNR > 3 in all four line measurements are shown.

emission lines, so we would prefer a stellar age indicator that can be measured for all galaxies. The strength of the Balmer break $D_n(4000)$ is measurable with a high SNR in all the galaxy spectra and is an indication of the age of the stellar population. Kauffmann et al. (2003a) find that galaxies separate into two distinct populations, with young, star–forming galaxies having $D_n(4000) \lesssim 1.6$. We find that the number of galaxies with $D_n(4000) < 1.6$ is very similar to the number of star–forming galaxies identified from the BPT diagram, for both the BCGs and non–BCGs (see Fig. 2.18). In Fig. 2.18, we plot $D_n(4000)$ against $M_u - M_g$ within the *iso23* aperture. $M_u - M_g$ also straddles the Balmer break and can thus serve to probe the average stellar population at radii larger than the fiber aperture. The percentage of galaxies with blue $M_u - M_g$ overall colors is compatible for BCGs and non–BCGs, i.e. again there is no indication for enhanced star formation in BCGs. Since we have matched in $M_g - M_r$ color and have argued that this is essentially a match in stellar mass-to-light ratio, we do not expect a systematic difference in $M_u - M_g$ (and thus this exercise may serve to confirm this argumentation). Without the match in $M_g - M_r$, the comparison sample contains more spiral galaxies, i.e. more star–forming galaxies than the BCG sample.

To conclude, we do not find evidence for increased amounts of star formation in BCGs. However, we would like to caution that our sample is not well suited for such an investigation: we probe only the very center of the galaxies (and thus cannot detect line emission on larger scales), and we do not have X-ray data for our sample (previous studies suggest there is a strong connection between the cluster X-ray properties and star formation).
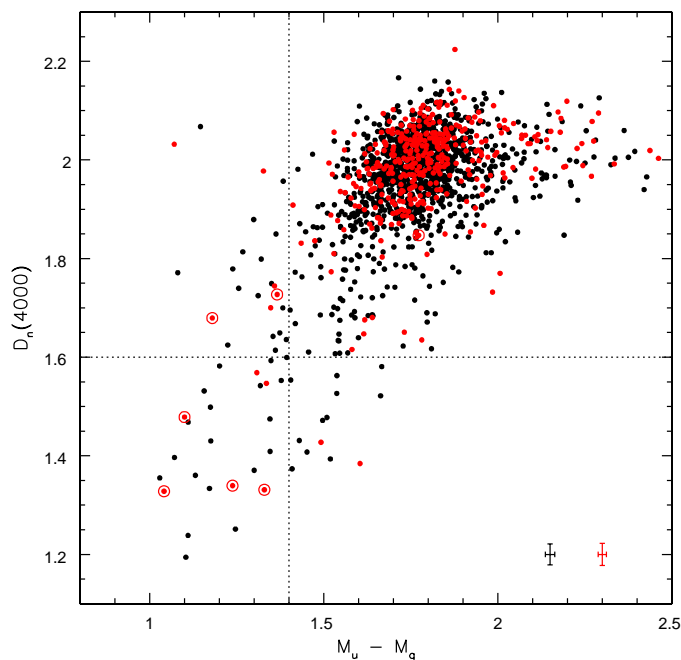
Figure 2.18: The Balmer break $D_n(4000)$ vs. $M_u - M_g$ for the BCGs (red) and the comparison sample CS3s (black). Typical error bars are shown in the lower right corner. The BCGs which were identified as star–forming from the BPT diagram are marked by circles. Note that only one of these is an early-type galaxy and is also in the CS1s sample. In the latter sample, there is no BCG and only one comparison galaxy with $D_n(4000) < 1.6$.

2.7 Summary and discussion

We have developed a refined algorithm for selecting brightest cluster galaxies (BCGs) in the C4 cluster catalog, and we have improved the determination of velocity dispersion and cluster membership. This refined cluster sample consists of 625 galaxy clusters at $z < 0.1$, and spans a wide range in velocity dispersion, from galaxy groups to rich clusters of galaxies. This, along with the detailed information available from SDSS for member galaxies, makes it a suitable local comparison sample for optically–selected, high–redshift cluster samples.

Since the original SDSS magnitude measurements of BCGs are affected by excessive sky subtraction, we have developed a procedure to recover more accurate magnitudes by adding a fraction of the difference between the `local` and `global sky` background estimates to the radial surface brightness profiles of the SDSS galaxies, and by determining new magnitudes from these corrected profiles. We show that this procedure removes the systematic bias in $z - J$ color as a function of angular size for elliptical galaxies with photometry from both the SDSS and the 2MASS surveys. We also show that our reconstructed surface brightness profiles of BCGs agree well with previously published aperture photometry, at least to the isophotal limit of $r = 23\mathrm{mag}/\square''$ within which we measure the flux.

The properties of BCGs are governed by two main factors: their large (stellar) masses and their locations at the bottom of the potential well of their host cluster. Our large sample of

BCGs enables us to disentangle the influence of these two factors and to assess the extent to which BCGs differ from 'ordinary' massive galaxies.

We investigate the occurence of radio–loud AGNs in the BCG population and we find that BCGs are more likely to be radio–loud than other galaxies of the same stellar mass. This enhancement ranges from a factor 10 at stellar masses of $5 \times 10^{10} M_\odot$ to less than a factor of two at masses larger than $4 \times 10^{11} M_\odot$. This difference is arguably the most striking difference between BCGs and non-BCGs, and is likely due to the additional hot gas available in groups and clusters to fuel the radio AGN.

The influence of the cluster environment is also evident as an increase in the fraction of dark matter in BCGs. The main observational signature of this excess dark matter is that BCGs have larger radii and higher velocity dispersions than non-BCGs. However, since the conversion of these quantities to dynamical mass depends on the shape of the mass and light profiles of the galaxy, this result could also be mimicked by non-homology between the BCGs and non-BCGs. Either case leads to a different slope of the fundamental plane for BCGs, one that is much closer to the virial plane than the observed fundamental plane of normal ellipticals.

It is interesting to note that the differences from 'normal' galaxies are particularly evident in lower-mass BCGs: these are the galaxies that have a factor 10 higher probability of being radio–loud and have a significantly larger dark matter mass to light ratio (or a larger degree of non-homology) when compared to the non-BCGs. The low mass BCGs also deviate most strongly from the generic fundamental plane.

We find that the slope of the Faber–Jackson relation is different for BCGs, in that their velocity dispersion rises less steeply for a given increase in luminosity than for non-BCGs. We also find evidence that this effect is stronger for BCGs in massive clusters. Such a change in the Faber–Jackson relation is predicted if these systems form in dissipationless mergers along elliptical orbits. Our results thus support the scenario where BCGs form mainly via dissipationless mergers, and imply that the merger orbits are preferentially radial in the most massive clusters.

A difference in the Faber–Jackson relation also implies that BCGs can follow at most one of the power–law relations often used to estimate the mass of the supermassive black hole at their center, i.e. either the $M_{BH} - \sigma_v$ or the $M_{BH} - L$ relation. In fact, this is already obvious from the parameter distributions shown in Figs. 2.9 and 2.10: for the same distributions in stellar mass and in luminosity, we find a systematically different distribution in velocity dispersion for our BCGs. The standard relations between black hole mass and bulge velocity dispersion (Tremaine et al. 2002) have likely been derived for non-BCGs and may lead to systematically wrong black hole estimates for the brightest group and cluster galaxies.

We find that BCGs have very similar mean stellar ages and metallicities to non–BCGs. They have slightly higher α/Fe ratios, indicating that their stars may have formed over a shorter time interval. Finally, BCGs display weaker optical emission lines than non-BCGs of the same stellar mass. In both BCGs and non-BCGs, the detected emission lines stem predominantly from low-luminosity optical AGNs. In the accompanying paper (Best et al. 2007), we further investigate the occurence of AGN activity in BCGs, and argue that the radio–loud and the emission–line AGN activity are independent, unrelated phenomena.

3

Galaxy distributions within the local clusters

In this chapter I characterize the average galaxy distribution in a sample of clusters drawn from the Sloan Digital Sky Survey. To account for the spectroscopic incompleteness at the centers of clusters, and to investigate galaxies fainter than the spectroscopic limit, I assign cluster membership probabilities based on luminosity, color, and position to galaxies in the photometric SDSS catalogs.

By stacking the individual clusters, I investigate the galaxy distribution in a composite cluster, which reflects the average properties of this cluster sample. I find that the composite number density profile is cuspy, and described adequately by an NFW profile. For red galaxies, I find that the ratio of faint-to-luminous galaxies increases towards the cluster center. In the very core of the cluster, on the other hand, there is a possible excess of luminous galaxies.

3.1 Photometric catalogs

Due to the fiber collisions, the dense centers of clusters are be considerably less complete than the overall SDSS spectroscopic survey. For example, of the 625 BCGs, 141 (i.e. 23% of the whole sample) are not contained in the spectroscopic SDSS catalogs. For analyses which make use only of photometric properties, and require a high completeness (e.g. the total cluster light from galaxies), we therefore construct photometric catalogs for the clusters. This also allows to probe the cluster population at fainter magnitudes than the spectroscopic limit ($r \lesssim 17.7$).

For each cluster, we retrieve galaxies within R_{200} from the BCG. We select only objects which have been classified as galaxies by PHOTO, and which have "clean photometry" in both g and r.

3.1.1 Geometric completeness

Also the photometric catalogs can be incomplete, due to survey boundaries, masks around bright stars, etc. We estimate this geometric (in-)completeness directly from the photometric

catalogs themselves: We download a version of the photometric catalogs without a magnitude cut-off, and not restricted to only galaxies. Furthermore, no flag indicating that the object is located within a mask of a bright star, a hole, a bleeding trail, or a satellite or asteroid trail must be set. We smooth the distribution of these objects with a top-hat filter and evaluate the resulting object number density on grid points within R_{200}, with a grid-spacing of $10''$. The radius of the top-hat filter is $1'$, and is chosen to typically encompass 10–20 galaxies, i.e. the mean number density is approximately 5 galaxies/arcmin^2. Masks and other holes cause the number density to decrease considerably. We consider any grid cell with < 1 galaxy/arcmin^2 to be 'empty'. The geometric completeness of the cluster is then the fraction of empty grid cells within R_{200}.

3.1.2 Statistical background subtraction

Without spectroscopic redshifts, the galaxies in the photometric catalogs lack the third dimension of their positional information. It is thus not possible to unambiguously distinguish between cluster members and galaxies in the foreground or background of the cluster. Although photometric redshifts are available for the SDSS, their accuracy at $z < 0.1$ is too low to be used for cluster membership estimation.

However, since clusters present galaxy overdensities on the sky, with knowledge of the expected average galaxy density we can apply a *statistical background subtraction* to estimate the likelihood of galaxies of a certain magnitude and colors to be part of a local galaxy overdensity (i.e. a cluster).

For this purpose, we split the galaxies into bins of certain properties. E.g. a common and non-biased approach to the statistical subtraction is to split the sample by magnitude and color, but we also employ another method which takes into account the density increase towards the center and the presence of a red sequence.

The galaxy population in each bin is made up of cluster and of other (i.e. *field*) galaxies:

$$N_{\text{all}} = N_{\text{cluster}} + N_{\text{field}} \;.$$

We estimate N_{field} with $\langle N_{\text{field}} \rangle$, the expected number of galaxies in that particular bin. $\langle N_{\text{field}} \rangle$ is calculated from the DR3 photometric catalog, appropriately scaled to the area of the cluster (DR3 has a total area of $\sim 5000\square^\circ$).

For a subset of galaxies, spectroscopic information is available, and we can assign them directly to the cluster (or the field):

$$N_{\text{cluster}} = N_{\text{cluster}}^{\text{spec}} + N_{\text{cluster}}^{\text{phot}} \;.$$

(We supplement the SDSS redshifts with redshifts retrieved from NED to enhance the spectroscopic completeness.)

The expected number of cluster galaxies without spectroscopy is then

$$\begin{aligned} N_{\text{cluster}}^{\text{phot}} &= N_{\text{cluster}} - N_{\text{cluster}}^{\text{spec}} \\ &= N_{\text{all}} - \langle N_{\text{field}} \rangle - N_{\text{cluster}}^{\text{spec}} \end{aligned}$$

A fraction p of the galaxies with only photometric information are cluster members:

$$
\begin{aligned}
N_{\text{cluster}} &= N^{\text{spec}}_{\text{cluster}} + p \cdot N^{\text{phot}}_{\text{all}} \\
p &= \frac{N^{\text{phot}}_{\text{cluster}}}{N^{\text{phot}}_{\text{all}}} \\
&= \frac{N_{\text{all}} - \langle N_{\text{field}} \rangle - N^{\text{spec}}_{\text{cluster}}}{N^{\text{phot}}_{\text{all}}} \, .
\end{aligned}
$$

p can be assigned to each galaxy (without spectroscopic information) in the respective bin, and can be interpreted as the galaxy's probability to be a cluster galaxy. Galaxies with spectroscopic information are assigned $p = 1$ if they are confirmed cluster galaxies, or $p = 0$ otherwise.

Due to the shot noise of the galaxy distribution, our prescription to calculate p, the probability of a galaxy to belong to the cluster, can yield values $p < 0$ (if the expected number of field galaxies exceeds the number of galaxies in the cluster area less any spectroscopically confirmed members) or $p > 1$ (if the number of photometric-only galaxies in the cluster area is less than the expected number of photometric-only cluster galaxies). A simple work-around to this problem would be to simply set these cases to 0 (or 1, respectively). However, this does not preserve the total number of cluster galaxies. Instead, we add neighboring bins to the one in question and evaluate the summed N_i .

We try three different methods for the sky subtraction:

3.1.2.1 2D background subtraction: binning by magnitude and one color

Other datasets often can rely on only two bands for the background subtraction, hence a background subtraction based on the apparent magnitude and one color is widely used. We split the galaxies into bins of cmodel r magnitude (width 0.5 mag) and model $(g-r)$ magnitude (width 0.33 mag).

For bins with unphysical values of p, we follow closely the method used by Pimbblet et al. (2002) to expand the grid. In the first step, we add to the problematic bin with the grid position (mag, col) the bin (mag+1, col). If the resultant p is still unphysical, we further expand the grid in the color dimension, i.e. we add the bins at (mag, col+1) and (mag+1, col+1). In the third step, we expand the bin in the opposite direction along the magnitude axes, i.e. we add the two bins (mag-1, col) and (mag-1, col+1). If necessary, we continue to expand then to col-1, and so on. We proceed until the original bin has been expanded by two bins in all directions (it should be noted that we only add bins in which $N^{\text{phot}}_{\text{all}} > 0$). If one of these steps causes p to have a value between 0 and 1, each bin in the final grid is then assigned the average number of galaxies of each category. If p is still unphysical in the final 5x5 bin, we refrain from actually rebinning (and thus smearing out that particular value over more bins), and set p to 0 or 1. This process is illustrated in Fig. 3.1.

3.1.2.2 4D background subtraction: binning by magnitude and three colors

The SDSS has the advantage of having homogeneous data quality in more than two bands; hence we can also make use of the information in the other bands. We therefore split the sample by cmodel r magnitude (bin width 0.5 mags), model $(g - r)$ color (width 0.33 mags),
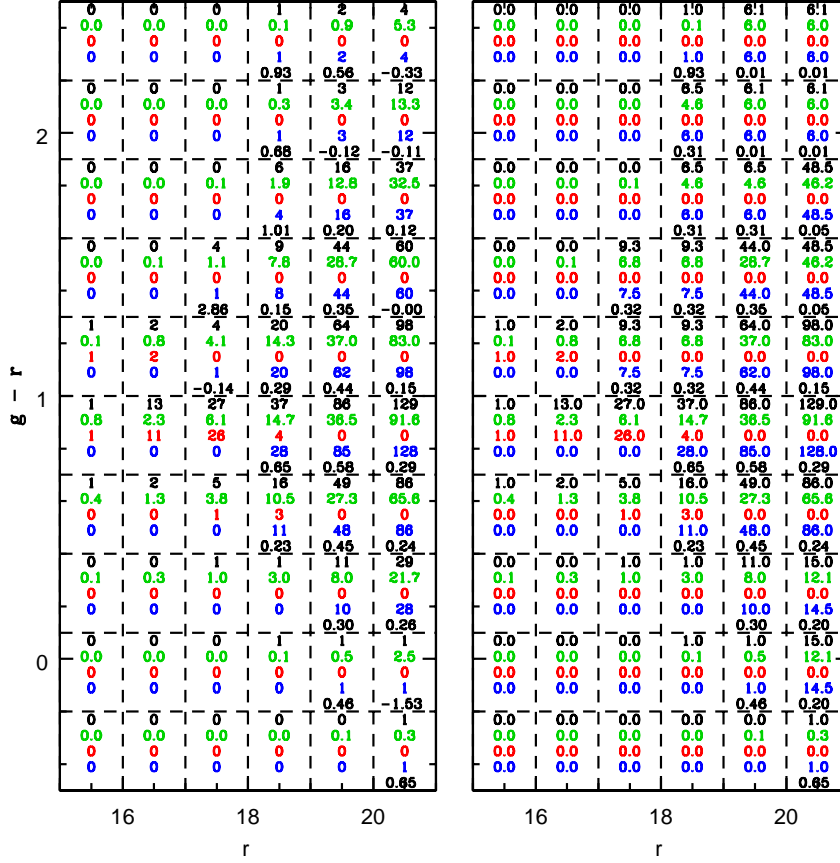
Figure 3.1: An example of the rebinning process employed in the statistical background subtraction, here shown for C4_DR3_1000. For each grid position, we list from top to bottom, N_{all} (black), $\langle N_{\text{field}} \rangle$ (green), $N_{\text{cluster}}^{\text{spec}}$ (red), $N_{\text{all}}^{\text{phot}}$ (blue), and p (black, only shown if $N_{\text{all}}^{\text{phot}} > 0$. The left panel shows the values before the rebinning process - a total of eight bins have unphysical values of p. The right panel shows the result of the rebinning: in all bins, $0 < p < 1$.

model $(r - i)$ color (width 0.3 mags), and model $(i - z)$ color (width 0.3 mags). Note that we do not make use of the u band, since its noise properties are too poor.

The rebinning procedure is the 4–dimensional expansion of the method used in the 2D version.

3.1.2.3 Radial background subtraction

The previously described background subtraction methods do not take into account that the number density of galaxies is usually higher at the centers of clusters. All galaxies with a certain magnitude and color(s) are assigned the same probability p, irrespective of their local number density. Particularly for studying the dependence of number counts as a function of distance from the cluster center, this needs to be taken into account.

Furthermore, the previous methods neglect the fact that a considerable fraction of cluster galaxies lie on a well-defined red sequence: although we have chosen the color bins such that the red sequences is contained within the same bins, the width of the color bins is much wider than the red sequence, and does not follow its tilt.

To perform a background subtraction motivated by these cluster properties, we start by fitting the red sequence (in apparent magnitudes) of spectroscopically confirmed cluster galaxies, which are classified as "red" galaxies by the spectral analysis performed in Chapter 4 in bins of redshift. I.e. we perform linear regressions with 3σ-clipping to the relation

$$(g - r)_{\text{model}} = m \cdot r_{\text{cmodel}} + \text{ZP}_{\text{app}}(z)$$

(see Fig. 3.2). We find that a slope of $m = -0.016$ describes the red sequence in each redshift bin very well.

We determine the redshift–dependent zero-point of the red sequence $\text{ZP}_{\text{app}}(z)$ and the width of the red sequence by fitting Gaussians to the residual colors of the red galaxies with respect to the average red sequence,

$$(g - r)_{\text{rect}} = (g - r)_{\text{model}} + 0.016 \cdot r_{\text{cmodel}} \quad .$$

In effect, these colors present a rectified color-magnitude diagram, i.e. one in which the slope of the red sequence has been taken out. The width of the distribution is again quite similar in all redshift bins ($\sigma \approx 0.043$, Fig. 3.3). This implies that the width is approximately constant across a range of galaxy luminosities; only in the lowest redshift bin, which probes the faintest galaxies, the width is slightly larger.

The zero-point of the red sequence in apparent magnitudes can be well fit with a linear dependence on redshift:

$$\text{ZP}_{\text{app}}(z) = (2.70 \pm 0.01)z + (0.943 \pm 0.001)$$

For each cluster (with redshift z) we consider galaxies with $\text{ZP}_{\text{app}}(z) - 0.12 \leq (g - r)_{\text{rect}} \leq \text{ZP}_{\text{app}}(z) + 0.12$ to be likely red sequence galaxies. The width is chosen to correspond to app. $2.5 - 3\sigma$, and split the red sequence from the other galaxy populations. Furthermore, galaxies with $\text{ZP}_{\text{app}}(z) - 0.24 \leq (g - r)_{\text{rect}} < \text{ZP}_{\text{app}}(z) - 0.12$ can be identified as green valley galaxies, and galaxies with $\text{ZP}_{\text{app}}(z) - 0.6 \leq (g - r)_{\text{rect}} < \text{ZP}_{\text{app}}(z) - 0.24$ as blue cloud (see Fig. 3.4). Note that later we will use colors from absolute magnitudes (rather than apparent magnitudes) to split the galaxies into these subsamples.
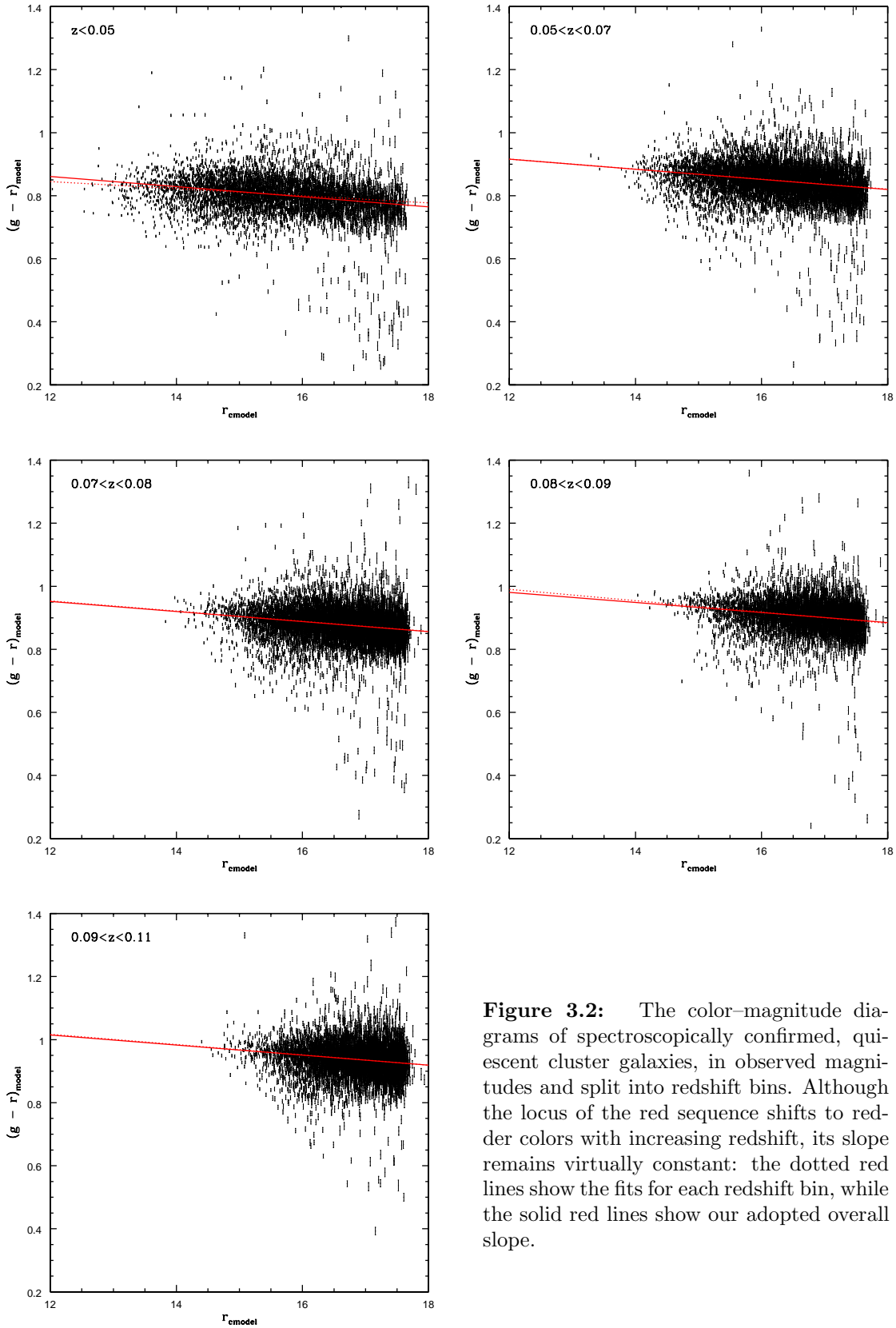
Figure 3.2: The color–magnitude diagrams of spectroscopically confirmed, quiescent cluster galaxies, in observed magnitudes and split into redshift bins. Although the locus of the red sequence shifts to redder colors with increasing redshift, its slope remains virtually constant: the dotted red lines show the fits for each redshift bin, while the solid red lines show our adopted overall slope.
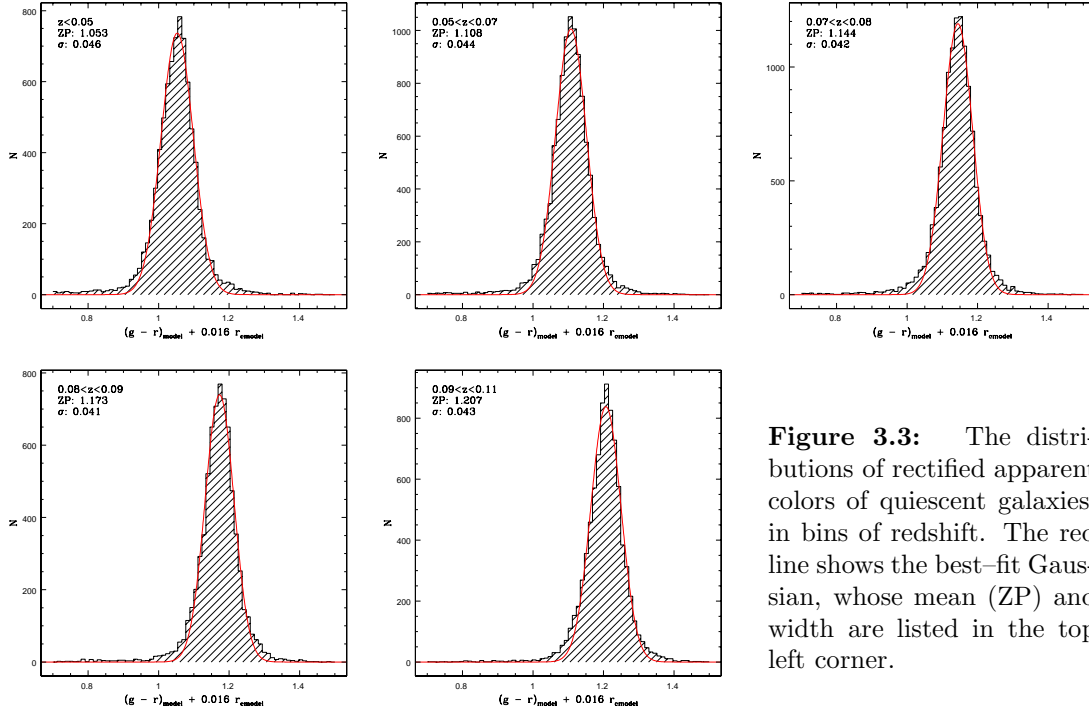
Figure 3.3: The distributions of rectified apparent colors of quiescent galaxies, in bins of redshift. The red line shows the best–fit Gaussian, whose mean (ZP) and width are listed in the top left corner.
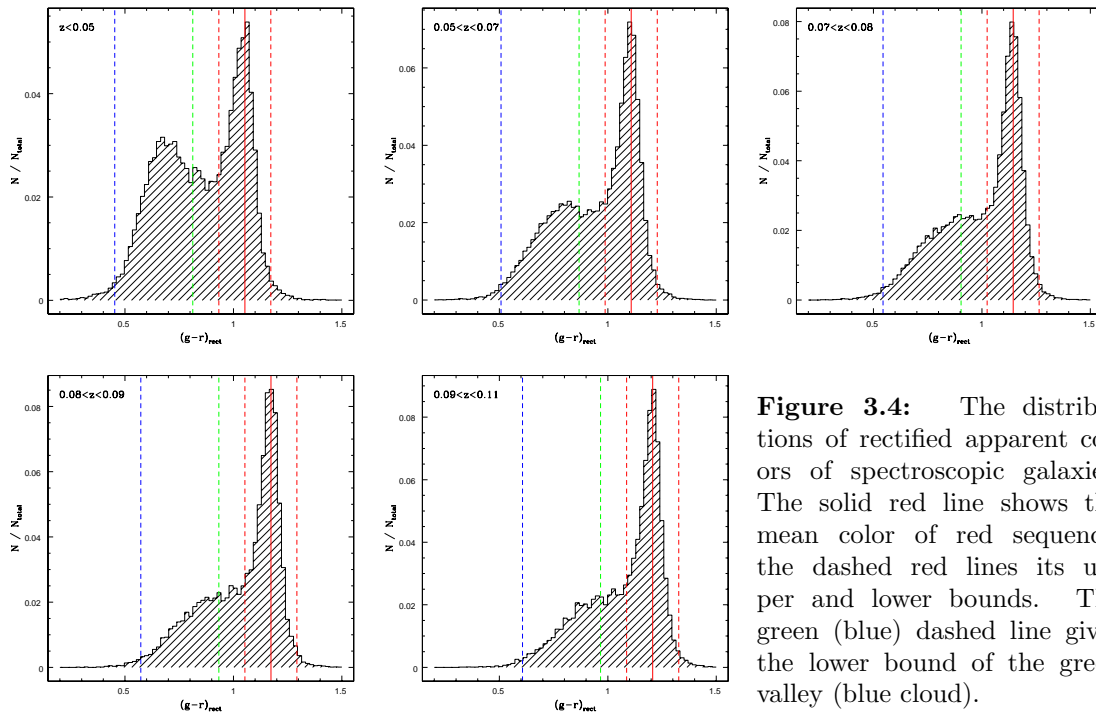

Figure 3.4: The distributions of rectified apparent colors of spectroscopic galaxies. The solid red line shows the mean color of red sequence, the dashed red lines its upper and lower bounds. The green (blue) dashed line gives the lower bound of the green valley (blue cloud).
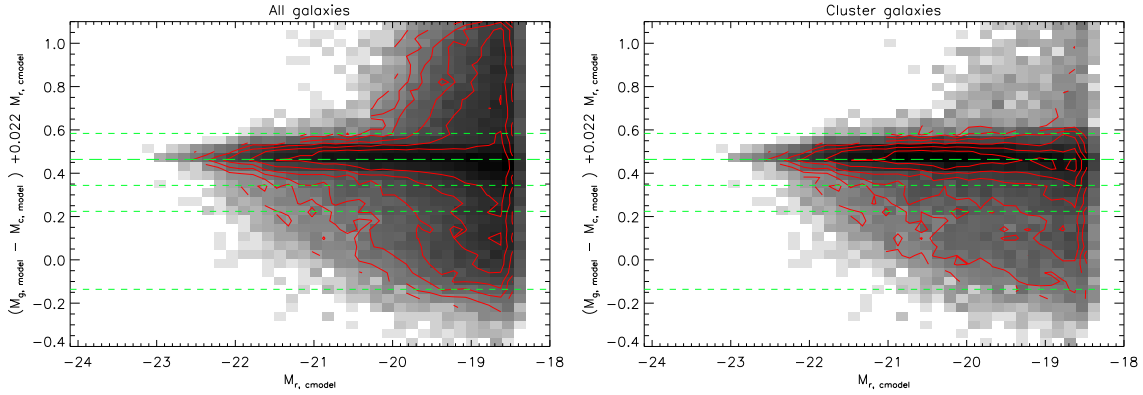
73

Figure 3.5:   The effect of the background subtraction on the joint color-magnitude diagram (in absolute magnitudes). In the left panel, all galaxies (which are not spectroscopically confirmed non–members) are shown; in the left panel, only galaxies whose membership probability p is larger than a random number are shown. The grayscale and the red contours show the logarithmic density in bins of magnitude and color. The green lines indicate the divisions into red sequence, green valley, and blue cloud. Note that also this CMD has been rectified.

We intend to study galaxies down to an absolute magnitude $M_r^{0.1}$, i.e. the absolute magnitude in the r-filter shifted bluewards by 10%. This definition has the advantage that for most galaxies the necessary k-corrections are smaller than for $M_r^{0.0}$ (the median redshift for SDSS is $z \sim 0.1$, and also our sample peaks at $z \sim 0.08$). Furthermore, by shifting all filters to the blue, the 4000Å break falls within the $g^{0.1}$ filter. Thus, $M_g^{0.1} - M_r^{0.1}$ colors are more sensitive to the break than $M_g^{0.0} - M_r^{0.0}$ colors. The absolute magnitude limit corresponds to an apparent magnitude limit of

$$m_r = M_r^{0.1} + 25 + 5\log(D_L(z)[\text{Mpc}]) + \text{K(z)}$$

where D_L is the luminosity distance of the cluster, and $K(z)$ is the k-correction between the observed and rest–frame filter (at $z = 0.1$). We choose $M_r^{0.1} \leq -18.5$, which ensures that the required apparent magnitudes are brighter than $m_r \lesssim 19$, at which photometric errors are still small.

For each cluster, we select from the DR3 database galaxies which are fainter than the apparent magnitude of the BCG, but brighter than $m_r + 0.2$ (where the 0.2 mags account for different k-corrections). These galaxies are further split into color classes (red sequence, green valley, etc.) as described above, into three magnitude bins, and into ten logarithmically spaced bins of distance from the BCG between 0.01 and $1R_{200}$. If rebinning is necessary, bins of fainter magnitude and larger distance are considered. In Fig. 3.5, we illustrate the effect of this background subtraction.
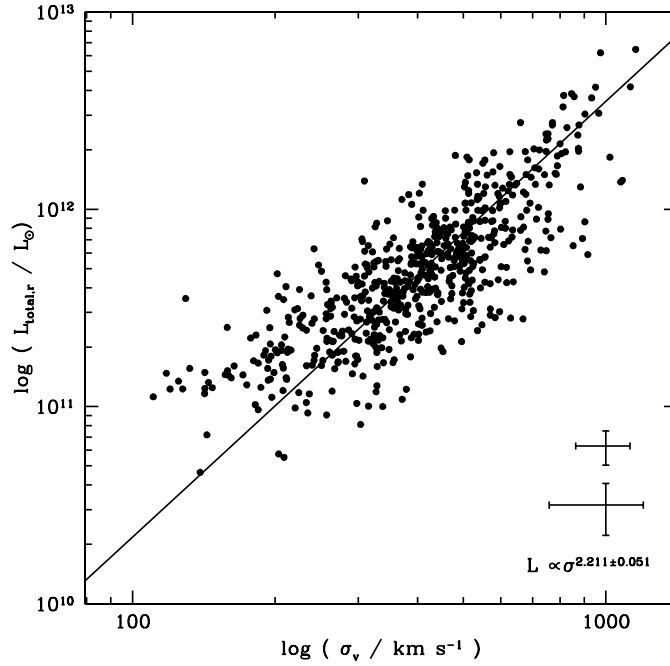
Figure 3.6: The integrated cluster luminosity from galaxies vs. the cluster velocity dispersion. Typical error bars are shown in the lower right corner: the upper symbol demonstrates the typical errors for clusters with $\sigma_v > 500$ km/s, the lower symbol for galaxy groups of lower velocity dispersion.

3.2 Total light

It has been suggested that the integrated optical light from cluster galaxies is a better tracer of cluster mass than the velocity dispersion (Weinmann et al. 2006). The latter is influenced by the dynamical state of the cluster, and can serve as an adequate mass proxy only in the case of virial equilibrium. Furthermore, many of our groups are poor systems, with redshifts for only a few galaxies. In these cases, the value of the velocity dispersion is particularly uncertain.

To determine the total luminosity of the clusters, we sum the galaxy luminosities weighted by the cluster membership probability p_{4d}:

$$\frac{L_{tot}}{L_\odot} = \frac{1}{f_{geom}} \sum_i p_{4d,i} 10^{0.4(M_{r,\odot}^{0.1} - M_{r,i}^{0.1})}$$

where f_{geom} is the geometric completeness of the cluster area coverage (cite text) and $M_{r,\odot}^{0.1} = 4.76$.

In Fig. 3.6, we compare the total luminosities and velocity dispersions of our clusters. A linear fit to the data yields

$$L_{tot} \propto \sigma_v^{2.211 \pm 0.051} \ , \tag{3.1}$$

which is in good agreement with the results obtained by Popesso et al. (2005a), $L_{tot} \propto \sigma_v^{2.33 \pm 0.15}$. If both velocity dispersion and total cluster light would scale linearly with cluster mass, then this relation should be $L \propto \sigma^3$ (since $M \propto \sigma^3$, according to the virial theorem).
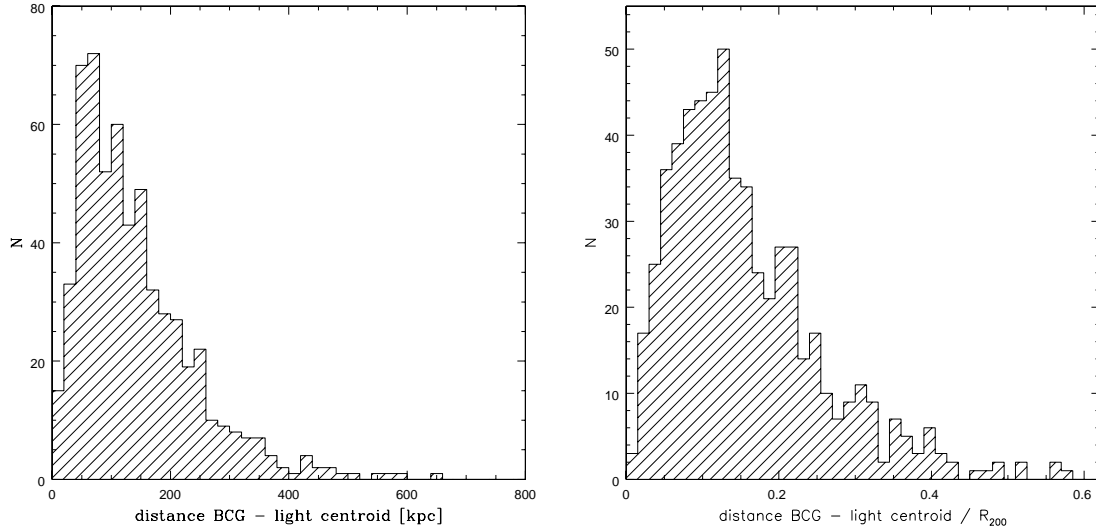
Figure 3.7: Histograms of the distances between BCG and light–weighted mean positions of the cluster galaxies, shown in physical units (left) and as fraction of R_{200}.

Our findings indicate that instead, the mass–to–light ratio of clusters is a function of cluster mass, i.e. more massive clusters are less luminous per unit mass.

Fig. 3.6 also illustrates that there is considerable scatter around this relation ($\sim$ 20%, which is similar to the scatter found by Popesso et al.), and that a few systems differ from the average by more than 2σ. To some degree, this reflects the assumption that the velocity dispersion is a good mass prior, which is only truly the case for virialized systems. This is not the case for all clusters, as some of them have substantial substructure (e.g. when selecting BCGs, we found that some clusters identified by C4 are in fact subclusters in larger systems, see Sect. 2.3.1). Furthermore, there may be intrinsic scatter in how well the optical light in galaxies brighter than our magnitude limit traces the total cluster mass.

3.3 Light centroids

For the present work, we assume that the BCG marks the center of the cluster. This is largely because the majority of our clusters lack X-ray observations: for relaxed clusters, the peak of the X-ray emission is the preferred indicator for the cluster center (as the X-ray luminosity scales with the square of the gas density, which is highest at the bottom of the cluster potential well - the cluster center).

However, instead of an X-ray light center, we can define an optical light center as the light-weighted mean position of the cluster galaxies. We consider only clusters with $f_{\mathrm{geom}} > 0.95$ (585 clusters). Again, each galaxy is weighted by the cluster membership probability p_{4d}.

Fig. 3.7 shows the distribution of $d_{\mathrm{BCG-L_c}}$, the distances between the BCG and the light–weighted center, both in physical units and scaled with R_{200}. For most clusters, the two agree fairly well; the medians of the distributions are 107 kpc, resp. 0.12 R_{200}. For comparison, the typical offset between the BCG position and detected X-ray centroids is 83 kpc in the maxBCG catalog (Koester et al. 2007).

Particularly large values of d_{BCG-L_c} may indicate complications in assigning cluster membership to galaxies without redshifts: the photometric membership criterion relies largely on the galaxy overdensity of a cluster on the sky. If there are fore- and/or background clusters along the line-of-sight, then some fraction of their galaxies would be associated with the main cluster. Alternatively, these offsets could reflect a highly unusual cluster structure, such as a double cluster. Either of these would increase the noise when stacking clusters and investigating trends with clustercentric distance, i.e. distance from the BCGs. Therefore, in the following, we consider only clusters with $d_{BCG-L_c} \leq 400$kpc and $d_{BCG-L_c} \leq 0.3R_{200}$, which leaves 524 clusters in the sample.

3.4 Test for substructure

For stacking clusters, we have to implicitly assume that their structure is similar. But many clusters show deviations from the generally assumed spherical symmetry, i.e. they have substructures. In the previous section we have used d_{BCG-L_c} as a possible indicator of significant substructure in the cluster (although it may indicate other complications).

The most widely used test for substructure is the Dressler-Shectman statistic (developed by Dressler & Shectman 1988), which tries to estimate local deviations of the mean redshift and velocity dispersion. For each galaxy, a local redshift $z_{local,i}$ and velocity dispersion $\sigma_{local,i}$ are calculated from it and its $(n-1)$ closest neighbors. The local deviation is then expressed as

$$\delta_i^2 = \frac{n}{\sigma^2} \left[c^2 (z_{local,i} - z_{cl})^2 + (\sigma_{local,i} - \sigma_{cl})^2 \right]$$

The original Dressler & Shectman (1988) worked used $n = 11$, but we follow the approach of Bird (1994) and use $\sqrt{N}$, where N is the total number of cluster galaxies.

The cumulative deviation is expressed as $\Delta = \sum_i \delta_i$. But since Δ scales with the number of cluster galaxies, N, by itself it cannot serve as an indicator for substructure. Instead, the significance of substructure is assessed by computing Δ for 10000 Monte–Carlo realizations of the cluster, where the redshifts have been randomized (thus removing any correlation between position and local offsets from the mean velocity). The significance can then be assessed by the fraction P of simulations that yield a larger value of Δ. I.e. small values of P indicate the presence of substructure.

Of course, the DS statistic requires a sufficient number of redshift measurements in order to be able to identify substructure. We calculate it for those clusters with $N \geq 16$, i.e. for about half of our cluster sample (272 of 584 clusters). Of these, 63 clusters have $P < 0.05$. In Fig. 3.8, we identify these clusters in the luminosity–velocity dispersion relation. One would expect that for clusters with significant substructure (which is usually a sign of merging), the virial relation is not valid, and that these clusters lie off any relation based on velocity dispersion. However, this is not the case: for both samples, the RMS scatter around the best-fit relation (Eq. 3.1) is very low. In the following, we do not make use of the Dressler-Shectman statistics.

3.5 Number density profile

One of the most remarkable results of N-body simulations is that virialized dark matter halos follow a universal density profile, regardless of their mass, the initial density fluctuation
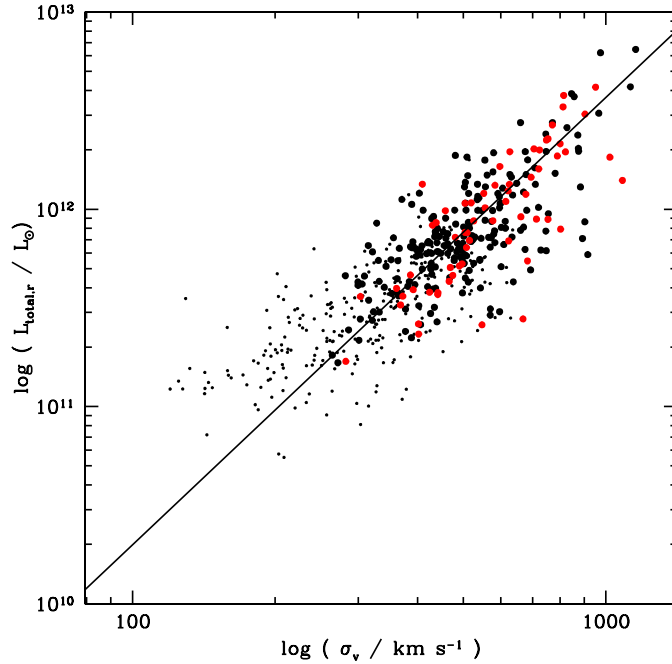
Figure 3.8: As Fig. 3.6, but the clusters are shown with symbols indicating the result of the Dressler-Shectman statistics. Clusters shown as large symbols have at least 16 spectroscopic members, and we have calculated the Dressler-Shectman statistic for them. Of these, those that are shown in red have values of $P < 0.05$, i.e. they could have significant substructure. The small circles show clusters with less than 16 spectroscopic members, i.e. too few to compute a meaningful measure of substructure.

spectrum, and cosmological parameters (Navarro et al. 1997):

$$\rho(x) = \frac{\rho_0}{x(1+x)^2} \ , \tag{3.2}$$

where x is the distance from the center expressed in units of a scale radius, i.e. $x = r/r_s$. Although the slope of the NFW profile is shallower at small radii than at large radii, it is not zero at the center. In this aspect, it differs from other models (such as the King profile), which call for a constant density at the center, i.e. a *core*. Profiles where the density increases towards the center, such as the NFW profile, are said to have a *cusp*.

Although this does not necessarily imply that also the galaxy distribution should follow the same profile, several authors find that the NFW profile provides an adequate description for the galaxy number density (e.g. Carlberg et al. 1997; Lin et al. 2004). Others find that the galaxy distributions display a core, i.e. the number density flattens towards the center (Popesso et al. 2007a). Adami et al. (1998) note that this may be dependent on the magnitude limit of the galaxy sample: they find that bright galaxies follow a cuspy profile, such as the NFW profile, whereas the faint galaxy population displays a core. Furthermore, in the cluster sample studies by Popesso et al. (2007a), the more massive clusters display a cusp, whereas the less massive ones have cores.

Fig. 3.9 the composite number density profile of our clusters, constructed from the galaxies brighter than $M_r^{0.1} < -18.5$ in the photometric catalogs. The galaxies without spectroscopic
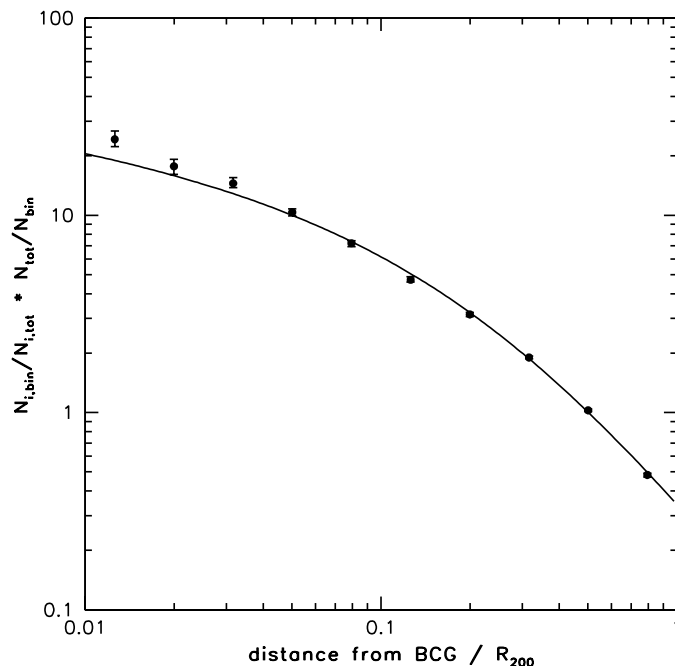
Figure 3.9: Number density profile of a composite cluster, assembled by stacking all the clusters in our sample. Galaxies brighter than $M_r^{0.1} < -18.5$ (but fainter than the respective BCG) are considered, and are weighted by their cluster membership probability p_{rad}. For each radial bin, the number of galaxies is normalized both by the bin area, and the total number of galaxies. The error bars indicate the 68% confidence intervals, derived from bootstrapping the clusters. The solid line is the best fit NFW profile.

redshift confirmation are weighted by the cluster membership probability p_{rad}, which is derived in radial bins from the cluster center (Sect. 3.1.2.3). Between 0.05 and $1R_{200}$, the galaxy distribution is well described by an NFW profile, with a concentration parameter of $c_g = 3.6$. consistent with previous works (e.g. $c_g = 3.7$, Carlberg et al. 1997). But our study is the first to probe cluster regions very close to the BCG. Our data points clearly refute a core at the cluster center; rather, the center is cuspy, with possibly even a slight excess number density than predicted by the NFW profile that best describes the outer radii (note that due to the much larger number of galaxies, the fit is constrained almost entirely by the outer radial bins).

Popesso et al. (2007a) found that the core is present predominantly in lower mass halos. In the left panel of Fig. 3.10, we have computed the number density profile in four bins of cluster velocity dispersion. Also here, we do not find a central core. Rather, the lower mass clusters appear to be slightly more cuspy than the higher mass ones. A steeper central slope implies a higher concentration, as is expected from simulations for the dark matter profiles (Dolag et al. 2004). This is not the case for the galaxy number density: there is a slight trend of increasing concentration with cluster mass. Due to the larger error bars in the center, the best fit is constrained mainly by the outer bins, i.e. it is sensitive to radii beyond $\sim 0.05 R_{200}$. In the right panel of Fig. 3.10, we have repeated the same analysis, but splitting the cluster sample by total optical light. Again, there is no indication of a core. The trend of concentration
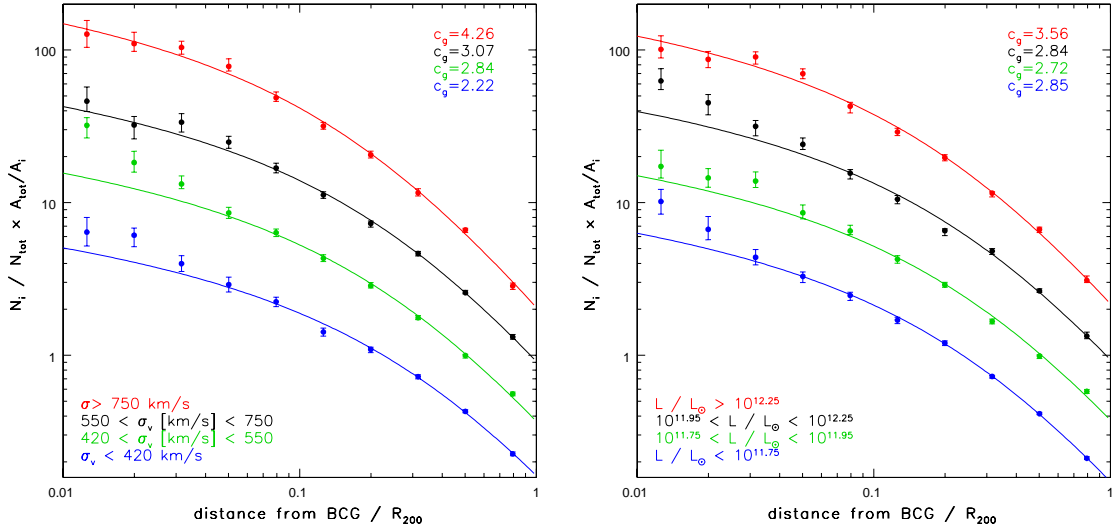
Figure 3.10: The number density profiles of composite clusters assembled from cluster subsamples split by mass, as traced by velocity dispersion (left) or total optical light (right). The subsamples have been chosen so that each contains a similar number of galaxies ($\sim$ 12000). The blue symbols indicate the lowest mass sample (the number density has been shifted downward by a factor of 2.5 to avoid confusion); the green ones the lower intermediate masses; the black ones the higher intermediate masses (shifted upward by a factor of 2.5); the red ones the most massive ones (shifted upward by a factor of 6.3). The solid lines show the respective best-fit NFW profile.

with halo mass is less pronounced than when the clusters are split by total light (although one should keep in mind that R_{200} is computed from σ).

Our results differ significantly from those of Popesso et al. (2007a), although both studies are based on SDSS data. Popesso et al. find a pronounced core, and even a drop in the number density in their central bin (at $0.05R_{200}$). The lower magnitude limit is similar in both works; our study uses $M_r^{0.1} < -18.5$ in `cmodel` magnitudes for our study, Popesso et al. use $M_r < -18.5$ in `model` magnitudes. The difference is therefore not due to different distributions of bright and faint galaxies, as proposed by Adami et al. (1998). There are a number of other reasons which might explain this discrepancy:

- A significant difference in the two studies lies in the background subtraction. Although both employ a statistical subtraction method, our method takes into account spectroscopic redshifts as far as available, as well as galaxy color. Popesso et al. do not make use of the spectroscopic data, and only measure the background number density in bins of apparent magnitude, but not in color. Galaxies on the red sequence make up a large fraction of the cluster population, and taking into account this color criterion substantially boosts the contrast of clusters against the background galaxy population, so much that two-band imaging surveys have become a powerful method to identify clusters (Gladders & Yee 2000). At the cluster core, $\gtrsim 80\%$ of the galaxies are red (Sect. 4.4.1). At least for these galaxies, our method should provide more accurate cluster membership criteria.

- Although both studies have a similar magnitude limit in terms of absolute magnitudes, Popesso et al. probe galaxies to much fainter apparent magnitudes, as their cluster sample

extends to higher redshifts. Our (absolute) magnitude limit was chosen so that galaxies are brighter than $m_r \lesssim 19$. Popesso et al. consider galaxies to $m_r \lesssim 21$, i.e. one magnitude brighter than the survey magnitude limit. While photometry of galaxies this faint may be reliable in the field, it can become a problem in the cluster core, where the galaxy density is high, and the sky background is difficult to determine (see the related discussion in Sect. 2.2.2). In the very core of the clusters, the BCG influences the sky background measurement, thereby lowering the signal-to-noise ratio of neighboring objects. For faint objects, this may well mean that they fall below the detection threshold.

Under the assumption that the BCG position is close to the X-ray centroid (which Popesso et al. use as cluster center), this problem could be a viable explanation for the dip in the number counts which Popesso et al. find for the innermost bin in the lowest mass clusters, as these have the lowest physical separation from the BCG.

- The low-mass clusters are typically also faint in X-rays. With less flux, the centroid may be difficult to constrain from the data. The true galaxy overdensity would then lie slightly offset from the X-ray center.

It is not clear whether any of these effects is strong enough to explain the dip in the core number density which Popesso et al. find at radii $\lesssim 0.1R_{200}$. In our analysis, the number densities at these radii start showing a slight excess compared to the best-fit number density profile, i.e. quite the opposite effect. Since our photometry is more secure, particularly for faint galaxies, we can speculate that the number counts of Popesso et al. are indeed affected by systematic photometry issues in the cluster center.

3.6 Luminosity segregation

For the number density profile, galaxies are considered regardless of their properties, apart from a lower magnitude cut. We now turn to the question whether galaxies of different properties are distributed differently within the cluster. It is well established that denser environments host predominantly red galaxies, and few blue galaxies (see also Sect. 4.4.1). The stellar populations of cluster galaxies, and their dependence on clustercentric radius, are studied in the next Chapter. Here, we investigate the luminosity dependence of the galaxy distribution.

The luminosity function of galaxies is generally described by a Schechter function:

$$\phi(L) = \phi^\star \left(\frac{L}{L_\star} \right)^\alpha \exp \left(-\frac{L}{L_\star} \right).$$

At luminosities brighter than the turn-over luminosity $L_\star$, the number of galaxies falls off exponentially. The number of galaxies in bins of magnitude follows a power-law with the slope of $\alpha + 1$ for luminosities fainter than $L_\star$ (resp. $M_\star$). If $\alpha < 1$, then the number of galaxies increases towards fainter magnitudes, the more negative α is, the steeper the slope.

It is a long-standing matter of debate whether the luminosity function is universal, or differs with environment, and if so, how. Much of the debate has been whether there is a possible up-turn in the number counts of dwarf galaxies, i.e. at magnitudes fainter than $M_r \gtrsim -18$ (for opposing views see e.g. Popesso et al. 2006; Rines & Geller 2007, and references therein). For the sake of reliable photometry, our sample does not probe this deeply. But even for brighter magnitudes, results from the literature are not unanimous: for example,
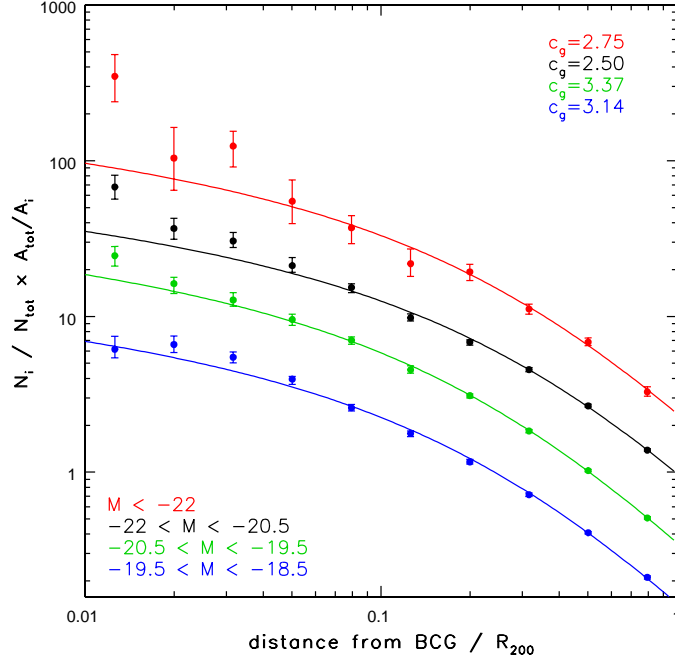
Figure 3.11: The number density profiles of cluster galaxies split by absolute $M_r^{0.1}$ luminosity. The points and lines are artificially offset to avoid confusion. The concentration parameter of the best-fit NFW profiles are indicated in the top right corner.

Popesso et al. (2005b) claim that $M_\star$ in clusters is brighter by 0.5 magnitudes than in the field, whereas Barkhouse et al. (2007) find that $M_\star$ becomes progressively fainter towards the cluster core.

Here, we do not investigate the functional form of the luminosity function, but whether we find differences in the distribution within clusters for galaxies of different luminosities.

3.6.1 Number density profiles in luminosity bins

Fig. 3.11 shows the number density profile of galaxies split into four bins of absolute magnitude, along with the best-fit NFW profiles. Interestingly, the two fainter bins show a higher concentration than the two brighter bins. When the galaxies are split according to color, this dichotomy is even stronger for the red galaxies (Fig. 3.12). The blue(+green) galaxies show a much less concentrated distribution, but even here, there is a slight indication that the concentration anti-correlates with brightness. Again, these trends are dominated by the galaxy distribution on the cluster outskirts. In the very core, the distribution of red galaxies is increasingly peaked with luminosity.

3.6.2 Faint-to-luminous ratio

Particularly for the red galaxies, these data indicate that the galaxy distribution is slightly different for galaxies brighter / fainter than the dividing magnitude, $M_r^{0.1} = -20.5$, between the fainter and brighter two bins. For comparison, Blanton et al. (2003a) measured the turn-over
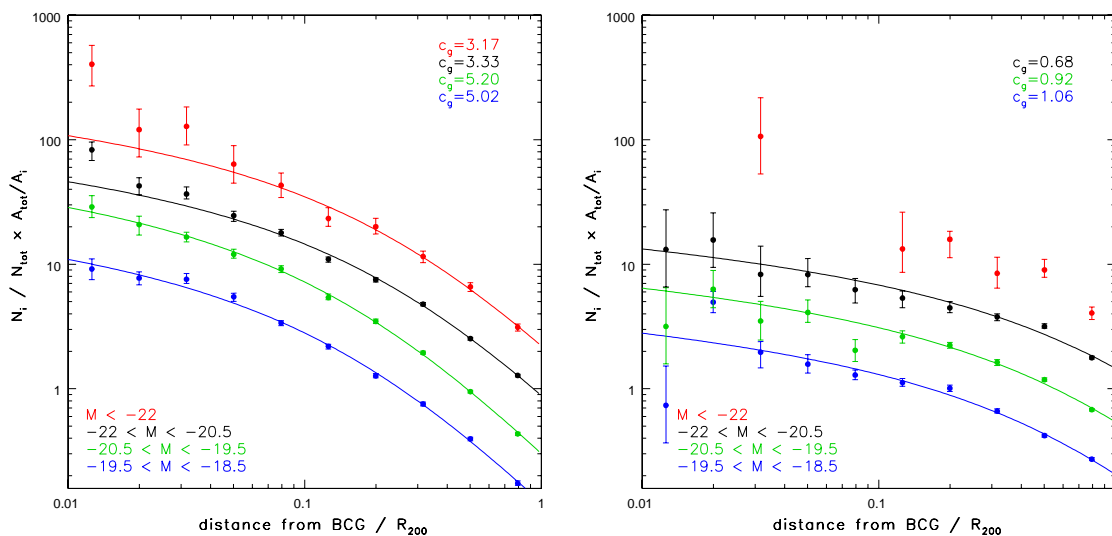
Figure 3.12: As Fig. 3.11, but for red galaxies (left) and for blue + green galaxies (right). There are too few blue galaxies more luminous than $M_r^{0.1} = -22$ to allow fitting an NFW profile.

magnitude of the luminosity function to be $M_{\star,r}^{0.1} = -21.21 \pm 0.01$, in petrosian magnitudes. Cmodel magnitudes have an offset of approximately -0.1 magnitudes (Abazajian et al. 2004), i.e. this threshold is 0.8 magnitudes fainter than $L_\star$. We can further quantify this difference as a "faint-to-luminous" ratio $R_{f/l}$: the number of galaxies with $-18.5 < M_r^{0.1} < -20.5$ to those with $M_r^{0.1} < -20.5$. However, it must be cautioned that all these galaxies are brighter than the typical luminosities of dwarf galaxies, and that this ratio mainly probes the luminosity region around $M_\star$. Fig. 3.13 shows the faint-to-luminous ratio as function of clustercentric distance, for both the red galaxy sample and the blue+green galaxies. The field value is estimated from galaxies with spectroscopic redshifts at distances $1 < r/R_{200} < 20$ from the BCGs of clusters at $z < 0.04$. At redshifts $z < 0.045$, the SDSS spectroscopic magnitude limit corresponds to $M_r^{0.1} = -18.5$ (for red galaxies). For the red galaxies, $R_{f/l}$ increases by a factor of two from the field to $\sim 0.1 R_{200}$, and is approximately constant further inward, apart from the central bin, where the value is similar to the cluster outskirts. The statistics for the blue galaxies is much more uncertain, but is broadly consistent with a similar trend. A significant difference is that the field value of $R_{f/l}$ is larger in the field than at the cluster outskirts.

With regard to previous results in the literature, this trend is at first sight surprising. Popesso et al. (2005b) define a "dwarfs-to-giants" ratio as the number of galaxies with $-17.3 \geq M \geq -18.8$ to those with $M \leq -20.8$, and found that it increases slightly with clustercentric distance. Phillipps et al. (1998) define a dwarfs-to-giants ratio as the number of galaxies with $-15.3 \geq M_r \geq -18.3$ to those with $M_r < -18.3$, and find an anti-correlation with the local galaxy density (as measured from the "giant" galaxies). However, as is clear from the absolute magnitude limits, our "faint" galaxies are brighter than the "dwarf" galaxies of these studies. Still, it is surprising that the trend should reverse from the "faint" to the "dwarf" galaxies. We therefore need to make certain that this is a real trend, and not caused by systematics. A major concern here is cluster membership probability. To recall, cluster
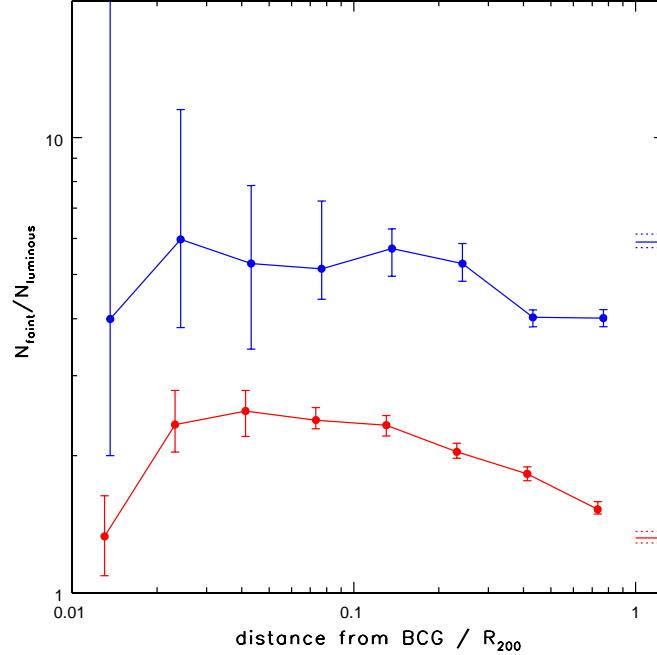
Figure 3.13: The faint-to-luminous ratio, i.e. the ratio of galaxies with $-18.5 < M_r^{0.1} < -20.5$ to those with $M_r^{0.1} < -20.5$ as function of clustercentric distance for red galaxies (red points / lines), and blue+green galaxies (blue points / lines). The field values from a low-redshift, spectroscopically complete field sample are indicated on the right.

membership probabilities were assigned based on color, apparent r-magnitude, and radial distance from the cluster center. If in one bin of these properties the probability p_{rad} is not in the range $0 \leq p_{\mathrm{rad}} \leq 1$, the bin size is increased by adding bins in the following order: fainter magnitudes, larger radii, brighter magnitudes, smaller radii. Since we preferentially add bins at larger radii first, this method could introduce a radius-dependent bias. The only truly reliable membership criterion are spectroscopic redshifts. However, the spectroscopic sample is incomplete both geometrically and in magnitude. The threshold magnitude, $M_r^{0.1} = -20.5$, is also the spectroscopic completeness limit at $z = 0.1$. Hence, the sample of "giant" galaxies is spectroscopically complete, apart from geometric incompleteness issues (the latter are of concern particularly in the cluster core). The magnitude completeness of "dwarf" galaxies, on the other hand, is a function of redshift. A systematic *overestimation* of the membership probability for red dwarfs could produce the trend we observe.

There are too few clusters at $z < 0.04$ (the spectroscopic completeness limit for faint galaxies) to reliably test this, but if the trend in $R_{f/l}$ is indeed a result of a systematic bias in the photometric cluster membership probability, we should see different trends with redshift. The left panel of Fig. 3.14 shows the radial dependence of $R_{f/l}$ for red galaxies in two subsamples, split according to redshift. The trends are very similar, with two notable exceptions: in the two outermost bins, and the two innermost bins, $R_{f/l}$ is higher in the lower redshift sample. In the two outermost bins, the number of luminous galaxies is largely complete. If anything, this would imply that we *underestimate* the number of faint galaxies
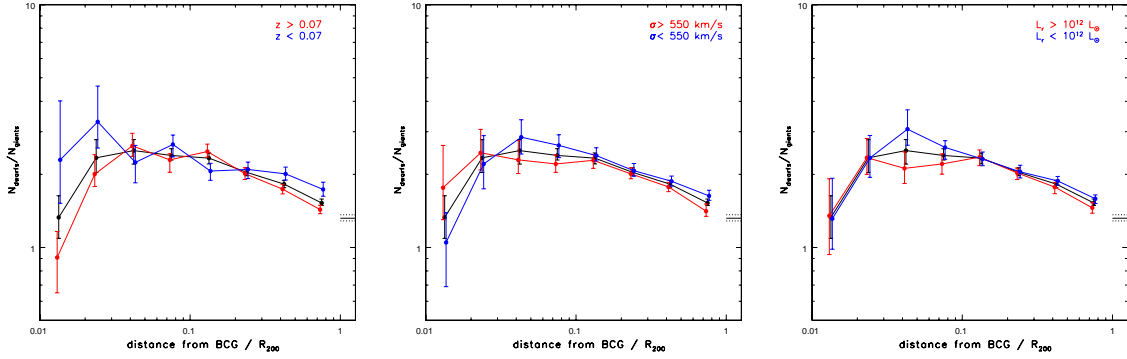
Figure 3.14: The faint-to-luminous ratio of red galaxies, computed for several cluster subsamples. In the left panel, the cluster sample is split according to redshift. For the middle panel, the split is according to cluster velocity dispersion, and for the right panel, according to total optical luminosity. The faint-to-luminous ratio of red galaxies for all clusters is shown as black points / lines.

with the photometric membership probability at these radii. (The innermost bin is discussed separately in Sect. 3.6.4.)

The other two panels of Fig. 3.14 show two other ways of splitting the cluster sample: by velocity dispersion and by optical luminosity. Neither of these shows significant variation with cluster property.

As a further test, we calculate $R_{f/l}^{\mathrm{nm}}$ by weighting the galaxies with $1 - p_{\mathrm{rad}}$, instead of p_{rad}. As p_{rad} estimates the probability that a galaxy belongs to a given cluster, $1 - p_{\mathrm{rad}}$ is the probability that it is not part of that cluster. However, $R_{f/l}^{\mathrm{nm}}$ cannot be taken as an estimate of the field value, since absolute magnitudes are calculated by assuming that the galaxy is at the cluster redshift. Still, $R_{f/l}^{\mathrm{nm}}$ can be a sensitive test of the reliability of estimating $R_{f/l}^{\mathrm{nm}}$ from photometric cluster membership criteria: if we indeed increasingly overestimate p_{rad} with decreasing cluster radius, then we are also underestimating the number of field faint galaxies, i.e. $N_f = \sum(1 - p_{\mathrm{rad},i})$. Due to the higher contrast compared to fainter background galaxies, we assume that p_{rad} is a good estimator of cluster membership probability for the luminous galaxies (the only luminous galaxies which enter the computation of $R_{f/l}^{\mathrm{nm}}$ are those which are missed due to fiber collisions). Hence, if the observed increase in $R_{f/l}$ is due to a systematic overestimation of p_{rad} for dwarf galaxies, we should also find a corresponding decrease of $R_{f/l}^{\mathrm{nm}}$ towards the cluster center. Fig. 3.15 shows $R_{f/l}^{\mathrm{nm}}$ as function of radial distance. For the red galaxies, $R_{f/l}^{\mathrm{nm}}$ is constant within the error bars (apart from the innermost bin). This is a further reassurance that the trend we observe is real.

Our result is indirectly supported by the study of Barkhouse et al. (2007), who find that for red galaxies, $M_\star$ becomes progressively fainter towards the cluster center. They also find a similar, though less significant trend for blue galaxies. Our galaxy sample probes the luminosity regime around $M_\star$, and is brighter than a possible population of dwarf galaxies. This makes the ratio of faint-to-luminous galaxies sensitive to changes in $M_\star$: a fainter $M_\star$ implies a larger faint-to-luminous ratio. Barkhouse et al. argue that the trend in $M_\star$ is mainly due to fading of galaxies infalling into the cluster. Since this would predict a stronger change in $M_\star$ for the blue galaxies than the red galaxies (which they assume to be mostly passively evolving), they further assert that massive galaxies preferentially merge with the central
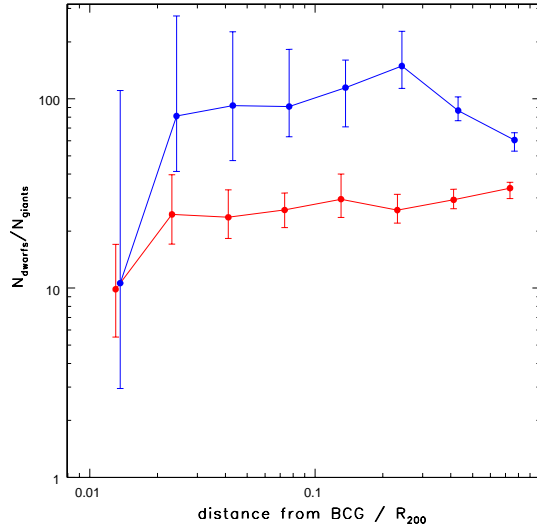
Figure 3.15: The luminous-to-faint ratio of non-members, i.e. each galaxy is weighted by $(1 - p_{rad})$, instead of p_{rad}. This is shown separately for red and blue+green galaxies.

galaxy (i.e. cannibalism), thus depleting the number of "giants", and decreasing $M_\star$. Also, they suggest that faint blue galaxies are destroyed in the central cluster region, rather than fade and redden to be faint red galaxies. Hence, their scenario requires processes which disrupt and destroy galaxies.

3.6.3 Average stellar mass

The scenario purported by Barkhouse et al. (2007) can be tested by investigating the stellar masses of the cluster galaxies. As galaxies fade and redden, their luminosities and colors change significantly, but the stellar mass changes only little. If there are indeed processes at play which affect the galaxy mass (mergers, tidal disruption), then we should see a systematic trend in the characteristic galaxy masses.

Fig. 3.16 shows the mass distributions separately for the red and blue+green galaxies. The completeness limit is $\log(M_\star/M_\odot) > 9.6$, as determined from the red galaxies, which have a lower M/L ratio. Fig. 3.17 shows the average galaxy mass (of galaxies more massive than $\log(M_\star/M_\odot) > 9.6$), as function of clustercentric distance. The average mass of all galaxies is almost constant (again, apart from the inner bin). This demonstrates that disruptive processes play only a minor role in altering cluster galaxy properties, with the possible exception of the very core of the cluster. For the red galaxies, the characteristic galaxy mass decreases significantly towards the cluster center. The same holds for the blue galaxies, although the trend is weaker and noisier.

These trends can be simply explained by the color – radius relation, which we will investigate in Sect. 4.4.1. As we show there, almost all galaxies in the cluster center are red. But we also show that the color – radius relation is most pronounced for low-mass galaxies: in the mass range $9.6 < \log(M_\star/M_\odot) < 10$, only 20% of field galaxies are red, but 80% in the cluster center. With increasing mass, the color – radius relation becomes progressively weaker, i.e.
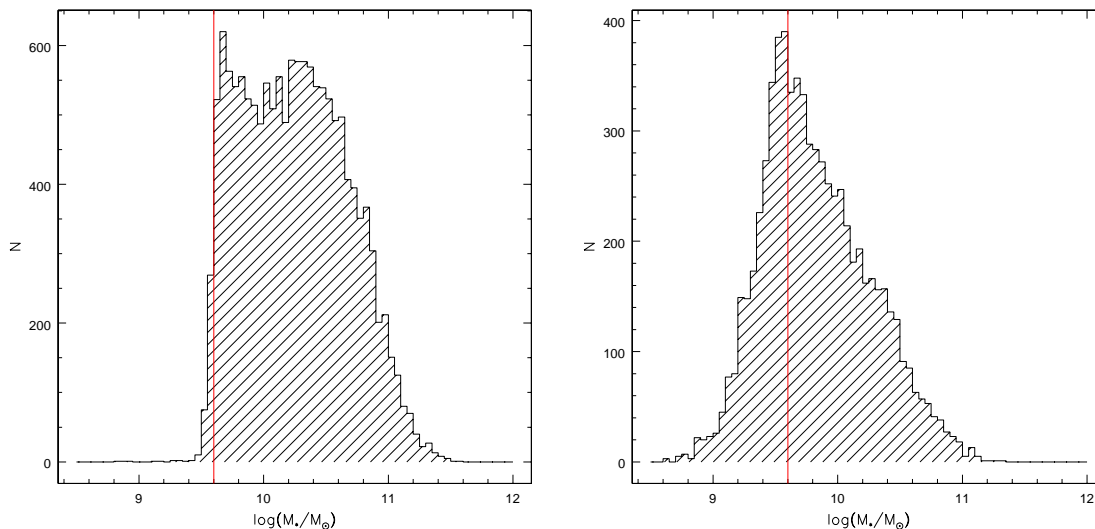
Figure 3.16: The mass distribution of red cluster galaxies (left panel), and of blue+green cluster galaxies (right panel). The red line indicates the mass completeness limit, as set by the red galaxies. For this plot, each galaxy is shown only if its cluster membership probability p is larger than a number drawn randomly between 0 and 1.

for galaxies with $\log(M_\star/M_\odot) > 10.7$, 60% of field galaxies are red, and 90% in the cluster center. As also Fig. 3.17 indicates, a significant number of low-mass galaxies at the cluster outskirts are blue. Towards the cluster center, progressively more low-mass galaxies are red, thus lowering the average mass of red galaxies. The fact that the average mass of blue galaxies also decreases shows that also the more massive blue galaxies fade and redden with decreasing clustercentric distance. However, most massive galaxies are red in all environments, and hence reddening of the few blue, massive galaxies does not significantly change the number of red, massive galaxies.

3.6.4 The cluster core

Several of these plots suggest that in the very center of the cluster, $r < 0.02R_{200}$, some of the observed trends reverse: the faint-to-luminous ratio is as low as in the field, and the typical mass of (red) galaxies increases by $\sim 60\%$. This is very intriguing in light of a prediction from the modeling by De Lucia et al. (2006): they combined the Millennium Simulation with a suite of semi-analytical models and found that the median mass of elliptical galaxies increases in the core of the cluster (Fig. 3.18). Their model implies that the stellar mass of ellipticals in the very core ($r < 0.02R_{200}$) is a factor of 6 larger than at the cluster outskirts. In their second bin, the stellar mass is approximately twice as large as at the cluster outskirts.

Several factors hinder us to directly associate our result with the prediction of De Lucia et al.:

- The prediction is for elliptical galaxies, whereas we have investigated red galaxies. These are not necessarily the same.

- As we have argued before, photometry is difficult in the vicinity of the BCG. This may work in two ways: on the one hand, faint (low-mass) galaxies are missed, either due to
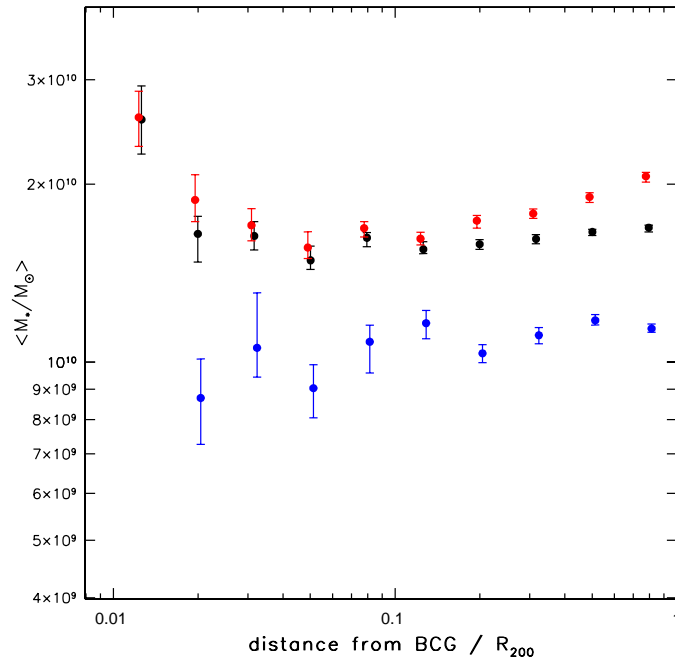
Figure 3.17: The average mass of all galaxies (black points), red galaxies (red) and blue+green galaxies (blue), computed from galaxies above the mass limit of $\log(M_\star/M_\odot) > 9.6$.
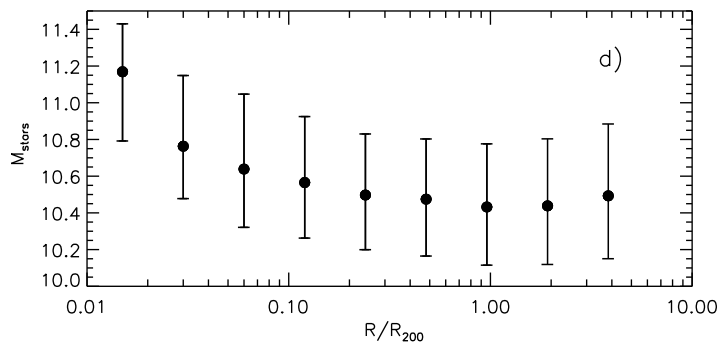

Figure 3.18: Fig. 8d) from De Lucia et al. (2006), depicting the median stellar mass of model elliptical galaxies in 51 clusters of the Millennium Simulation.
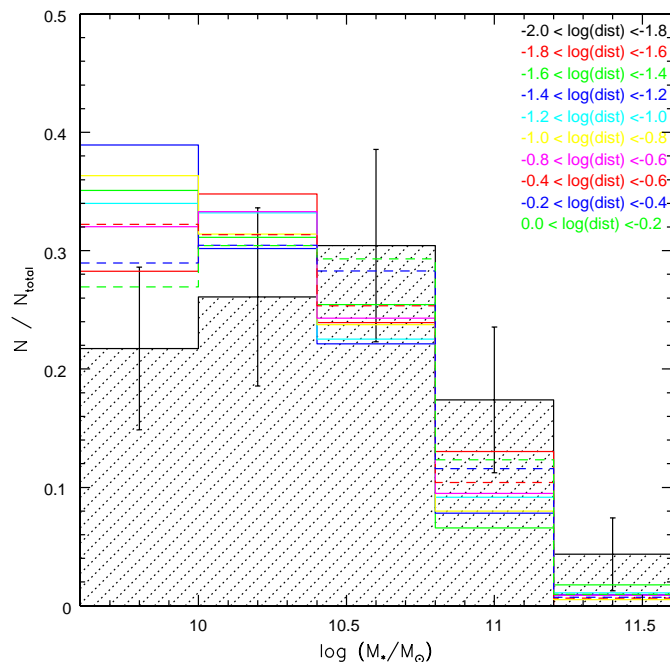
Figure 3.19: The mass distributions of red galaxies in bins of distance from the BCG. The black, shaded histogram shows the distribution in the central bin, with $\sqrt{N}$ error bars. The colored histograms show the distributions in the other radial bins (those bins at distances greater than $10^{-0.4}R_{200}$ are shown as dashed lines).

increased noise, or in fact, they might be "hidden" by the BCG. On the other hand, luminosities and stellar masses of BCG neighbors are likely underestimated (Sect. 2.2.2). Furthermore, the SDSS pipeline may "shred" large galaxies into multiple detections, thus creating "false detections". We have verified by visual inspection that due to the rather bright magnitude limit, this is not a major influence on our sample - virtually all objects are individual galaxies, or secondary nuclei to the BCG.

- The dip in the faint-to-luminous ratio is almost entirely caused by the clusters at $z > 0.07$ (Fig. 3.14). With increasing redshift, the BCG neighbors are at smaller angular separation from the BCG, i.e. they are more likely to be in the same "box" in which the local sky is estimated. This could cause fainter galaxies to miss the detection limit. On the other hand, this also causes the luminosity to be underestimated, and it is not clear which effect is stronger. A similar argumentation applies to the observation that the "dip" is stronger in clusters with lower velocity dispersions (where distances in units of R_{200} correspond to smaller physical distances).

It is difficult to estimate how much these points can contribute to masking the effect predicted by De Lucia et al., or whether they could create a false detection of such a trend. However, Fig. 3.11 shows an excess of galaxies in the central bin at all but the faintest magnitudes (where the number is compatible with the best-fit NFW). If we are indeed missing a substantial fraction of galaxies in this bin, then the excess of galaxies must be even stronger than observed.

Another clue to the reality of this result lies in the distribution of stellar mass within each bin in radial distance. This is shown in Fig. 3.19, which suggests that the mass distribution in the central bin is systematically different than in the other bins: there is both a deficiency of galaxies with masses lower than $\log(M_\star/M_\odot) < 10.4$, and an excess of galaxies with masses larger than $\log(M_\star/M_\odot) > 10.8$. Thus, unless one argues that the shortcomings in the SDSS photometric pipeline can cause an over-/underestimation of stellar masses of the order of 0.5 dex, or in fact, miss galaxies with masses of $\log(M_\star/M_\odot) \sim 10.2$ altogether, this result can be taken as an indication that the mass distribution in the very cluster core is indeed different than at larger radii.

A possible cause for this is dynamical friction. As Fig. 3.11 indicates, there is an excess of bright (red) galaxies of galaxies compared to the best-fit NFW profile. Dynamical friction causes the more massive galaxies to sink to the cluster center. If they do not merge immediately with the BCG, then indeed an overdensity of massive galaxies is observed in the cluster center. The galaxy excess does not imply a steeper dark matter profile than NFW in the center. On a different scale, Goerdt et al. (2006) have argued that the presence of several globular clusters in the center of the Fornax dwarf spheroidal (i.e. an excess of test particles) suggests a cored mass profile, since the merging time for these in objects in a cuspy mass profile would be substantially shorter. If similar processes are at work on the much larger scales of galaxy clusters, then the excess of bright galaxies could indicate a flattening of the mass profile. Some strong lensing studies have indeed argued in favor of a cored mass profile in clusters. E.g. Rzepecki et al. (2007) find a core radius of $0.025R_{200}$ in the cluster RCS0224-0002, which is comparable to the scale where our data show a galaxy excess.

3.7 Summary and discussion

We have found that, on average, the number density profile of clusters is well described by an NFW profile. This applies to radii $\gtrsim 0.05R_{200}$, at smaller radii, there is a slight excess of galaxies. The distribution of blue galaxies is significantly more extended than that of red galaxies, which is a result of the color–density relation. For the red galaxies (and thus also for the overall galaxy population), the distribution of galaxies fainter than $M_r^{0.1} > -20.5$ is more concentrated than that of galaxies brighter than this. This is also apparent in the ratio of faint-to-luminous red galaxies, which decreases with increasing cluster radius. However, the average stellar mass of galaxies remains approximately constant. We have argued that this is predominantly due to the quenching of star formation in cluster galaxies, along with a subsequent fading and transition to the red sequence. Apart from the innermost bin, the galaxy mass distribution does not change significantly. This indicates that the process(es) which terminate star formation in cluster galaxies do not significantly alter their stellar mass. The excludes mergers from playing a dominant role within R_{200}. If disruptive process such as tidal disruption play a role, then only at masses below $\lesssim 10^{9.6}M_\odot$.

The mass distribution in the core, on the other hand, differs from that at other radii, in that there are more massive galaxies. With increasing mass, dynamical friction causes galaxies sink to the cluster center on shorter timescales. But if they were to merge on a short timescale with the BCG, then no galaxy excess would be seen. A flattening of the central slope of the mass profile could increase the merger timescale in the very center, so that a galaxy excess would be seen.

4

Population gradients in local clusters

In this chapter, I investigate the recent and current star formation activity of galaxies as function of distance from the cluster center, in the sample of SDSS clusters. To characterize the recent star formation history, I use the Principal Component Analysis of Wild et al. (2007), which is sensitive to the star formation history over the last $\sim 2\,Gyr$. I find a marked star formation–radius relation in that most galaxies in the cluster core are quiescent, i.e. have terminated star formation a few Gyr ago. This star formation–radius relation is most pronounced for low-mass galaxies. The fraction of galaxies with young stellar populations which have spectra indicative of a recent starburst, or truncation of star formation, is constant with cluster radius. The typical star formation rate of non-quiescent galaxies declines by approximately a factor of 2 towards the cluster center. These results are consistent with a scenario in which star formation is quenched on timescales similar to the cluster crossing time, i.e. a few Gyr. I furthermore find that the fraction of galaxies which host optical AGN declines towards the cluster center, largely due to a decline of AGN activity in quiescent galaxies. This suggests that the processes which trigger optical AGN activity are subject to similar environmental influences as star formation.

4.1 Radial cluster profiles as density probes

In galaxy clusters, the star formation–density relation translates to a star formation–radius relation, since the density decreases with increasing (projected) clustercentric radius. Measurements of local density, such as the distance to the 5$^{\text{th}}$ neighbor have the disadvantage of strong shot noise, as well as selection and projection effects. In this sense, radial distance presents a cleaner measurement. However, individual clusters are rarely axisymmetric systems, and thus the true strength of this method is investigate radial profiles in composite clusters. We have shown in Sect. 3.5 that the number density profiles of our composite cluster is well described by an NFW profile, and hence radial distance is directly related to average density. Furthermore, stacking individual clusters to one composite cluster allows for vastly improved number statistics than possible with any individual cluster.

Nevertheless, studying radial profiles of composite clusters has some obvious disadvantages. On the one hand, it neglects the influence of subclustering. A considerable fraction of galaxies arrive into the cluster as part of an infalling group of galaxies. The group environment may play an important role to "preprocessing" the galaxies (Zabludoff & Mulchaey 1998). Also, the properties of individual clusters differ significantly from the *average* cluster properties; even clusters with similar masses may have very different galaxy populations (Moran et al. 2007). This scatter seems to be mostly stochastic in nature: Goto (2005a) find that there is no systematic trend of varying galaxy populations with cluster mass. Furthermore, the radial distance is only the projected distance along the line-of-sight, i.e. for individual galaxies, it is only a lower limit to the true distance. This observational limitation necessarily dilutes the three-dimensional trend.

Clustercentric distance has a second interpretation apart from a local density measure: it also relates to the time since infall into the cluster (Gao et al. 2004). Of the galaxies at or beyond the virial radius, a considerable fraction has not (yet) experienced the dense cluster environment. Galaxies at the cluster core, on the other hand, were either born in a dense environment, or they must have traversed the cluster from the outskirts to the center at least once. The cluster crossing time is of the order of R_{200}/σ_v, i.e. 2.5 Gyr for a cluster with $\sigma_v \sim 400$ km/s, and $R_{200} \sim 1$ Mpc. Therefore, clustercentric distance is also an approximate timescale, and is sensitive to processes occurring on timescales of the order of Gyr. This timescale is particularly interesting for the processes which have been proposed to quench star formation in galaxies entering the cluster environment (Sect. 1.5.5). Processes which quench star formation on similar timescales, such as strangulation or harassment, would induce gradients over the complete radial range. Processes which act on shorter timescales are likely to effect distinctive signatures at radii where they are most effective - e.g. ram-pressure stripping could be detectable as an increase in the (post-)starburst rate, presumably mostly in the cluster center, where the gas densities are highest. Mergers could induce (post-)starbursts primarily at outer cluster radii, where the relative galaxy velocities allow frequent mergers.

Using [OII] as a tracer of star formation, Balogh et al. (1997) showed that the star formation rate declines gradually in cluster galaxies between 2 and $0.3R_{200}$. Also, they find that a lower fraction of cluster galaxies displays strong emission lines indicative of a starburst than field galaxies. They conclude that the quenching of star formation is not accompanied by a brief enhancement of star formation, and that it is likely to proceed gradually, rather than instantaneously. In the same cluster sample, Balogh et al. (1999) find no enhancement of (post-)starburst galaxies, neither relative to the intermediate-redshift field, nor to low-redshift environments. This supports the conclusion of their previous work, that star formation is suppressed gradually, rather than truncated, and that a likely mechanism is strangulation. Interestingly, the results of Dressler et al. (1999) on the incidence of (post-)starburst galaxies are markedly different. In a different intermediate-redshift cluster sample, Dressler et al. found that "k+a" galaxies, which they take to be post-starburst galaxies, are more frequent in intermediate-redshift clusters than the field. They find that these galaxies avoid the cluster center, but are more concentrated than the actively star-forming galaxies. Dressler et al. and Poggianti et al. (1999) argue that the increased rate of "k+a" galaxies in clusters is due to the cluster environment triggering (brief) episodes of star formation, before truncating star formation. They suggest that the most likely process quenching star formation in infalling galaxies is ram-pressure stripping. They further argue that the enhancement of star formation is a possible cause of the Butcher-Oemler effect, i.e. the higher incidence of blue galaxies in

high-redshift clusters. The lack of blue galaxies in local clusters is then a consequence of the lower infall rates of galaxies, and a decrease of the star formation density in the field. Using the same cluster sample as Balogh et al., Ellingson et al. (2001) have argued that these two effects alone are enough to explain the Butcher-Oemler effect, without the necessity of a star formation enhancement in clusters.

In this chapter, we concentrate on galaxies which have been observed spectroscopically, for a number of reasons. Foremost, the information on stellar populations and star formation histories available from the spectra rather than just the galaxies' photometric colors is much greater (colors can be thought of as very low resolution spectra). Furthermore, galaxies can be clearly associated with clusters with an available redshift measurement, and we do not need to rely on statistical subtraction methods to assign cluster membership. This is particularly crucial in the cluster outskirts, where the number densities of galaxies are too low to use statistical subtraction to identify cluster members.

In this work, we investigate only the spectral properties, not the morphological ones. Therefore, our aim is to measure the *star formation – radius* relation, rather than the morphology–density relation.

4.2 Measures of star formation history

4.2.1 Spectroscopic indices: 4000Å break and Hδ

The presence of emission lines (most prominently Hα and [OII]) signals *on-going* star formation: radiation from young, hot O and B stars photo-ionizes the surrounding gas clouds, which subsequently emit in the recombination lines. Once star formation ceases and the O and B stars die out, radiation from the cooler stars is no longer powerful enough to photo-ionize the gas clouds at appreciable levels, and thus the emission lines fade. However, the continuum light (and the absorption lines) of the galaxy comes from the integrated light from its constituent stars, and thus follows the light-weighted average of the characteristic stellar populations. As stellar populations age, the hotter, more massive stars die, so that with increasing age the integrated light becomes more and more dominated by the low-mass, cool, red stars. With decreasing stellar mass and temperature, the strength of the Balmer break at 4000Å strengthens (Fig. 4.1). The 4000Å break is therefore a good indicator of the light-weighted age of the stellar population(s). On the other hand, the strength of the Balmer absorption lines (such as Hδ) is strongest in A stars (since these have the optimal temperature where Hydrogen atoms populate excited states, but are not ionized).

The light of a stellar population created in a single burst of star formation is dominated by consecutively cooler stars and thus evolves with time approximately as stellar spectra evolve with decreasing temperature (i.e. in Fig. 4.1 it would pass from an O-star like spectrum to an F-star like spectrum). The time-scale for this evolution is determined by the main sequence life-times of these stars, e.g. ∼0.5 Gyr for A stars, ∼2 Gyrs for F stars. Fig. 4.2 illustrates the track such a *starburst* follows in a diagram of Hδ vs. the strength of the 4000Å break. However, the star formation histories of most galaxies are more complicated than a single burst. Fig. 4.2 also shows the typical values of Hδ and $D_n(4000)$ for galaxies with continuous star formation, usually characterized by an exponentially declining star formation rate. The majority of galaxies appears to be well described by continuous star formation, as shown by the underlying population of Hδ and $D_n(4000)$ values of SDSS galaxies. For old populations

$(\mathrm{D}_n(4000){\gtrsim}1.6)$, the tracks from the burst models and continuous models converge.

4.2.2 Higher SNR indices from Principal Component Analysis

Some galaxies at intermediate redshifts are observed to have an excess of galaxies with stronger than average Hδ absorption lines (Sect. 1.6). This implies that these galaxies underwent a burst of star-formation within the last Gyr, hence they are often referred to as *post-starburst* galaxies. The key measurement to identify these galaxies is the Hδ line; however, this generally requires a very good signal-to-noise ratio spectrum. Wild et al. (2007) have recently developed an alternative method to measure the strength of the 4000Å break and the Balmer absorption lines. Rather than concentrating on the two indices $\mathrm{D}_n(4000)$ and Hδ_A, their method utilizes all the flux in the region of the 4000Å break, i.e. in the wavelength region 3750-4150Å. They generate model spectra from the Bruzual & Charlot (2003) stellar population synthesis code for a range of star formation histories, and apply a Principal Component Analysis[1] to

---

[1] A spectrum with M pixels can be thought of as one point in an M-dimensional space, with the coordinates given by the flux in each pixel. The ensemble of model spectra then corresponds to a cloud of points in this
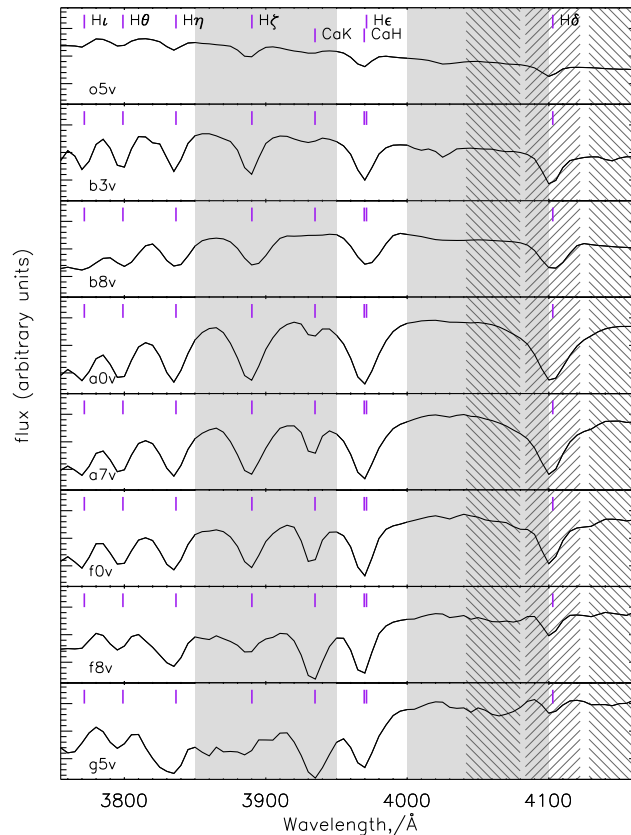

Figure 4.1: Spectra of main sequence stars in the region of the 4000Å break. The stars are ordered according to temperature, with the hottest (O stars) at the top. Grey areas indicate the regions from which $\mathrm{D}_n(4000)$ is measured (Balogh et al. 1999); the hashed regions those to measure Hδ (Worthey & Ottaviani 1997). From Wild et al. (2007).
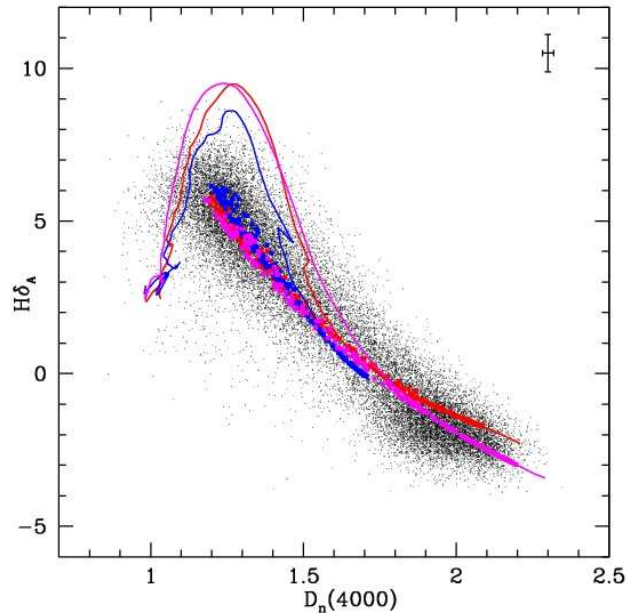
Figure 4.2: Hδ vs. $D_n(4000)$ for different star formation histories. The blue, red, and magenta lines follow three model starbursts of 20% solar, solar, and 2.5 times solar metallicity. The symbols are for models of continuous star formation, with varying formation times and varying exponential star-formation time-scales (the color-coding again indicates the metallicity). The black dots are a subset of SDSS galaxies. From Kauffmann et al. (2003a).

the ensemble of model spectra within this wavelength range. This identifies the Principal Components of this model population. They find that the first Principal Component (PC1) measures the strength of the 4000Å break similarly to the more conventional $D_n(4000)$ index measurement (Fig. 4.3). The second Principal Component (PC2) measures the *excess* Balmer absorption compared to the expectation value for a given 4000Å break strength (the locus of galaxies with continuous star formation). I.e. the combination -PC1+PC2 corresponds to the measurement of Hδ (Fig. 4.3). The great advantage of this new index is that it can be applied to spectra with considerable lower SNR than required for measuring Hδ.

Fig. 4.4 shows the model tracks of starbursts of different strengths in the diagrams of PC2 vs. PC1 and Hδ vs. $D_n(4000)$. Both diagnostic diagrams suffer from an age–burst strength degeneracy: although the regions in the diagrams populated by post-starbursts can be identified, more recent weak starbursts cannot be distinguished from older, stronger ones. With the PCA method, post-starburst galaxies can be identified quite easily by the value of the second Principal Component: galaxies with PC2$\gtrsim$ 0 and PC1$\lesssim$ −1 are likely to have undergone a starburst. But PC2$\gtrsim$ 0 is not only a post-starburst signature: also stellar populations in which star formation is truncated, i.e. shut off on a very short timescale,

---

space. PCA identifies the directions of greatest variance in this point distribution - these vectors are the "eigenspectra" or "Principal Components" of the distribution. The Principal Components are constrained to be orthogonal; i.e. a spectrum can represented as a linear combination of Principal Components.
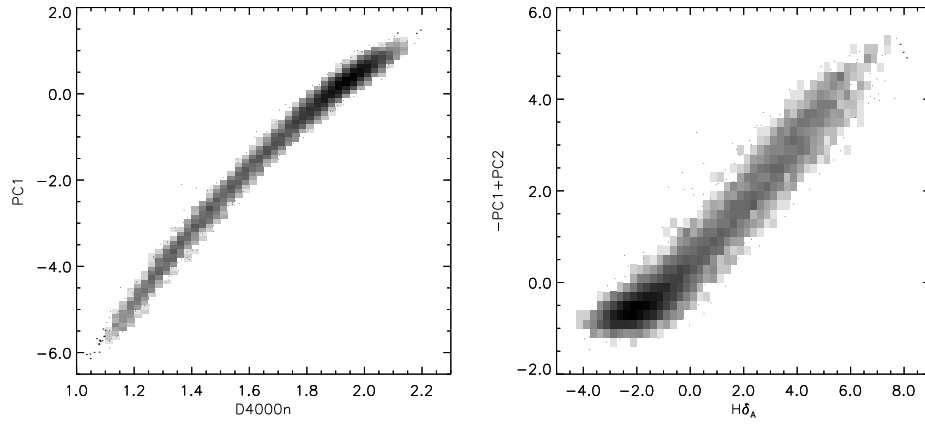
Figure 4.3: Correspondence of the spectral indices developed by Wild et al. (2007) to the more traditional indices, for a sample of bulge-dominated galaxies with high signal-to-noise SDSS spectra. From Wild et al. (2007).

move upward in the PC2-PC1 diagram (Fig. 4.5). If star formation subsides more gradually, then PC2 remains negative. This makes PC2 an interesting indicator for investigating the stellar populations of cluster galaxies, since it can test whether cluster galaxies are prone to experience starbursts (e.g. through mergers) or truncation (by ram-pressure stripping) more often than field galaxy.
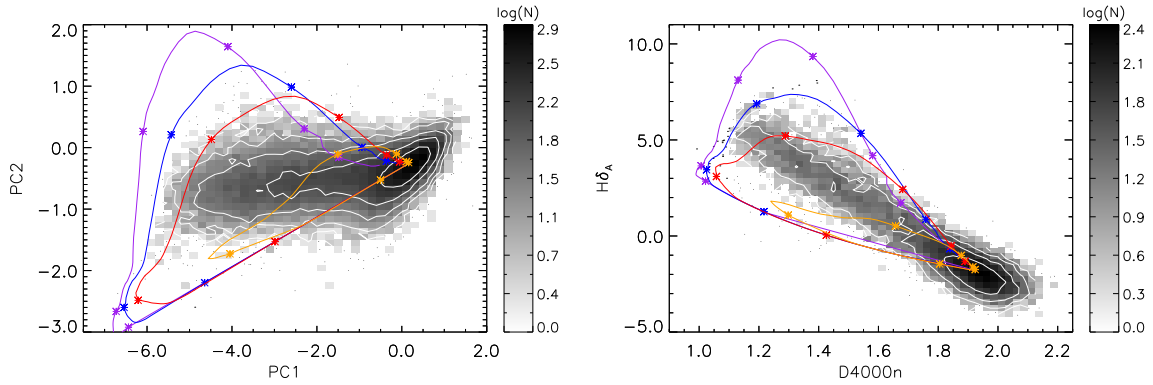
Figure 4.4: The tracks of four model starbursts in diagrams of PC2 vs. PC1 (left) and Hδ vs. $D_n(4000)$ (right). The model galaxies start out as quiescent (PC1∼ 0, $D_n(4000)$∼ -1.9), and experience a 0.03Gyr starburst where 0.5%(orange), 1% (red), 3% (blue), or 20% of the stellar mass is added in the burst. Stars indicate time intervals 0.001, 0.01, 0.1, 0.5, 1.0, and 1.5 Gyr after the start of the burst (the tracks run clockwise in both diagrams). The underlying grayscale represents the distribution of a sample of bulge-dominated galaxies in the SDSS. From Wild et al. (2007).
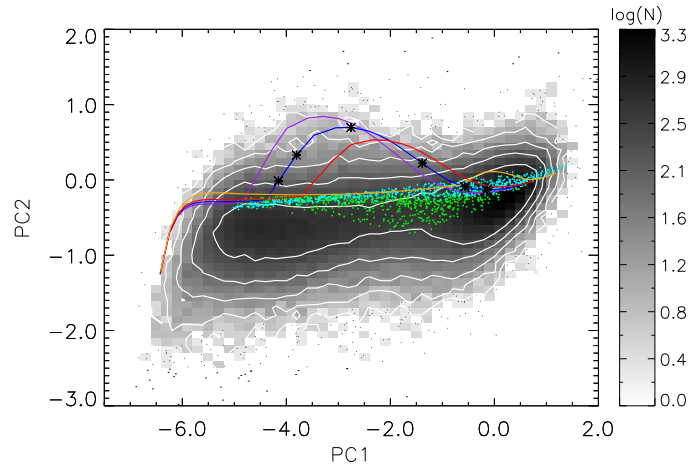

Figure 4.5: Model tracks of truncated and exponentially decreasing star formation histories. This lines follow stellar populations in which star formation is switched off after 10.5 Gyr. Prior to truncation, the star formation is constant (purple), or exponentially decreasing with timescales of 10, 5 and 2 Gyr (blue, red, orange lines). The time elapsed since truncation is indicated by the tick marks on the blue line (0.001,0.01,0.1,0.5,1.0,1.5 Gyr). The green and cyan points show stellar populations with exponentially decreasing star formation between 6 and 10 Gyr in age. Green points are for populations with subsolar metallicities, cyan points for solar metallicities.

4.3 Applying PCA to cluster galaxies

For the 524 clusters in our sample, we select the galaxies within $\pm 3\sigma_v$ and the larger of $20R_{200}$ and 20Mpc. This large radial range will allow us to probe radial dependences to distances (far) beyond the turn-around radius. If a galaxy could be associated with more than one cluster, we assign it to the "closest" cluster, according to the distance measure is $\Delta^2 = (d/R_{200})^2 + (\Delta_v/\sigma_v)^2$, where d is the radial distance from the BCG, and Δ_v the velocity offset. For this association of galaxies with clusters, not only the final 524 clusters are taken into account, but also those in the original C4 catalog. For those clusters that were removed in the BCG selection process (Sect. 2.3), we use the velocity dispersion as given in the original catalog. According to Miller et al. (2005), the C4 cluster catalog is about 90% complete. Hence, our sample of field galaxies should be quite clean from galaxies in undetected clusters. Within R_{200}, galaxy spectra from all data releases up to DR4 are considered, but beyond R_{200}, only until DR3, since the C4 catalog was compiled from DR3.

4.3.1 PC1 vs. stellar mass

Fig. 4.6 presents the distribution of these galaxies in the PC1 vs. stellar mass diagram (without any cuts on completeness or $V_{\max}$ weighting). The stellar masses have been determined from the cmodel magnitudes, via the `kcorrect_v4.1.4` algorithm. Both a red sequence (strong 4000Å break, PC1~ 0) and a blue sequence (PC1~ −4) are clearly visible. But unlike the counterpart of this diagram at higher redshifts (Fig. 5.3), the two sequences are not entirely parallel across the diagram. While the red sequence could be reasonably described
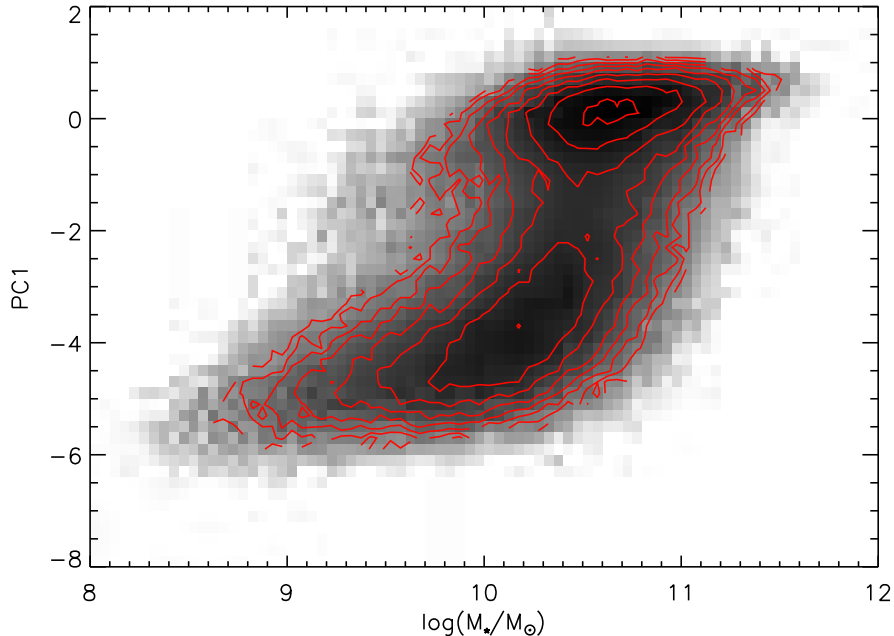

Figure 4.6: The distribution of PC1 vs. stellar mass for galaxies within 3σ and the larger of $20R_{200}$ and 20Mpc of our clusters. The distribution is shown both as grayscale, and as contours; both of these are scaled logarithmically with the galaxy number.

by a linear relation with higher PC1 values at larger stellar masses, the behavior of the blue sequence changes with mass. At low stellar masses, the blue sequence is approximately parallel to the red sequence. But at masses $\log(M_\star/M_\odot) \gtrsim 10.3$, the blue sequence curves upward towards the red sequence.

This diagram is reminiscent of the more traditional color-magnitude diagrams (CMDs), in that both color and PC1 are indicators of the recent star formation history, whereas luminosity and stellar mass measure the "size" of the system. Stellar mass is arguably a more fundamental galaxy property, as luminosity is highly dependent on the age of the stellar population: young stars are very luminous, hence galaxies with young stellar populations have low M/L ratios. Furthermore, the M/L ratio varies with the observed band: blue bands are particularly dominated by young stars, whereas red bands are sensitive also to older stellar populations. This means effectively that the red and blue sequences are shifted in CMDs of different bands. Stellar mass on the other hand, changes much less with the age of the stellar population, and is much less biased towards young, but low-mass systems.

Baldry et al. (2004) fitted bimodal Gaussians to the red and blue sequences in a color-magnitude diagram of a large sample of SDSS galaxies in bins of luminosity. We follow the same approach here and fit the distribution in PC1 in bins of stellar mass, shown in Fig. 4.8. Clearly, the distributions are not well described by two Gaussians - there is an excess of galaxies between the red and blue peaks. In CMDs, the region between the red and blue
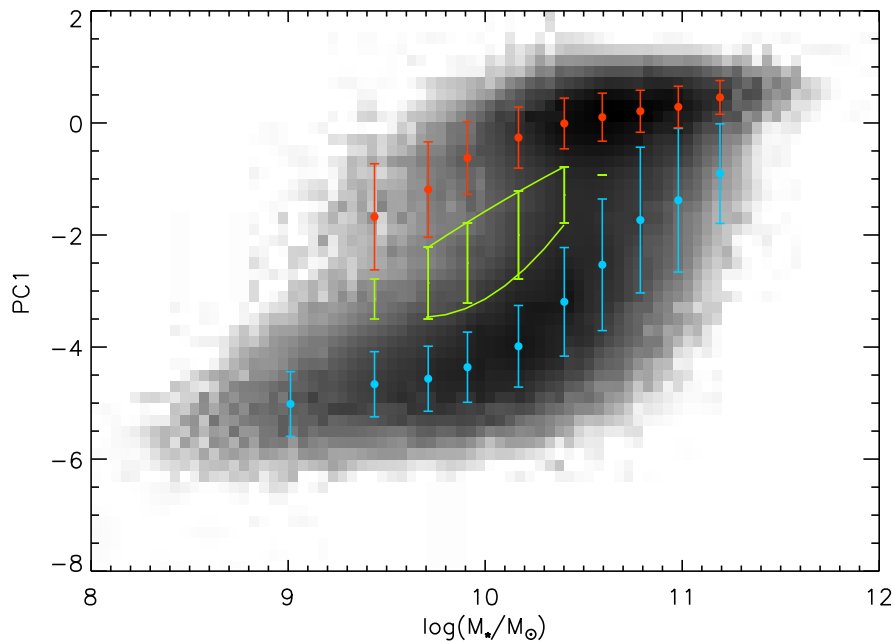

Figure 4.7: The location of the red and blue sequence in bins of stellar mass. For each mass bin, the red (blue) circle gives the peak of the Gaussian curve fitted to the distribution of the red (blue) sequence, and is shown at the median mass of the particular mass range. The error bars indicated the respective 1σ width. The green intervals for each mass bin indicate the region where the sum of the two Gaussians does not account for more than 50% of the galaxies. The green lines are 2nd-order polynomial fits to the boundaries of these intervals. The underlying grayscale is identical to the one shown in Fig. 4.6.
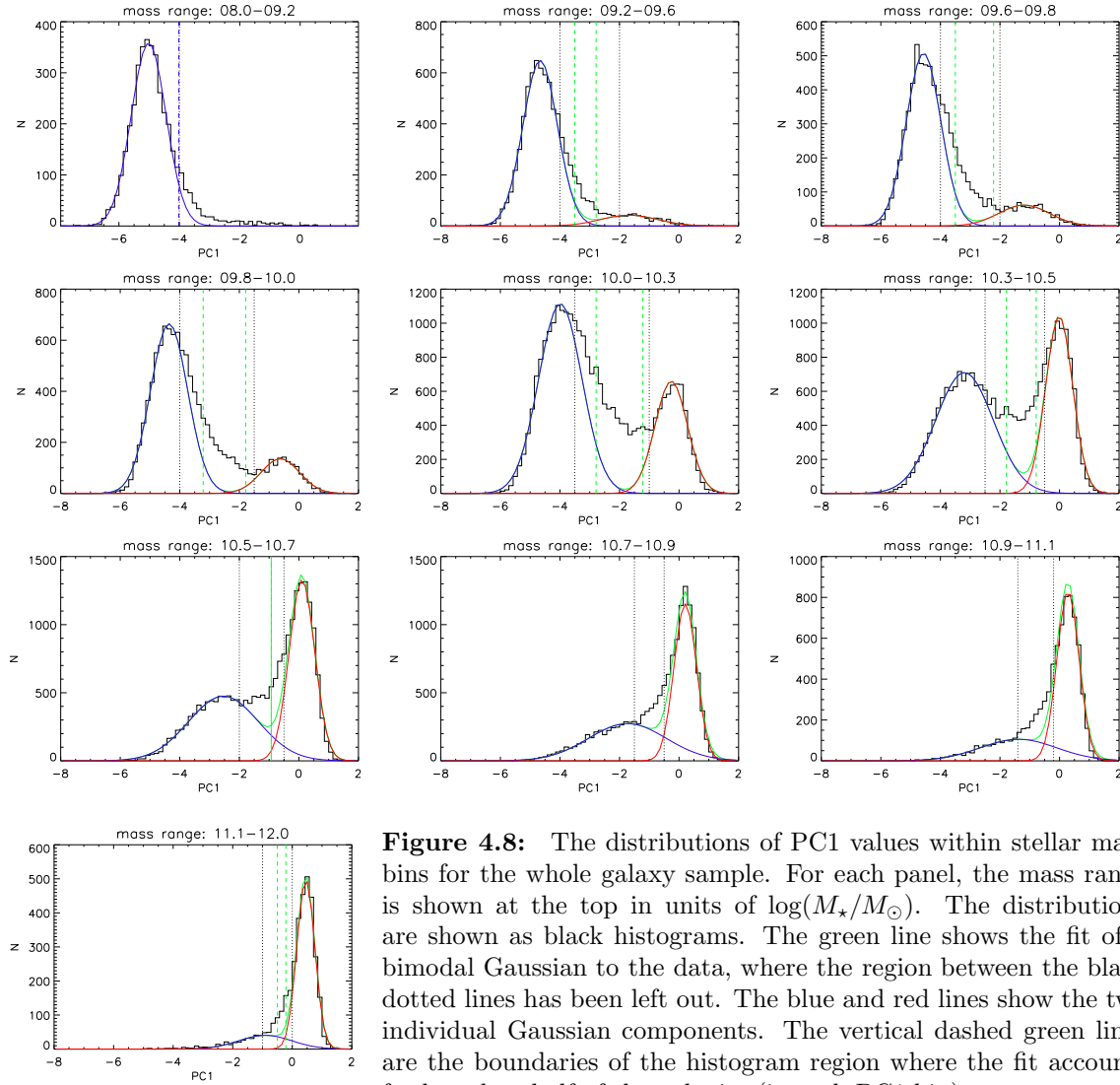
Figure 4.8: The distributions of PC1 values within stellar mass bins for the whole galaxy sample. For each panel, the mass range is shown at the top in units of $\log(M_\star/M_\odot)$. The distributions are shown as black histograms. The green line shows the fit of a bimodal Gaussian to the data, where the region between the black dotted lines has been left out. The blue and red lines show the two individual Gaussian components. The vertical dashed green lines are the boundaries of the histogram region where the fit accounts for less than half of the galaxies (in each PC1 bin).

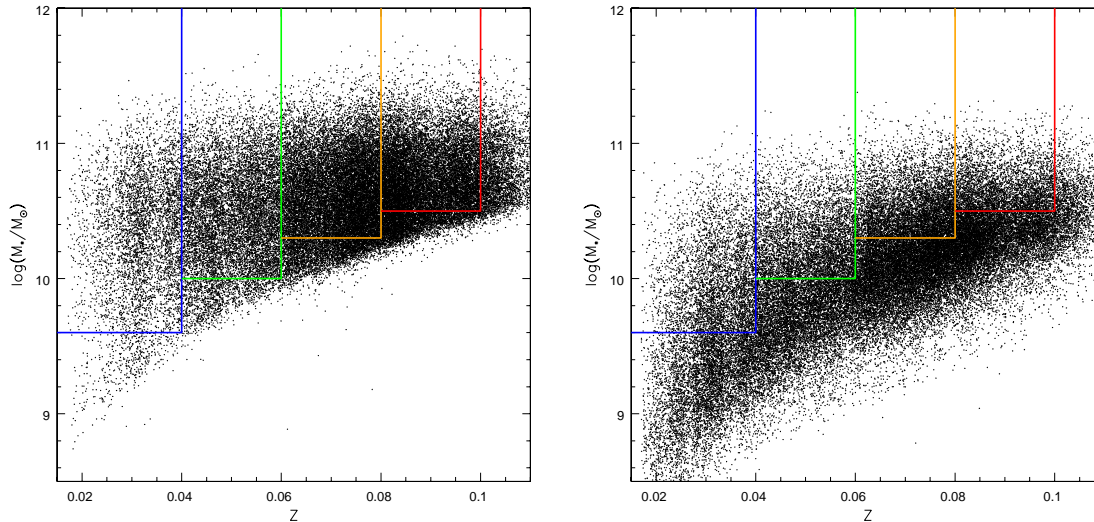**Figure 4.9:** The stellar masses of galaxies on the PC1 red/blue sequence (left/right panel) against their redshift. The four boxes describe the four redshift subsamples described in the text, each of which is complete in stellar mass to the lower limit indicated by the lower boundary of each box.

sequences has been coined the *green valley*, and we adopt this term here, as well. We fit two Gaussian curves to the distribution, but ignoring the green valley region for the fit. The fits provide adequate descriptions for the blue edge of the blue sequence and the red edge of the red sequence. In each mass bin, we identify the green valley the range in PC1 values where the sum of the two Gaussians accounts for less than half of the galaxies (in each histogram bin). Fig. 4.7 shows the peaks and 1σ widths of the red and blue sequences, and the location of the green valley. We fit the blue and red limits of the green valley as functions of stellar mass with second-order polynomials to gain an analytic form for the distinction between the three regions in the PC1 distribution as functions of mass.

4.3.2 Mass completeness

The lack of galaxies on the red sequence with masses $\log(M_\star/M_\odot) \lesssim 10$ is a clear sign of incompleteness in the sample. In Fig. 4.9 we plot the stellar masses of galaxies on the red sequence as a function of redshift. For the whole sample, the sample is complete in red galaxies only for $\log(M_\star/M_\odot) > 10.5$. But by defining subsamples of clusters (and their galaxies) in redshift bins, the completeness limit can be pushed to lower mass values. We define four such samples: the lowest redshift one ($z < 0.04$) is complete in red galaxies with stellar masses as low as $\log(M_\star/M_\odot) > 9.6$, but it contains only 39 clusters. The sample with $0.04 < z < 0.06$ (107 clusters) includes red galaxies with $\log(M_\star/M_\odot) > 10.0$. The sample in the range $0.06 < z < 0.08$ (200 clusters) is the one best matched to the lower mass limit ($\log(M_\star/M_\odot) > 10.3$) of the high-redshift EDisCS clusters. The highest redshift sample $0.08 < z < 0.10$ (175 clusters) is complete only for ($\log(M_\star/M_\odot) > 10.5$).
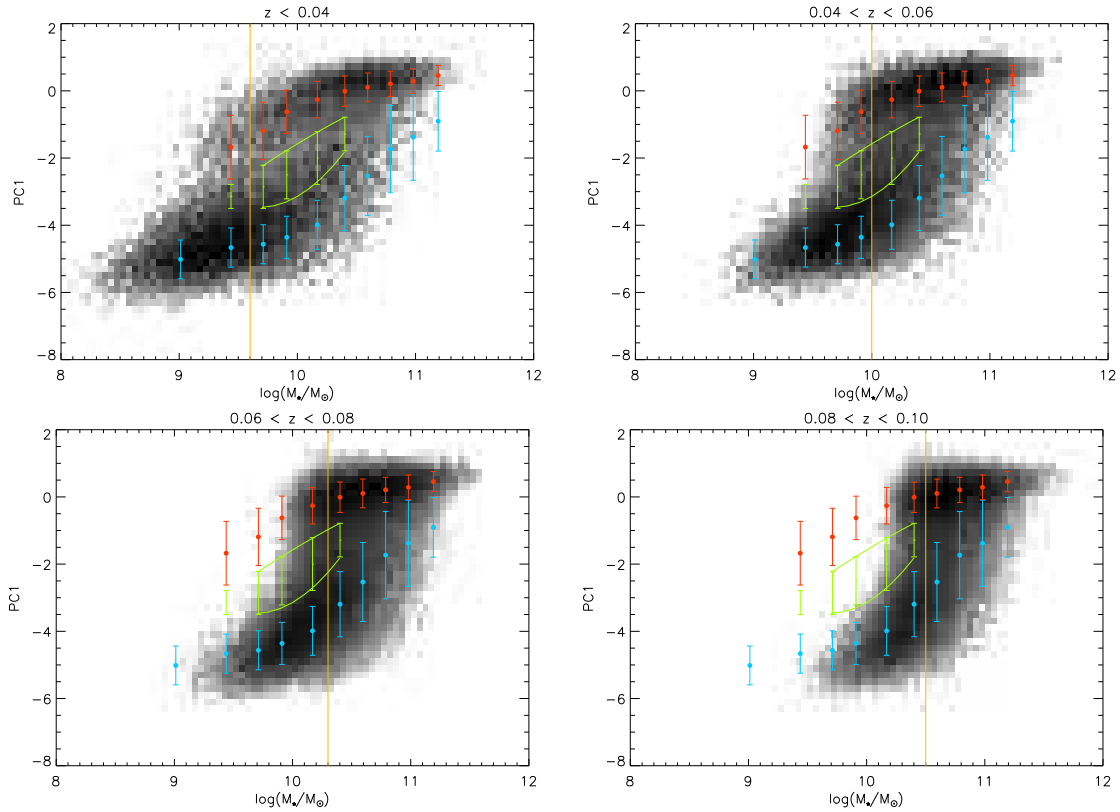
Figure 4.10: The red and blue sequences derived for the whole galaxy sample, (i.e. the same symbols as shown in Fig. 4.7) superposed on the distributions of galaxies in the four cluster subsamples (shown as grayscale). The vertical orange line indicates the mass limit for red galaxies in each sample. The previously derived description for the blue sequence is clearly not adequate for the individual subsamples.

4.3.3 Aperture bias

However, the characterization of the PC1-mass diagram we have derived for the whole galaxy sample is not a good description of the samples in the more narrow redshift bins. This is shown in Fig. 4.10: particularly for the lowest-redshift sample, the blue sequence lies at larger PC1 values than the locus of the blue sequence we have derived for the whole sample. Larger PC1 values indicate older, redder stellar populations.

This apparent discrepancy / redshift trend is a consequence of the aperture bias of the SDSS spectroscopic survey: the spectra are obtained via fibers of $3''$ diameter. This is an issue particularly in the lowest redshift sample, where $3''$ corresponds to $\sim 2-3\mathrm{kpc}$, and thus only the inner regions of large (resp. massive) galaxies. Many massive disk galaxies also have a bulge component, with a stellar populations older than the one in the disk. If only the inner part of the galaxy is observed, then the light of the bulge with its old stellar population is dominant.

Due to the aperture bias, the location of the blue sequence changes in different redshift bins. The "green valley", i.e. the excess of galaxies between the red and blue sequences is partially due to this, see Fig. 4.10. However, the aperture bias is likely to be also at least

partially the reason that the blue sequence in the SDSS sample does not run approximately parallel to the red sequence (as in the EDisCS sample), but turns "upward": generally, the bulge-to-total fraction increases with stellar mass for disk galaxies. Thus, the more massive the galaxy, the more prominent the bulge, and the redder the population.

It is therefore necessary to characterize the PC1 vs. stellar mass diagram for each redshift sample. Although this cannot "cure" the aperture bias, it accounts for the systematic shift of the blue and red sequences with redshift.

Fig. 4.11 shows the PC1 distributions in each mass subset of the $0.06 < z \leq 0.08$ cluster sample. Again, the sum of the two Gaussians that describe the red and blue sequences does not account for all the galaxies in the intermediate region - the green valley. When fitting the bimodal Gaussian curve, we again exclude the green valley region.

Fig. 4.12 shows the resulting location and width of the red and blue sequences for each redshift sample. The ridgeline of the red sequence can we well described by two linear relations (the highest redshift bin does not probe low enough masses, hence only one line is fit), whereas the blue ridge is better described by a parabola. With these fits, we have continuous descriptions of the red and blue sequences with mass: $PC1_{RS}(\log M_\star/M_\odot)$ refers to the ridgeline of the red sequence, $PC1_{BS}(\log M_\star/M_\odot)$ to that of the blue sequence.

4.3.4 Galaxy classification

The widths of both the red and blue sequences changes with mass, most notably for the blue sequence. This makes it unsatisfactory to define the extent of each sequence in terms of the widths; e.g. in the higher mass subsets, the green valley region is within $1 - 2\sigma$ of the peak of the blue sequence, simply because the blue sequence is very broad. Instead, we use a fixed offset from each ridge to separate the three regions of the distribution. For simplicity, we take this offset to be one unit in PC1. This corresponds to $\sim 2\sigma$ of the red sequence at masses $\sim 10^{10.2} M_\odot$, and $\sim 3\sigma$ for masses $\sim 10^{10.7} M_\odot$. For the blue galaxies, this value is closer to 1σ, but $\sim 2\sigma$ for masses $\lesssim 10^{10} M_\odot$. Each galaxy is classified via the following scheme (also illustrated in Fig. 4.11):

1. If $PC1 > PC1_{RS} - 1$, the galaxy is classified as "red".

2. If $PC1_{BS} + 1 < PC1 < PC1_{RS} - 1$, the galaxy is classified as "green".

3. If $PC1_{BS} < PC1 < PC1_{RS} + 1$, the galaxy is classified as "cyan".

4. If $PC1 < PC1_{BS}$, the galaxy is classified as "blue".

While "green" may actually signify an intermediate class of galaxies between the red and blue sequence, the term "cyan" has been introduced only to ease terminology, and "cyan" should be considered a subclass of blue galaxies in the more general sense. "Blue" galaxies generally have higher levels of star formation than "cyan" galaxies.

It is important to make the classification in this order: the red sequence is well defined in all mass bins (above the mass limit), but according to this definition, not every mass bin has a green valley. Extreme cases of this are the highest mass bins, where it is not possible to fit a peak to the blue sequence.
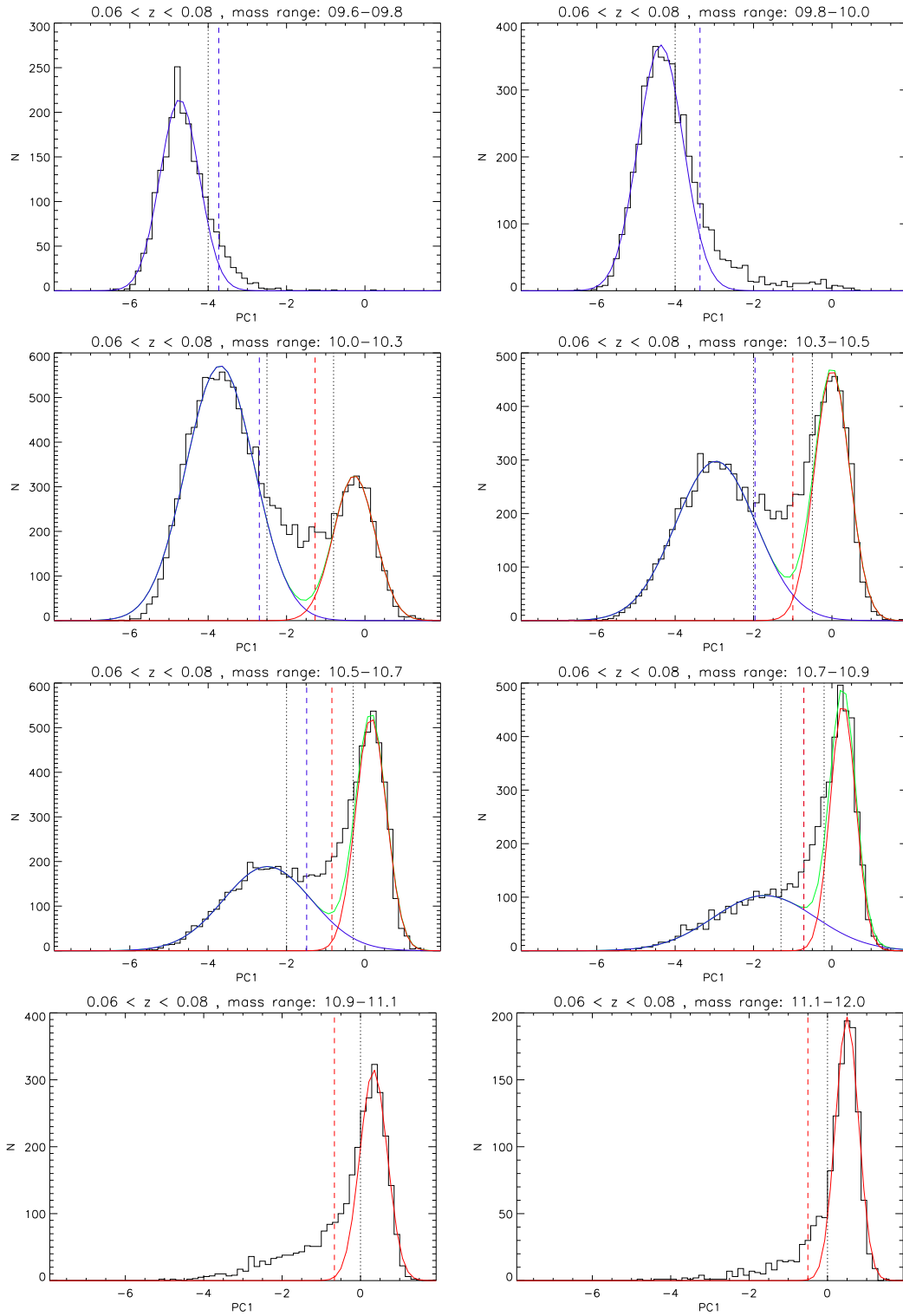
Figure 4.11: The distribution in PC1 for galaxies in the $0.06 < z \leq 0.08$ cluster sample. The line coding is the same as in Fig. 4.9. The red dashed lines indicate the lower limit of the red sequence; the blue dashed lines the upper limit of the blue sequence (but is shown only if it does not fall within the red sequence). Note that the mass ranges shown in the top two panels are below the mass completeness limit of red galaxies.
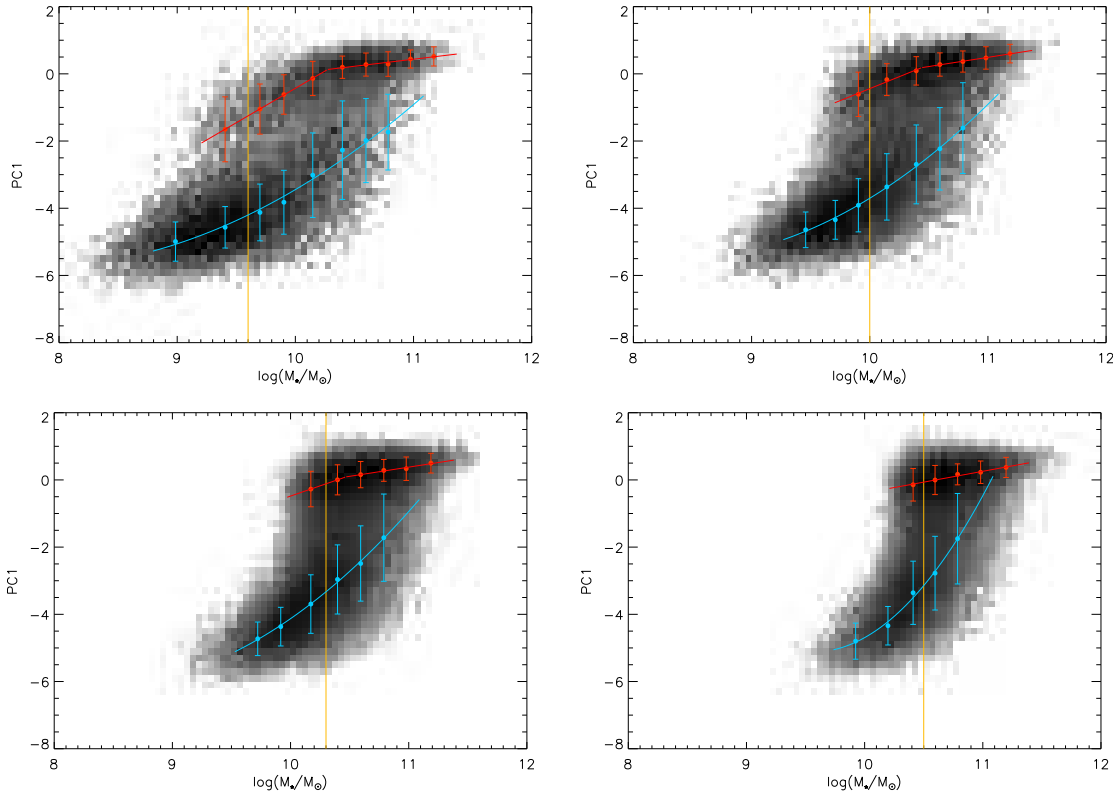
Figure 4.12: The equivalent of Fig. 4.10, shown for the distributions in the four redshift subsamples.

4.4 Radial profiles

4.4.1 Star formation–radius relation

In Fig. 4.4.1 we investigate how each population (red, green, cyan, and blue) contributes to the number of galaxies within bins of mass and of clustercentric distance. For each mass range, we use the maximal number of clusters for which this mass range is complete, i.e. for the lowest mass range, $9.6 < \log(M_\star/M_\odot) < 10$, only the lowest-redshift subsample with $z \leq 0.04$ is used, for the mass range $10 < \log(M_\star/M_\odot) < 10.3$ clusters with $z \leq 0.06$ are used (cf. Fig. 4.9). For each mass range, we find a strong color–radius relation: within about $1R_{200}$, clusters are dominated by red galaxies. In the center, they make up more than 80% of the galaxy population, regardless of mass. The color-radius relation is particularly pronounced for low masses: in the lowest mass range, only about 20% of the field galaxies are red galaxies. This fraction is approximately constant till the virial radius, where it changes abruptly with a steep increase in the red fraction towards the cluster center. With increasing stellar mass, the red fraction in the field galaxies also increases, but also here, the strongest change is between $\sim 0.3R_{200}$ and $\sim 2R_{200}$. This is in fact the same radial range over which Balogh et al. (1997) found a decline in the star formation rate of cluster galaxies. For our sample, it has to kept in mind that the mass dependence could be partially due to aperture effects: with increasing mass and size, the SDSS fiber probes only the galaxy center. The
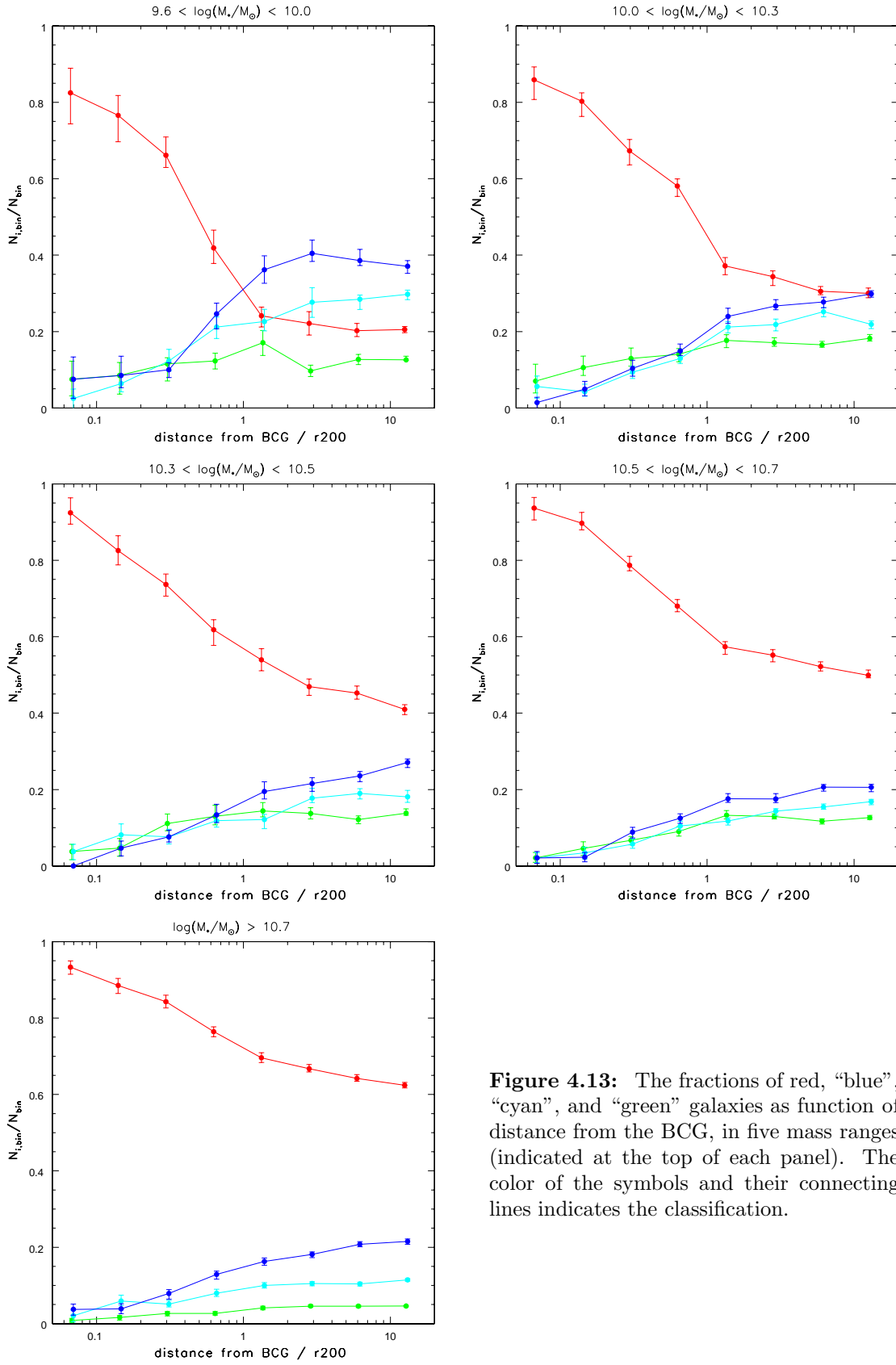
Figure 4.13: The fractions of red, "blue", "cyan", and "green" galaxies as function of distance from the BCG, in five mass ranges (indicated at the top of each panel). The color of the symbols and their connecting lines indicates the classification.

star formation–radius relation may be stronger in the outer galaxy regions also for massive galaxies.

The galaxies not on the red sequence have been divided into three classes (see also Sect. 4.3.4): galaxies bluer than the peak of the blue sequence (which we will refer to as *blue*), galaxies redwards of the peak of the blue sequence but bluer than the green valley (*cyan*), and galaxies in the green valley (*green*).

By construction, the majority of field galaxies which are not red, are "blue". Interestingly, within the cluster, the fractions of these three galaxy types are quite similar. Clearly, the "blue" galaxies are most strongly affected by the cluster environment. This is most obvious in the lowest two mass ranges, with a pronounced decrease of the "blue" fraction around the virial radius. The fraction of "cyan" galaxies decreases more gradually. The fraction of "green" galaxies, however, is almost constant across all radii. Only in the very cluster center ($\lesssim 0.2R_{200}$) is it significantly lower than in the field.

These trends suggest that star formation is affected by a physical process effective already at $2 - 3R_{200}$. As star formation shuts off, "blue" and "cyan" galaxies redden and move onto the red sequence. This transition apparently does not occur instantaneously, rather, these galaxies are seen as "green valley" objects for a time span somewhat shorter than a cluster crossing time. Hence the fraction of green galaxies decreases slower than the number of blue galaxies, as it is replenished by the latter ones as they redden. This could also be the cause for the slight the increase of low-mass green galaxies at $\sim 1R_{200}$. Similarly, "blue" galaxies will be first seen as "cyan", hence the fraction of the latter declines more slowly.

4.4.2 Fraction of post-starburst galaxies

We have argued that the color distribution of cluster galaxies suggests that star formation is not shut off instantaneously. This hypothesis can be tested via the occurrence of post-starburst galaxies (Sect. 4.2). If a galaxy experiences a brief starburst, or if a significant level of star formation is truncated on short timescales ($< 10^6$yr), the galaxy spectrum displays strong Balmer absorption lines for $\sim 0.5 - 1$Gyr. From the PCA, the strength of the Balmer lines is measured by the second Principal Component, PC2. We identify post-starburst galaxies as blue, cyan, or green galaxies with PC2> 0 (Fig. 4.4 and Fig. 4.5).

PC2 is more sensitive to noise in the spectra than PC1. Hence, this analysis is carried out only for galaxies with SNR$\geq$8 spectra. This actually applies to the majority of galaxies (86% - 98% in the five different mass bins).

Fig. 4.14 shows the fraction of blue, cyan, and green galaxies classified as post-starburst, as a function of distance from the cluster center, and in the five mass ranges. The number of post-starbursts is very low, and approximately constant with clustercentric distance. This supports the hypothesis that star formation is quenched on timescales longer than that necessary to induce a post-starburst signature.

Since this fraction is measured relative to the number of non-quiescent galaxies, the absolute fraction of post-starburst galaxies decreases towards the cluster center. This is consistent with the results of Zabludoff et al. (1996), who found that "E+A" galaxies are predominantly field galaxies. In our terminology, this is simply a reflection of the higher field abundances of blue, cyan, and green galaxies.

The lack of a trend of the occurrence of post-starburst galaxies with cluster environment shows that the physical process(es) which cause a post-starburst signature in the spectrum
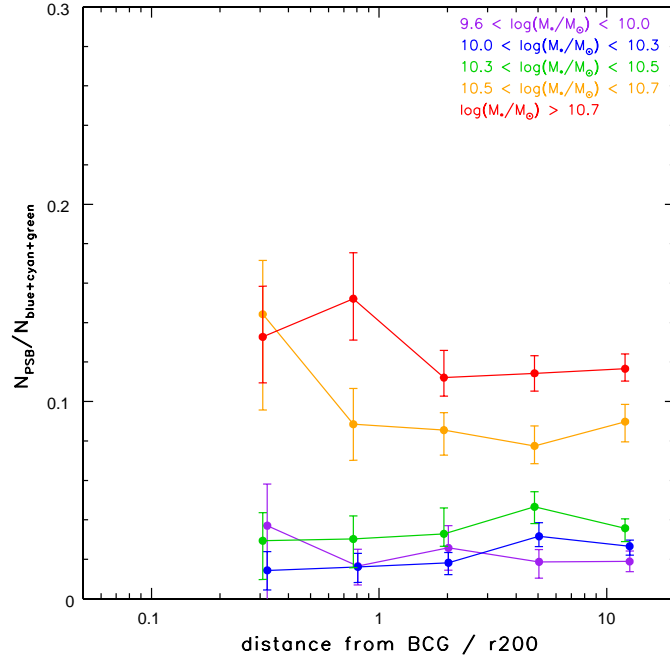
Figure 4.14: The fraction of "blue", "cyan", and "green" galaxies with post-starburst spectra in each of the five mass ranges, as function of clustercentric distance. This *relative* post-starburst fraction is approximately constant, but since the number of blue/cyan/green galaxies decreases towards the cluster center (Fig. 4.4.1), the *absolute* post-starburst fraction also decreases.

operate no differently in the cluster environment as at low-density environments. Since a (moderate) post-starburst signature results not only from a recent star-burst, but also if star formation is truncated very quickly, this indicates that the process(es) which quench star formation in galaxy clusters operate on longer timescales.

Fig. 4.14 indicates that the post-starburst signature is more common in galaxies with stellar masses $\log(M_\star/M_\odot) \gtrsim 10.5$. This mass also marks the threshold of the galaxy bimodality as investigated by Kauffmann et al. (2003b): more massive galaxies are predominantly quiescent galaxies with old stellar populations. The galaxies which contribute to Fig. 4.14 are the exceptions to this trend: their PC1 value suggests younger stellar ages. Presumably, there are at least two mechanisms responsible to generate a post-starburst signature: truncation of (strong) star formation, and/or a starburst. Galaxies with post-starburst spectra may therefore either be transitioning from the blue to the red sequence, or they may be quiescent galaxies in which a starburst has been ignited. The argumentation presented above applies mainly to the scenario where a post-starburst spectrum is indicative of the truncation of star formation. But above the mass threshold, galaxies with continuous star formation are increasingly rare (since most galaxies are quiescent). In the most extreme case, *all* post-starburst galaxies could be quiescent galaxies with a central starburst. We would then have to consider the ratio of post-starburst galaxies to red galaxies. Due to the constant post-starburst fraction in blue, cyan, and green galaxies, and the increase of the red fraction, this
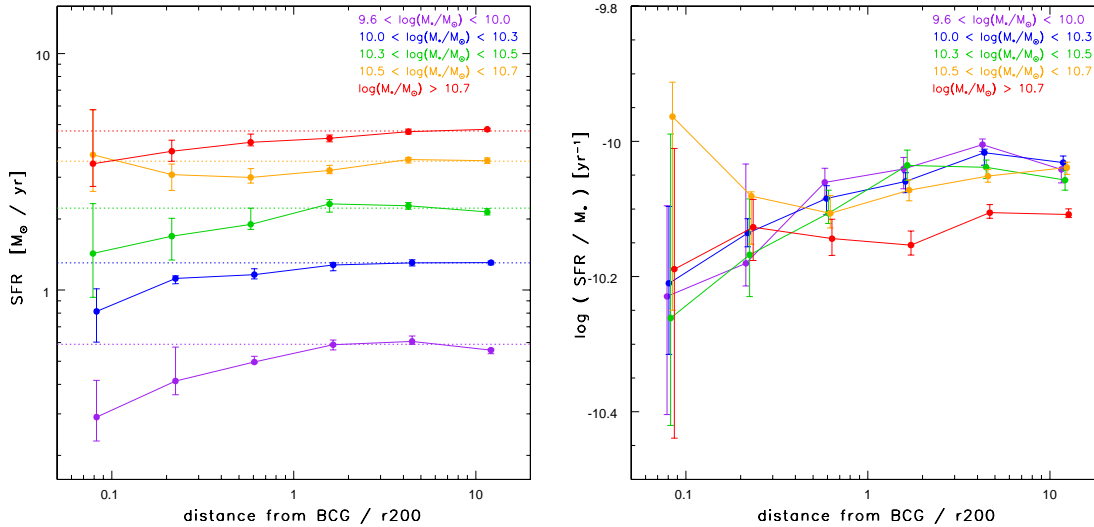
Figure 4.15: The median star formation rate (left panel) and median specific star formation rate (right panel) of the "blue", "cyan", and "green" galaxies. The dotted lines in the left panel show the median value for galaxies beyond the virial radius.

ratio obviously declines steeply towards the cluster center. With this interpretation, we can tentatively conclude that the triggering of central star-bursts in quiescent galaxies decreases in the cluster. However, it is then a curious coincidence that the number of post-starbursts relative to the number of non-quiescent galaxies is independent of environment. If anything, then this might imply a tight relation in the processes which cause central star-bursts, and those which cause galaxies to transition from the blue to the red sequence.

4.4.3 Star formation rate

Averaging over the whole galaxy population, the star formation rate clearly declines towards the cluster center, as the fraction of "red" galaxies, which have little or no star formation rises steeply towards the center (Fig. 4.4.1). But in the "red" galaxies, star formation has already shut off, and we cannot tell the timescale (or the process) by which this happened. Thus, here we investigate the typical star formation rate of those galaxies with young stellar population - the "blue", "cyan", and "green" galaxies.

We use the star formation rate measurements of Brinchmann et al. (2004), which are mostly based on model fits to the spectra. For low signal-to-noise spectra, the star formation rate is estimated from the Hα luminosity (corrected for dust attenuation). For spectra with an AGN component, the star formation rate has been estimated from D(4000). These star formation rates have been corrected for aperture effects by also using the galaxy colors outside the fiber (see Brinchmann et al. 2004, for a detailed discussion).

Fig. 4.15 shows the median star formation rate and the specific star formation rates (i.e. the star formation rate scaled by the galaxy stellar mass) of the "blue", "cyan", and "green" galaxies as function of cluster distance, again in five mass bins. The star formation rate clearly decreases towards the cluster, though not very strongly (about a factor of 2). This is consistent with the scenario we proposed earlier: as galaxies fall into the cluster, their star

formation declines. The subsequent aging of the average stellar population causes the PC1 value of the galaxies to increase - they transition from "blue" via "cyan" and "green" to "red".

The gradual decline of the typical star formation rate over most of the radial range form the cluster outskirts to the cluster center suggests that the quenching of star formation takes places on timescales similar to the cluster crossing time, i.e. a few Gyr. Indeed, Balogh et al. (2000) modeled the star formation gradients in clusters, assuming that star formation declines on Gyr timescales, and predict a decline by a factor of about 3, which is similar to what we observe.

Our results differ somewhat from those of Balogh et al. (2004a), who investigated the star formation as function of galaxy density rate in SDSS and 2dFGRS galaxies. While they also find that the fraction of actively star-forming galaxies is a function of density, they do not find a significant difference in the distribution of Hα equivalent widths (which they take as measure of star formation) of star-forming galaxies in different environments. Possible causes for this difference are that their density estimator, the distance to the fifth nearest neighbor, is a more noisy density measurement than clustercentric radius in our composite cluster, or that the dust content (which Balogh et al. do not correct for) changes with density, as well.

4.4.4 Fraction of Active Galactic Nuclei

A different viewing angle to the galaxy population mix is the occurrence of Active Galactic Nuclei (AGN). The details of the link between AGN activity and the properties of the host galaxy, particularly its star formation history, are still a matter of debate. But the mere existence of the linear correlation between the mass of the central black hole and the mass of the bulge (e.g. Magorrian et al. 1998) is a strong indication that the formation of the two must be closely linked (e.g. Cattaneo et al. 1999; Heckman et al. 2004). A possible mechanism for this is the scenario where bulges are formed by major mergers of galaxies. Simulations of major mergers of disk galaxies show that the merger remnants have spheroidal characteristics, and also that they efficiently transport gas to the center of the remnant (Barnes & Hernquist 1991). Gas flux to the galaxy center is the prerequisite for an active galactic nucleus, which is assumed to signal mass accretion onto a central black hole. By assuming that a fraction of the gas is accreted by the central black hole, Kauffmann & Haehnelt (2000) were able to show that the black hole – bulge relation follows naturally from hierarchical structure formation. If this merger scenario is the predominant mechanism to fuel the black hole, then the AGN population is a tracer of the merger rate.

However, the space density of AGN is much higher than that of major mergers. Furthermore, only a subset of AGN hosts show disturbed morphologies indicative of a merger event (Kauffmann et al. 2003c). Therefore, less spectacular processes must be able to trigger an AGN, as well. Galaxies with on-going star formation have a reservoir of cold gas, and if a fraction of this gas is available for accretion onto the black hole, then there must be a link between star formation and AGN activity, as well. But this scenario requires a process to transport gas into the galaxy center, so the link might not be direct. Possible mechanisms are kinematic instabilities of the disk, such as bars (Shlosman et al. 1990), and minor mergers. The AGN – star formation connection is supported by mounting observational evidence that (post-)starbursts are frequently accompanied by an AGN (e.g. Kauffmann et al. 2003c; Wild et al. 2007). Also, powerful optical AGN are found predominantly in galaxies with

massive, but young, bulges (Kauffmann et al. 2003c).

Apart from the cold gas in the disk, galaxies also have a halo of hot gas, which could serve as fuel for the AGN. In massive dark matter halos, the gas density in the center is high enough that the gas can cool and sink to the center. The cooling rate scales with the mass of the halo, and as we have shown in von der Linden et al. (2007) and Best et al. (2007), central cluster galaxies are indeed more likely to host a radio-loud AGN (see Sect. 2.5).

Most likely, AGN can be triggered by more than just one of these proposed mechanisms. The environmental dependence of AGN occurrence may then provide clues on the relative importance of each AGN channel: e.g. mergers are less frequent in rich clusters due to the high relative velocities. Likewise, cluster galaxies have less ongoing star formation. On the other hand, tidal forces from close encounters with other cluster galaxies (i.e. galaxy harassment) may cause kinematic instabilities which could funnel gas to the center. Finally, the cluster provides a large reservoir of hot gas which could cool onto the galaxy core.

Previous results on the environmental dependence of AGN occurrence find various trends. E.g. in Best et al. (2007) we found that while galaxies in the very core of the clusters show enhanced radio-AGN activity, optical AGN activity is suppressed within $\sim 0.3R_{200}$. Best et al. (2005b) have argued that radio-loud and optical AGN may be two independent phenomena, and suggest that radio-loud AGN are fueled by hot gas cooling from the halo, and optical AGN by cold disk gas. This scenario would naturally explain the observed trend: as star formation is suppressed in the cluster environment, also the incidence of optical AGN decreases. Galaxies within the cooling radius, on the other hand, are subject to an increased amount of cooling hot gas from the intracluster medium.

Other works generally support the scenario that optical AGN are suppressed in dense environments, although this may be dependent on the AGN luminosity: (Kauffmann et al. 2004) find a stronger dependence on local galaxy density for powerful optical AGN than for weaker ones. For X-ray selected AGN, there is no evidence for a suppression within the cluster (Martini et al. 2007).

Here, we investigate the fraction of galaxies with an optical AGN. The AGN classification is taken from Brinchmann et al. (2004), based on the optical line ratios. We consider both pure AGN and composite populations, i.e. with both AGN and star formation lines. Fig. 4.4.4 shows the fraction of optical AGN as function of clustercentric distance, both as total number, and split according to the classification of the host galaxies.

In all but the lowest mass bin, the total fraction of AGN decreases towards the center. This is mainly driven by a decline of the AGN fraction in "red" galaxies, which are the dominant cluster population, and the dominant massive galaxies population. In the blue, cyan, and green galaxies, the AGN fraction is consistent with being constant with radius. Nevertheless, as the number of these galaxies declines towards the center, the overall AGN number also declines.

These trends could be interpreted in the following way: in star-forming galaxies, AGN activity is linked primarily to the star formation activity, and a set fraction of star-forming galaxies hosts an optical AGN. In the "red" galaxies, on the other hand, star formation has ceased and it takes other processes to fuel the AGN. One possibility would be merger events - these are indeed rarer in the cluster environment, which could explain the decline of the AGN fraction. However, it is unlikely that mergers account for the majority of AGN even in "red" field galaxies: a large population of weak emission line AGN resides in old, massive galaxies, without signs of merger activity (Kauffmann et al. 2003c; Kewley et al. 2006). Recently,
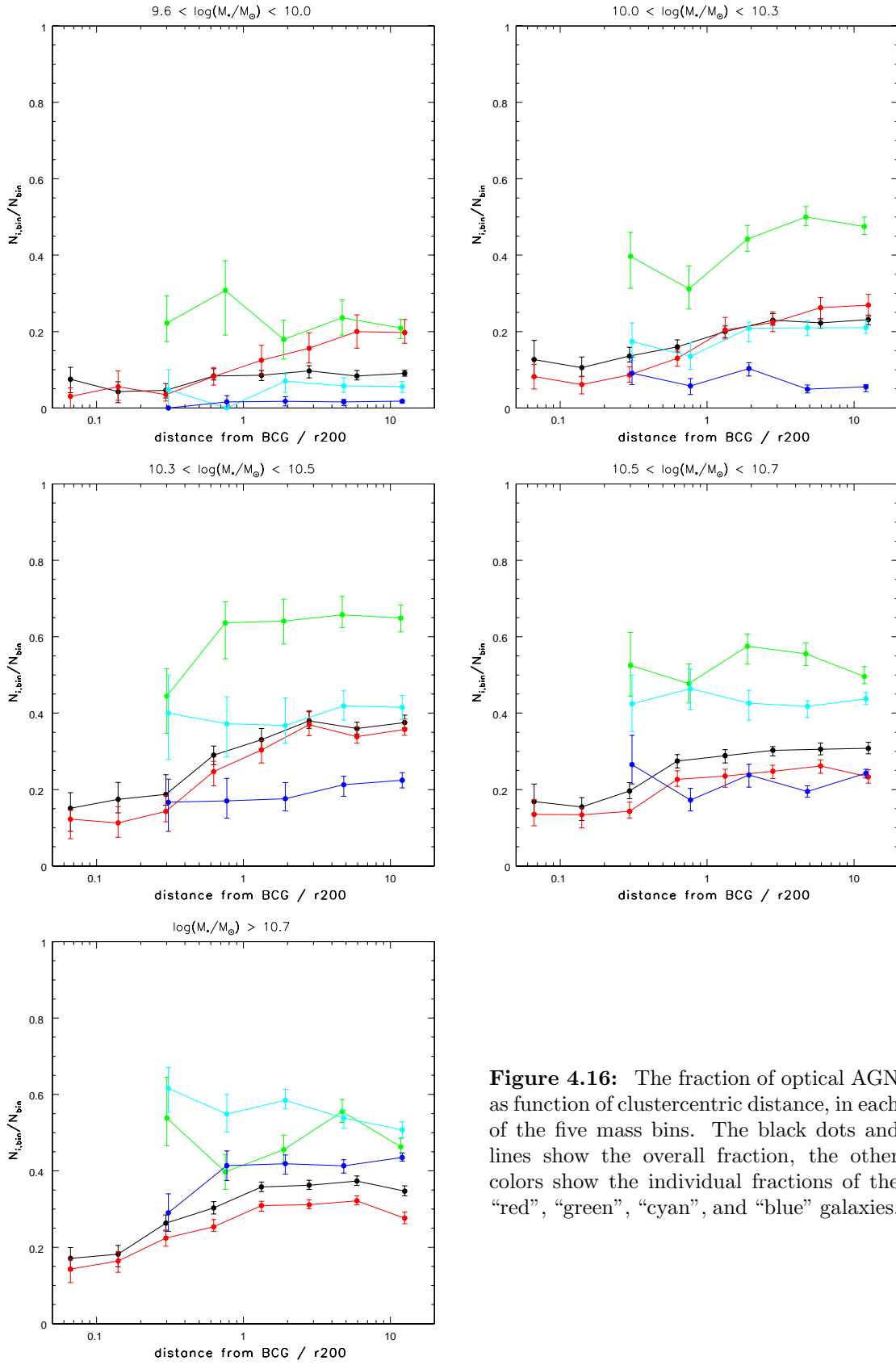
Figure 4.16: The fraction of optical AGN as function of clustercentric distance, in each of the five mass bins. The black dots and lines show the overall fraction, the other colors show the individual fractions of the "red", "green", "cyan", and "blue" galaxies.

Kauffmann et al. (2006) showed that a substantial fraction of massive, early-type galaxies have residual small levels of star formation in an outer disk, traceable only via ultraviolet radiation. Interestingly, most of these galaxies host an AGN, suggesting that also in these galaxies, there is a link between star formation and AGN activity. These star-forming outer disks likely trace a (low-mass) reservoir of cold gas, which is available to fuel star formation and AGN activity. We have shown that star formation in star-forming galaxies is suppressed upon infall into the cluster environment. This is likely to affect these galaxies with "hidden", residual star formation, as well. Likely, this process disperses the cold gas reservoir, thereby also removing the fuel for the optical AGN. This scenario should be easy to verify: it predicts that the incidence of ultraviolet-bright outer disks should be less in optically red cluster galaxies.

Fig. 4.4.4 shows that the galaxy type with the highest fraction of optical AGN are the "green" galaxies Also the "cyan" galaxies have a higher AGN fraction than the "blue" galaxies. This might be largely a selection effect: strong star formation lines may mask weak AGN signatures. Nonetheless, there is some evidence that AGN are frequent in green valley galaxies, though most of it has been deduced from X-ray selected AGN (e.g. Silverman et al. 2007). The incidence of AGN in "green" galaxies is interesting to note with respect to our results from Sect. 4.4.1, where we found that, unlike for the "blue" galaxies, the fraction of "green" galaxies is almost constant with radius. We have argued that "blue" galaxies need to pass through the "green valley" as they are transformed to red sequence galaxies. The high AGN fraction in green galaxies could suggest that this transformation is frequently accompanied by an optical AGN.

4.5 Summary and Conclusions

We have measured the star formation – radius relation as the fractions of galaxies with different stellar population ages. We find that in the cluster center, star formation has largely terminated in $>80\%$ of the cluster galaxies. The contrast to the field population depends on galaxy mass; in the mass range $9.6 < \log(M_\star/M_\odot) < 10$, only 20% of field galaxies are dominated by old stellar populations, compared to 60% at masses $\log(M_\star/M_\odot) > 10.7$. The fraction of the youngest stellar populations declines most rapidly towards the cluster center, less rapidly for slightly older stellar populations, and is almost constant for the transition "green valley" galaxies. We suggest that this due to a slow quenching of star formation in the infalling galaxy population: galaxies with the youngest stellar populations evolve gradually to the slightly older populations, the "green valley", and finally the red sequence. This is confirmed by a factor ~ 2 decline of the typical star formation rate of non-quiescent galaxies. Since these trends take place over the full radial range from the cluster outskirts to the cluster core, this suggests that the quenching of star formation takes place on timescales similar to the cluster crossing time, i.e a few Gyr. This hypothesis is supported by the observation that the fraction of non-quiescent galaxies with spectral post-starburst signatures (which may indicate either a recent starburst, or the truncation of appreciable levels of star formation) is constant with cluster radius, and declines overall.

This scenario is in agreement with our results from Chapter 3, where we have argued that the increase in the faint-to-luminous ratio of red galaxies is consistent with a scenario where infalling blue galaxies cease forming stars, and subsequently fade and redden, on Gyr

timescales. Since the mass distribution of all galaxies does not change significantly (apart from the very core), we argued that the processes driving this star formation cessation are predominantly non-disruptive.

Our results suggest that strangulation is a viable mechanism to halt star formation in galaxies infalling into clusters. Strangulation removes the hot gaseous halo of infalling galaxies, thus removing the long-term fuel for star formation (Larson et al. 1980). The star formation in galaxies then gradually declines while the cold (disk) gas is used up. The timescale for this process is estimated to be of the order of Gyr (Bekki et al. 2002), very similar to our hypothesis.

From our analysis alone, we cannot exclude galaxy harassment as another possible process to quench star formation. The timescale for harassment is similar to that of strangulation (Moore et al. 1998). Under the assumption that harassment causes only weak starbursts (which we could not detect), and does not significantly alter the galaxy stellar mass, harassment could explain most of the trends we see. Harassment also makes the prediction about a transition in morphology: it is predicted to act primarily on disk galaxies and transform them into spheroidals on the same timescale as quenching star formation. In a detailed study of galaxy spectra and morphologies in two clusters, Moran et al. (2007) have argued that "gentle harassment" on group scales plays a significant role in terminating star formation (although they cannot exclude that strangulation plays an equally important role). Conversely, in recent study of central and satellite galaxies in SDSS galaxy groups van den Bosch et al. (2007) find that galaxy colors are more strongly affected upon infall into the cluster than their morphologies, thus arguing that strangulation is the more important mechanism. Our results are fully consistent with this.

5

Stellar populations in high-redshift vs. low-redshift clusters

In this chapter I extend the characterization of the cluster galaxy population to the clusters and groups of the EDisCS sample, at redshifts 0.4-0.8 , and compare these to the local SDSS clusters. The Principal Component Analysis of Wild et al. (2007) splits the EDisCS galaxies into two distinct populations along the red sequence (old stellar populations) and the blue sequence (young stellar populations), with a small, but significant "green valley" transition population. I find that at stellar masses $> 10^{10.2} M_\odot$, the majority of galaxies in both high- and low-redshift clusters is quiescent ($\sim$ 60% at $z \sim 0.8$, $\sim$ 80% at $z = 0$). The EDisCS composite cluster has a similar star formation–radius relation as the SDSS clusters, with $\sim$ 90% of the core galaxies being quiescent, and a decline of the red fraction to the field value at about the virial radius. Also the green fraction is approximately constant with environment, apart from the cluster core. The number of post-starburst galaxies increases with higher redshift, but it does so both for clusters and lower-density environments. As in the low-redshift SDSS sample, the fraction of post-starburst galaxies does not show any trend with clustercentric radius. Hence, post-starburst galaxies are not a cluster-specific galaxy population. Galaxies with young stellar populations are similar in all environments also in terms of their line emission. Galaxies with old stellar populations, on the other hand, are less likely to have emission lines when they are in the cluster center.

Most of the results at high redshifts are at least qualitatively similar to those at low redshifts, suggesting that there is little evolution in the average physical properties of clusters with redshift. As in the low-redshift sample, the quenching of star formation in high-redshift clusters appears to proceed on timescales of a few Gyr. The quantitative differences, e.g. in the number of post-starbursts, are most likely driven by the evolution of the infalling galaxy population. However, there is an intriguing evolutionary trend in the PC1-PC2 distribution of red galaxies: at $z \sim 0.4$, this is similar to the local sample, but at $z \sim 0.8$, it is markedly offset. The cause for this offset is not clear.

5.1 The ESO Distant Cluster Survey (EDisCS)

The **E**SO **D**istant **C**luster **S**urvey (**EDisCS**) is a survey of 20 fields which contain about 30 galaxy groups and clusters ranging in redshift from ∼0.4 to ∼0.8 . It is one of the first high-redshift cluster samples that was optically selected. Most high-redshift clusters are detected and selected based on their X-ray emission; however, X-ray selection introduces a considerable bias towards massive, relaxed systems.

EDisCS is based on the cluster candidates identified by the *Las Campanas Distant Cluster Survey* (LCDCS, Gonzalez et al. 2001). LCDCS employed the rather novel technique of tracing the integrated light from unresolved galaxies in high-redshift clusters to identify the candidates: a region of $90° \times 1.5°$ was observed in drift-scan mode from the Las Campanas 1m telescope, and any resolved objects (stars and galaxies) were masked from the images and replaced with randomly drawn local sky pixels. The remaining light is then due to unresolved background sources. By smoothing the images with a kernel matched to the expected size of galaxy clusters at $z \sim 0.8$, about 1000 high-redshift cluster candidates were identified.

EDisCS is the follow-up program of the strongest LCDCS cluster candidates, with the aim of selecting 10 clusters at $z \sim 0.5$ and 10 at $z \sim 0.8$. Short optical imaging from FORS2 at the VLT in two bands provided the first selection / confirmation step: only fields with an apparent galaxy overdensity (including a brightest cluster member of the expected magnitude) and a red sequence in the color-magnitude diagram were retained. For the selected 20 fields, deep optical imaging was obtained with FORS2@VLT in BVI for the mid-z fields and in VRI for the high-z fields (White et al. 2005). The fields were further imaged in the near-infrared (the K_s band for the mid-z sample and the JK_s bands for the high-z sample) using SOFI@NTT.

An important aspect of the EDisCS data is the spectroscopy data (Halliday et al. 2004; Milvang-Jensen et al. 2007). The resolution and signal-to-noise of the spectra allow not only to determine the redshift, velocity dispersion and cluster members, but also for stellar population studies. The data were acquired using the multi-slit capacity of FORS2. For each field, one mask was first taken with a short exposure, to confirm the existence of a significant peak in the redshift histogram (one field was rejected at this stage as it contained no obvious cluster). For 18 fields, deep spectroscopy was then acquired using 3 - 5 masks per cluster. The aim for the spectroscopic selection was to target all galaxies at the cluster redshift above a limiting magnitude, while rejecting as many objects at other redshifts as possible. The main selection criterion was the I-band magnitude: galaxies of similar brightness to the BCG (selected from the imaging data and the short spectroscopy masks) or fainter, but brighter than $I < 22$ (mid-z) or $I < 23$ (high-z) were considered. Furthermore, their photometric redshift, as determined from two algorithms, had to place them within ±0.2 of the cluster redshift, as determined from the short masks (two fields showed two redshift peaks in the histogram; both were considered).

In all fields, the deep spectroscopic data confirmed the existence of a cluster. In all but one field, the cluster redshift is very close to the target redshift chosen from the short masks. The one exception (field 1103.7-1245) is a rather curious case: the target redshift was $z = 0.70$, but the deeper data revealed that the cluster detected by the LCDCS is at $z = 0.96$. However, there are two foreground clusters at $z = 0.63$ and $z = 0.70$, both of them somewhat offset from the LCDCS centroid. Also in other fields there are secondary structures apart from the main cluster. However, the selection function of those structures not within the target redshift range should be considered highly biased (and simply not known) and thus, these structures
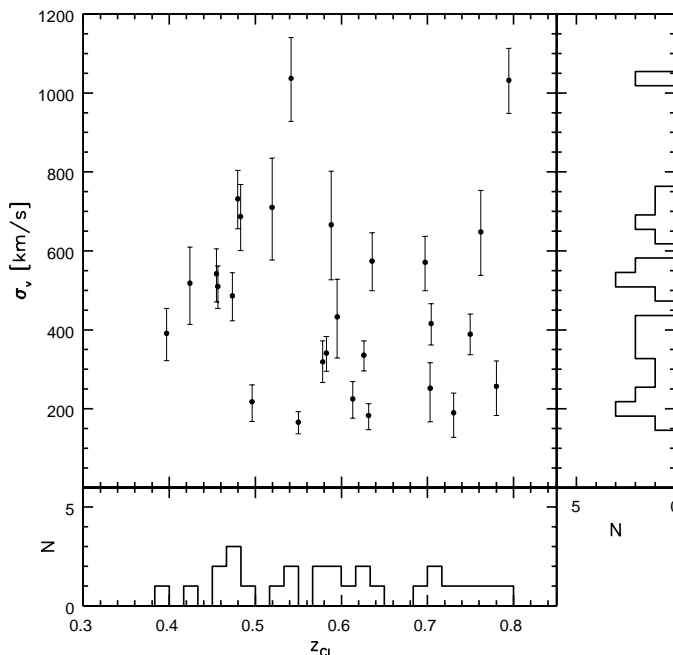
Figure 5.1: Distributions of the redshifts and velocity dispersions for the EDisCS cluster sample. The marginal histograms show the distribution binned in redshift (lower panel) and in velocity dispersion (right panel).

are difficult to consider in studies focusing on the spectroscopic data (this also applies to $z = 0.96$ in the 1103.7-1245 field). Still, there is a total of 27 systems (17 targeted clusters and 10 serendipitous ones) that meet these specifications, and have at least 7 spectroscopic members. The sample spans a large range in velocity dispersion, with several galaxy groups, as well as rich clusters (Fig. 5.1).

Table 5.1 gives an overview of the systems used in this study. We consider only structures within ± 0.1 of the targeted redshift: galaxies were targeted for spectroscopy if their photometric redshifts placed them within ± 0.2 of the cluster redshift, as estimated from the short masks. The typical error of the photometric redshifts should be ~ 0.1, hence the target selection can be considered complete within ± 0.1 of the target redshift.

The cluster velocity dispersions were calculated via a 3σ clipping iterative algorithm in a similar fashion as for the local sample (Sect. 2.3.2), but with the notable difference that galaxies over the whole field were considered, without a cut at $1R_{200}$. Also, the initial maximum velocity dispersion was set to 300 km/s (instead of 500 km/s, as for the local sample). Note that we have recalculated the velocity dispersions and redshifts of the five clusters presented in Halliday et al. (2004) so that now the same method is used for all clusters (as presented in Milvang-Jensen et al. 2007).

5.1.1 The spectroscopic dataset

The selection, data reduction, and properties of the EDisCS spectroscopic data has been described in detail in Halliday et al. (2004) and Milvang-Jensen et al. (2007). Within the

Table 5.1: The 27 EDisCS clusters and groups used in this work. Column (1) gives the short Cluster ID; column (2) the complete name - this is composed of "cl", the field ID (the central RA and Dec), and a letter indicating whether this is a serendipitous structure, i.e. the main cluster has no letter, the serendipitously discovered systems are labelled "a", "b", etc. Column (3) lists the cluster redshift z, column (4) its velocity dispersion σ_v, and column (5) the number of spectroscopic members, from which z and σ_v were determined.

Cluster	Cluster name	z	σ_v [km/s]	N_{memb}
(1)	(2)	(3)	(4)	(5)
cl1018	cl1018.8-1211	0.4734	486^{+59}_{-63}	32
cl1037	cl1037.9-1243	0.5783	319^{+53}_{-52}	16
cl1040	cl1040.7-1155	0.7043	416^{+50}_{-54}	30
cl1040b[1]	cl1040.7-1155b	0.6316	183^{+30}_{-36}	11
cl1040c	cl1040.7-1155c	0.7801	257^{+64}_{-74}	8
cl1054	cl1054.4-1146	0.6973	571^{+66}_{-72}	47
cl1054a	cl1054.4-1146a	0.6132	225^{+44}_{-49}	8
cl1054	cl1054.7-1245	0.7497	389^{+51}_{-52}	32
cl1054a	cl1054.7-1245a	0.7304	190^{+50}_{-62}	10
cl1059	cl1059.2-1253	0.4564	510^{+52}_{-56}	41
cl1103a[2]	cl1103.7-1245a	0.6261	336^{+36}_{-40}	14
cl1103b	cl1103.7-1245b	0.7031	252^{+65}_{-85}	11
cl1119	cl1119.3-1129	0.5500	166^{+27}_{-29}	17
cl1138	cl1138.2-1133	0.4796	732^{+72}_{-76}	45
cl1138a	cl1138.2-1133a	0.4548	542^{+63}_{-71}	11
cl1202	cl1202.7-1224	0.4240	518^{+92}_{-104}	19
cl1216	cl1216.8-1201	0.7945	1032^{+81}_{-84}	64
cl1227	cl1227.9-1138	0.6357	574^{+72}_{-75}	22
cl1227a	cl1227.9-1138a	0.5826	341^{+42}_{-46}	11
cl1232	cl1232.5-1250	0.5415	1037^{+103}_{-109}	51
cl1301	cl1301.7-1139	0.4828	687^{+81}_{-86}	34
cl1301a	cl1301.7-1139a	0.3969	391^{+63}_{-69}	17
cl1353	cl1353.0-1137	0.5882	666^{+136}_{-139}	18
cl1354	cl1354.2-1230	0.7620	648^{+105}_{-110}	20
cl1354a	cl1354.2-1230a	0.5952	433^{+95}_{-104}	14
cl1411	cl1411.1-1148	0.5195	710^{+125}_{-133}	21
cl1420	cl1420.3-1236	0.4962	218^{+43}_{-50}	22

[1] cl1040a with 11 members at $z = 0.54$ is not within 0.1 from the targeted redshift.
[2] The main cluster in this field, cl1103, is at $z = 0.96$, and thus beyond the targeted redshift range.
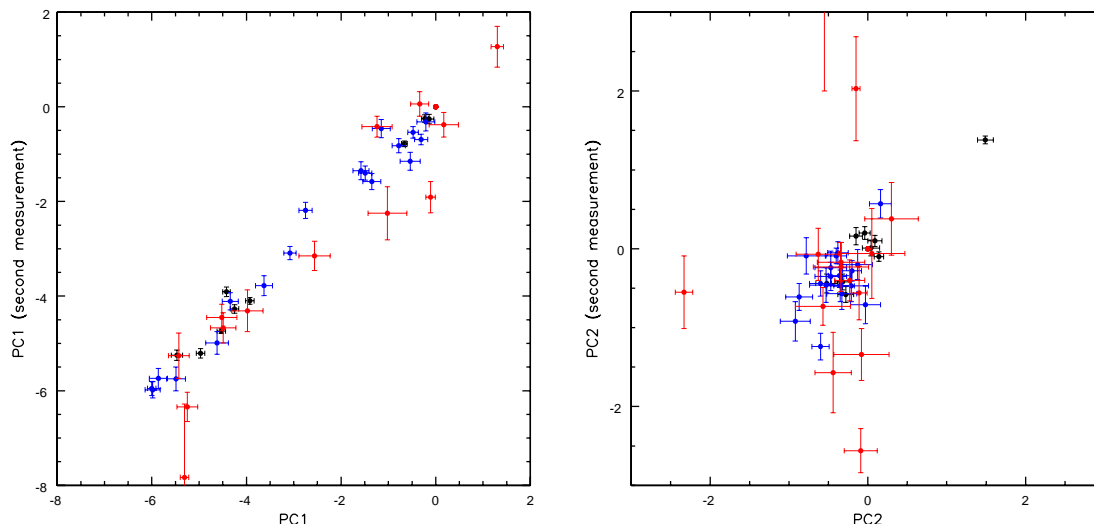
Figure 5.2: Comparison of PC1 (left) and PC2 (right) measurements for galaxies which have been observed twice. Black points denote objects for which both measurements have SNR$\geq$8, red points those for which at least one measurement has SNR<4, and blue the rest, i.e. objects where both measurements have SNR$\geq$4, but at most one has SNR$\geq$8.

EDisCS spectroscopic catalogs, there are 1584 spectra of unique galaxies with accurate redshift determinations and cross-reference to the photometric catalogs. Of these, 526 are associated with the structures listed in Table 5.1. As in Poggianti et al. (2006), we further identify galaxies in lower density environments: 82 of these galaxies are in "poor groups" of three to six galaxies, and a further 148 in the "field". The rest of the spectra (828) are too far from the targeted redshift in the respective field, hence their selection function is unknown and we refrain from assigning them to structures.

The principal component analysis described in Sect. 4.2.2 was applied to all the spectra in the spectroscopic database, if the required wavelength range was covered by the spectrum (this is not the case for only 20 spectra in the clusters, poor groups, and field samples). This leaves 736 galaxies in our sample.

Although the PCA is designed to be applicable to spectra with lower signal-to-noise ratios than traditional indices as Hδ, the higher principal components need a minimum SNR to be meaningful. In Fig. 5.2 we compare the values of PC1 and PC2 for 49 galaxies which have multiple observations. The relation between two measurements is bound to have some intrinsic scatter, because the details of the observations and the data reduction (extraction region, etc.) may differ. Overall, PC1 is exceptionally consistent in these double measurement for objects with SNR>=4. But also for lower SNR, the measurements are trustworthy in the sense that objects would be correctly classified as quiescent (PC1$\gtrsim -2$) or star-forming. This is clearly different for PC2, where the low SNR spectra scatter considerably from the one-to-one relation. For analyses based on PC2, we will therefore need to impose a SNR cut of SNR>4.
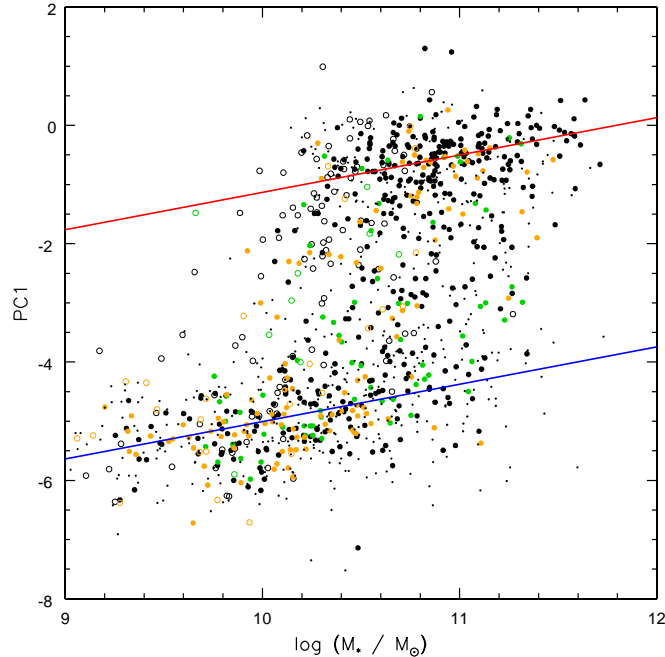
Figure 5.3: PC1 (as a measure of the strength of the 4000Å break) vs. stellar mass. Large black circles denote galaxies associated with our cluster/group sample, i.e. the structures listed in Table 5.1. Those with SNR>=4 are shown as filled circles, those with SNR<4 as open. Green circles are for galaxies in the "poor group" environment, and orange circles in the "field" environment. Again, filled and open circles indicate the SNR. The small black dots show galaxies not associated with any of these, i.e. with redshifts too far from the targeted redshift. These are only shown if SNR>=4. The red line shows the result of a linear regression with 2σ clipping to the galaxies with PC1> -2 that are associated with clusters or the field (i.e. all but the small symbols). The blue line is a fit to the galaxies with PC1< -3.5, but with the slope fixed to be the same as for the quiescent galaxies.

5.1.2 Stellar masses

For all the objects in the spectroscopic database we have derived stellar masses from their photometric data via the `kcorrect_v4.1.4` algorithm (Blanton & Roweis 2007). We choose to estimate the stellar masses from the photometric data rather than the spectroscopy since the latter can only characterize the stellar populations within the slit, rather than the overall light. With photometry in multiple bands (BVIK for the mid-z fields, VRIJK for the high-z fields), the overall SED of the galaxy is constrained quite well, and allows for stellar mass estimates based on the total light of the galaxy. We use the "total" magnitudes as described in White et al. (2005) and Rudnick et al., in prep., which include an aperture correction for light missed due to the extended wings of the PSF.

5.2 An alternative CMD: 4000Å break vs. stellar mass

In Fig. 5.3 we present a diagram of PC1 against the stellar mass of the galaxy. PC1 measures the strength of the 4000Å break (Sect. 4.2.2), and is thus a good indicator of the recent star

formation history of a galaxy. Such a diagram of PC1 vs. $\log(M_\star/M_\odot)$ is analogous to the more traditional color-magnitude diagrams (CMDs): luminosity scales with mass (although the scaling is different for red and blue galaxies!) and PC1 (or the 4000Å break) indicates the color (or mean stellar age) of the population. Indeed, we find that most galaxies belong either to the *red sequence* (PC1~ 0) or the *blue cloud* (PC1~ −5). In fact, the blue cloud is so well confined that it can also be referred to as a "sequence" rather than a "cloud". The apparent lack of lower mass red sequence galaxies simply reflects the magnitude limit of our survey: blue, star-forming galaxies have a much lower M/L ratio, and can therefore be traced to lower masses. However, particularly for evolutionary studies, it is of advantage to work in terms of mass instead of light: as galaxies cease to form stars, they become fainter and thus can move out of the selection criteria of magnitude-limited samples.

Both the red and blue sequence show an increase of PC1 with increasing stellar mass. This is likely to be mostly a metallicity effect: the 4000Å break is mostly caused by an accumulation of metal lines and should thus be stronger in metal-rich galaxies. The metallicity of both passive and star-forming galaxies is found to increase with the mass of the galaxy (Tremonti et al. 2004; Gallazzi et al. 2005), hence more massive galaxies should indeed have larger PC1 values. The increase in PC1 could also be due to increasing age of the stellar populations with mass.

Within the scatter, the two sequences are remarkably parallel. We determine the slope of this relation from the quiescent galaxies in clusters, groups, poor groups, and the field (i.e. we leave out the galaxies with unknown selection functions, since these will not be used in the final analysis). The fit is only determined from galaxies with SNR≥4. From linear regression with 2σ clipping for galaxies with PC1> −2 we find:

$$\mathrm{PC1_Q} = (0.61 \pm 0.02)\log(M_\star/M_\odot) - (7.31 \pm 0.24) \tag{5.1}$$

A linear relation of the same slope is also a good fit for the star-forming galaxies, as indicated in Fig. 5.3.

5.2.1 Bimodality in PC1

With large datasets such as SDSS, the state of the art technique for following the red sequence and the blue cloud in CMDs is to fit bimodal Gaussians within luminosity bins (Baldry et al. 2004; Li et al. 2006). Unfortunately, we lack a large enough sample of galaxies for such an analysis. However, we can make use of the fact that the red and blue sequence are essentially parallel. For each galaxy, we calculate PC1-$\mathrm{PC1_Q}$ (with $\mathrm{PC1_Q}$ from Eq. 5.1), thereby rectifying the PC1–mass diagram. Fig. 5.4 shows the resultant distribution of PC1-$\mathrm{PC1_Q}$ for the galaxies in our cluster, groups, and field sample. We model both the red and blue sequence as Gaussian distributions, which is a good description for the peaks, the blue side of the blue sequence, and the red side of the red sequence. However, the region of overlap between the two sequences is not adequately described by this model: we find an excess of galaxies over the sum of the two Gaussian distributions. This is the region of the *green valley*, and PC1 is able to identify "green" galaxies which cannot be accounted for simply by the overlap of the distributions of red and blue distributions.

Such an excess of green galaxies is in contrast to CMDs with optical colors, where for each luminosity bin the sum of two Gaussians is found to be a good description of the galaxy distribution (Baldry et al. 2004). Furthermore, in optical CMDs the blue sequence is found to approach the red sequence at high luminosities, rather than remain approximately parallel
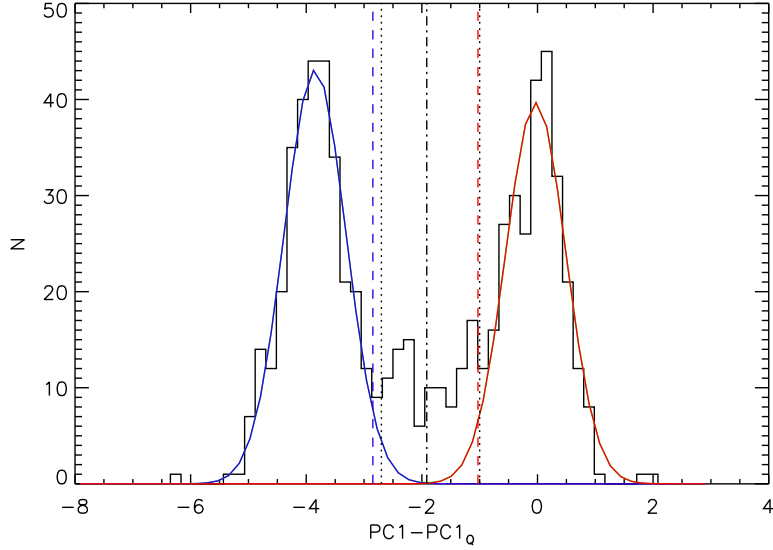
Figure 5.4: The distribution of PC1, projected along the lines indicated in Fig. 5.3 for galaxies in the cluster, group, and field sample with SNR$\geq$4. The solid red and blue lines represent fits of Gaussian distribution to the bins clearly attributed with either the red or blue sequence, i.e. outside the region marked by the dotted vertical lines. The black dash-dotted lines marks the transition between the red and blue sequences, chosen to be the same distance in units of the dispersion from each distribution (3.6σ). The vertical dashed lines are 2σ from the mean of each distribution - they delineate a region where the sum of the Gaussian fits cannot account for the majority of the galaxies.

as in our diagram. It is likely that this reflects an increasing amount of dust in more massive spirals (Baldry et al. 2004; Labbé et al. 2007), which has a reddening effect on colors, but less effect on PC1. A population of galaxies between the red and blue sequences has however been identified in CMDs using ultra-violet–optical colors (Wyder et al. 2007). Although observations in the ultraviolet are also partial to dust reddening, they are very sensitive to even small amounts of star formation, and may thus be more successful at distinguishing the blue and red sequences than optical colors alone.

Fig. 5.4 is the basis for dividing our galaxy sample into "red", "blue", and "green" galaxies. For a sample of SDSS galaxies, we had defined the limits of the red and blue sequences towards the green valley to be -1.0 and +1.0 (in units of PC1) from the ridge (see Chapter 4). We use the same criterion here, i.e. we define the red sequence to be galaxies with PC1-PC1$_Q$ > -1.03, and the blue sequence to be galaxies with PC1-PC1$_Q$ < -2.85. Galaxies between these bounds are identified as green valley galaxies. For the EDisCS sample, the width of 1.0 in PC1 can be additionally motivated as being close to the 2σ widths of the Gaussians that describe the red and blue sequences: $\sigma_{red} = 0.52$, $\sigma_{red} = 0.53$. It is remarkably how similar these dispersions are, demonstrating that PC1 is a very good estimator for recent star formation histories.
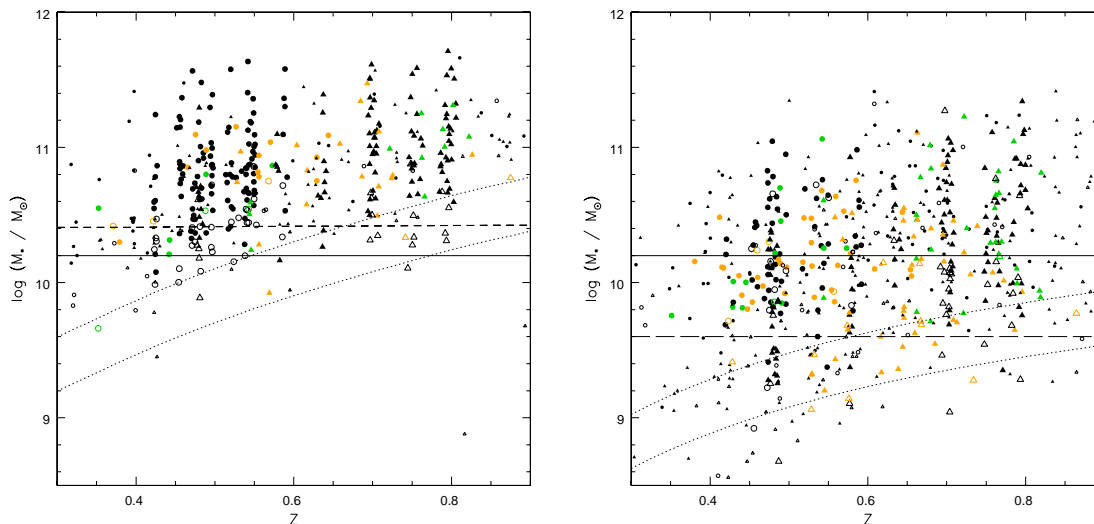
Figure 5.5: Stellar masses and redshifts of the galaxies in our sample for galaxies on the red sequence (left) and the blue sequence (right). The symbols are the same as in Fig. 5.3, except that galaxies in the high-z fields are shown as triangles. In both panels, the solid black line shows our adopted lower mass limit, $\log(M_\star/M_\odot) \geq 10.2$. In the left panel, the dotted lines indicate the stellar mass of an SSP formed at $z_f = 3$ with twice solar metallicity which would be detected with $I = 22$ (upper line, applicable to the mid-z fields) or $I = 23$ (lower line, applicable to the high-z fields). The dashed line shows the stellar mass which corresponds to an SSP with $M_V = -20$ today (this corresponds to the division between luminous and faint galaxies adopted by De Lucia et al. 2007). In the right panel, the dotted lines indicate the minimum stellar mass of a galaxy which has been forming stars at a constant rate since $z_f = 3$. The long-dashed line indicates the completeness limit for blue galaxies.

5.2.2 Mass completeness

We aim to work with a sample of galaxies that is complete in stellar masses (rather than luminosity). The completeness limit has to be determined from the galaxies with the largest M/L ratios, i.e. the faintest ones for a given mass. The extreme of this population will be galaxies which formed their stars very early in a single starburst, and have been evolving passively ever since. Such *simple stellar populations* (SSP) are indeed found to yield good descriptions of galaxies on the red sequence, e.g. in De Lucia et al. (2007) we found that the red sequence of the EDisCS clusters is well described by an SSP which formed at a redshift of $z_f \sim 2 - 3$.

In Fig. 5.5 we show the stellar masses of red galaxies against redshift. Also shown are two lines predicting the lower mass limit as a function of redshift, for the two magnitude limits of the survey fields ($I = 22$ and $I = 23$). These are derived from a Bruzual & Charlot (2003) SSP, with a formation redshift of $z_f = 3$, a Chabrier IMF, and twice solar metallicity. The formation redshift is chosen based on the results of De Lucia et al. (2007), but the predictions are similar for higher formation redshifts (for $z_f = 10$, the predicted lower mass limit would be ~ 0.1 dex larger). The metallicity is higher than generally found for the faint red sequence galaxies; however, we need to estimate the extreme of the M/L distribution rather than the mean, and higher metallicities lead to higher M/L ratios. At each redshift, we calculate the

stellar mass of this SSP which corresponds to the apparent magnitude limit. It is important to note that kcorrect uses a set of spectral templates derived from Bruzual & Charlot (2003) SSPs, hence the stellar masses and these predictions should be comparable. Galaxies which have been classified as red, but fall below the lines, likely have younger formation ages, and/or lower metallicities, both leading to lower M/L ratios. However, we find only few such galaxies, indicating that the red galaxies generally have quite old ages. In fact, the range around the predicted mass limits is sparsely populated, particularly for the high-z fields. In De Lucia et al. (2007), we showed that the ratio of luminous to faint galaxies on the red sequence is an increasing function of redshift. The division between luminous and faint galaxies was chosen to correspond to an SSP of $z_f = 3$ of solar metallicity with a magnitude of $M_V = -20$ at $z = 0$. For comparison, we also show the stellar mass of this SSP in Fig. 5.5. The lack of galaxies less massive than this is at least partially a real effect, and due to the lack of faint red galaxies in high redshift clusters De Lucia et al. (2007).

We choose $\log(M_\star/M_\odot) \geq 10.2$ as the lower mass limit. This mass corresponds to the predicted lower mass limit of a metal-rich SSP with $z_f = 3$ at $z \sim 0.55$ for the mid-z sample, and at $z \sim 0.78$ for the high-z sample.

Some of the fields targeted as part of the high-z sample contain structures in the redshift range of the mid-z sample. We therefore rephrase the definition of the mid-z and high-z samples to correspond to the actual redshift of the structure (rather than the apparent magnitude limit). The mid-z sample comprises galaxies with $z < 0.605$, the high-z sample those with $z \geq 0.605$. The dividing redshift is chosen such that the galaxies from each structure in Table 5.1 belong to the same redshift sample.

The mass distributions of red galaxies in the mid-z and high-z samples are shown in Fig. 5.6. At the low mass end, about half of the galaxies have SNR<4. But as we have shown in Sect. 5.1.1, PC1 is a reliable estimator of the approximate age of a stellar population (old and red or young and blue) even in low signal-to-noise spectra. Including these spectra in the analysis allows us to probe also some galaxies which were classified as "faint" by De Lucia et al. (2007).

This mass limit misses about half of the star-forming galaxies, however - this is an inherent disadvantage to using a mass selection instead of a luminosity cut-off. Studies of luminosity-limited samples, on the other hand, probe different mass ranges of the red and the blue sequence. They are thus equivalent to choosing red galaxies more massive than a certain mass cut-off, and blue galaxies more massive than another (lower) mass cut-off. For star-forming galaxies, a lower mass limit can be derived from a model stellar population which is forming stars at a constant rate. Such a stellar population has produced a substantial population of low-mass stars, which largely determine the stellar mass, but is classified as star-forming at each epoch. Again, we choose a Chabrier IMF, $z_f = 3$, and a metallicity of twice the solar value. The resulting lower mass limits are shown in the right panel of Fig. 5.5, and imply a lower mass limit of $\log(M_\star/M_\odot) \geq 9.6$ (chosen to match the predicted mass limit for the mid-z cluster with the highest redshift, $z \sim 0.55$).

However, for the blue (and green) galaxies, the signal-to-noise ratio of the spectra is important, since for these galaxies, the second principal component of the PCA contains information whether star formation has recently been truncated. In Fig. 5.7 we show the mass distributions of blue and green galaxies in the mid-z and high-z samples, color-coded by the SNR of the spectrum. The fraction of galaxies with low SNR is not a clear function of stellar mass; even some high-mass galaxies have SNR<4, while some low-mass galaxies have SNR>8. In
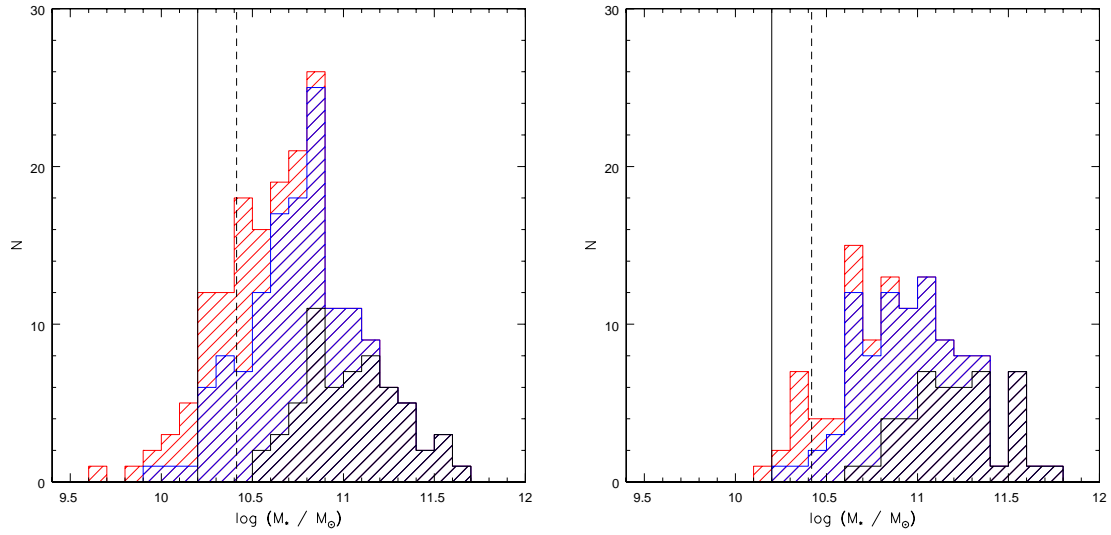
Figure 5.6: The mass distributions of galaxies on the red sequence in the mid-z sample (left) and the high-z sample (right). The red histograms shows the distribution of all galaxies, the blue the subset of galaxies with SNR$\geq$4, and the black the subset with SNR$\geq$8. The solid black line shows our adopted lower mass limit of $\log(M_\star/M_\odot) \geq 10.2$, the dashed line the division between faint and luminous galaxies by De Lucia et al. (2007).
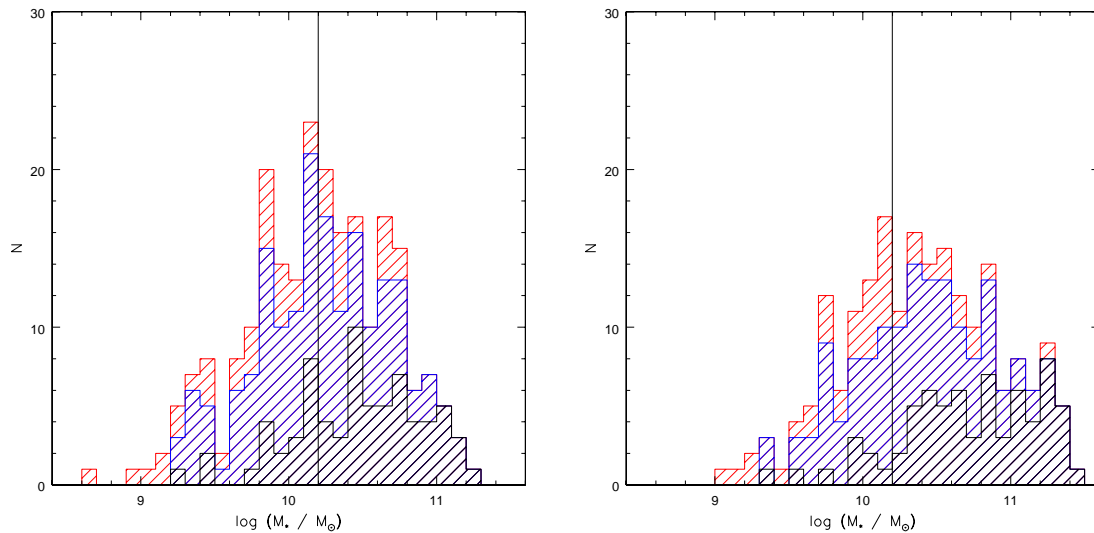

Figure 5.7: The mass distributions of galaxies on the blue sequence and in the green valley in the mid-z sample (left) and the high-z sample (right). The color coding of the histograms is the same as in Fig. 5.6. The solid black line shows our adopted lower mass limit of $\log(M_\star/M_\odot) \geq 10.2$.
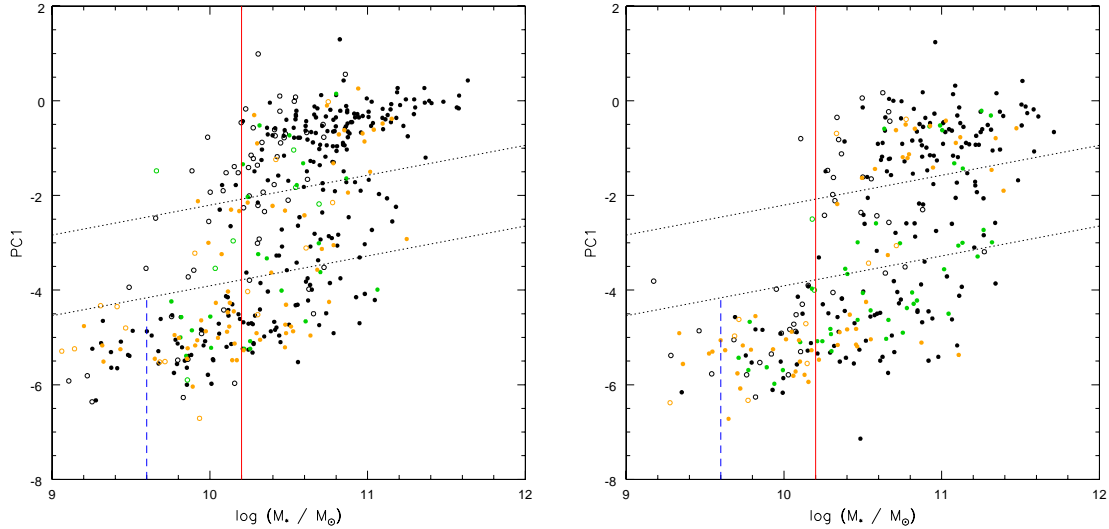
Figure 5.8: The PC1-mass diagram for the mid-z sample (left) and the high-z sample (right). The symbols are the same as in Fig. 5.3. The dotted lines illustrate the division into red, green, and blue galaxies. The solid red line marks the mass completeness limit for the whole sample ($\log(M_\star/M_\odot) \geq 10.2$). For the blue galaxies, a separate mass limit can be defined at $\log(M_\star/M_\odot) \geq 10.2$ (green dashed line).

the mid-z sample, about 10%-20% of galaxies with $\log(M_\star/M_\odot) < 11$ have SNR<4, whereas in the high-z sample, the fraction increases at lower masses. It is clear that a simple mass cut cannot reduce the sample to one which is more complete in high-SNR galaxies. However, it is also apparent that the subset of galaxies with SNR>4 is a fair representation of the overall sample, particularly above our chosen mass limit of $\log(M_\star/M_\odot) \geq 10.2$.

For both the red and blue galaxies, the mass range is only sparsely populated in the vicinity of the mass limits computed from the stellar population models (Fig. 5.5). For the red galaxies, this is partially due to an actual lack of faint galaxies on the red sequence (De Lucia et al. 2007). However, also the spectroscopic target selection of EDisCS needs to be taken into account: slits were assigned preferentially to brighter galaxies (Halliday et al. 2004; Milvang-Jensen et al. 2007). This strategy could introduce a significant bias into our mass-selected sample, as for a given stellar mass, blue, bright galaxies are more likely to be selected than red, faint galaxies. In Poggianti et al. (2006), we computed completeness corrections by comparing the number of observed galaxies to the number of galaxies which pass the selection criteria in bins of apparent magnitude. This completeness correction is also applied in the present work.

5.2.3 Redshift dependence

Apart from differences in metallicity, the spread in the distribution of PC1 for the quiescent galaxies can be due to different ages of the stellar populations. The colors of early-type galaxies generally indicate that their stellar populations formed relatively early, at redshifts $z_f \gtrsim 2-3$ (e.g. De Lucia et al. 2007). PC1 increases with stellar age, although the change is
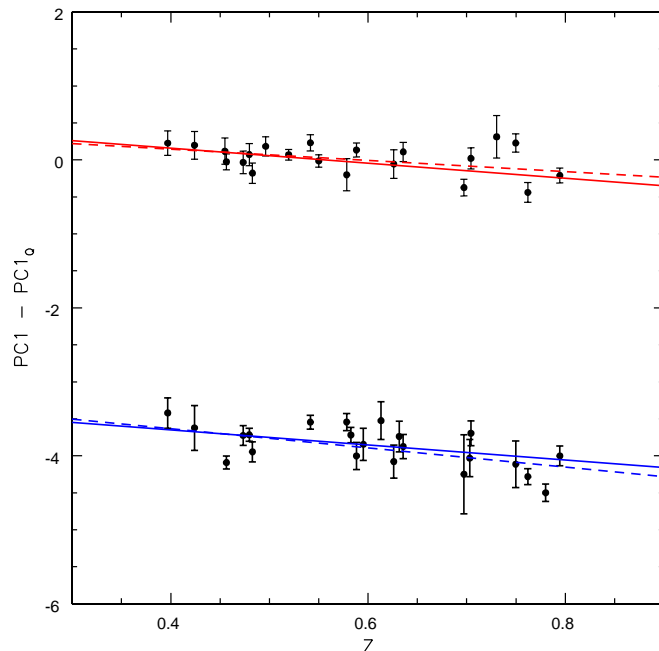
Figure 5.9: The evolution of the mean of the red sequence (top) and blue sequence (bottom) for the cluster sample. The solid lines show the fit to the data points, with the constraint that the slope is the same for each sequence. The dashed lines indicate the individual fits.

comparatively slow for ages larger than $\sim 1\mathrm{Gyr}$.

In Fig. 5.8 we show the PC1–mass diagram for the two redshift subsamples. Indeed, the red sequence in the mid-z sample lies at slightly larger values of PC1 than in the high-z sample, indicating older stellar populations. Also the blue sequence lies at higher PC1 values in the mid-z sample compared to the high-z sample. A similar result was found by Labbé et al. (2007), who find that the zero-point of the blue sequence in ultraviolet-optical colors decreases almost linearly with redshift. Although they ascertain that at least part of this evolution can be explained simply by aging of the stellar population, they find that they cannot adequately reproduce the evolution with simple prescriptions for star formation histories, such as constant or exponentially declining star formation.

For our clusters and groups, we determine the weighted mean value of $\mathrm{PC1}$-$\mathrm{PC1_Q}$ of the red and blue sequences. In each cluster, each sequence is only considered if it has at least four galaxies. Note, however, that we do not impose a mass cut at this stage - any dependence on mass should be taken out by considering the rectified values of PC1. The results are shown in Fig. 5.9. For both sequences, the mean PC1 value evolves to bluer values at higher redshifts. The evolution is slightly stronger for the blue sequences, albeit with more scatter. We fit the redshift dependence with the constraint that the slope is the same for both sequences (this is done by "shifting" the points for the blue sequence by the difference in the peak values of the red and blue distributions, see Fig 5.4). This yields:

$$\Delta_z = (\mathrm{PC1} - \mathrm{PC1_Q})(z) = (-1.02 \pm 0.18)z + (0.57 \pm 0.10) \tag{5.2}$$

127

for the evolution of the red sequence. The evolution of the blue sequence is accordingly described by the same relation, with an additional offset of -3.81. This Δ_z is applied to the boundaries between the green valley and the red / blue sequences.

A striking difference between the two samples is that the red sequence is much more confined for the mid-z sample. For these clusters, the mean of the red sequence is very similar, whereas for the high-z clusters, the mean varies much more between clusters. This is further investigated in Sect. 5.3.5.

5.2.4 The SDSS comparison sample

In Chapter 4, we applied the PCA method to galaxies in a sample of ~ 500 optically selected clusters in the Sloan Digital Sky Survey. From this cluster sample, we draw a subsample to serve as the local, $z \sim 0$ comparison sample for EDisCS.

To ensure that the local clusters are as complete in mass as the EDisCS clusters, i.e. $\log(M_\star/M_\odot) \geq 10.2$, we select clusters with $z \leq 0.07$ (cf. Fig. 4.9). This leaves 220 clusters in the sample. However, only one of these clusters (C4_DR3_2035) has a velocity dispersion of $\sigma_v > 1000 \mathrm{km/s}$. Despite its large velocity dispersion, this cluster has not been detected in X-rays (Shen et al., in prep), and is comparably faint in total optical luminosity, as well: the mass-to-light ratio inferred from the velocity dispersion and the integrated light is $> 1400 M_\odot/L_\odot$. In order to better probe the high velocity dispersion end of the distribution, we choose to add the cluster C4_DR3_3004, at $z = 0.08$, to the sample. This cluster is better known as Abell 2255, is X-ray luminous, and is the cluster with the highest velocity dispersion in our sample. It has been suggested that this cluster has recently undergone a merger (Sakelliou & Ponman 2006), and thus may not be a relaxed cluster. Nonetheless, its mass-to-(optical)light ratio is more typical ($\sim 370 M_\odot/L_\odot$) of what is found from weak lensing studies (Mellier 1999). It is interesting to note that the Dressler-Shectman statistic detects substructure in C4_DR3_2035 ($P_{DS} = 0.03$), but not in Abell 2255 ($P_{DS} = 0.43$). For Abell 2255 it has to be kept in mind that it is slightly incomplete in low-mass, red galaxies.

The comparison between any spectroscopic index between EDisCS and SDSS has to be done particularly careful, as the aperture effects are very different in the two samples. For SDSS, $3''$ fibers are placed on the centers of the galaxies. At the redshifts we are probing, this corresponds only to the central ~ 3 kpc of the galaxies. In massive early-type spiral galaxies, this is comparable to, or even smaller than, the size of the bulge. Hence, particularly if these galaxies are seen face-on, the light within the fiber aperture will be dominated by the bulge component. The stellar population of the bulge is typically old, and similar to the stellar population of elliptical galaxies. The stellar population of the bulge itself could therefore be classified as "red". However, if enough light from the young, blue disk shines through the bulge, then we should expect the light-averaged stellar population to be younger and bluer than the red sequence. In our comparison SDSS sample, there are 15230 galaxies that have been classified as "red" according to the criteria described in Sect. 4.3.4. Of these, only 877 have `frac_DeV`< 0.5 in the r-band. The SDSS PHOTO pipeline fits both an exponential profile (to describe the disk) and a de Vaucouleur profile (to describe the bulge) to the radial light profiles of the galaxies, and then determines the linear combination of the two which best described the profile. The parameter `frac_DeV` is the linear coefficient of the de Vaucouleur profile, and can therefore be considered to estimate the contribution of the bulge. Galaxies

with a low `frac_DeV` are therefore likely to be disk galaxies. We have inspected a subsample of the "red' galaxies with `frac_DeV`< 0.5 and find that about 30-50% of these are indeed face-on, early-type spiral galaxies. The overall "contamination" of the red sequence galaxies is therefore rather small, and of the order of 2-5%.

We are therefore confident that our method is successful in selecting an almost "clean" sample of red sequence galaxies in SDSS. For EDisCS, slits were placed on the galaxies, and the light-averaged spectrum contains a larger contribution from the outer disk, if present. The distinction between true red sequence galaxies, with very little star formation, and galaxies with active star formation, should therefore be easier in EDisCS. This is in part demonstrated by the tight blue sequence in the EDisCS PC1–mass diagram, which runs parallel to, and well separated from, the red sequence. In the SDSS PC1–mass diagram, on the other hand, the blue sequence curves and approaches the red sequence with increasing galaxy mass (cf. Fig. 4.6). This is largely a reflection of the increasing role of the aperture bias with increasing galaxy size (see also the discussion in Sect. 4.3.3). Although we were able to define a blue "ridge" and a "green valley" for the SDSS sample, we will not attempt to compare the number of "green" galaxies in EDisCS and SDSS, as it is particularly this region of the PC1–mass diagram that could be affected by the different aperture effects, i.e. different contributions from the bulge vs. disk component.

The quantities that thus can be compared in the SDSS and EDisCS samples therefore are the fraction of "red" galaxies, and the fraction of post-starburst galaxies (jointly for blue and green galaxies). In both samples, the lower boundary of the red sequence is defined as -1.0 below the ridge / peak of the red sequence.

5.2.5 The fraction of red galaxies in a mass-limited sample

The classical Butcher–Oemler effect measures the fraction of blue galaxies in clusters. As argued in Sect. 1.6, this may introduce a strong bias towards low-massive, star-forming galaxies. But at masses higher than our mass completeness limit, the blue sequence is rather sparse, and almost as many galaxies are in the green valley. Instead of the blue fraction, we first investigate the red fraction, i.e. the number of galaxies with aged stellar populations.

In Fig. 5.10 we show the fraction of galaxies on the red sequence at masses larger than $\log(M_\star/M_\odot) \geq 10.2$, and within R_{200}, as function of the cluster velocity dispersion. The scatter of the red fraction is quite large, particularly for the less massive systems, which have a small number of members. In the clusters with $\sigma > 550$km/s, generally a large fraction of the galaxies are quiescent. In EDisCS, this is between 40% and 80% in all but one case. In the low-redshift SDSS sample, most massive clusters have about 80% red galaxies, although also here, some systems have about 50% blue galaxies. This is also demonstrated by the two clusters with the highest velocity dispersion: Abell 2255, which is X-ray luminous, has a "normal" mass-to-light ratio, and little substructure according to the Dressler-Shectman statistic, has a red fraction of 80%, whereas C4_DR3_2035, without strong X-ray emission, a high mass-to-light ratio inferred from the velocity dispersion, and possible substructure has a red fraction of 50%.

In individual lower-mass systems, the fraction is highly variable in the EDisCS sample. In the SDSS sample, the fraction also varies, but the clusters clearly concentrate at $f_{\rm red} \sim 0.8$.

The left panel Fig. 5.11 shows the red fraction of the individual clusters as function of redshift. Clearly, the locus of the SDSS clusters is at higher red fractions than the EDisCS
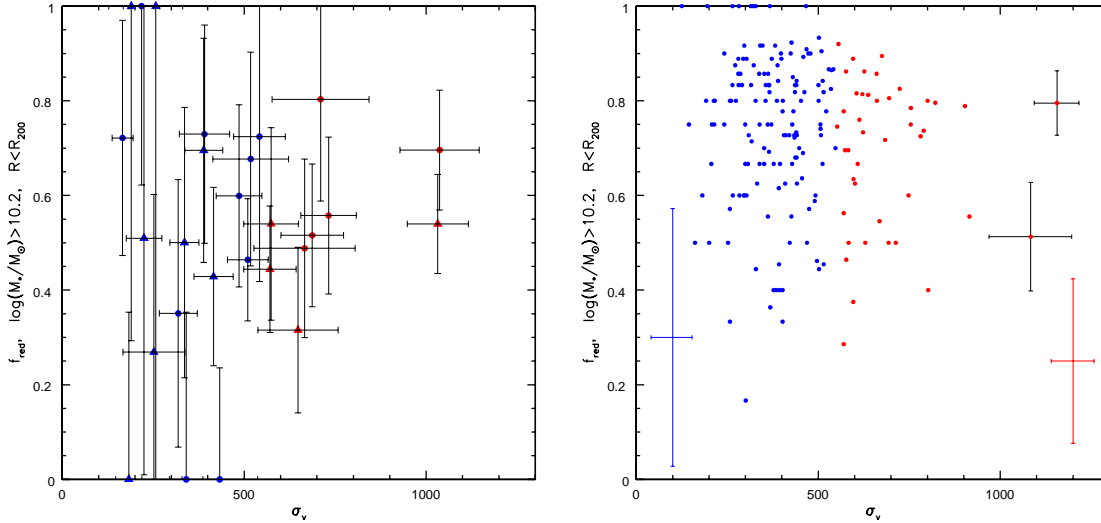
Figure 5.10: The fraction of red galaxies, at masses greater than $\log(M_\star/M_\odot) \geq 10.2$, and within R_{200}, as a function of cluster velocity dispersion σ_v in the EDisCS sample (left) and in the SDSS comparison sample (right). Clusters with $\sigma > 550$km/s are shown as red symbols, groups with $\sigma < 550$km/s as blue symbols. In the EDisCS sample, the shape of the symbols indicates the redshift: systems at $z < 0.6$ are shown as circles, those at $z > 0.6$ as triangles. For the SDSS sample, individual error bars are shown only for the two clusters with the highest velocity dispersion; the median error bars for the other clusters are shown in the lower left (for the $\sigma < 550$km/s clusters) and lower right corner(for the $\sigma > 550$km/s clusters) .

clusters, for both velocity dispersion ranges. For the more massive clusters, the redshift dependence continues within the EDisCS sample: the higher the redshift, the lower the red fraction.

We split the EDisCS galaxies into four subsamples: for each of the two redshift samples (with the division at $z = 0.605$), we split by the velocity dispersion of the cluster, with the division at $\sigma > 550$km/s. The SDSS galaxies are split into two samples according to the cluster velocity dispersion. For each sample, we can consider the composite cluster as the average cluster. In the right panel of Fig. 5.11 we show the red fractions of these composite clusters, and also the red fractions of the EDisCS poor groups and field samples. For the SDSS galaxies, we define the field sample to be those galaxies at distances larger than 10 Mpc from the BCG.

Despite the large scatter in the red fraction of the individual low velocity dispersion systems, their average red fraction is quite similar to that of the more massive clusters, at all redshifts. The composite red fraction is largest in the SDSS clusters (about 75%), but also the EDisCS clusters have high red fractions, particularly within $0.5R_{200}$. In the SDSS sample, the field red fraction is 50%, and thus substantially lower than in the clusters. This demonstrates that the color–density relation is well in place at low redshifts. The red fraction in the EDisCS poor groups is significantly lower than in the cluster environment, as would be expected from the color-density relation. Puzzlingly, the red fractions we find in the EDisCS field sample are counter-intuitive to this expectation: since it should be the lowest density environment we probe, it should have the lowest red fraction. Instead, the red fraction in the
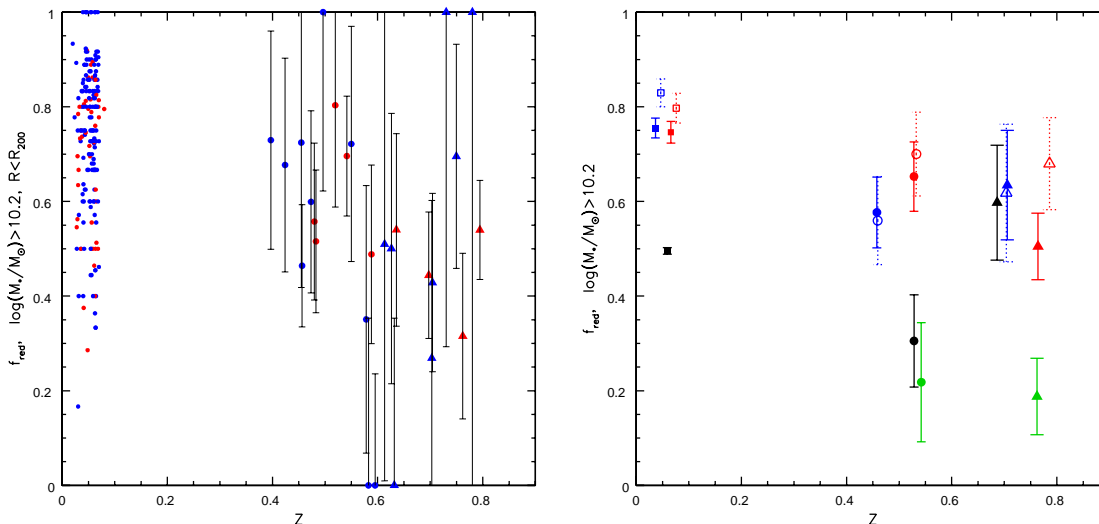
Figure 5.11: The fraction of red galaxies, at masses greater than $\log(M_\star/M_\odot) \geq 10.2$, and within R_{200}, as a function of redshift. In the left panel, individual clusters are shown; in the right panel, the red fractions of the composite clusters, the field, and the poor groups are shown. Clusters with $\sigma > 550$km/s are shown as red symbols, groups with $\sigma < 550$km/s as blue symbols. The shape of the symbols indicates the redshift: EDisCS systems at $z < 0.6$ are shown as circles, those at $z > 0.6$ as triangles. SDSS systems are shown as small circles in the left panel, and as squares in the right panel. The error bars in the right panel are Poissonian.

high-z field subsample is comparable to that in clusters. At mid-z, it is identical to the poor groups. As can be seen from Fig. 5.8, many blue field galaxies lie just beyond our mass limit. The high red fraction for the high-z field may thus just be a statistical fluke. Without the distinction into mid-z and high-z samples, the field red fraction is 60%, which is still higher than in the SDSS sample.

If we rephrase the Butcher-Oemler effect such that high-redshift clusters contain fewer quiescent galaxies, then Fig. 5.11 confirms such a trend even in a mass-limited sample. At least partially, this is due to a dearth of low-mass red galaxies, as also suggested by De Lucia et al. (2007) and Stott et al. (2007) (but see Andreon 2007, for a different result, i.e. no decrease of red sequence galaxies with redshift).

5.2.6 Blue-to-total ratio

The majority of previous studies did not work with mass-limited galaxy samples, but rather with luminosity-limited sample. Particularly for high-redshift samples, this frequently selects galaxies at blue rest-wavelengths. De Propris et al. (2003) found that the strength of the Butcher-Oemler effect depends both on the selection band, as well as the luminosity cut-off. By including lower-mass blue galaxies, we can approximate a selection in a bluer wave band: star-forming galaxies have a lower M/L ratio, particularly at blue wavelengths. Thus, we define a "blue-to-total" ratio by extending the mass limit for blue galaxies to $\log(M_\star/M_\odot) > 9.6$. For red and green galaxies, we keep the mass limit of $\log(M_\star/M_\odot) \geq 10.2$. (The mass
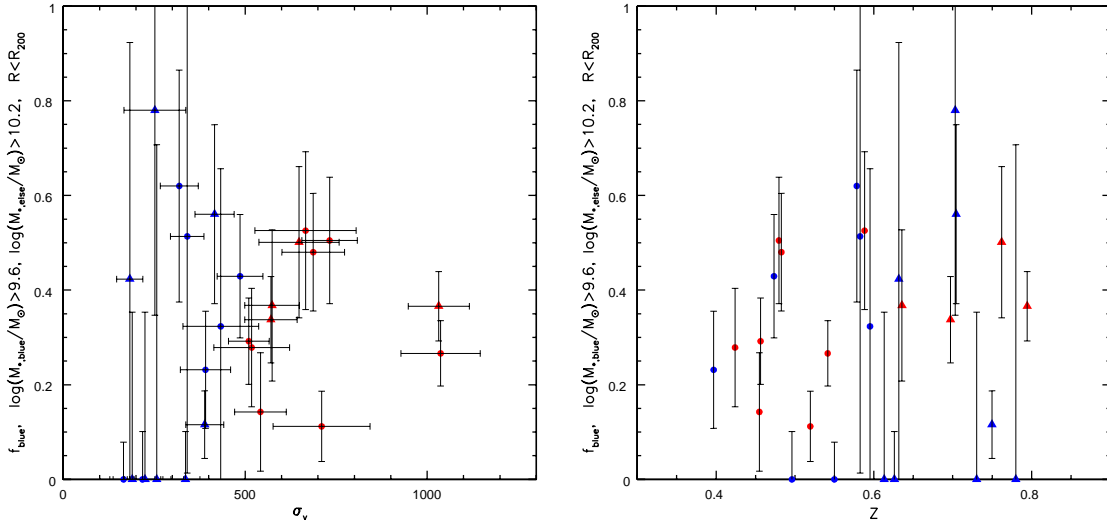
Figure 5.12: As Fig. 5.10, but showing the blue-to-total ratio. The mass limit for the blue galaxies is $\log(M_\star/M_\odot) \geq 9.6$, for other galaxies it is $\log(M_\star/M_\odot) \geq 10.2$.

limit for green galaxies is difficult to predict / determine, hence we use the same one as for the red galaxies as a conservative limit.) We refrain from comparing this "blue fraction" to SDSS data, as the distinction between "blue" and "green" is likely to be influenced by the different aperture effects in the two samples.

Fig. 5.12 shows the resultant blue fractions as functions of velocity dispersion and redshift. The trend is similar as for the fraction of [OII]-emitting galaxies we have computed in Poggianti et al. (2006), in that there seems to be an upper limit to the fraction of star-forming galaxies, which decreases with cluster velocity dispersion, and little trend with redshift. But the spread between this upper limit and no occurrence of star-forming galaxies is large. Furthermore, we find six systems with no blue galaxies. This seems somewhat contradictory to the results Poggianti et al. (2006); however, it needs to be kept in mind that a large fraction of green galaxies also emit in [OII] (Fig. 5.16).

In the right panel of Fig. 5.13 we compare the blue fractions for the four composite clusters defined in the previous section. They are quite similar for all four samples, apart from the blue fraction in the high-z, low-σ sample, where it is lower by about 1σ. This is primarily because four of the six groups without blue galaxies are in this sample; other low-σ groups have larger blue fractions. For all cluster samples, the blue fraction is significantly lower than in both the poor groups and the field, as would be expected from the color–density relation. It seems that the dearth of massive blue galaxies in the field is made up for by a considerable number of smaller blue galaxies.

At least in the redshift range $0.4 < z < 0.8$, we do not detect a significant evolutionary trend in the number of star-forming galaxies. This is consistent with the classical Butcher-Oemler effect, but some previous studies already found little evolution beyond a redshift of $z > 0.2$ (Fairley et al. 2002). Ellingson et al. (2001) have argued that the fraction of star-forming galaxies reflects the infall population arriving at the cluster. Following their argumentation, we consider the consequences of the simple assumption that infalling star-forming galaxies
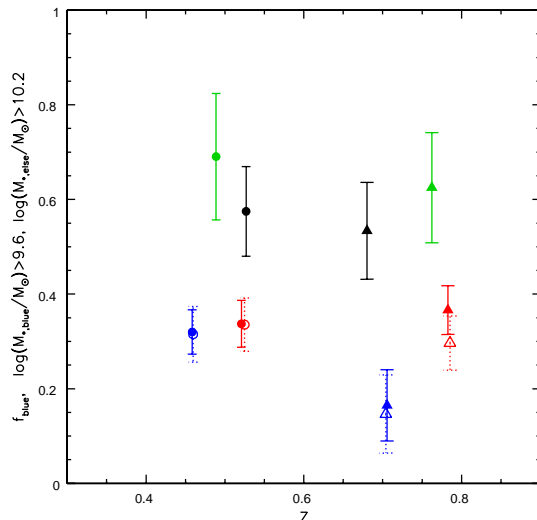
Figure 5.13: The blue-to-total ratio in the four composite clusters. Blue symbols denote the low velocity dispersion systems, red ones the high velocity dispersion ones. The filled (open) symbols show the fraction computed within $1R_{200}$ ($0.5R_{200}$). The green (black) symbols show the red fraction in the poor groups (in the field). Each symbol is shown at the median redshift of the sample.

keep forming stars for 1 Gyr (3 Gyr). Then, the last galaxy population which as been transformed entered the $z \sim 0.4$ clusters at $z \sim 0.5$ ($z \sim 0.9$), and the $z \sim 0.8$ clusters at $z \sim 1$ ($z \sim 1.3$). Interestingly, Tresse et al. (2007) find a transition at $z \simeq 1$ in the cosmic star formation density: it declines steeply to lower redshifts, but does not show a strong trend at higher redshifts (to $z \simeq 3$). The constant blue-to-total ratio then suggests that the star formation timescale is of the order of 3 Gyr.

The constant blue-to-total ratio in the poor groups could suggest a similarly slow quenching of star formation in these environments as in clusters. The lack of a population of old galaxies in poor groups could be explained by a much more recent formation time of these systems. Once again, the field sample is not consistent with this picture: according to the findings of Tresse et al., the blue-to-total ratio should follow the "downsizing" scenario and decrease towards lower redshifts (unlike for the clusters and the poor groups, there is no accretion process for the field, and no environmental quenching of star formation).

5.2.7 Radial dependence of the galaxy population mix

From the red and blue fractions we have found few significant differences between the four EDisCS composite clusters. Thus, also a single composite cluster should be a good representative average cluster. This maximizes the number of galaxies, allowing a more detailed study of the mix of galaxy populations, similar to the study of the local sample in Chapter 4.

In Fig. 5.14 we show the fractions of galaxies identified as red, green, and blue (according to their PC1 value) as a function of distance from the BCG of their respective cluster (note that BCGs selected according to their luminosity, color, and position are only available for the 18 systems presented in White et al. (2005), for the others, simply the brightest spectroscopic member is used; see also Milvang-Jensen et al. (2007)).

Within R_{200}, there is a clear dependence of the relative contributions on clustercentric radius (and thus on local density): the cluster core is dominated by red galaxies. The fraction of red galaxies decreases by almost a factor of two from the cluster core to R_{200}, while the number of blue and green galaxies increases. In particular the "blue fraction", which takes into account also low-mass blue galaxies changes from almost zero to more than 50% at $\sim 1 - 3R_{200}$. The number of green galaxies on the other hand changes only within the very cluster center ($R \lesssim 0.1R_{200}$), and is almost constant beyond the core. This is remarkably similar to our results at low redshifts (Sect. 4.4.1), where we also found the number of green galaxies to be approximately constant from the field to within $\sim 0.5R_{200}$ (unfortunately, the quantitative green fractions cannot be compared directly because of the aperture bias and the different definitions of the blue sequence and green valley).

Only few of our fields extend beyond $\sim 1-3R_{200}$, and thus we cannot probe the distributions further outwards. Still, the galaxy mix at $\sim 1 - 3R_{200}$ is similar to that in the average field. In the local sample, we found that a notable change in the galaxy population occurs at $\sim 1 - 2R_{200}$, possibly best illustrated by the levelling off of the red fraction beyond this radius. In the EDisCS sample, the red fraction levels off already at $\sim 0.5R_{200}$. On the other hand, the "blue fraction" increases noticeably until $\sim 2R_{200}$, as in the SDSS sample. It should also be kept in mind that the red fraction in the high-z field sample is surprisingly
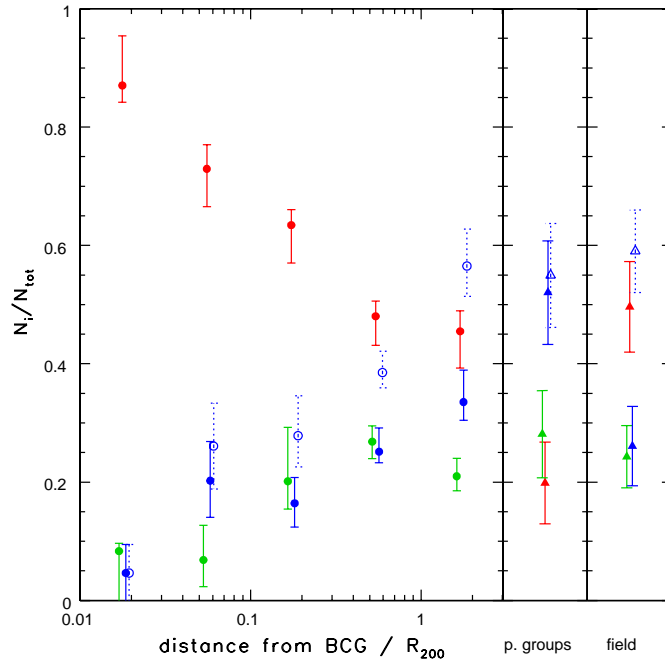
Figure 5.14: The fractions of red, green, and blue galaxies in the composite cluster in bins of distance from the BCG, scaled by the virial radius. The filled symbols show the fractions of the mass-limited sample with $\log(M_\star/M_\odot) > 10.2$. The open symbols and dotted lines show the blue fraction if the mass limit for blue galaxies is instead set to $\log(M_\star/M_\odot) > 9.6$. The respective fractions in the poor groups and the field are shown in the two panels on the right. For the clusters, the error bars are the 68% confidence intervals when boot-strapping the clusters; for the poor groups and the field, the error bars are Poissonian.

high (Sect. 5.2.5), but as low as in the poor groups at mid-z. Thus, it is only when averaging over redshift that the red fraction in the field is comparable to that in the cluster outskirts. This field evolution is unlikely to be a real effect, but rather an illustration of cosmic variance combined with the poorer number statistics of the EDisCS sample. All in all, the radial profile supports the scenario we deduced from the local clusters, that the radius at which the cluster environment starts to affect star formation is approximately $1 - 2R_{200}$.

The galaxy mix in the poor groups deviates from this picture. As we noted before, the poor groups have the lowest red fraction of all the environments we consider, and Fig. 5.14 shows that the red fraction is considerably lower than in the cluster outskirts and the average field, at $2 - 3\sigma$ significance. On the other hand, the fraction of green galaxies and the low-mass "blue fraction" are similar to these other two low-density environments. The poor groups are the sample with the least number of galaxies, and thus the poorest statistics. The "blue fraction", which is based on a larger number of galaxies than the red fraction, is constant between the cluster outskirts, poor groups, and the field. It thus suggests that all three are similar low-density environments.

5.3 Further star formation diagnostics

The classification by PC1 serves well to distinguish old stellar population, where star formation has subsided $\gtrsim$ 1Gyr ago from younger stellar populations. But there are other star formation indicators, which can characterize the star formation history on shorter timescales.

5.3.1 PC2 vs. PC1

As described in Sect. 4.2.2, the second principal component, PC2 measures the excess Balmer absorption, which arises primarily when star formation has been truncated on a very short timescale. It is therefore a sensitive indicator for stellar populations which have recently experienced a burst of star formation (*post-starbursts*).

In Fig. 5.15 we show the diagnostic diagram for post-starbursts, PC2 vs. PC1. The post-starburst classification applies only to blue and green galaxies (cf. Fig. 4.4). We place the division between star-forming and post-starburst at PC2= 0, where there is a small gap in the distribution of blue galaxies. It is important to keep in mind, however, that the distinction between the two classes is somewhat arbitrary, as there is a continuum of PC2 values rather than two distinct classes.

5.3.2 Emission lines: Comparison of recent and current star formation activity

As we have pointed out, the PCA is sensitive to the *recent* star formation history. The *current* star formation rate is better traced by emission line indicators, although these suffer the disadvantage of possible contamination from an AGN. The emission line which is linked most directly to the star formation rate is Hα; however, for high-redshift samples, this is usually shifted too far into the infrared to be observed. Instead, the [OII] line is often used as a star formation rate indicator (Poggianti et al. 2006). The strength of the line is affected by dust and metallicity, but its presence can be taken to signal active star formation (or an AGN).

In Fig. 5.16 we compare the equivalent width of the [OII] line to the PC1 classification for all our galaxies in the clusters, groups, and field samples. There is clearly a correspondence
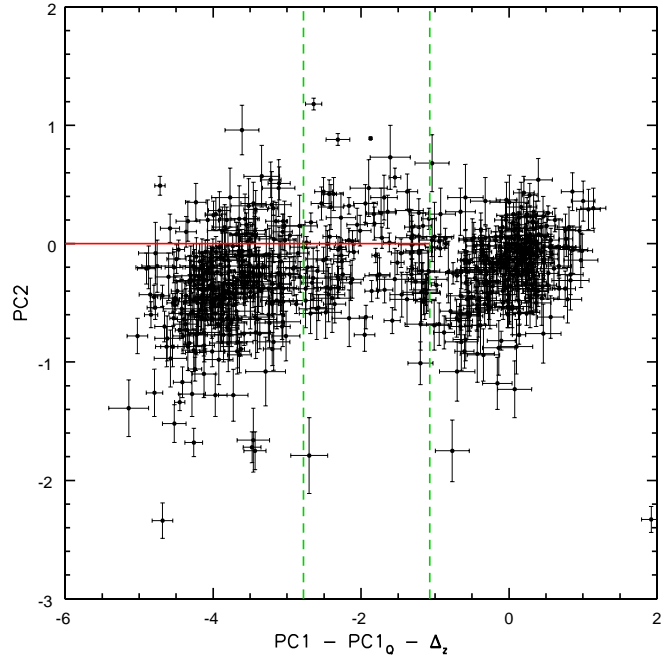
Figure 5.15: PC2 (a measure of the Balmer absorption line strength) vs. PC1, corrected for mass dependence and redshift evolution, for the galaxies in our cluster, groups, and field samples. As in Fig.5.16, the vertical green dashed lines show our classification into blue, green, and red galaxies. The horizontal red line indicates the distinction between post-starburst galaxies (PC2¿0) and (continuously) star-forming galaxies.

between the PC1 classification and the strength of the [OII] line: [OII] is detected in the majority of blue galaxies, but in only a few red galaxies, and the equivalent width increases with decreasing PC1. In Poggianti et al. (2006) we had defined EW([OII])> 3 as the division between star-forming and passive galaxies, but Fig. 5.16 suggests that this limit is very similar to requiring that [OII] is detected with at least 3σ significance.

The large equivalent widths of the [OII] emission in the blue galaxies assert that the line emission stems predominantly from (strong) star formation. Many of the green and red galaxies with [OII] detection, however, have low [OII] equivalent widths (EW([OII])$\lesssim$ 10). In these cases, the line emission could stem from Low Ionization Nuclear Emission Regions (LINERs), i.e. low-luminosity AGN. In a large sample of red galaxies from SDSS, Yan et al. (2006) find that while half of the galaxies have detectable line emission, only ∼6% have line ratios typical for star formation. In the majority of "active" red galaxies, the line emission is due to an AGN. Furthermore, Yan et al. (2006) find that about half of the galaxies in a sample of post-starburst galaxies have detectable [OII] emission, and that also in these cases, it stems predominantly from AGN emission. Only <5% of these post-starburst galaxies actually have residual star formation.

A distinction between AGN activity and star formation is not possible without further emission line measures, particularly low-ionization lines such as [NII] and Hα. However, these lines generally do not lie in the wavelength region covered by our spectra. For the moment, we will refer to these galaxies as "active", purposefully keeping the ambiguity of
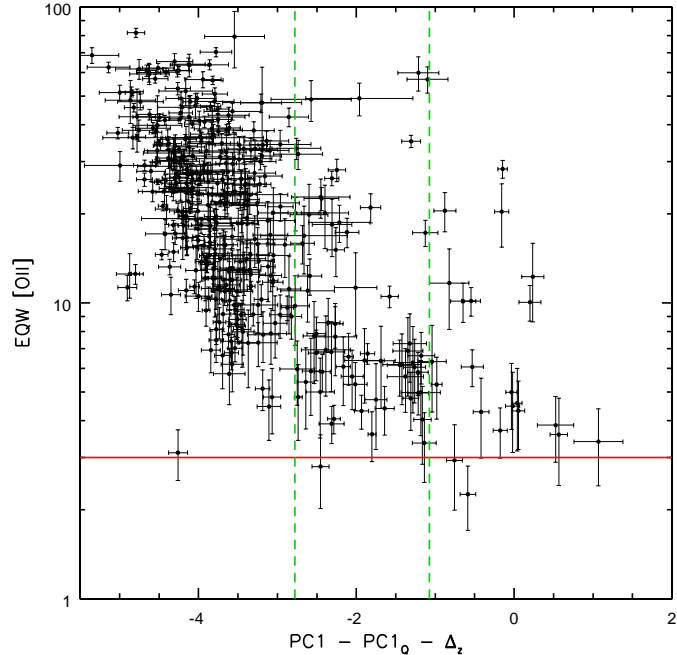
Figure 5.16: The equivalent width of the [OII] line vs. the PC1 component corrected for its mass dependence and redshift evolution. The vertical green dashed lines show our classification into blue, green, and red galaxies, whereas the horizontal red line indicates the distinction between active and passive galaxies. Galaxies are shown only if [OII] is detected with at least 3σ significance.

this term. Yan et al. (2006) argue that Hβ is better star formation indicator for high-redshift galaxies than [OII]. We will use a joint approach and classify galaxies as "active" if either [OII] or Hβ are detected with 3σ, or both with 2.5σ signficance.

5.3.3 The fraction of post-starburst galaxies

(Dressler et al. 1999) claim an unusually high number ($\sim 30\%$) of E+A galaxies in the MORPHS clusters, an X-ray selected cluster sample of intermediate redshifts. In another intermediate-redshift cluster sample, Balogh et al. (1999) find only about 1% E+A galaxies; other studies ususaly find numbers in between these two extremes (Tran et al. 2003).

In our terminology, E+A galaxies correspond to post-starburst galaxies. The classical E+A classification requires the absence of emission lines in order to exclude even low residual star formation levels. But as Yan et al. (2006) pointed out, [OII] emission in galaxies with an otherwise post-starburst spectrum may be predominantly due to AGN activity rather than star formation. The PCA classification, on the other hand, is independent of emission lines, and therefore also sensitive to post-starburst galaxies with AGNs (or residual small levels of star formation).

In Fig. 5.17 we show the fraction of post-starbursts in galaxies with $\log(M_\star/M_\odot) \geq 10.2$, as functions of the velocity dispersion and redshift of the clusters/groups. Only in a few systems is the number of post-starbursts similar to the value quoted by Dressler et al. (1999),
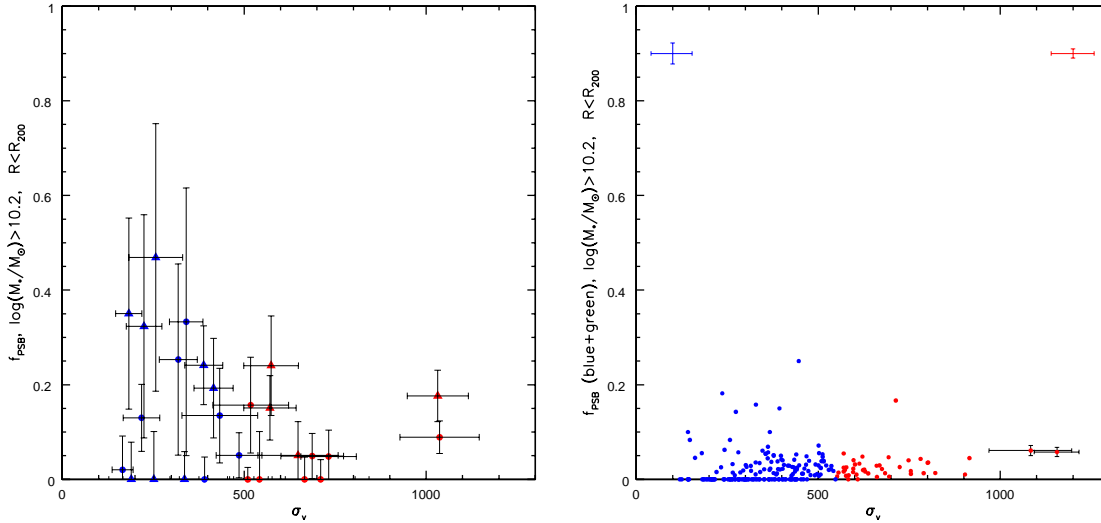
Figure 5.17: As Fig. 5.10, but showing the fraction of post-starburst galaxies relative all galaxies with masses $\log(M_\star/M_\odot) > 10.2$.

and these have rather large error bars. Overall, the fraction in the EDisCS clusters is more compatible with ∼10-20%. In the SDSS clusters, it is even lower $\lesssim 10\%$. Of course it has to be kept in mind that the definitions of post-starburst, though aiming for the same objects, are fundamentally different in the two studies. That said, our limit on PC1 is rather inclusive for even weak post-starburst signatures. Furthermore, our classification of post-starburst includes those with AGN, a population not considered in the traditional E+A classification. Our data therefore do not support the large numbers quoted by Dressler et al. (1999).

The number of post-starbursts is driven largely by the number of blue and green galaxies, as in our terminology, they are a subclasssification of the latter. For the comparison to SDSS clusters, which have generally a lower fraction of blue and green galaxies, it is therefore more interesting to investigate the *relative* post-starburst fraction, i.e. the number of post-starbursts relative to the number of blue and green galaxies. This is shown in Fig. 5.18 as function of cluster velocity dispersion, and in Fig. 5.19 as function of redshift. In the SDSS clusters, the post-starburst fraction is very low; only in one system (with 6 galaxies) is it higher than 30%. In the EDisCS sample, there is a larger amount of scatter, but many systems have higher post-starbursts fractions, with 30-50%. Interestingly, for the massive clusters, this trend is driven entirely by the high-z sample.

The increase in the post-starburst fraction with redshift is also seen in the field and the poor group environment. Thus, while we confirm previous results of an increased number of post-starbursts in high redshift clusters, our data suggests that this is mainly due to an overall increase in their numbers.
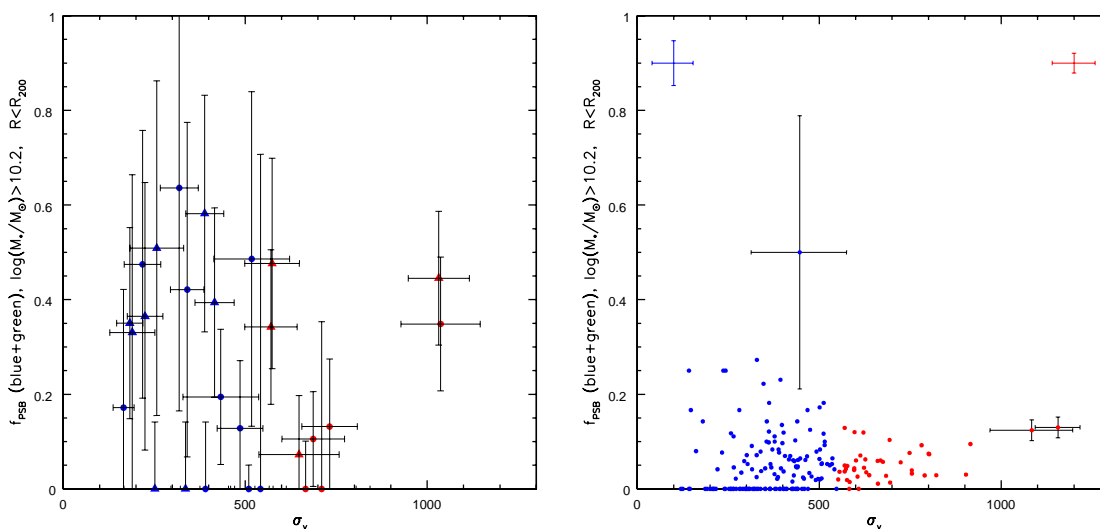
Figure 5.18: As Fig. 5.10, but showing the number of post-starburst galaxies relative to the number of blue and green galaxies with masses $\log(M_\star/M_\odot) > 10.2$.
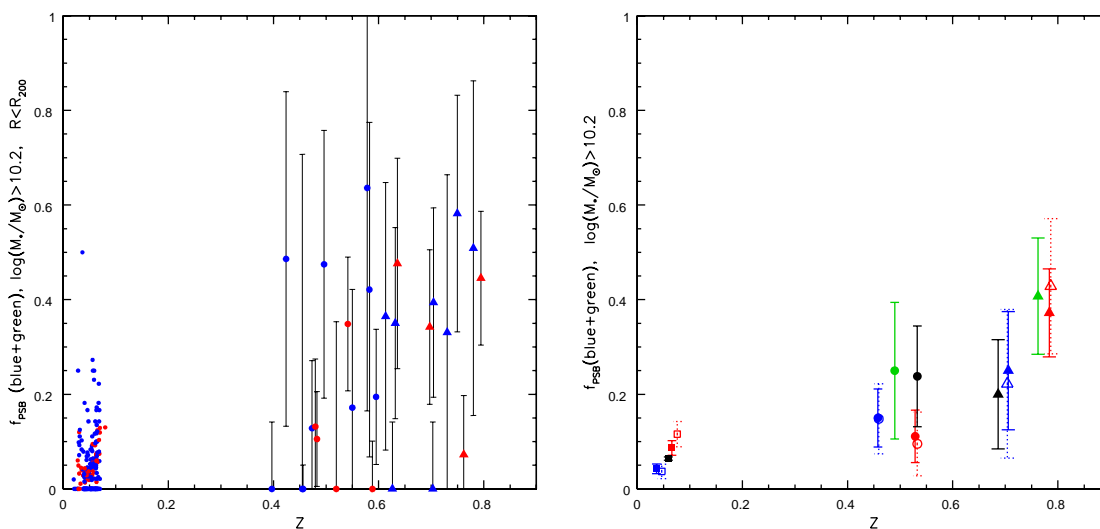

Figure 5.19: As Fig. 5.11, but showing the fraction of post-starburst galaxies relative to the number of blue and green galaxies with galaxy masses $\log(M_\star/M_\odot) > 10.2$.
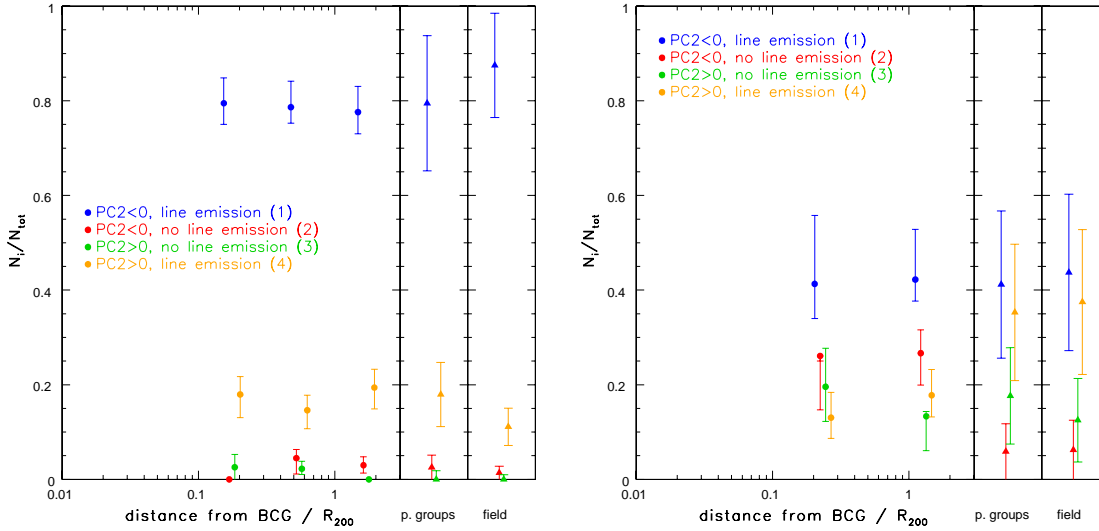
Figure 5.20: Left: the fractions of blue galaxies that are classified as active (with line emission in [OII] and/or Hβ, blue symbols); no line emission (red); post-starburst (PC2> 0) without line emission (green); and post-starbursts with line emission (orange) as function of clustercentric distance, and in the poor groups and field environment. The mass cut-off is $\log(M_\star/M_\odot) > 9.6$. Right: the same for green galaxies with $\log(M_\star/M_\odot) > 10.2$.

5.3.4 Subclasses of blue galaxies

Among those galaxies classified as "blue" by the PC1 component we can distinguish four types:

1. Galaxies with line emission ([OII] or Hβ detected with at least 3σ significance, or both lines with at least 2.5σ), but no post-starburst signature (PC2< 0). These should be the most common blue galaxies, with on-going star formation.

2. Galaxies without emission lines, and no post-starburst signature. This category should apply mainly to galaxies where star formation has subsided recently, before an excess of Balmer absorption lines becomes visible, or where the quenching timescale was too long to result in an excess of Balmer absorption lines. However, it may also pick out very dusty star-forming galaxies, where the dust suppresses the line emission.

3. Post-starburst galaxies (PC2> 0) without emission lines. In these galaxies, star formation has been quenched on short timescales.

4. Post-starburst galaxies with emission lines. The line emission may stem either from residual star formation or from an AGN.

In Fig. 5.20 we investigate the contributions of these four subclasses to the number of blue galaxies more massive than $\log(M_\star/M_\odot) > 9.6$ as a function of clustercentric distance. Indeed, the majority of blue galaxies are associated with emission lines. This applies to all environments - in fact, the relative fractions of all four subclasses are remarkably constant over all environments. This is quite similar to our results at low redshifts (Sect. 4.4.2), where

we found the fraction of post-starburst galaxies to be constant with clustercentric radius and only a weak decline of the typical star formation rate towards the cluster center.

The overall number of blue galaxies declines steeply towards the cluster center (Fig. 5.14), but the process(es) which shut off star formation in infalling galaxies do not cause in increased number of "disturbed" blue galaxies - galaxies with a post-starburst signature and/or a lack of emission lines. Fig. 5.14 suggests that blue galaxies are transformed first to green galaxies, then to red galaxies, on timescales somewhat shorter than the cluster crossing time, i.e. Gyr. To follow the evolution of galaxies, it is thus important to track the galaxies as they leave the blue sequence. As star formation ceases, they move into the green valley; if star formation is truncated on a short timescale, they also show post-starburst signatures. But with the cessation of star formation the number of bright, young stars declines rapidly, and the galaxies fade. Thus, only the most massive ones are detectable in the green valley. We can distinguish the same four sub–classes of green galaxies as for blue galaxies. In the right panel of Fig. 5.20 we show the contributions of these four subclasses in radial bins, for galaxies with $\log(M_\star/M_\odot) > 10.2$ (the distributions of blue galaxy subclasses is similar for this mass cut as for the lower mass cut we used, therefore we can relate the two distributions). Unlike for the blue galaxies, the population mix of green galaxies shows a slight dependence on environment: the fraction of galaxies with a post-starburst signature (PC2>0) and emission lines is smaller in the cluster, whereas the fraction of galaxies with PC2<0, and no emission lines is larger in the cluster. It is not easy to connect these two classes with a single evolutionary model, and any attempt would be quite contrived. Possibly, there are two processes involved: the low–density field and poor groups environment may be more efficient at triggering post-starbursts e.g. by an increased merger rate. On the other hand, we have argued that star formation in the cluster is not shut off immediately, i.e. without inducing post-starburst signatures. Galaxies with an exponentially declining star formation rate would move to the green valley, and at the same time, the star formation activity would decline and fall below the threshold.

The majority of green galaxies have emission lines, although the fraction is lower than for blue galaxies. In the local sample, we found that $\gtrsim 50\%$ of green galaxies host an optical AGN. This might be the case also for the EDisCS galaxies, although we lack other emission lines to fully classify them into star-forming / AGN. But very few galaxies in our sample have a post-starburst signature, and no emission lines, which would correspond to the classical 'E+A' classification. Our data do not support previous claims that post-starbursts are associated with the cluster environment.

5.3.5 Tightness of the red sequence

In Sect. 5.2.3, we remarked on the tightness of the red sequence in the mid-z sample compared to the high-z sample. We have verified that this is not simply due to larger errors on PC1 in the high-z sample: due to the longer exposure times in the high-z masks, the errors are comparable in both samples.

PC2 and the emission lines provide further tools to investigate the star formation history/activity, although it must be cautioned that this PCA is not designed to investigate the properties of quiescent galaxies - it is sensitive to the star formation history within the past $\sim 2\mathrm{Gyr}$, not necessarily for longer timescales.

In Fig. 5.21 we investigate PC2 as a function of stellar mass for red galaxies with SNR$\geq$4, for both the EDisCS and SDSS samples. In the SDSS sample, the region in PC2 – stellar mass space populated by galaxies is roughly triangular, with an approximately constant upper
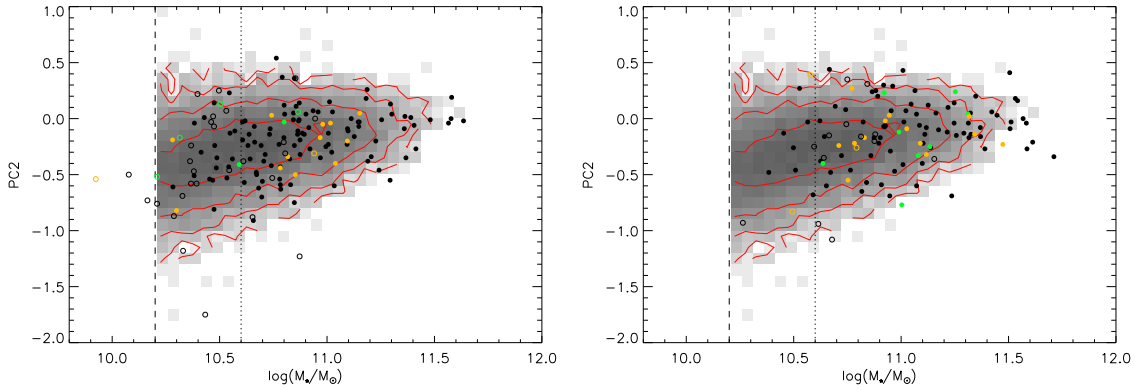
Figure 5.21: PC2 against stellar mass for galaxies on the red sequence in the SDSS sample, the mid-z sample (left) and the high-z sample (right). The distribution of SDSS galaxies is shown as logarithmic grayscale and red contours in both panels. For the EDisCS galaxies, the color-coding is the same as in Fig. 5.3. Only galaxies with SNR$\geq$4 are shown; those with 4$\leq$SNR$<$5 are shown as open symbols. The dashed line shows the mass cut-off at $\log(M_\star/M_\odot) \geq 10.2$, the dotted line the mass cut-off used for the next Figure, $\log(M_\star/M_\odot) \geq 10.6$.

limit, and tapering towards higher masses. In effect, there is a slight trend of increasing PC2 with increasing mass. The distribution of EDisCS galaxies in the mid-z sample is similar to the SDSS distribution, apart from the deficit of galaxies at lower masses. Remarkably, the scatter in the high-z sample is larger than in the mid-z sample, similar to PC1.

Fig. 5.22 shows the PC1-PC2 diagram for red galaxies with $\log(M_\star/M_\odot) \geq 10.6$. Above this mass, the red sequences in both EDisCS samples are well populated (cf. Fig. 5.6). The mass dependence in PC1 is taken into account, but PC2 shows too little trend with mass to correct for. Fig. 5.22 demonstrates that the locus of the red sequence shifts between the two samples. The locus of galaxies of red galaxies in the mid-z sample approximately coincides with the locus of red galaxies in SDSS. In the high-z sample, this clearly not the case: the locus is shifted to lower PC1 values (which we take into account with Δ_z), and has a more elongated shape: along the locus, PC2 correlates with PC1.

The PCA we have applied is not designed to investigate red galaxies, and so the interpretation of this locus shift is difficult. Wild et al. (2007) found that variation along the red sequence in PC2-PC1 space is mainly due to stellar mass. However, the mass distribution above $\log(M_\star/M_\odot) \geq 10.6$ in the two samples is sufficiently similar to rule out stellar mass as the main driver of the difference. Also, the mass dependence in PC1 has been accounted for by using PC1-PC1$_Q$, whereas we don't find a significant dependence of PC2 on stellar mass. Could the locus shift be due to "frosting", low levels of star formation in otherwise old stellar populations? This could possibly explain the lower PC1 in the high-z sample. In Fig. 5.22 we identify those galaxies with detectable [O$_{II}$] and/or Hβ emission. But line emission does not seem to correlate with position on the PC1-PC2 diagram, and thus there is no strong indication that the locus shift of the red sequence is driven by star formation activity. It would be interesting, but is beyond the scope of this work, to investigate these galaxies with other tools, such as a PCA tuned for quiescent galaxies (e.g. Rogers et al. 2007).
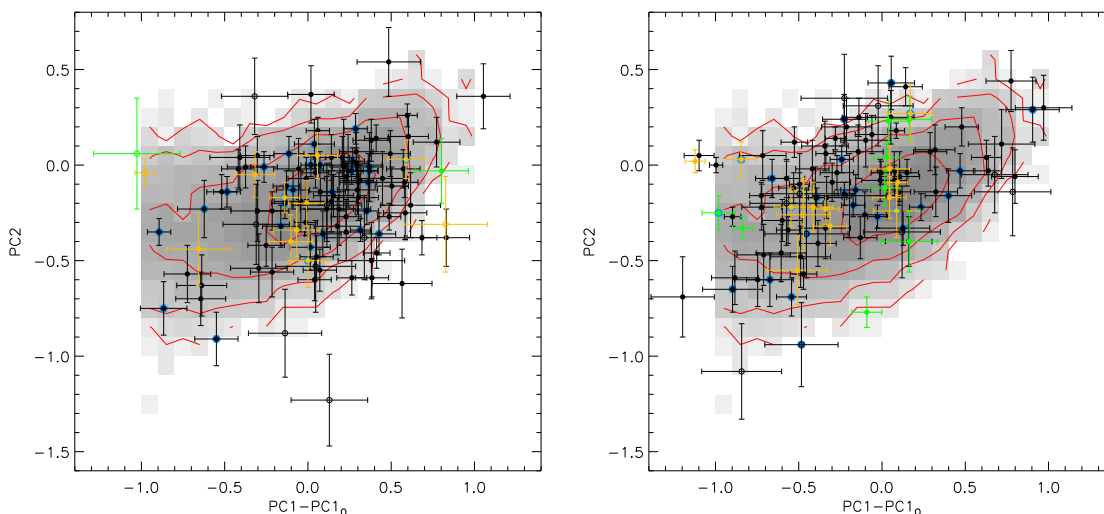
Figure 5.22: PC2 vs. PC1-PC1$_Q$ for galaxies on the red sequence in the SDSS sample, the mid-z sample (left) and the high-z sample (right). Only galaxies with $\log(M_\star/M_\odot) \geq 10.6$ and SNR≥ 4 spectra are shown. The distribution of SDSS galaxies is shown as underlying grayscale and red contours - for SDSS, PC$_Q$ refers to the ridge of the red sequence (Sect. 4.3.3). The color and symbol coding for EDisCS galaxies is the same as in Fig. 5.21. Galaxies in which either [OII] or Hβ have been detected with at least 3σ significance (or both lines with 2.5σ) are marked with blue circles.

5.3.6 Active red galaxies

From Fig. 5.16 we see that some of the red galaxies display an [OII] emission line, due to residual star formation or AGN activity. In Fig. 5.23 we investigate the contribution of these galaxies to the number of red galaxies as a function of clustercentric distance. Galaxies are considered "active" if either [OII] or Hβ is detected with at least 3σ significance, or both lines with at least 2.5σ. The same classification is applied to the SDSS "red" galaxies[1]. For the SDSS galaxies, it is possible to classify the line emission according to whether it originates from AGN activity or star formation. Hence, we distinguish between pure AGN line emission and emission with at least some contribution from star formation.

The fraction of line-emitting galaxies roughly 20% with a slight dependence on environment. In both samples, the fraction of "active" red galaxies clearly declines towards the cluster core (this is more significant in the SDSS sample due to the better number statistics. In the SDSS sample, the contributions from star-forming galaxies and from pure AGNs are roughly similar, but it is interesting to note that in the field and the cluster outskirts there are more AGNs than star-forming "active" red galaxies.

5.4 Summary and Discussion

We have investigated the stellar population of galaxies in the EDisCS high-redshift cluster sample and a local comparison cluster sample drawn from SDSS. For the slit-based spectra in

---

[1]We have applied the scaling to the formal error bars (2.2 for the errors in [OII] and 1.9 for the errors in Hβ) as suggested on `http://www.mpa-garching.mpg.de/SDSS/DR4/raw_data.html`.
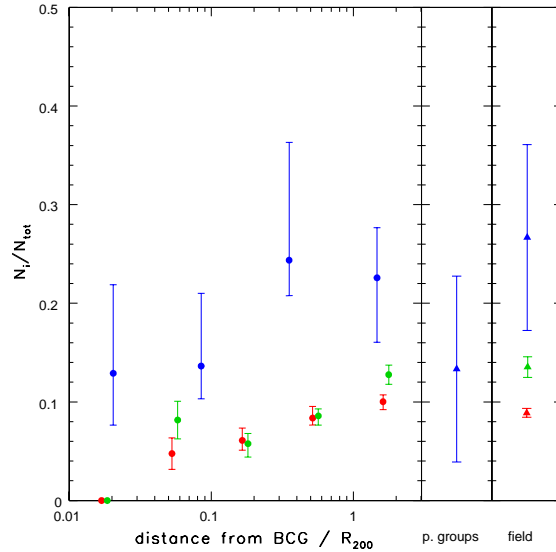
Figure 5.23: For red galaxies, the fraction of "active" galaxies, i.e. with [OII] line emission. The blue circles denote the EDisCS sample; the red circles the SDSS sample where the line emission is from a pure AGN; the green circles the SDSS sample where there is at least some contribution from star formation to the line emission (i.e. star-forming or composite objects). As in Fig. 5.14, the fractions in the poor groups and in the field are shown as lines at the outer radii.

the EDisCS dataset, the Principal Component Analysis of Wild et al. (2007) splits the galaxies into distinct, and largely parallel red and blue sequences. This is different for the low-redshift SDSS sample, where the blue sequence approaches the red sequence for higher galaxy masses. This reflects the aperture bias in the fiber-based SDSS survey. Nonetheless, galaxies can be classified as red (or blue) relative to the ridgelines of the red and blue sequences in both samples. This is the basis for our comparison of the numbers of galaxies with old/young stellar populations as function of redshift.

Qualitatively, the galaxy populations of clusters at redshifts $z \sim 0.08$, $z \sim 0.4$, and $z \sim 0.8$ are quite similar: for galaxy masses $> 10^{10.2} M_\odot$ (our mass completeness limit), the majority of cluster galaxies have stellar populations older than $\gtrsim 2 \mathrm{Gyr}$ ("red galaxies"). The red fraction evolves slightly from $\sim 60\%$ at $z \sim 0.8$ to $\sim 80\%$ at $z \sim 0.08$. The star formation–radius relation which we have observed at low redshifts (Sect. 4.4.1) is largely in place already at high-redshifts: also here, $\sim 90\%$ of the galaxies in the core are red. Also the transition radius, $\sim 2 R_{200}$, is similar in both samples.

The fraction of post-starburst galaxies increases with redshift, but it does so in all environments. Furthermore, the number of post-starburst galaxies as fraction of blue and green galaxies is constant with cluster radius, as we found also in the low-redshift sample. Post-starburst galaxies are therefore not a galaxy population connected to the cluster environment. If anything, we find that they are more common in low-density environments such as the field and the poor groups.

For the low-redshift clusters, we had argued that these trends indicate that the timescale on which star formation is quenched in infalling galaxies is similar to the cluster crossing time, i.e. of the order of a few Gyr. The same argumentation can be applied to the high redshift

sample. The average physical properties of clusters are therefore similar over the redshift range we studied. In the low-redshift sample, support for a slow quenching of star formation comes from the factor ~ 2 decrease of the star formation rate of galaxies with young stellar populations. For the high-redshift spectra, we have probed the current star formation only by the presence/absence of the [OII] and/or Hβ emission lines (either of these scales to star formation rate only with much more uncertainty than Hα, on which the low-redshift star formation rate measurements are largely based). Within the error bars, we have not detected a decrease in the number of galaxies with emission lines towards the center. However, support for a timescale of ~ 3Gyr comes from the number of blue galaxies (extended to lower masses) compared to the total number of galaxies: this is approximately constant, and if it truly reflects an infalling galaxy population, then this is consisten with the star formation density of the field only if $\gtrsim 3$Gyr pass between infall and termination of star formation.

In Poggianti et al. (2006) we also assumed that the timescale to quench star formation is ~ 3Gyr. In that work, we found that in EDisCS clusters with low velocity dispersion ($\sigma < 550$ km/s), more than half of the galaxies display [OII] lines. Interpreting the [OII] emission to trace star formation, this led us to conclude that the quenching of star formation is not efficient in low-mass clusters. However, as Popesso & Biviano (2006) point out, [OII] emission from galaxies in low-mass clusters is predominantly due to AGN activity, at least in local clusters. Indeed, in the present work we find that while there is large scatter for individual systems, the *average* number of galaxies with young stellar population does not depend on the mass of the host cluster. This implies that the threshold mass beyond which galaxy groups/clusters quench star formation is lower than we had deduced in Poggianti et al. (2006). Since we observe a significantly higher number of galaxies with young stellar populations in the poor groups, this threshold must lie close to the transition between these and our low-mass cluster, i.e. at ~ 200km/s.

Possible processes which can quench star formation on a timescale of 3Gyr are strangulation and galaxy harassment, although the latter is only a candidate if it is not associated with a significant starburst. To distinguish between the two requires additional information, namely morphology. The morphology of EDisCS galaxies has been studied in Desai et al. (2007) and Simard et al. (2007). Simard et al. found that for clusters with $\sigma > 600$km/s, the fraction of early-type galaxies anti-correlates with the fraction of [OII]-emitting galaxies. This suggests that in high-mass clusters, the quenching of star formation and the morphological transformation to an early-type galaxy are closely related processes, and take place on similar timescales. There is no such correlation for lower mass clusters, which Simard et al. have used to assert that the timescale for morphological transformations must be longer than that for star formation, with the argumentation that galaxies in low-mass clusters have typically spent less time in high-density environments than galaxies in high-mass clusters, and that this time falls between the (shorter) star formation quenching timescale, and the (longer) morphological transformation timescale. However, the lack of any correlation may simply be due to the increased AGN contamination in low-mass clusters found by Popesso & Biviano (2006). Using HST-based morphologies, Desai et al. find a correlation in the morphological content of the $z \sim 0.8$ clusters with velocity dispersion. From the present work, there is no indication for a correlation between the galaxy population content and the cluster velocity dispersion. This suggests that the efficiency of morphological transformations may depend differently on the environment than the quenching of star formation.

However, it must be cautioned that these EDisCS studies use slightly different selection effects (e.g. luminosity-limited vs. mass-limited), and the studies of Poggianti et al. and

Desai et al. add data from other cluster samples. Before conclusive evidence can be drawn from these different results, the dataset must be homogenized. The most straightforward method for this is to combine the present work, which works with a mass-limited sample, and makes no assumptions on the origin of [OII] emission, with the morphology measurements from Simard et al..

6

Discussion and outlook

This thesis has underlined the importance of environmental influences on the evolution of galaxies. I have shown that the assembly of Brightest Cluster Galaxies (BCGs) must be tightly linked to the assembly of the host cluster, and that there is a strong correlation between the star formation properties and distance from the cluster center, which is valid in local clusters to redshifts of (at least) $z \sim 0.8$.

These results are consistent with a hierarchical scenario in which larger structures grow by merging of smaller structures. The properties of local BCGs suggest that they have formed through a multitude of gas-poor mergers. As galaxies are accreted onto clusters, their star formation subsides on a timescale similar to a cluster crossing time, i.e. a few Gyrs. This suggests that the quenching of star formation takes place gradually, without the need of disruptive, short-term processes. The removal of the hot gas reservoir of infalling galaxies (strangulation) is likely to play a large role in this, but a contribution from weak galaxy-galaxy interactions (harassment) cannot be ruled out without further information on morphological transformations.

These conclusions can be reached both from local, as also from high-redshift clusters. There is therefore no need to evoke evolutionary trends in cluster properties which may affect infalling galaxies differently as function of cosmic time. The higher fractions of star-forming galaxies in high-redshift clusters may be simply attributed to a higher star formation density in the infalling galaxy population, as well as a higher infall rate.

This thesis also provides several starting points for future studies:

One of the key results of the study of Brightest Cluster Galaxies (BCGs) is the possible higher dark matter fraction in these galaxies. This conclusion was reached under the assumption that elliptical galaxies are a homologous class of galaxies, i.e. that their density profiles are self-similar. To truly distinguish between non-homology and a different dark matter fraction requires further investigation. Spectroscopy with Integral Field Units (IFUs) provides spatially resolved kinematic information, and in conjunction with high resolution optical imaging can be used to constrain the galaxy density profiles and thus directly deter-

mine the dark matter fraction (e.g. Cappellari et al. 2006). A study of a sample of BCGs and matched non-BCGs could therefore confirm (or refute) a higher dark matter fraction in BCGs. Such a study could be further extended to BCGs with multiple nuclei, in order to determine whether these are simply galaxies seen in projection, or indeed on-going mergers. Determining the merger rate of BCGs is an important constraint for the hierarchical scenario, where BCGs are assembled primarily by dry mergers. As part of the merging process, also the central black holes of the merging galaxies are bound to merge. For some timespan, the merger remnant could thus host two supermassive black holes. Gerke et al. (2007) found evidence for a spatially well separated, dual AGN in a high-redshift, massive elliptical galaxy. If BCGs are indeed prone to frequent mergers, then the sample of local BCGs could host such systems. Several of the BCGs in my sample have unusually low Balmer decrements, and inspection of their spectra reveals that at least in some cases, this is due to double-peaked emission lines, which are not accounted for in the emission line fitting algorithm. These galaxies are the prime candidates to identify further dual AGN. Again, an IFU study could reveal any spatial offset between the emission line sources. I have applied for an ESO short programme for a pilot IFU study of seven BCGs, which addresses these issues. If this proves to be successful, the program could be extended to a larger sample of BCGs and a comparison sample of non-BCGs.

For the cluster galaxies in the local sample, I have concentrated on the relation between distance from the cluster center and the star formation properties. Although I was able to identify the timescale on which star formation is quenched in infalling galaxies, this study alone cannot determine if, and how, morphological transformations are associated with the quenching of star formation. By extending this study to the morphologies of cluster galaxies, this could be further constrained. Furthermore, while the properties of a composite cluster are now well constrained, the scatter of individual systems from the average properties needs to be quantified.

Also for galaxies in the EDisCS clusters, star formation and morphology have so far been studied largely independently. With the present work and the bulge-to-disk composition of Simard et al. (2007), the data are readily available for a study which takes into account both the star forming properties and morphology of cluster galaxies.

An intriguing result of the study of the EDisCS galaxies is the systematically different distribution of quiescent galaxies in the high-redshift and the mid-redshift subsamples in terms of the first two principal components of the PCA. From this study alone, the physical origin for this difference is not clear, and the population of these galaxies needs to be studied with further tools, e.g. a broader range of spectroscopic indices, or a PCA specifically designed to study old stellar populations.

Some of the interpretation at high redshifts has been hampered by the small number of field galaxies in the EDisCS sample. In order to securely quantify the contrast between cluster and field environment also at high redshifts, the PCA analysis of recent star formation histories needs to be extended to field samples at high redshifts, such as the VIMOS-VLT Deep Survey (Le Fèvre et al. 2004) and DEEP2 (Davis et al. 2004). Together, these datasets provide powerful tools to study the environmental effects on galaxies over a large range in cosmic time.

A

Improving SDSS Magnitudes for BCGs

As described in Sect. 2.2.2, we need to correct the photometry of the BCGs and around 200,000 galaxies at $z \lesssim 0.1$ for the fact that the standard SDSS photometric pipeline overestimates the sky background.

The SDSS photometric pipeline PHOTO estimates the `global sky` within a frame (2048×1498 pixels; $13\rlap{.}'5 \times 9\rlap{.}'8$) from the median value of the pixels in that frame, clipped at 2.3σ. The `local sky` background is then determined with the same sigma–clipping within a box of 256×256 pixels ($1\rlap{.}'7 \times 1\rlap{.}'7$) on a grid every 128 pixels, and interpolated between these positions. This sky estimate is then subtracted from the image, and the photometry is performed on the sky-subtracted image.

If a large fraction of the pixels in a 256×256 pixels box is part of an object rather than blank sky, this procedure causes the `local sky` to be an overestimate of the true sky background. This may happen for large galaxies, in crowded fields, and also around stars, since the wings of the PSF result in a considerable stellar halo.

An overestimation of the sky background results in an underestimate of the surface brightness of the object's pixels – thus, the total effect this has on the flux of an object scales with the square of its radius. This effect is therefore particularly severe for large galaxies. Indeed, Lauer et al. (2006) analyze the photometry of BCGs analyzed in Postman & Lauer (1995) that lie in the SDSS DR4 and show that the discrepancy in the estimated luminosity is a function of BCG radius (see also below).

It has been suggested that the true flux of an object may be recovered by using the `global sky` estimate instead of the `local sky` estimate (Masataka Fukugita; SDSS mailing list). This approach should allow a new flux measurement without performing a new, independent photometric analysis of the raw images. For each object, the 1D radial surface brightness profile, measured in 15 radial bins, is available. By adding the difference between `local sky` and `global sky` to these surface brightnesses, the flux of an object, assuming the `global sky` level in the respective field, can be measured.

A.1 Neighboring objects

For isolated objects, the above argument implies that the `global sky` is generally a better sky estimate than the `local` one. However, for blended objects, we find that the `local sky` accounts for a large fraction of the flux from the respective neighbors; in these cases, therefore, using the `global sky` estimates would include flux from the neighbors and thus lead to an overestimate of the luminosity of the object. This is particularly true if the neighbor is a star of similar brightness to the object in question.

We thus need a 'trigger' to determine for which objects the `local sky` should be kept, and for which it should be replaced by the `global sky`.

We make the trigger for each galaxy i a function of the ratio LR_i of its luminosity L_i to the luminosity L_{nb} of its neighbors (within $1'.6$), defined in the following way:

$$
\begin{aligned}
\mathrm{LR}_i &= -2.5 \log \left(L_i \,/\, L_{\mathrm{nb}} \right) \\
L_{\mathrm{nb}} &= \frac{\sum\limits_{j \in \{\text{galaxies}\}} L_j w_j}{\sum\limits_{j \in \{\text{galaxies}\}} w_j} + 10 \, \frac{\sum\limits_{j \in \{\text{stars}\}} L_j w_j}{\sum\limits_{j \in \{\text{stars}\}} w_j} \\
w_j &= \mathrm{e}^{-\frac{d_{i,j}^2}{2\left(2 r_{p,i}\right)^2}}
\end{aligned}
$$

where $r_{p,i}$ is the petrosian radius of the galaxy i, and $d_{i,j}$ is the distance between galaxy i and its neighbor j. Thus, the contribution of a neighbor to L_{nb} is weighted by a Gaussian of width equal to twice the petrosian radius of the galaxy i – this is the aperture within which the SDSS petrosian flux is measured. Since we find that the presence of a star close to the object results in a substantial overestimate of the galaxy luminosity if the `global sky` is used, stars are weighted with an additional factor of 10 (the exact value of this factor makes only little difference, but we do find slightly better results using a factor of 10 rather than 5). We suspect that the stellar halo due to the broad PSF wings is accounted for primarily as `local sky` background.

We find that for $\mathrm{LR}_i < -2.5$, the flux of neighboring objects is negligible enough for the `global sky` to be the superior sky estimate. For $\mathrm{LR}_i > -1$, the flux of neighboring objects contributes a substantial fraction of the `local sky` estimate, so that it cannot be substituted by the `global sky`.

A.2 The method

Rather than simply substituting the `global sky` for the `local sky` (or not), we calculate the fraction f_{sky} of the difference between `local` and `global sky` to be added to the surface brightness profile of each galaxy according to the following criteria:

1. If $\Delta_{\mathrm{sky}} = \mathrm{sky}_{\mathrm{local}} - \mathrm{sky}_{\mathrm{global}} < 0$ in any one of the five bands, then $f_{\mathrm{sky}} = 0$. In these cases, the two sky measurements are essentially equivalent, and subtracting flux from the surface brightness profile will add noise to the flux measurement.

2. Values of Δ_{sky} are constrained to be $\leq 10^{-9}$ maggies arcsec^{-2} ('maggie' is the linear measure of flux used for the profiles; see Stoughton et al. 2002).

3. The maximum value for f_{sky} is 0.7 . In Sect. A.4 we show that this is superior to using $f_{\mathrm{sky}}^{\mathrm{max}} = 1$. This value is assigned to objects with $\mathrm{LR}_i \leq -2.5$.

4. The minimum (non-zero) value for $f_{\mathrm{sky}}^{\mathrm{min}}$ is 0.1 . This value is assigned to objects with $\mathrm{LR}_i \geq -1$.

5. For objects with $-2.5 < \mathrm{LR}_i < -1$, f_{sky} is a linear function of LR_i, being continuous at the endpoints with $f_{\mathrm{sky}}^{\mathrm{max}}$ and $f_{\mathrm{sky}}^{\mathrm{min}}$.

A.3 Comparison for the BCGs of Postman & Lauer (1995)

In order to assess the performance of our method to correct the SDSS magnitudes, we need (an) external dataset(s) with accurate photometry. We rely on two such datasets: the aperture photometry of BCGs published in Postman & Lauer (1995, referred to as PL95 hereafter), and the 2MASS survey (Skrutskie et al. 2006). The method is considered successful if it can simultaneously reproduce the curve-of-growth of a large fraction of the PL95 BCGs, and if galaxies do not show any systematic bias in their median SDSS–2MASS colors.

In Fig. A.1 we demonstrate that our method can reproduce the aperture photometry of the PL95 BCG sample. Of the 119 BCGs in that sample, 35 have imaging data from DR5, and 12 are also in our BCG sample (which was based on DR3). We show the curve-of-growth of six representative BCGs in Fig. A.1. We assume $r' - R_C = 0.25$ as the typical color of an elliptical at $z = 0$ (Fukugita et al. 1995) in order to compare measurements taken in different bands.

The examples show how the original SDSS photometry breaks down at radii larger than $\sim 20''$. Our improved photometry is able to reproduce the PL95 aperture photometry much better, out to $\gtrsim 80''$. Of the 12 BCGs in common with our sample, our photometry fails to accurately reproduce PL95 only for the BCG of Abell 160 (C4_DR3_2025): this is because PHOTO attributes a large fraction of the BCG luminosity to a secondary nucleus; hence LR is rather large, and only little sky background is added to the brightness profile. Of the 35 BCGs in DR5, this is also the case for the BCG of Abell 1185 (not shown). The crowding in the fields around the BCGs of Abell 2040 and Abell 2052 also leads to an underestimation of the flux by about 0.2 mag (not shown).

In addition to bad sky subtraction, noise in the surface brightness profile plays an important role particularly at large radii, as can be seen in the curve-of-growth of the BCG of Abell 779 (Fig. A.1). The last non-zero bin of the SDSS surface brightness profile causes a jump in total magnitude of more than 0.5 mag, which is not seen in the PL95 photometry. To avoid such jumps, we compare the cumulative flux for each bin of radius $\geq 18''$ to the flux predicted for that bin from the slope of the curve-of-growth from the two bins prior in radius. If the flux is more than 30% larger than predicted (or if the surface brightness in the respective bin is negative), the measured flux is substituted by the predicted flux. For several BCGs this procedure improves the agreement between the SDSS and PL95 brightness profiles. For one (the BCG of Abell 2147), this causes disagreement at large radii. However, this occurs at a significantly larger radius than the one within which we measure the magnitudes.
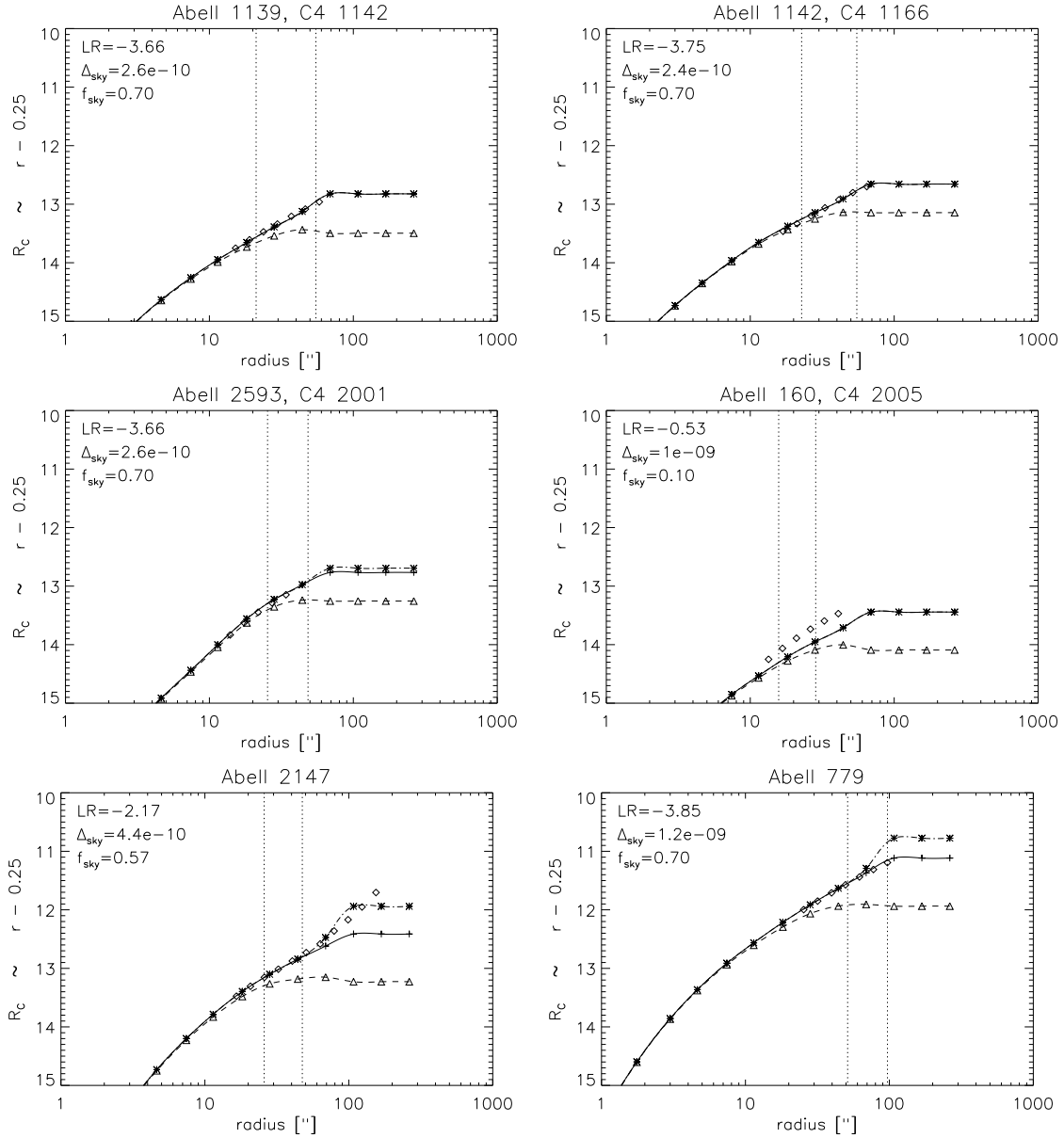
Figure A.1: Comparison of the aperture photometry of Postman & Lauer (1995) (shown as diamonds) and SDSS photometry for 6 BCGs. The uncorrected SDSS magnitudes are shown as triangles, with the respective cubic spline fit as a dashed line. By adding flux of $f_{sky}\Delta_{sky}$, we obtain the curve-of-growth shown by + symbols and as dash-dotted line. Noisy photometry at large radii can cause jumps in the curve-of-growth; this can be alleviated by the method described in the text, and is shown as $\times$ symbols, and as solid line. The dotted lines indicate the radii at which the surface brightness profile reaches a magnitude of $r = 23 \, \mathrm{mag}/\square''$ (left line) and $r = 24 \, \mathrm{mag}/\square''$ (right line).
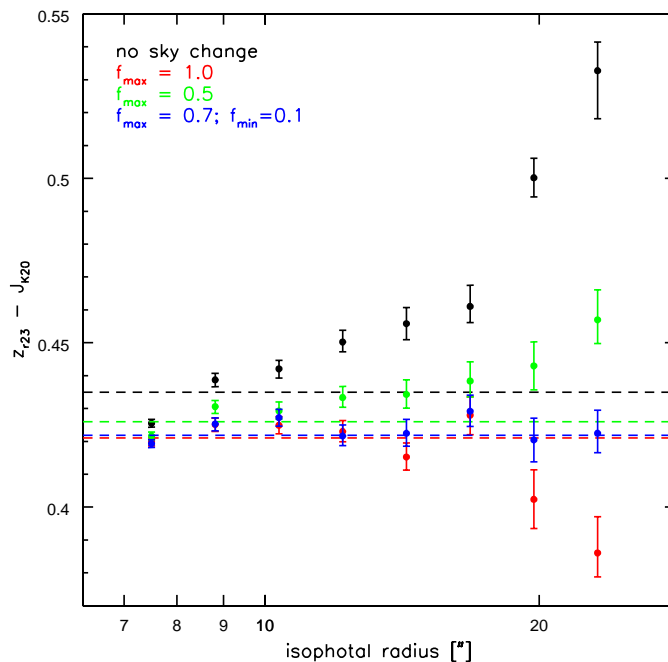
Figure A.2: The difference between SDSS z magnitude (measured within the $r = 23\,\mathrm{mag}/\square''$ radius) and 2MASS J magnitude (measured within the $K = 20\,\mathrm{mag}/\square''$ radius) as a function of galaxy size (given by the $r = 23\mathrm{mag}/\square''$ isophotal radius). We measure the median difference in bins of radius; the error bars denote the 68% levels of the distribution in each bin, divided by the square root of the number of galaxies in that bin. For the black symbols, the sky subtraction has not been changed from the original SDSS value. For the red symbols, $f_{\mathrm{sky}}^{\max} = 1.0$, i.e. if an object meets the criteria to replace the `local` by the `global sky`, the full difference is added (see Section A.2 for details). For the green symbols, $f_{\mathrm{sky}}^{\max} = 0.5$, and for the blue symbols, $f_{\mathrm{sky}}^{\max} = 0.7$ and $f_{\mathrm{sky}}^{\min} = 0.1$. The dashed lines show the median values for all galaxies.

A.4 Comparison to 2MASS magnitudes

Of the 200,000 unique SDSS galaxies at $z < 0.1$, about half have a counterpart in the 2MASS survey's Extended Source Catalog (XSC); we made use of the list of 2MASS objects matched to SDSS galaxies provided via the NYU VAGC (Blanton et al. 2005b) to identify these galaxies and obtain their 2MASS properties.

In order to be able to directly compare the SDSS and XSC data, we work with isophotal magnitudes. One of the magnitude measurements provided by 2MASS is measured within the $K = 20\,\mathrm{mag}/\square''$ isophote. $K = 20$ corresponds approximately to $r = 23$, hence we measure SDSS magnitudes within the radius where the surface brightness profile drops to $r = 23\,\mathrm{mag}/\square''$. We compare these magnitudes for elliptical galaxies, selected using standard cuts that have been used in previous SDSS studies (i.e. $c_{\mathrm{SDSS}} = R_{90}^{\mathrm{SDSS}}/R_{50}^{\mathrm{SDSS}} > 2.86$ and $g_{\mathrm{petro}}^{\mathrm{SDSS}} - r_{\mathrm{petro}}^{\mathrm{SDSS}}$). We also limit the sample to galaxies where the SDSS and 2MASS radii agree to within 30% (this criterion changes for each magnitude measurement). We consider only galaxies with a radius larger than $7''$, the minimum radius necessary to avoid PSF effects for 2MASS data (Jarrett et al. 2000). After correcting for galactic extinction (and converting

Table A.1: Comparison of the results of Kolmogorov–Smirnov tests (expressed as the decimal logarithm of 1 minus the confidence level at which the null hypothesis, that the distributions are drawn from an identical parent population, can be rejected) on BCG and non–BCG distributions of various parameters, for different versions of sky subtraction applied to the SDSS photometry.

sky subtraction	R_{50}	R_{iso23}	c'	μ_{50}	μ_{iso23}	b/a	$\Delta(g-r)$
$f_{\mathrm{sky}}^{\max} = 0.7$	-5.44	-3.60	-4.58	-8.78	-12.43	-7.28	-3.13
$f_{\mathrm{sky}}^{\max} = 0.5$	-6.13	-3.37	-4.84	-10.38	-14.46	-7.71	-2.61
$f_{\mathrm{sky}}^{\max} = 1.0$	-4.91	-3.29	-3.48	-6.44	-12.76	-6.44	-2.16

sky subtraction	σ_{v}	$M_{\mathrm{dyn,50}}/M_{\star}$	$D_n(4000)$	$\mathrm{H}\delta_{\mathrm{A}}$	$\mathrm{L(H\alpha)}$	$\mathrm{L(H\beta)}$
$f_{\mathrm{sky}}^{\max} = 0.7$	-2.06	-13.33	-0.88	-2.67	-1.60	-0.01
$f_{\mathrm{sky}}^{\max} = 0.5$	-2.27	-14.00	-0.57	-2.71	-1.04	-0.04
$f_{\mathrm{sky}}^{\max} = 1.0$	-2.19	-12.57	-0.61	-2.74	-1.75	-0.01

the J-band magnitude to an AB magnitude), we compare the SDSS z-band magnitudes to the 2MASS J-band magnitudes, since these bands are adjacent in wavelength and thus color differences from different stellar populations can be expected to be minimal.

In Fig. A.2, we investigate the color $(z_{r23} - J_{K20})$ as a function of galaxy size (given by the $r = 23\,\mathrm{mag}/\square''$ isophotal radius in the SDSS) for four different sky subtractions. Clearly, for the original SDSS sky subtraction, the color term is a strong function of galaxy size, indicating that the sky is systematically oversubtracted in the optical band. This accounts for a systematic difference of the order of 0.1 mag for galaxies larger than $20''$ (for individual galaxies, this may be much more, as demonstrated by Lauer et al. 2006). However, substituting the `local sky` estimate by the `global` one (i.e. $f_{\mathrm{sky}}^{\max} = 1.0$) leads to an underestimation of the sky, and thus an overestimation of the luminosity. We find that with $f_{\mathrm{sky}}^{\max} = 0.7$, there is little variation of the median color term with galaxy size, and no systematic trend (note that setting $f_{\mathrm{sky}}^{\min} = 0.1$ makes only a small difference).

A.5 Final magnitudes

The isophotal magnitudes are not redshift independent because of cosmological surface brightness dimming. We thus modify the algorithm to correct both for $(1 + z)^4$ surface brightness dimming and for galactic extinction (i.e. these corrections applied directly to the radial profile before the magnitudes are measured).

We choose to use isophotal magnitudes corresponding to $r = 23$ at $z = 0$ (i.e. $r = 23.41$ at $z = 0.1$). This is a rather bright cut-off, but is less sensitive to residual errors in the sky subtraction and/or surface brightness measurements (cf. Fig. A.1).

A.6 Influence of the sky subtraction on our results

Our analysis of BCG properties (Sect. 2.6) as a function of stellar mass depends critically on the correct determination of the luminosities of the objects in our sample. If the luminosities

we assign to BCGs are underestimated, then the comparison galaxies (which are matched in stellar mass) would be systematically less massive than the BCG, leading to possibly spurious differences in their physical properties.

To estimate the effect that sky subtraction has on our results, we repeat the analysis presented in Sect. 2.6 with photometry derived with values of $f_{\rm sky}^{\rm max} = 0.5$ and $f_{\rm sky}^{\rm max} = 1.0$. To evaluate whether there could be significant quantitative effects on our results, we compare the results of the Kolmogorov–Smirnov test on the BCG and non–BCG distributions for several parameters (as shown also in Figures 2.9 and 2.10) in Table A.1. We find only minor differences to our initial results; none of our conclusions are altered as a result of using a different value of $f_{\rm sky}^{\rm max}$.

B

Examples of local clusters

In the following we present finding charts and redshift histograms for clusters referred to in the text. The finding charts are centered on the BCG, and spectroscopically confirmed cluster members are marked by triangles. In the redshift histograms, a short-dashed line indicates the cluster redshift, the long-dashed line the redshift of the BCG, and the dotted lines the $\pm 3\sigma_{\mathrm{v,cl}}$ limits. Also, the redshift (both the C4 and our measurement) as well as the velocity dispersion measurements (given in km/s) are listed in the redshift histograms.
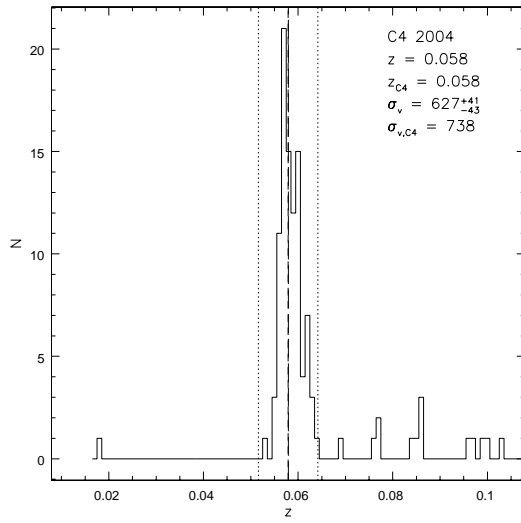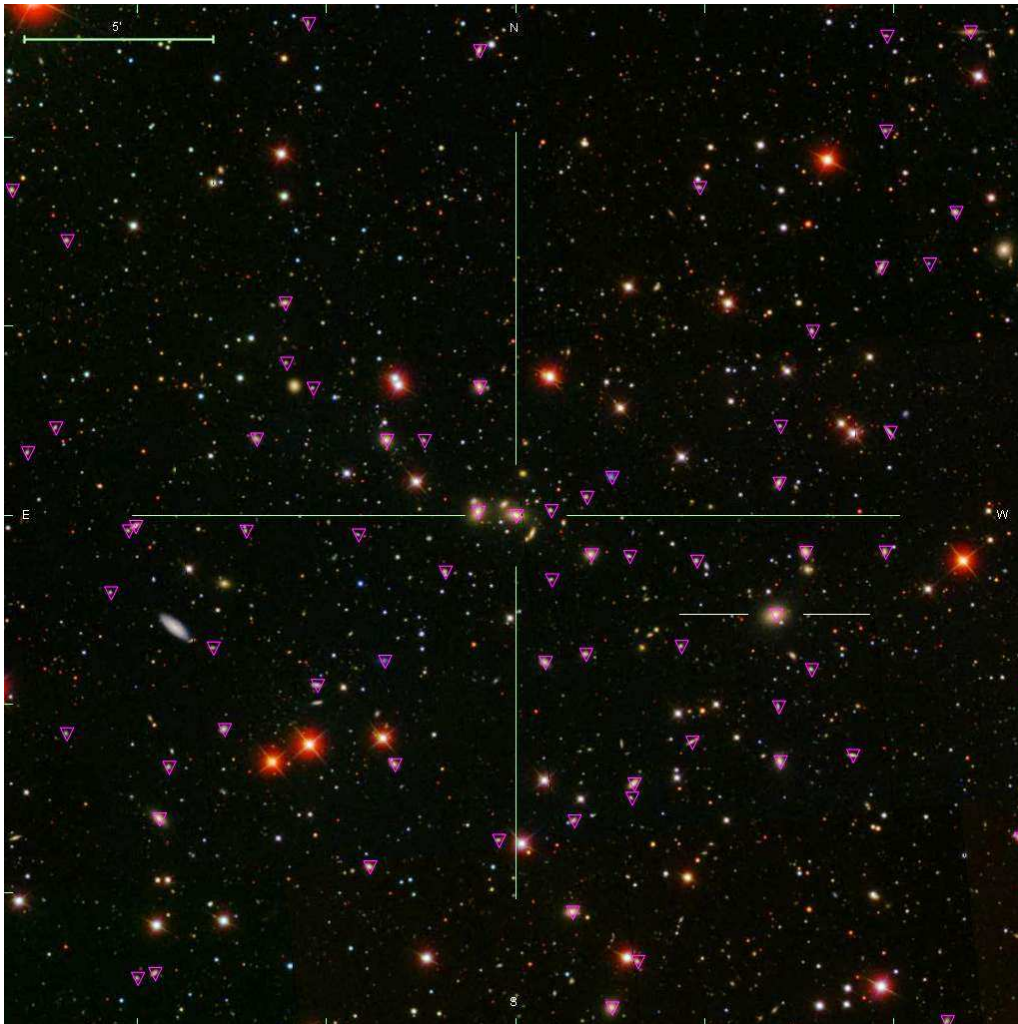
Figure B.1: **C4_2003.** Since most galaxies seem to cluster around the galaxy shown at the center of this image, this is the galaxy we identify as the BCG, even though the galaxy about 6′ west-south-west of the center (marked by two lines) is brighter by a third of a magnitude. The R_{200} of this cluster is 1.5 Mpc, which translates to $\sim 20'$.
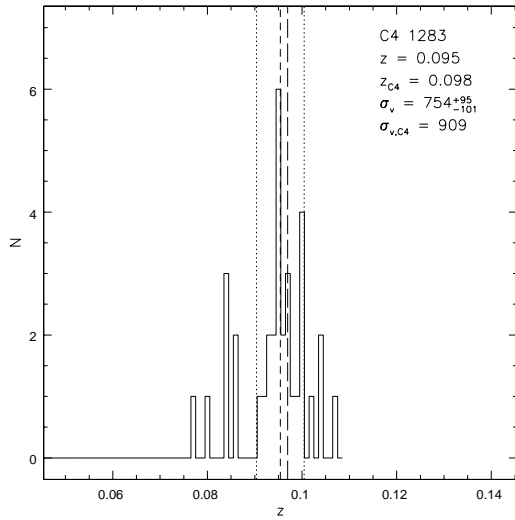
Figure B.2: C4_DR3_1283. For this cluster, the C4 mean galaxy (marked by diagonal lines in the finding chart) lies 2.8 Mpc from the BCG which we identify. The large-scale distribution of galaxies at the cluster redshift suggests that C4 selected part of the infall region of this cluster, but fails to pick up the cluster itself. Note that the brightest galaxy in the field is IC 0504 at $z = 0.013$, whereas many of the other bright galaxies in the foreground belong to C4_DR3_1356 at $z = 0.03$. Below, we show thumbnail images of the C4 mean galaxy (left) and our BCG (right).
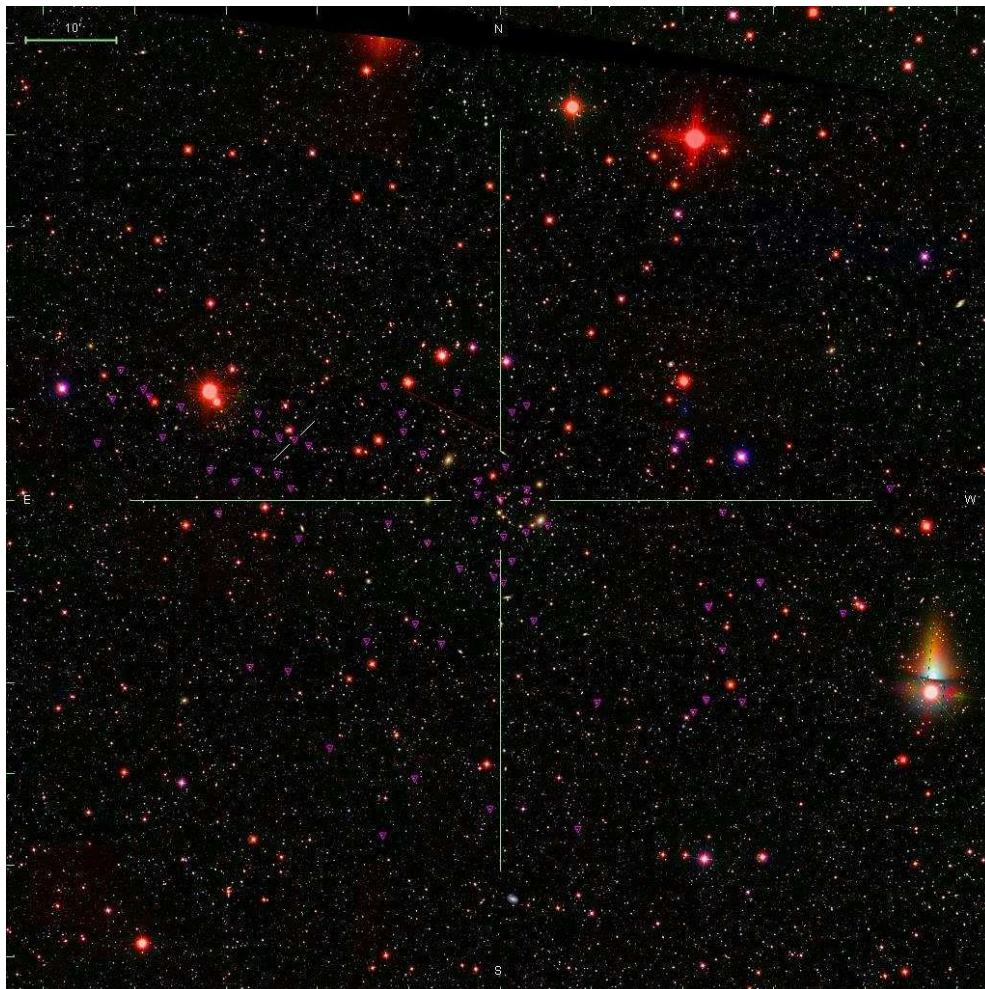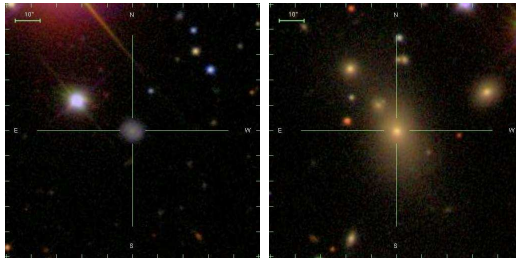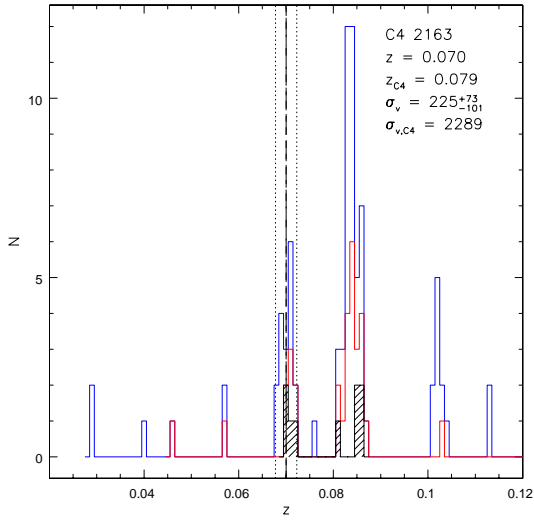
Figure B.3: C4_DR3_2163. In the C4 catalog, this cluster is listed as a structure at $z = 0.079$, with $\sigma_{v,cl} > 2000$ km/s. The mean galaxy is marked in the finding chart below and is part of the group of galaxies at $z = 0.07$, which our algorithm identifies. In the redshift histogram, we show the distribution of galaxies within projections of $1R_{200}$ (black, shaded), $3R_{200}$ (red), and $5R_{200}$ (blue). Obviously, the difference in the redshift measurements as well as the large C4 velocity dispersion are due to another structure at $z \sim 0.082$. In Fig. B.4, we show that this background structure is associated with C4_2124.
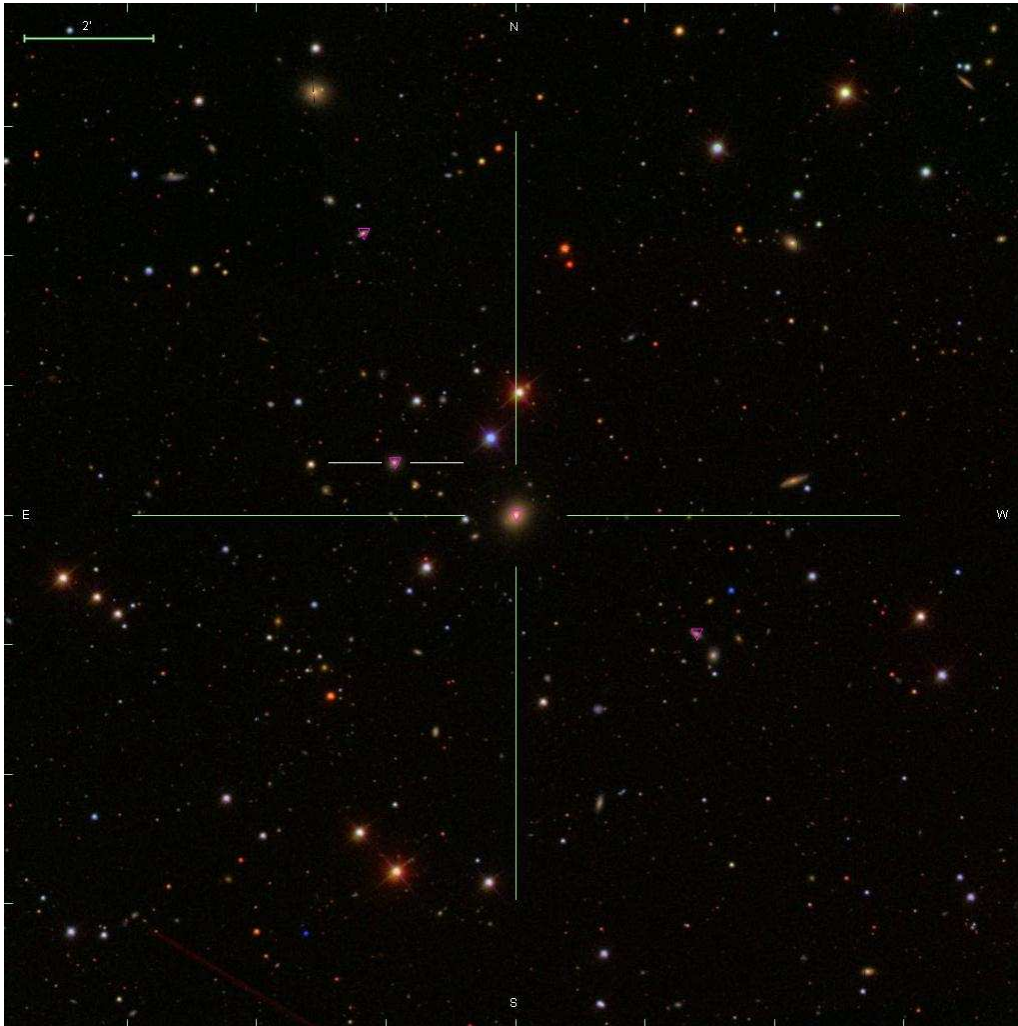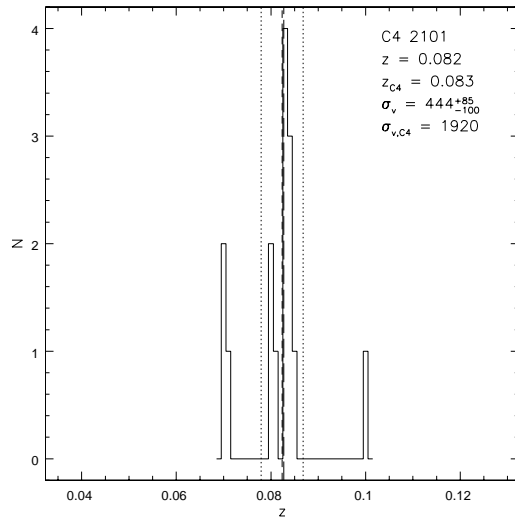
Figure B.4:   C4_2124. The finding chart below is not centered on the BCG of C4_2124, but on the BCG of C4_DR3_2163, in order to illustrate the sheet-like structure at $z \sim 0.082$ which led to the deviating redshift measurement for C4_DR3_2163. The BCG of C4_2124 is marked in the finding chart, and its R_{200} (equivalent to 1 Mpc) is indicated by a dashed circle.

C4 2101
$z = 0.082$
$z_{C4} = 0.083$
$\sigma_v = 444^{+85}_{-100}$
$\sigma_{v,C4} = 1920$
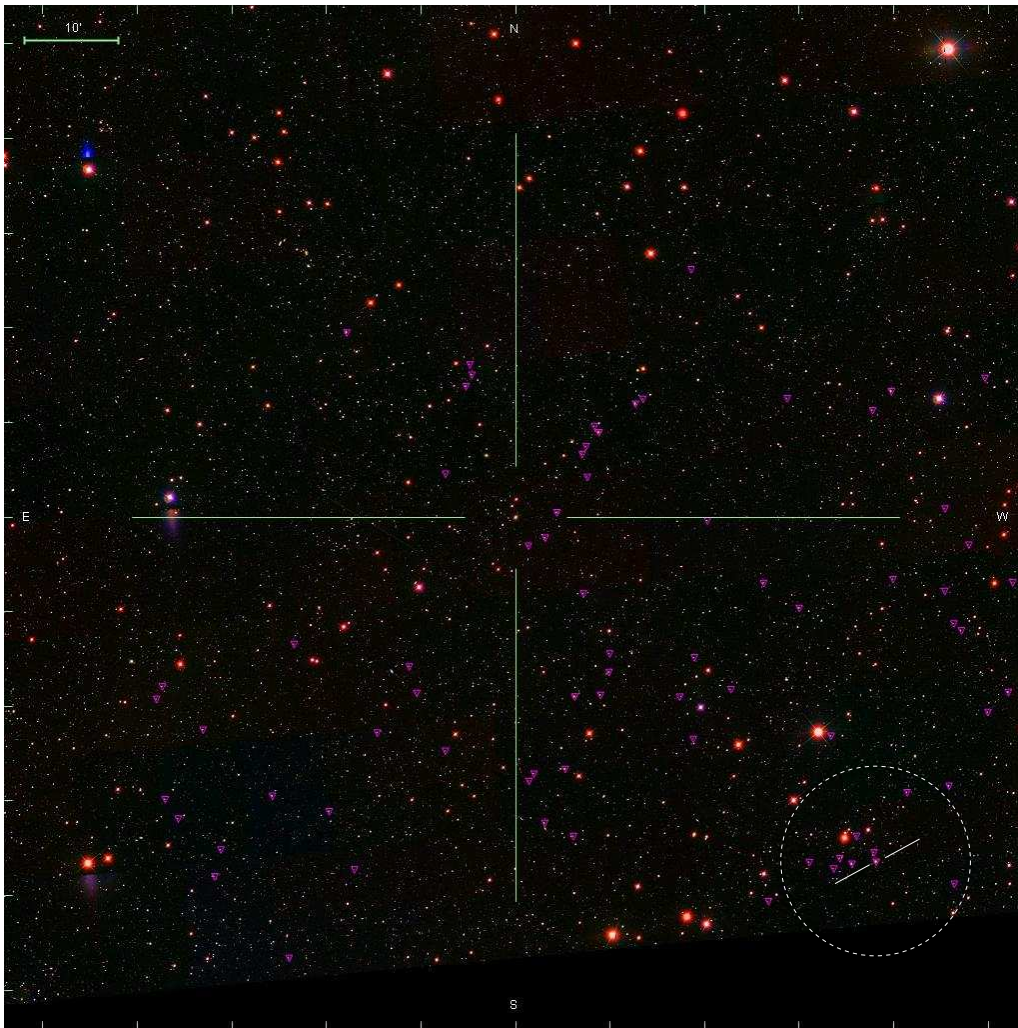
References

Abadi, M. G., Moore, B., & Bower, R. G.: *Ram pressure stripping of spiral galaxies in clusters.* MNRAS 1999, **308**, p. 947.

Abazajian, K., Adelman-McCarthy, J. K., Agüeros, M. A., et al.: *The Second Data Release of the Sloan Digital Sky Survey.* AJ 2004, **128**, p. 502.

Abell, G. O.: *The Distribution of Rich Clusters of Galaxies.* ApJS 1958, **3**, p. 211.

Adami, C., Mazure, A., Katgert, P., & Biviano, A.: *The ESO nearby Abell cluster survey. VII. Galaxy density profiles of rich clusters of galaxies.* A&A 1998, **336**, p. 63.

Allen, S. W., Fabian, A. C., Edge, A. C., et al.: *ASCA and ROSAT observations of distant, massive cooling flows.* MNRAS 1996, **283**, p. 263.

Allen, S. W., Rapetti, D. A., Schmidt, R. W., et al.: *New constraints on dark energy from Chandra X-ray observations of the largest relaxed galaxy clusters.* ArXiv e-prints 0706.0033 2007, **706**.

Andreon, S.: *The history of mass assembly of faint red galaxies in 28 galaxy clusters since z=1.3.* ArXiv e-prints 2007, **710**.

Aragon-Salamanca, A., Baugh, C. M., & Kauffmann, G.: *The K-band Hubble diagram for the brightest cluster galaxies: a test of hierarchical galaxy formation models.* MNRAS 1998, **297**, p. 427.

Baldry, I. K., Glazebrook, K., Brinkmann, J., et al.: *Quantifying the Bimodal Color-Magnitude Distribution of Galaxies.* ApJ 2004, **600**, p. 681.

Baldwin, J. A., Phillips, M. M., & Terlevich, R.: *Classification parameters for the emission-line spectra of extragalactic objects.* PASP 1981, **93**, p. 5.

Balogh, M., Eke, V., Miller, C., et al.: *Galaxy ecology: groups and low-density environments in the SDSS and 2dFGRS.* MNRAS 2004, **348**, p. 1355.

Balogh, M. L., Baldry, I. K., Nichol, R., et al.: *The Bimodal Galaxy Color Distribution: Dependence on Luminosity and Environment.* ApJ 2004, **615**, p. L101.

Balogh, M. L., Morris, S. L., Yee, H. K. C., Carlberg, R. G., & Ellingson, E.: *Star Formation in Cluster Galaxies at 0.2 < Z < 0.55.* ApJ 1997, **488**, p. L75+.

Balogh, M. L., Morris, S. L., Yee, H. K. C., Carlberg, R. G., & Ellingson, E.: *Differential Galaxy Evolution in Cluster and Field Galaxies at z~0.3.* ApJ 1999, **527**, p. 54.

References

Balogh, M. L., Navarro, J. F., & Morris, S. L.: *The Origin of Star Formation Gradients in Rich Galaxy Clusters.* ApJ 2000, **540**, p. 113.

Barkhouse, W. A., Yee, H. K. C., & López-Cruz, O.: *The Luminosity Function of Low-Redshift Abell Galaxy Clusters.* ArXiv e-prints 0709.0983 2007, **709**.

Barnes, J. E. & Hernquist, L. E.: *Fueling starburst galaxies with gas-rich mergers.* ApJ 1991, **370**, p. L65.

Batcheldor, D., Marconi, A., Merritt, D., & Axon, D. J.: *How Special Are Brightest Cluster Galaxies? The Impact of Near-Infrared Luminosities on Scaling Relations for BCGs.* ApJ 2007, **663**, p. L85.

Becker, R. H., White, R. L., & Helfand, D. J.: ApJ 1995, **450**, p. 559, FIRST radio survey.

Beers, T. C., Flynn, K., & Gebhardt, K.: *Measures of location and scale for velocities in clusters of galaxies - A robust approach.* AJ 1990, **100**, p. 32.

Bekki, K., Couch, W. J., & Shioya, Y.: *Passive Spiral Formation from Halo Gas Starvation: Gradual Transformation into S0s.* ApJ 2002, **577**, p. 651.

Berlind, A. A., Frieman, J., Weinberg, D. H., et al.: *Percolation Galaxy Groups and Clusters in the SDSS Redshift Survey: Identification, Catalogs, and the Multiplicity Function.* ApJS 2006, **167**, p. 1.

Bernardi, M., Hyde, J. B., Sheth, R. K., Miller, C. J., & Nichol, R. C.: *The luminosities, sizes and velocity dispersions of Brightest Cluster Galaxies: Implications for formation history.* submitted to AJ, astro-ph/0607117 2006.

Bernardi, M., Sheth, R. K., Annis, J., et al.: *Early-Type Galaxies in the Sloan Digital Sky Survey. I. The Sample.* AJ 2003, **125**, p. 1817.

Bernardi, M., Sheth, R. K., Annis, J., et al.: *Early-type Galaxies in the Sloan Digital Sky Survey. II. Correlations between Observables.* AJ 2003, **125**, p. 1849.

Bernardi, M., Sheth, R. K., Annis, J., et al.: *Early-Type Galaxies in the Sloan Digital Sky Survey. III. The Fundamental Plane.* AJ 2003, **125**, p. 1866.

Bertone, S., De Lucia, G., & Thomas, P. A.: *The recycling of gas and metals in galaxy formation: predictions of a dynamical feedback model.* MNRAS 2007, **379**, p. 1143.

Best, P. N., Kaiser, C. R., Heckman, T. M., & Kauffmann, G.: *AGN-controlled cooling in elliptical galaxies.* MNRAS 2006, **368**, p. L67.

Best, P. N., Kauffmann, G., Heckman, T. M., & Ivezić, Ž.: *A sample of radio-loud active galactic nuclei in the Sloan Digital Sky Survey.* MNRAS 2005, **362**, p. 9.

Best, P. N., Kauffmann, G., Heckman, T. M., et al.: *The host galaxies of radio-loud active galactic nuclei: mass dependences, gas cooling and active galactic nuclei feedback.* MNRAS 2005, **362**, p. 25.

Best, P. N., von der Linden, A., Kauffmann, G., Heckman, T. M., & Kaiser, C. R.: *On the prevalence of radio-loud active galactic nuclei in brightest cluster galaxies: implications for AGN heating of cooling flows.* MNRAS 2007, **379**, p. 894.

Bird, C. M.: *Substructure in clusters and central galaxy peculiar velocities.* AJ 1994, **107**, p. 1637.

Biviano, A. *From Messier to Abell: 200 Years of Science with Galaxy Clusters.* in: Constructing the Universe with Clusters of Galaxies. 2000.

Blanton, M. R., Dalcanton, J., Eisenstein, D., et al.: *The Luminosity Function of Galaxies in SDSS Commissioning Data.* AJ 2001, **121**, p. 2358.

Blanton, M. R., Eisenstein, D., Hogg, D. W., Schlegel, D. J., & Brinkmann, J.: *Relationship between Environment and the Broadband Optical Properties of Galaxies in the Sloan Digital Sky Survey.* ApJ 2005, **629**, p. 143.

Blanton, M. R., Hogg, D. W., Bahcall, N. A., et al.: *The Galaxy Luminosity Function and Luminosity Density at Redshift z = 0.1.* ApJ 2003, **592**, p. 819.

Blanton, M. R., Lin, H., Lupton, R. H., et al.: *An Efficient Targeting Strategy for Multiobject Spectrograph Surveys: the Sloan Digital Sky Survey "Tiling" Algorithm.* AJ 2003, **125**, p. 2276.

Blanton, M. R. & Roweis, S.: *K-Corrections and Filter Transformations in the Ultraviolet, Optical, and Near-Infrared.* AJ 2007, **133**, p. 734.

Blanton, M. R., Schlegel, D. J., Strauss, M. A., et al.: *New York University Value-Added Galaxy Catalog: A Galaxy Catalog Based on New Public Surveys.* AJ 2005, **129**, p. 2562.

Böhringer, H., Schuecker, P., Guzzo, L., et al.: *The ROSAT-ESO flux limited X-ray (REFLEX) galaxy cluster survey. I. The construction of the cluster sample.* A&A 2001, **369**, p. 826.

Böhringer, H., Voges, W., Huchra, J. P., et al.: *The Northern ROSAT All-Sky (NORAS) Galaxy Cluster Survey. I. X-Ray Properties of Clusters Detected as Extended X-Ray Sources.* ApJS 2000, **129**, p. 435.

Bower, R. G., Benson, A. J., Malbon, R., et al.: *Breaking the hierarchy of galaxy formation.* MNRAS 2006, **370**, p. 645.

Boylan-Kolchin, M., Ma, C.-P., & Quataert, E.: *Red mergers and the assembly of massive elliptical galaxies: the fundamental plane and its projections.* MNRAS 2006, **369**, p. 1081.

Brinchmann, J., Charlot, S., White, S. D. M., et al.: *The physical properties of star-forming galaxies in the low-redshift Universe.* MNRAS 2004, **351**, p. 1151.

Brough, S., Collins, C. A., Burke, D. J., Lynam, P. D., & Mann, R. G.: *Environmental dependence of the structure of brightest cluster galaxies.* MNRAS 2005, **364**, p. 1354.

Bruzual, G. & Charlot, S.: *Stellar population synthesis at the resolution of 2003.* MNRAS 2003, **344**, p. 1000.

References

Burkert, A. & Naab, T. *The Formation of Spheroidal Stellar Systems.* in: Coevolution of Black Holes and Galaxies, ed. L. C. Ho. 2004, p. 421.

Burns, J. O.: *The radio properties of cD galaxies in Abell clusters. I - an X-ray selected sample.* AJ 1990, **99**, p. 14.

Butcher, H. & Oemler, Jr., A.: *The evolution of galaxies in clusters. V - A study of populations since Z approximately equal to 0.5.* ApJ 1984, **285**, p. 426.

Byrd, G. & Valtonen, M.: *Tidal generation of active spirals and S0 galaxies by rich clusters.* ApJ 1990, **350**, p. 89.

Cappellari, M., Bacon, R., Bureau, M., et al.: *The SAURON project - IV. The mass-to-light ratio, the virial mass estimator and the Fundamental Plane of elliptical and lenticular galaxies.* MNRAS 2006, **366**, p. 1126.

Carlberg, R. G., Yee, H. K. C., Ellingson, E., et al.: *The Average Mass Profile of Galaxy Clusters.* ApJ 1997, **485**, p. L13+.

Cattaneo, A., Haehnelt, M. G., & Rees, M. J.: *The distribution of supermassive black holes in the nuclei of nearby galaxies.* MNRAS 1999, **308**, p. 77.

Cayatte, V., van Gorkom, J. H., Balkowski, C., & Kotanyi, C.: *VLA observations of neutral hydrogen in Virgo Cluster galaxies. I - The Atlas.* AJ 1990, **100**, p. 604.

Christlein, D. & Zabludoff, A. I.: *Disentangling Morphology, Star Formation, Stellar Mass, and Environment in Galaxy Evolution.* ApJ 2005, **621**, p. 201.

Chung, A., van Gorkom, J. H., Kenney, J. D. P., & Vollmer, B.: *Virgo Galaxies with Long One-sided H I Tails.* ApJ 2007, **659**, p. L115.

Colless, M., Dalton, G., Maddox, S., et al.: *The 2dF Galaxy Redshift Survey: spectra and redshifts.* MNRAS 2001, **328**, p. 1039.

Colless, M., Peterson, B. A., Jackson, C., et al.: *The 2dF Galaxy Redshift Survey: Final Data Release.* astro-ph/0306581 2003.

Condon, J. J., Cotton, W. D., Greisen, E. W., et al.: AJ 1998, **115**, p. 1693, the NVSS Survey.

Couch, W. J. & Sharples, R. M.: *A spectroscopic study of three rich galaxy clusters at Z = 0.31.* MNRAS 1987, **229**, p. 423.

Crawford, C. S., Allen, S. W., Ebeling, H., Edge, A. C., & Fabian, A. C.: *The ROSAT Brightest Cluster Sample - III. Optical spectra of the central cluster galaxies.* MNRAS 1999, **306**, p. 857.

Crawford, C. S., Sanders, J. S., & Fabian, A. C.: *The giant Hα/X-ray filament in the cluster of galaxies A1795.* MNRAS 2005, **361**, p. 17.

Croton, D. J., Springel, V., White, S. D. M., et al.: *The many lives of active galactic nuclei: cooling flows, black holes and the luminosities and colours of galaxies.* MNRAS 2006, **365**, p. 11.

Davis, M., Gerke, B. F., & Newman, J. A.: *Constraining Dark Energy with DEEP2.* ArXiv Astrophysics e-prints 2004.

De Lucia, G. & Blaizot, J.: *The hierarchical formation of the brightest cluster galaxies.* MNRAS 2007, **375**, p. 2.

De Lucia, G., Kauffmann, G., & White, S. D. M.: *Chemical enrichment of the intracluster and intergalactic medium in a hierarchical galaxy formation model.* MNRAS 2004, **349**, p. 1101.

De Lucia, G., Poggianti, B. M., Aragón-Salamanca, A., et al.: *The Buildup of the Red Sequence in Galaxy Clusters since z ˜ 0.8.* ApJ 2004, **610**, p. L77.

De Lucia, G., Poggianti, B. M., Aragón-Salamanca, A., et al.: *The build-up of the colour-magnitude relation in galaxy clusters since z ˜ 0.8.* MNRAS 2007, **374**, p. 809.

De Lucia, G., Springel, V., White, S. D. M., Croton, D., & Kauffmann, G.: *The formation history of elliptical galaxies.* MNRAS 2006, **366**, p. 499.

De Propris, R., Colless, M., Peacock, J. A., et al.: *The 2dF Galaxy Redshift Survey: the blue galaxy fraction and implications for the Butcher-Oemler effect.* MNRAS 2004, **351**, p. 125.

De Propris, R., Stanford, S. A., Eisenhardt, P. R., & Dickinson, M.: *The K-selected Butcher-Oemler Effect.* ApJ 2003, **598**, p. 20.

Desai, V., Dalcanton, J. J., Aragón-Salamanca, A., et al.: *The Morphological Content of 10 EDisCS Clusters at* $0.5 < z < 0.8$. ApJ 2007, **660**, p. 1151.

Desroches, L.-B., Quataert, E., Ma, C.-P., & West, A. A.: *Luminosity dependence in the Fundamental Plane projections of elliptical galaxies.* MNRAS 2007, **377**, p. 402.

Djorgovski, S. & Davis, M.: *Fundamental properties of elliptical galaxies.* ApJ 1987, **313**, p. 59.

Dolag, K., Bartelmann, M., Perrotta, F., et al.: *Numerical study of halo concentrations in dark-energy cosmologies.* A&A 2004, **416**, p. 853.

D'Onghia, E. & Burkert, A.: *Bulgeless Galaxies and Their Angular Momentum Problem.* ApJ 2004, **612**, p. L13.

Dressler, A.: *Galaxy morphology in rich clusters - Implications for the formation and evolution of galaxies.* ApJ 1980, **236**, p. 351.

Dressler, A., Oemler, A. J., Couch, W. J., et al.: *Evolution since Z = 0.5 of the Morphology-Density Relation for Clusters of Galaxies.* ApJ 1997, **490**, p. 577.

Dressler, A. & Shectman, S. A.: *Evidence for substructure in rich clusters of galaxies from radial-velocity measurements.* AJ 1988, **95**, p. 985.

Dressler, A., Smail, I., Poggianti, B. M., et al.: *A Spectroscopic Catalog of 10 Distant Rich Clusters of Galaxies.* ApJS 1999, **122**, p. 51.

Dubinski, J.: *The Origin of the Brightest Cluster Galaxies.* ApJ 1998, **502**, p. 141.

References

Ebeling, H., Edge, A. C., Bohringer, H., et al.: *The ROSAT Brightest Cluster Sample - I. The compilation of the sample and the cluster log N-log S distribution.* MNRAS 1998, **301**, p. 881.

Ebeling, H., Edge, A. C., & Henry, J. P.: *MACS: A Quest for the Most Massive Galaxy Clusters in the Universe.* ApJ 2001, **553**, p. 668.

Edwards, L. O. V., Hudson, M. J., Balogh, M. L., & Smith, R. J.: *Line emission in the brightest cluster galaxies of the NOAO Fundamental Plane and Sloan Digital Sky Surveys.* MNRAS 2007, **379**, p. 100.

Ellingson, E., Lin, H., Yee, H. K. C., & Carlberg, R. G.: *The Evolution of Population Gradients in Galaxy Clusters: The Butcher-Oemler Effect and Cluster Infall.* ApJ 2001, **547**, p. 609.

Fabian, A. C.: *Cooling Flows in Clusters of Galaxies.* ARA&A 1994, **32**, p. 277.

Fairley, B. W., Jones, L. R., Wake, D. A., et al.: *Galaxy colours in high-redshift, X-ray-selected clusters - I. Blue galaxy fractions in eight clusters.* MNRAS 2002, **330**, p. 755.

Ferrara, A. & Tolstoy, E.: *The role of stellar feedback and dark matter in the evolution of dwarf galaxies.* MNRAS 2000, **313**, p. 291.

Finn, R. A., Zaritsky, D., McCarthy, D. W., et al.: *Hα-derived Star Formation Rates for Three z˜=0.75 EDisCS Galaxy Clusters.* ApJ 2005, **630**, p. 206.

Freedman, W. L., Madore, B. F., Gibson, B. K., et al.: *Final Results from the Hubble Space Telescope Key Project to Measure the Hubble Constant.* ApJ 2001, **553**, p. 47.

Fukugita, M., Shimasaku, K., & Ichikawa, T.: *Galaxy Colors in Various Photometric Band Systems.* PASP 1995, **107**, p. 945.

Gallazzi, A., Charlot, S., Brinchmann, J., White, S. D. M., & Tremonti, C. A.: *The ages and metallicities of galaxies in the local universe.* MNRAS 2005, **362**, p. 41.

Gao, L., White, S. D. M., Jenkins, A., Stoehr, F., & Springel, V.: *The subhalo populations of ΛCDM dark haloes.* MNRAS 2004, **355**, p. 819.

Garilli, B., Sangalli, G., Andreon, S., et al.: *Two-Color Surface Photometry of Brightest Cluster Members.* AJ 1997, **113**, p. 1973.

Gavazzi, G., Zibetti, S., Boselli, A., et al.: *1.65 μm (H-band) surface photometry of galaxies. VII. Dwarf galaxies in the Virgo Cluster.* A&A 2001, **372**, p. 29.

Gerke, B. F., Newman, J. A., Lotz, J., et al.: *The DEEP2 Galaxy Redshift Survey: AEGIS Observations of a Dual AGN at z = 0.7.* ApJ 2007, **660**, p. L23.

Gilbank, D. G., Yee, H. K. C., Ellingson, E., et al.: *The Red-Sequence Luminosity Function in Galaxy Clusters since z˜1.* ArXiv e-prints 2007, **710**.

Gioia, I. M., Henry, J. P., Maccacaro, T., et al.: *The Extended Medium Sensitivity Survey distant cluster sample - X-ray cosmological evolution.* ApJ 1990, **356**, p. L35.

Gladders, M. D. & Yee, H. K. C.: *A New Method For Galaxy Cluster Detection. I. The Algorithm.* AJ 2000, **120**, p. 2148.

Gnedin, O. Y.: *Tidal Effects in Clusters of Galaxies.* ApJ 2003, **582**, p. 141.

Goerdt, T., Moore, B., Read, J. I., Stadel, J., & Zemp, M.: *Does the Fornax dwarf spheroidal have a central cusp or core?* MNRAS 2006, **368**, p. 1073.

Gómez, P. L., Nichol, R. C., Miller, C. J., et al.: *Galaxy Star Formation as a Function of Environment in the Early Data Release of the Sloan Digital Sky Survey.* ApJ 2003, **584**, p. 210.

Gonzalez, A. H., Zabludoff, A. I., & Zaritsky, D.: *Intracluster Light in Nearby Galaxy Clusters: Relationship to the Halos of Brightest Cluster Galaxies.* ApJ 2005, **618**, p. 195.

Gonzalez, A. H., Zaritsky, D., Dalcanton, J. J., & Nelson, A.: *The Las Campanas Distant Cluster Survey: The Catalog.* ApJS 2001, **137**, p. 117.

Goto, T.: *Do star formation rates of galaxy clusters depend on mass? Blue/late-type fractions and total star formation rates of 115 galaxy clusters as a function of cluster virial mass.* MNRAS 2005, **356**, p. L6.

Goto, T.: *Velocity dispersion of 335 galaxy clusters selected from the Sloan Digital Sky Survey: statistical evidence for dynamical interaction and against ram-pressure stripping.* MNRAS 2005, **359**, p. 1415.

Goto, T., Sekiguchi, M., Nichol, R. C., et al.: *The Cut-and-Enhance Method: Selecting Clusters of Galaxies from the Sloan Digital Sky Survey Commissioning Data.* AJ 2002, **123**, p. 1807.

Granato, G. L., De Zotti, G., Silva, L., Bressan, A., & Danese, L.: *A Physical Model for the Coevolution of QSOs and Their Spheroidal Hosts.* ApJ 2004, **600**, p. 580.

Gunn, J. E. & Gott, J. R. I.: *On the Infall of Matter Into Clusters of Galaxies and Some Effects on Their Evolution.* ApJ 1972, **176**, p. 1.

Halliday, C., Milvang-Jensen, B., Poirier, S., et al.: *Spectroscopy of clusters in the ESO Distant Cluster Survey (EDisCS). Redshifts, velocity dispersions and substructure for 5 clusters.* A&A 2004, **427**, p. 397.

Heckman, T. M., Armus, L., & Miley, G. K.: *On the nature and implications of starburst-driven galactic superwinds.* ApJS 1990, **74**, p. 833.

Heckman, T. M., Kauffmann, G., Brinchmann, J., et al.: *Present-Day Growth of Black Holes and Bulges: The Sloan Digital Sky Survey Perspective.* ApJ 2004, **613**, p. 109.

Hernquist, L.: *An analytical model for spherical galaxies and bulges.* ApJ 1990, **356**, p. 359.

Hoessel, J. G., Oegerle, W. R., & Schneider, D. P.: *The surface-brightness-effective-size relation for elliptical galaxies in the cores of clusters.* AJ 1987, **94**, p. 1111.

Hogg, D. W., Blanton, M. R., Brinchmann, J., et al.: *The Dependence on Environment of the Color-Magnitude Relation of Galaxies.* ApJ 2004, **601**, p. L29.

References

Hogg, D. W., Masjedi, M., Berlind, A. A., et al.: *What Triggers Galaxy Transformations? The Environments of Poststarburst Galaxies.* ApJ 2006, **650**, p. 763.

Holden, B. P., Illingworth, G. D., Franx, M., et al.: *Mass-Selection and the Evolution of the Morphology-Density Relation from z=0.8 to z=0.* ArXiv e-prints 0707.2782 2007, **707**.

Hubble, E. P.: Realm of the Nebulae ().

James, P. A., Salaris, M., Davies, J. I., Phillipps, S., & Cassisi, S.: *Optical/near-infrared colours of early-type galaxies and constraints on their star formation histories.* MN-RAS 2006, **367**, p. 339.

Jarrett, T. H., Chester, T., Cutri, R., et al.: *2MASS Extended Source Catalog: Overview and Algorithms.* AJ 2000, **119**, p. 2498.

Jørgensen, I., Franx, M., & Kjaergaard, P.: *Spectroscopy for E and S0 galaxies in nine clusters.* MNRAS 1995, **276**, p. 1341.

Kauffmann, G.: *The observed properties of high-redshift cluster galaxies.* MNRAS 1995, **274**, p. 161.

Kauffmann, G., Colberg, J. M., Diaferio, A., & White, S. D. M.: *Clustering of galaxies in a hierarchical universe - I. Methods and results at z=0.* MNRAS 1999, **303**, p. 188.

Kauffmann, G. & Haehnelt, M.: *A unified model for the evolution of galaxies and quasars.* MNRAS 2000, **311**, p. 576.

Kauffmann, G., Heckman, T. M., White, S. D. M., et al.: *Stellar masses and star formation histories for 10^5 galaxies from the Sloan Digital Sky Survey.* MNRAS 2003, **341**, p. 33.

Kauffmann, G., Heckman, T. M., White, S. D. M. a. S., et al.: *The dependence of star formation history and internal structure on stellar mass for 10^5 low-redshift galaxies.* MN-RAS 2003, **341**, p. 54.

Kauffmann, G., Heckman, T. M., Budavari, T., et al.: *Ongoing Formation of Bulges and Black Holes in the Local Universe: New Insights from GALEX.* astro-ph/0609436 2006.

Kauffmann, G., Heckman, T. M., Tremonti, C., et al.: *The host galaxies of active galactic nuclei.* MNRAS 2003, **346**, p. 1055.

Kauffmann, G., White, S. D. M., & Guiderdoni, B.: *The Formation and Evolution of Galaxies Within Merging Dark Matter Haloes.* MNRAS 1993, **264**, p. 201.

Kauffmann, G., White, S. D. M., Heckman, T. M., et al.: *The environmental dependence of the relations between stellar mass, structure, star formation and nuclear activity in galaxies.* MNRAS 2004, **353**, p. 713.

Kennicutt, Jr., R. C.: *The Global Schmidt Law in Star-forming Galaxies.* ApJ 1998, **498**, p. 541.

Kewley, L. J., Dopita, M. A., Sutherland, R. S., Heisler, C. A., & Trevena, J.: *Theoretical Modeling of Starburst Galaxies.* ApJ 2001, **556**, p. 121.

Kewley, L. J., Groves, B., Kauffmann, G., & Heckman, T.: *The host galaxies and classification of active galactic nuclei.* MNRAS 2006, p. 1072.

Kitzbichler, M. G. & White, S. D. M.: *Pure luminosity evolution models: too few massive galaxies at intermediate and high redshift.* MNRAS 2006, **366**, p. 858.

Koester, B. P., McKay, T. A., Annis, J., et al.: *A MaxBCG Catalog of 13,823 Galaxy Clusters from the Sloan Digital Sky Survey.* ApJ 2007, **660**, p. 239.

La Barbera, F., de Carvalho, R. R., Gal, R. R., et al.: *Color Gradients in Early-Type Galaxies: Dependence on Environment and Redshift.* ApJ 2005, **626**, p. L19.

Labbé, I., Franx, M., Rudnick, G., et al.: *The Color-Magnitude Distribution of Field Galaxies to z~3: The Evolution and Modeling of the Blue Sequence.* ApJ 2007, **665**, p. 944.

Lacey, C. & Silk, J.: *Tidally triggered galaxy formation. I - Evolution of the galaxy luminosity function.* ApJ 1991, **381**, p. 14.

Larson, R. B.: *Effects of supernovac on the early evolution of galaxies.* MNRAS 1974, **169**, p. 229.

Larson, R. B., Tinsley, B. M., & Caldwell, C. N.: *The evolution of disk galaxies and the origin of S0 galaxies.* ApJ 1980, **237**, p. 692.

Lauer, T. R., Faber, S. M., Richstone, D., et al.: *The Masses of Nuclear Black Holes in Luminous Elliptical Galaxies and Implications for the Space Density of the Most Massive Black Holes.* submitted to ApJ, astro-ph/0606739 2006.

Le Fèvre, O., Vettolani, G., Paltani, S., et al.: *The VIMOS VLT Deep Survey. Public release of 1599 redshifts to $I_{\mathrm{AB}} \leq 24$ across the Chandra Deep Field South.* A&A 2004, **428**, p. 1043.

Lewis, I., Balogh, M., De Propris, R., et al.: *The 2dF Galaxy Redshift Survey: the environmental dependence of galaxy star formation rates near clusters.* MNRAS 2002, **334**, p. 673.

Li, C., Kauffmann, G., Jing, Y. P., et al.: *The dependence of clustering on galaxy properties.* MNRAS 2006, **368**, p. 21.

Lin, Y.-T., Mohr, J. J., & Stanford, S. A.: *K-Band Properties of Galaxy Clusters and Groups: Luminosity Function, Radial Distribution, and Halo Occupation Number.* ApJ 2004, **610**, p. 745.

Lupton, R., Gunn, J. E., Ivezić, Z., et al. *The SDSS Imaging Pipelines.* in: ASP Conf. Ser. 238: Astronomical Data Analysis Software and Systems X, eds. F. R. Harnden, F. A. Primini, & H. E. Payne. 2001, p. 269.

Magorrian, J., Tremaine, S., Richstone, D., et al.: *The Demography of Massive Dark Objects in Galaxy Centers.* AJ 1998, **115**, p. 2285.

Martini, P., Mulchaey, J. S., & Kelson, D. D.: *The Distribution of Active Galactic Nuclei in Clusters of Galaxies.* ApJ 2007, **664**, p. 761.

References

Meekins, J. F., Gilbert, F., Chubb, T. A., Friedman, H., & Henry, R. C.: *X-rays from the Coma Cluster of Galaxies.* Nature 1971, **231**, p. 107.

Mei, S., Blakeslee, J. P., Stanford, S. A., et al.: *Evolution of the Color-Magnitude Relation in High-Redshift Clusters: Blue Early-Type Galaxies and Red Pairs in RDCS J0910+5422.* ApJ 2006, **639**, p. 81.

Mellier, Y.: *Probing the Universe with Weak Lensing.* ARA&A 1999, **37**, p. 127.

Merritt, D.: *Relaxation and tidal stripping in rich clusters of galaxies. I - Evolution of the mass distribution.* ApJ 1983, **264**, p. 24.

Merritt, D.: *Relaxation and tidal stripping in rich clusters of galaxies. III - Growth of a massive central galaxy.* ApJ 1985, **289**, p. 18.

Mihos, J. C.: *Morphology of galaxy mergers at intermediate redshift.* ApJ 1995, **438**, p. L75.

Miller, C. J., Nichol, R. C., Reichart, D., et al.: *The C4 Clustering Algorithm: Clusters of Galaxies in the Sloan Digital Sky Survey.* AJ 2005, **130**, p. 968.

Milvang-Jensen, B., Noll, S., Halliday, C., et al.: *Spectroscopy of clusters in the ESO Distant Cluster Survey (EDisCS) part 2. Redshifts, velocity dispersions and substructure in the last 15 fields.* in prep. 2007.

Moore, B., Lake, G., & Katz, N.: *Morphological Transformation from Galaxy Harassment.* ApJ 1998, **495**, p. 139.

Moran, S. M., Ellis, R. S., Treu, T., et al.: *A Wide-field Survey of Two Z~0.5 Galaxy Clusters: Identifying the Physical Processes Responsible for the Observed Transformation of Spirals into S0s.* ArXiv e-prints 0707.4173 2007, **707**.

Morgan, W. W. & Lesh, J. R.: *The Supergiant Galaxies.* ApJ 1965, **142**, p. 1364.

Nagashima, M., Lacey, C. G., Baugh, C. M., Frenk, C. S., & Cole, S.: *The metal enrichment of the intracluster medium in hierarchical galaxy formation models.* MNRAS 2005, **358**, p. 1247.

Navarro, J. F., Frenk, C. S., & White, S. D. M.: *A Universal Density Profile from Hierarchical Clustering.* ApJ 1997, **490**, p. 493.

Oegerle, W. R. & Hoessel, J. G.: *Fundamental parameters of brightest cluster galaxies.* ApJ 1991, **375**, p. 15.

Oemler, A. J.: *The Systematic Properties of Clusters of Galaxies. Photometry of 15 Clusters.* ApJ 1974, **194**, p. 1.

Osterbrock, D. E.: Astrophysics of gaseous nebulae and active galactic nuclei (Research supported by the University of California, John Simon Guggenheim Memorial Foundation, University of Minnesota, et al. Mill Valley, CA, University Science Books, 1989, 422 p., 1989).

Ostriker, J. P. & Tremaine, S. D.: *Another evolutionary correction to the luminosity of giant galaxies.* ApJ 1975, **202**, p. L113.

Padmanabhan, N., Seljak, U., Strauss, M. A., et al.: *Stellar and dynamical masses of ellipticals in the Sloan Digital Sky Survey.* New Astronomy 2004, **9**, p. 329.

Pahre, M. A., Djorgovski, S. G., & de Carvalho, R. R.: *Near-Infrared Imaging of Early-Type Galaxies. III. The Near-Infrared Fundamental Plane.* AJ 1998, **116**, p. 1591.

Peterson, J. R. & Fabian, A. C.: *X-ray spectroscopy of cooling clusters.* Phys. Rep. 2006, **427**, p. 1.

Phillipps, S., Driver, S. P., Couch, W. J., & Smith, R. M.: *The Luminosity Distribution in Galaxy Clusters: A Dwarf Population-Density Relation?* ApJ 1998, **498**, p. L119+.

Pimbblet, K. A., Smail, I., Kodama, T., et al.: *The Las Campanas/AAT Rich Cluster Survey - II. The environmental dependence of galaxy colours in clusters at z˜0.1.* MNRAS 2002, **331**, p. 333.

Poggianti, B. M., Smail, I., Dressler, A., et al.: *The Star Formation Histories of Galaxies in Distant Clusters.* ApJ 1999, **518**, p. 576.

Poggianti, B. M., von der Linden, A., De Lucia, G., et al.: *The Evolution of the Star Formation Activity in Galaxies and Its Dependence on Environment.* ApJ 2006, **642**, p. 188.

Popesso, P. & Biviano, A.: *The AGN fraction-velocity dispersion relation in clusters of galaxies.* A&A 2006, **460**, p. L23.

Popesso, P., Biviano, A., Böhringer, H., & Romaniello, M.: *RASS-SDSS Galaxy cluster survey. IV. A ubiquitous dwarf galaxy population in clusters.* A&A 2006, **445**, p. 29.

Popesso, P., Biviano, A., Böhringer, H., & Romaniello, M.: *RASS-SDSS galaxy cluster survey. VII. On the cluster mass-to-light ratio and the halo occupation distribution.* A&A 2007, **464**, p. 451.

Popesso, P., Biviano, A., Böhringer, H., Romaniello, M., & Voges, W.: *RASS-SDSS galaxy cluster survey. III. Scaling relations of galaxy clusters.* A&A 2005, **433**, p. 431.

Popesso, P., Biviano, A., Romaniello, M., & Böhringer, H.: *RASS-SDSS galaxy cluster survey. VI. The dependence of the cluster SFR on the cluster global properties.* A&A 2007, **461**, p. 411.

Popesso, P., Böhringer, H., Brinkmann, J., Voges, W., & York, D. G.: *RASS-SDSS Galaxy clusters survey. I. The catalog and the correlation of X-ray and optical properties.* A&A 2004, **423**, p. 449.

Popesso, P., Böhringer, H., Romaniello, M., & Voges, W.: *RASS-SDSS galaxy cluster survey. II. A unified picture of the cluster luminosity function.* A&A 2005, **433**, p. 415.

Porter, A. C., Schneider, D. P., & Hoessel, J. G.: *CCD observations of Abell clusters. V - Isophotometry of 175 brightest elliptical galaxies in Abell clusters.* AJ 1991, **101**, p. 1561.

Postman, M., Franx, M., Cross, N. J. G., et al.: *The Morphology-Density Relation in $z \sim 1$ Clusters.* ApJ 2005, **623**, p. 721.

References

Postman, M. & Lauer, T. R.: *Brightest cluster galaxies as standard candles.* ApJ 1995, **440**, p. 28.

Press, W. H., Teukolsky, S. A., Vetterling, W. T., & Flannery, B. P.: Numerical recipes in C. The art of scientific computing (Cambridge: University Press, —c1992, 2nd ed., 1992).

Quintero, A. D., Berlind, A. A., Blanton, M., & Hogg, D. W.: *The asymmetric relations among galaxy color, structure, and environment.* Submitted to ApJ, astro-ph/0611361 2006.

Riess, A. G., Filippenko, A. V., Challis, P., et al.: *Observational Evidence from Supernovae for an Accelerating Universe and a Cosmological Constant.* AJ 1998, **116**, p. 1009.

Rines, K., Finn, R., & Vikhlinin, A.: *An Extremely Massive Dry Galaxy Merger in a Moderate Redshift Cluster.* ApJ 2007, **665**, p. L9.

Rines, K. & Geller, M. J.: *Spectroscopic Determination of the Faint End of the Luminosity Function in the Nearby Galaxy Clusters A2199 and Virgo.* ArXiv e-prints 0710.1082 2007, **710**.

Rogers, B., Ferreras, I., Lahav, O., et al.: *Decoding the spectra of SDSS early-type galaxies: new indicators of age and recent star formation.* MNRAS 2007, p. 972.

Ryden, B. S., Lauer, T. R., & Postman, M.: *The shapes of brightest cluster galaxies.* ApJ 1993, **410**, p. 515.

Rzepecki, J., Lombardi, M., Rosati, P., Bignamini, A., & Tozzi, P.: *Strong lensing analysis of the cluster RCS0224-0002 at z = 0.77.* A&A 2007, **471**, p. 743.

Sakelliou, I. & Ponman, T. J.: *XMM-Newton observations of Abell 2255: a test case of a merger after 'core crossing'.* MNRAS 2006, **367**, p. 1409.

Sandage, A.: *The redshift-distance relation. II. The Hubble diagram and its scatter for first-ranked cluster galaxies: a formal value for q0.* ApJ 1972, **178**, p. 1.

Schmidt, M.: *The Rate of Star Formation.* ApJ 1959, **129**, p. 243.

Schneider, D. P., Gunn, J. E., & Hoessel, J. G.: *CCD photometry of Abell clusters. I - Magnitudes and redshifts for 84 brightest cluster galaxies.* ApJ 1983, **264**, p. 337.

Schombert, J. M.: *The structure of brightest cluster members. II - Mergers.* ApJS 1987, **64**, p. 643.

Shlosman, I., Begelman, M. C., & Frank, J.: *The fuelling of active galactic nuclei.* Nature 1990, **345**, p. 679.

Silk, J.: *Accretion by galaxy clusters and the relationship between X-ray luminosity and velocity dispersion.* ApJ 1976, **208**, p. 646.

Silverman, J. D., Mainieri, V., Lehmer, B. D., et al.: *The Evolution of AGN Host Galaxies: From Blue to Red and the Influence of Large-Scale Structures.* ArXiv e-prints 0709.3455 2007, **709**.

174

Simard, L., Clowe, D., Desai, V., et al.: *Evolution of the Early-Type Galaxy Fraction in Clusters since $z = 0.8$.* å, submitted 2007.

Skrutskie, M. F., Cutri, R. M., Stiening, R., et al.: *The Two Micron All Sky Survey (2MASS).* AJ 2006, **131**, p. 1163.

Smail, I., Edge, A. C., Ellis, R. S., & Blandford, R. D.: *A statistical analysis of the galaxy populations of distant luminous X-ray clusters.* MNRAS 1998, **293**, p. 124.

Somerville, R. S. & Primack, J. R.: *Semi-analytic modelling of galaxy formation: the local Universe.* MNRAS 1999, **310**, p. 1087.

Spergel, D. N., Bean, R., Doré, O., et al.: *Three-Year Wilkinson Microwave Anisotropy Probe (WMAP) Observations: Implications for Cosmology.* ApJS 2007, **170**, p. 377.

Springel, V., White, S. D. M., Jenkins, A., et al.: *Simulations of the formation, evolution and clustering of galaxies and quasars.* Nature 2005, **435**, p. 629.

Stott, J. P., Smail, I., Edge, A. C., et al.: *An Increase in the Faint Red Galaxy Population in Massive Clusters since z ˜ 0.5.* ApJ 2007, **661**, p. 95.

Stoughton, C., Lupton, R. H., Bernardi, M., et al.: *Sloan Digital Sky Survey: Early Data Release.* AJ 2002, **123**, p. 485.

Strauss, M. A., Weinberg, D. H., Lupton, R. H., et al.: *Spectroscopic Target Selection in the Sloan Digital Sky Survey: The Main Galaxy Sample.* AJ 2002, **124**, p. 1810.

Tanaka, M., Kodama, T., Arimoto, N., et al.: *The build-up of the colour-magnitude relation as a function of environment.* MNRAS 2005, **362**, p. 268.

Thomas, D., Maraston, C., & Bender, R.: *Stellar population models of Lick indices with variable element abundance ratios.* MNRAS 2003, **339**, p. 897.

Thuan, T. X. & Romanishin, W.: *The structure of giant elliptical galaxies in poor clusters of galaxies.* ApJ 1981, **248**, p. 439.

Toomre, A. *Mergers and Some Consequences.* in: Evolution of Galaxies and Stellar Populations, eds. B. M. Tinsley & R. B. Larson. 1977, p. 401.

Tran, K.-V. H., Franx, M., Illingworth, G., Kelson, D. D., & van Dokkum, P.: *The Nature of E+A Galaxies in Intermediate-Redshift Clusters.* ApJ 2003, **599**, p. 865.

Tran, K.-V. H., van Dokkum, P., Franx, M., et al.: *Spectroscopic Confirmation of Multiple Red Galaxy-Galaxy Mergers in MS 1054-03 ($z = 0.83$)1,.* ApJ 2005, **627**, p. L25.

Tremaine, S., Gebhardt, K., Bender, R., et al.: *The Slope of the Black Hole Mass versus Velocity Dispersion Correlation.* ApJ 2002, **574**, p. 740.

Tremonti, C. A., Heckman, T. M., Kauffmann, G., et al.: *The Origin of the Mass-Metallicity Relation: Insights from 53,000 Star-forming Galaxies in the Sloan Digital Sky Survey.* ApJ 2004, **613**, p. 898.

References

Tresse, L., Ilbert, O., Zucca, E., et al.: *The cosmic star formation rate evolution from z = 5 to z = 0 from the VIMOS VLT deep survey.* A&A 2007, **472**, p. 403.

van den Bosch, F. C., Aquino, D., Yang, X., et al.: *The Importance of Satellite Quenching for the Build-Up of the Red Sequence of Present Day Galaxies.* ArXiv e-prints 0710.3164 2007, **710**.

van Dokkum, P. G., Franx, M., Fabricant, D., Kelson, D. D., & Illingworth, G. D.: *A High Merger Fraction in the Rich Cluster MS 1054-03 at Z = 0.83: Direct Evidence for Hierarchical Formation of Massive Galaxies.* ApJ 1999, **520**, p. L95.

Voit, G. M. & Donahue, M.: *A Deep Look at the Emission-Line Nebula in Abell 2597.* ApJ 1997, **486**, p. 242.

von der Linden, A., Best, P. N., Kauffmann, G., & White, S. D. M.: *How special are brightest group and cluster galaxies?* MNRAS 2007, **379**, p. 867.

Wake, D. A., Collins, C. A., Nichol, R. C., Jones, L. R., & Burke, D. J.: *The Environmental Dependence of Galaxy Colors in Intermediate-Redshift X-Ray-selected Clusters.* ApJ 2005, **627**, p. 186.

Wang, J., De Lucia, G., Kitzbichler, M. G., & White, S. D. M.: *The Dependence of Galaxy Formation on Cosmological Parameters: Can we distinguish the WMAP1 and WMAP3 Parameter Sets?* ArXiv e-prints 2007, **706**.

Weinmann, S. M., van den Bosch, F. C., Yang, X., & Mo, H. J.: *Properties of galaxy groups in the Sloan Digital Sky Survey - I. The dependence of colour, star formation and morphology on halo mass.* MNRAS 2006, **366**, p. 2.

White, S. D. M.: *Dynamical friction in spherical clusters.* MNRAS 1976, **174**, p. 19.

White, S. D. M., Clowe, D. I., Simard, L., et al.: *EDisCS - the ESO distant cluster survey. Sample definition and optical photometry.* A&A 2005, **444**, p. 365.

White, S. D. M. & Frenk, C. S.: *Galaxy formation through hierarchical clustering.* ApJ 1991, **379**, p. 52.

White, S. D. M. & Rees, M. J.: *Core condensation in heavy halos - A two-stage theory for galaxy formation and clustering.* MNRAS 1978, **183**, p. 341.

Whitmore, B. C., Gilmore, D. M., & Jones, C.: *What determines the morphological fractions in clusters of galaxies?* ApJ 1993, **407**, p. 489.

Wild, V., Kauffmann, G., Heckman, T., et al.: *Bursty stellar populations and obscured AGN in galaxy bulges.* submitted to MNRAS, arXiv:0706.3113 2007.

Willman, B., Governato, F., Wadsley, J., & Quinn, T.: *The origin and properties of intra-cluster stars in a rich cluster.* MNRAS 2004, **355**, p. 159.

Worthey, G. & Ottaviani, D. L.: *H gamma and H delta Absorption Features in Stars and Stellar Populations.* ApJS 1997, **111**, p. 377.

Wyder, T. K., Martin, D. C., Schiminovich, D., et al.: *The UV-optical Galaxy Color-Magnitude Diagram I: Basic Properties.* submitted to ApJS, arXiv:0706.3938 2007, **706**.

Yan, R., Newman, J. A., Faber, S. M., et al.: *On the Origin of [O II] Emission in Red-Sequence and Poststarburst Galaxies.* ApJ 2006, **648**, p. 281.

Yang, X., Mo, H. J., van den Bosch, F. C., et al.: *Galaxy Groups in the SDSS DR4: I. The Catalogue and Basic Properties.* ArXiv e-prints 0707.4640 2007, **707**.

Yee, H. K. C., Ellingson, E., & Carlberg, R. G.: *The CNOC Cluster Redshift Survey Catalogs. I. Observational Strategy and Data Reduction Techniques.* ApJS 1996, **102**, p. 269.

Yee, H. K. C., Hsieh, B. C., Lin, H., & Gladders, M. D.: *The Dependence of Galaxy Colors on Luminosity and Environment at $z \sim 0.4$.* ApJ 2005, **629**, p. L77.

York, D. G., Adelman, J., Anderson, J. E., et al.: *The Sloan Digital Sky Survey: Technical Summary.* AJ 2000, **120**, p. 1579.

Zabludoff, A. I. & Mulchaey, J. S.: *The Properties of Poor Groups of Galaxies. I. Spectroscopic Survey and Results.* ApJ 1998, **496**, p. 39.

Zabludoff, A. I., Zaritsky, D., Lin, H., et al.: *The Environment of "E+A" Galaxies.* ApJ 1996, **466**, p. 104.

Zibetti, S., White, S. D. M., Schneider, D. P., & Brinkmann, J.: *Intergalactic stars in z˜ 0.25 galaxy clusters: systematic properties from stacking of Sloan Digital Sky Survey imaging data.* MNRAS 2005, **358**, p. 949.

Zwicky, F.: *Die Rotverschiebung von extragalaktischen Nebeln.* Helvetica Physica Acta 1933, **6**, p. 110.

References

Acknowledgements

Studying the stars is a lot easier if you can stand on the shoulders of giants...

My very personal giants are my family: my parents Dr. Bernd and Dagmar von der Linden, my brother Carsten, and my aunt Gudrun Zimmermann. They have always been there for me, and I am deeply grateful for all their love and support. Without them, I would not be where I am today.

I have had the honor to climb on the shoulders of two giants in the field of astrophysics: Dr. Guinevere Kauffmann and Prof. Simon White. I thank them for giving me the opportunity to work on this interesting project, their constructive criticism, their support, and the many, many things I have learned from them.

Gabriella De Lucia and Vivienne Wild were of invaluable help particularly during the last months of thesis-writing. The path from my office to either of theirs is well-trotten, and be it the peculiarities of the EDisCS dataset, or the interpretation of PCA, I always returned with new insights.

For most of my time at MPA, I had the pleasure of sharing an office with Manfred Kitzbichler, from whose computer knowledge and insights into the Millenium Run I profited very much. Various debates about the merits of Austrian, Bavarian, and German culture were never quite settled, but certainly entertaining. Thanks for good office atmosphere also go to my shorter-term office mates, Dima Docenko, Andreas Faltenbacher, and Cheng Li.

I have profited from scientific discussion with many others, particularly: Bianca Poggianti, Greg Rudnick, Bo Milvang-Jensen and the rest of the EDisCS team, Philip Best, Brent Groves, Ben Panter, Stefano Zibetti, Mateusz Ruszkowski, Shiyin Shen, Hans Böhringer, Alexis Finoguenov, and many others.

My home during my time in Munich was the (in-)famous AstroWG. I thank Karina, Michael, Marcelo and Carolina for all the good times we had, the talks, the parties, the pancakes, the video evenings, and sharing the thesis-stress. We will soon be strewn across three continents, but I hope our friendship continues and I wish them all the best of luck.

Various other people have made my stay in Munich enjoyable, be it by silly lunch conversations, tea breaks, going out, hiking, or sailing. Thanks go to 'da gingerbread man' Andre for speaking in Brazilian slang, to Gloria and Luis Carlos for hiking and barbecue, to Brent for many 'cuppas' of tea, to Stefan and Norbi for backpacking through Mexico with me, to Andi for making fun of me and letting me make fun of him, to Dimitri for pretty galaxy pictures,

to Mona for being the other female German PhD student, and to many others for just being around. And thanks to Maria, Cornelia, Kate, and Gabi for making sure that the institute runs so smoothly.

Thanks also go to my friends from IAYC, for reminding me that astronomy is also about lying on a camping mat under the stars, watching meteors. Special thanks go to my "twin" Ania, for making me her witness at her wedding and for trying to convince me that there is life beyond the thesis.

And finally, thanks go to another giant of astrophysics, Prof. Peter Schneider, for fostering my interest in astronomy already early my studies.

Thank y'all!

Curriculum vitae

PERSONAL INFORMATION:

Full name:	Anja Bernadette von der Linden
Date of birth:	April 26th, 1979, Stuttgart, Germany
Parents:	Dr. Bernd and Dagmar von der Linden
Nationality:	German

EDUCATION:

PhD in astronomy, *expected end of 2007*
- enrolled at **Ludwig–Maximilians–Universität, München**, Germany
- employed at **Max–Planck–Institut für Astrophysik, Garching**, Germany
- member of the **International Max–Planck Research School** (IMPRS) on Astrophysics
- Thesis supervisors: Dr. Guinevere Kauffmann and Prof. Dr. Simon D. M. White
- Thesis project:
  ### *Galaxy Evolution from the SDSS and EDisCS Surveys*
- Thesis contents:
  - construction of a local ($z < 0.1$) sample of galaxy clusters from SDSS to serve as a comparison sample for the high–redshift clusters from the EDisCS survey
  - investigation of the properties of brightest cluster galaxies
  - investigation of the stellar populations of galaxies in the SDSS and EDisCS samples

Diplom in physics, March 16th, 2004
- obtained from **Rheinische Friedrich–Wilhelms–Universität, Bonn**, Germany
- grade average of "1.0 mit Auszeichung" ("very good with distinction")
- Thesis supervisor: Prof. Dr. Peter Schneider
- Thesis title:
  ### *The Dark Clump near Abell 1942: Dark Matter Halo or Statistical Fluke?*
- Thesis content:
  - weak lensing analyses of a candidate dark matter halo with an abnormally high mass–to–light ratio in ground–based and space–based imaging

Abitur, June 10th, 1998
- grade average of 1.7 ("good plus")
- Freiherr–vom–Stein–Gymnasium, Leverkusen, Germany (1989-93, 96-98)
- Little Cypress–Mauriceville Senior High School, Orange, Texas, U.S.A. (1993-96)

HONORS:

June 2001 - March 2004: scholar of the **Studienstiftung des deutschen Volkes** (German National Merit Foundation)

June 2001: student attendant of the 51. Meeting of Nobel Laureates in Lindau

April 1997: scholarship of the **Carl–Duisberg–Gesellschaft** for a one–week visit to the Deutsches Museum, München

REFEREED PUBLICATIONS:

Best, P. N., **von der Linden, A.**, Kauffmann, G., Heckman, T. M., Kaiser, C. R.: *On the prevalence of radio–loud AGN in brightest cluster galaxies: implications for AGN heating of cooling flows.* MNRAS, 2007, 379, 894.

von der Linden, A., Best, P. N., Kauffmann, G., White, S. D. M.: *How special are Brightest Group and Cluster Galaxies?* MNRAS, 2007, 79, 867.

De Lucia, G., Poggianti, B. M., Aragón-Salamanca, A., White, S. D. M., Zaritsky, D., Clowe, D. I., Halliday, C., Jablonka, P., **von der Linden, A.**, Milvang-Jensen, B., Pello, R., Rudnick, G., Saglia, R., Simard, L.: *The build–up of the colour–magnitude relation in galaxy clusters since $z \sim 0.8$.* MNRAS, 2007, 374, 809.

von der Linden, A., Erben, T., Schneider, P., Castander, F. J.: *The dark clump near Abell 1942: dark matter halo or statistical fluke?* A&A, 2006, 454, 37.

Poggianti, B. M., **von der Linden, A.**, De Lucia, G., Desai, V., Simard, L., Halliday, C., Aragón-Salamanca, A., Bower, R., Varela, J., Best, P., Clowe, D. I., Dalcanton, J., Jablonka, P., Milvang-Jensen, B., Pello, R., Rudnick, G., Saglia, R., White, S. D. M., Zaritsky, D.: *The Evolution of the Star Formation Activity in Galaxies and Its Dependence on Environment.* ApJ, 2006, 642, 188.

NON–REFEREED PUBLICATIONS:

von der Linden, A., Best, P., Kauffmann, G.: *"Radio–active" Brightest Cluster Galaxies.* Proceedings of the conference: From Dark Halos to Light, XXVIth Astrophysics Moriond Meeting, La Thuile, Italy, 2006.

von der Linden, A., Poggianti, B. M., White, S. D. M., Kauffmann, G.: *Star formation activity in galaxy clusters near and far.* AN, 2005, 326, 519.

Price, A., et al. (**von der Linden, A.** 42nd of 44 authors) *GRB030329: Multicolor Light Curve and Ionospheric Detection.* Informational Bulletin on Variable Stars, 2003, 5415, 1.